INFORMATION TO USERS

University of Alberta

MODELLING CREEP DEFORMATION IN FLOATING ICE

By

Karen Anne van Steenis ©

A thesis submitted to the Faculty of Graduate Studies and Research in partial fulfillment
of the requirements for the degree of Master of Science

in

Water Resources Engineering

Department of Civil & Environmental Engineering

Edmonton, Alberta

Spring 2001

0-612-60509-4

Canada

University of Alberta

Library Release Form

Name of Author: Karen Anne van Steenis

Title of Thesis: Modelling Creep Deformation in Floating Ice

Degree: Master of Science

Year this Degree Granted: 2001

Permission is hereby granted to the University of Alberta Library to reproduce single copies of this thesis and to lend or sell such copies for private, scholarly or scientific research purposes only.

The author reserves all other publication and other rights in association with the copyright in the thesis, and except as herein before provided, neither the thesis nor any substantial portion thereof may be printed or otherwise reproduced in any material form whatever without the author's prior written permission.

K van Steenis

2 Peace River Drive
Devon, Alberta
T9G 1N4

Date: *March 2, 2001*
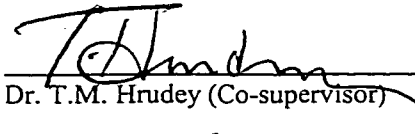
University of Alberta

Faculty of Graduate Studies and Research

The undersigned certify that they have read, and recommend to the Faculty of Graduate Studies and Research for acceptance, a thesis entitled **Modelling Creep Deformation in Floating Ice** submitted by **Karen Anne van Steenis** in partial fulfillment of the requirements for the degree of **Master of Science** in **Water Resources Engineering**.
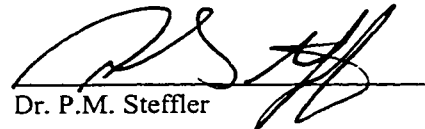
Dr. F.E. Hicks (Supervisor)

Dr. T.M. Hrudey (Co-supervisor)

Dr. A.W. Lipsett

Dr. P.M. Steffler

Date: March 1, 2001

ABSTRACT

A two dimensional axisymmetric finite element model was developed to examine the behaviour of a homogeneous, transversely isotropic, infinite ice cover under long term loading. A power law relationship was used to predict incremental creep strains at each time step and a 4th Order Runge-Kutta method was used to advance the solution through time. The creep parameters consisted of a coefficient (η) and exponent (n). Using experimental field data, the model was calibrated against 33 tests, of which most were either constant load or increasing load tests. The values obtained for η consistently ranged from 1.5×10^{-25} to 2.5×10^{-25} $s^{-1}Pa^{-n}$, and n ranged from 3.02 to 3.50. Young's modulus (E) was also calibrated, with values obtained ranging from 0.1×10^{9} to 5.0×10^{9} Pa.

The power law was found to be an acceptable method for predicting the creep behaviour of ice for the types of situations examined here.

ACKNOWLEDGEMENTS

TABLE OF CONTENTS

LIST OF TABLES

LIST OF FIGURES

LIST OF PLATES

LIST OF SYMBOLS

The following symbols are used:

A is the area being loading;

A_0 is a function of y_0 used in the Bessel function equations (Appendix D);

A_a is any numerical value in a matrix (Appendix A);

A' is a constant (Barnes *et. al.*, 1971);

A'' is a constant (Barnes *et. al.*, 1971);

a is the length of an element ($a = r_2 - r_1$);

$a_0 - a_6$ are polynomial coefficients (Hicks and Fayek, 1999);

B is a constant (Michel and Gagnon, 1975);

$B_1 - B_5$ are constants (coefficients used in chapter 3 by various researchers);

B_a is any numerical value in a matrix (Appendix A);

$B(T)$ is a function of temperature (Szyszkowski *et. al.*, 1985);

b is the ratio of radius of load to characteristic length of the ice (α/l);

$b_1 - b_3$ are constants (used in chapter 3 by various researchers);

C is in-plane stiffness;

C_a is any numerical value in a matrix (Appendix A);

D is bending stiffness;

D_a is any numerical value in a matrix (Appendix A);

$d_1 - d_2$ are constants (exponents on stress quantities, chapter 3);

d^* is ice grain size;

E is Young's modulus of elasticity;

E_1, E_2 are elastic moduli (spring constants);

E_a is any numerical value in a matrix (Appendix A);

E_L is the lower bound for calibrated values of E;

E_T is a constant (Szyszkowski *et. al.*, 1985);

E_U is the upper bound for calibrated values of E;

e an index referring to an individual element in the finite element model;

F_a is any numerical value in a matrix (Appendix A);

F_i is a body force;

f_r is a slope in the radial direction (4th order Runge-Kutta method);

f_θ is a slope in the tangential direction (4th order Runge-Kutta method);

$f(p,s)$ is any function in a p,s coordinate system (Gaussian quadrature);

$f(t)$ is a function of time (Szyszkowski *et. al.*, 1985);

G is the rigidity modulus of ice;

G_a is any numerical value in a matrix (Appendix A);

H_a is any numerical value in a matrix (Appendix A);

h is the thickness of the ice cover (elastic plate);

I is an integrand (Gaussian quadrature);

I_a is any numerical value in a matrix (Appendix A);

i is a counting index;

J_a is any numerical value in a matrix (Appendix A);

j is a counting index;

K is the bulk modulus of ice;

K_0-K_2 are constants (coefficients used in chapter 3 by various researchers);

K_a is any numerical value in a matrix (Appendix A);

K_c is the fluidity coefficient;

K_{ij} is a value in the i,j location in the global stiffness matrix;

k^u_{ij} is a value in the i,j location in the horizontal element stiffness matrix;

k^w_{ij} is a value in the i,j location in the vertical element stiffness matrix;

$k^w_{f\,ij}$ is a value in the i,j location in the foundation element stiffness matrix;

k_1-k_2 are constants (coefficients used in chapter 3 by various researchers);

L is the diameter of a plate;

L_a is any numerical value in a matrix (Appendix A);

l is the characteristic length of the ice cover;

m is a constant (Szyszkowski *et. al.*, 1985);

m_1, m_2 are the number of sampling points for Gaussian quadrature;

N is the number of interpolation functions;

N_e is the total number of elements in a finite element formulation;

N_n is the total number of nodes in a finite element formulation;

n is a material parameter for ice (creep exponent);

n_1-n_9 are constants (creep exponents used in chapter 3 by various researchers);

n_L is the lower bound for calibrated values of n;

n_U is the upper bound for calibrated values of n;

P is the penalty number;

P_o is a concentrated (point) load;

p is a variable for Gaussian quadrature;

p^w_i is a value in location i in the element vertical load vector;

Q is the heat of activation (also known as activation energy);

q_o is a uniform applied load (vertical);

R is the universal gas constant;

R_i is a value in location i in the global mechanical load vector;

r is the radial direction (from the centre of the load);

r_1 is the inner radius of an element;

r_2 is the outer radius of an element;

r_o is the outside radius of the farthest element from the load;

S is the total number of equations to be solved in a matrix system;

s is a variable for Gaussian quadrature;

T is temperature;

T_o is temperature in °C below zero;

T_r is relaxation time;

T_e is the time at the end of a test;

t is time;

t_i denotes the time step at which the solution is known;

t_{i+1} denotes the time step for which a solution is being calculated;

t' is a constant (Szyszkowski *et. al.*, 1985);

U is elastic strain energy density;

U is elastic strain energy;

U_1-U_3 are components of elastic strain energy;

U_f is the strain energy associated with the deflection of the foundation;

u is radial displacement (or radial displacement field);

u_1 is the radial displacement at node 1 of an element;

u_2 is the radial displacement at node 2 of an element;

u_i is the radial displacement at any node, i;

V is volume;

W is the work done on a body;

w is vertical deflection (or transverse displacement field);

w_1 is the vertical displacement at node 1 of an element;

w_2 is the vertical displacement at node 2 of an element;

w_e is elastic deflection;

w_i is the vertical displacement at any node, i;

w_r is rotation in the vertical direction (slope $= dw/dr$);

w_{r1} is the slope at node 1 of an element;

w_{r2} is the slope at node 2 of an element;

w_{ri} is the slope at any node, i;

$w_{x,y}$ is the vertical deflection of any solution (using x and y number of integration points in the radial and vertical directions, respectively);

$w_{10,10}$ is the vertical deflection of the "exact" solution (using 10 integration points in each direction);

x is a non-dimensional coordinate;

x_o is a quantity based on x, a, and r_1;

y is a non-dimensional coordinate;

y_0 is any variable in the Bessel function equations (Appendix D);

z is the transverse direction;

z_0 is distance measured up from the bottom of an ice sheet;

α	is the radius of a load;
α_0	is a constant (Barnes *et. al.*, 1971);
β	is an angle in the Bessel function equations (Appendix D);
Δt	is a time step increment;
$\Delta t_1, \Delta t_2$	are unequal time step increments;
δ	is a least squares value;
ε	is strain (uniaxial);
$\dot{\varepsilon}$	is strain rate (uniaxial);
ε_0	is instantaneous strain;
$\dot{\varepsilon}_0$	is the proof strain rate;
ε^c	is creep strain;
ε_c	is an average strain;
$\dot{\varepsilon}^c$	is creep strain rate;
$\dot{\varepsilon}_e$	is effective shear strain rate;
ε_i	is initial elastic settlement;
ε_{ij}	are elastic strains;
$\dot{\varepsilon}_n$	is a material parameter in the creep model;
ε_r	is total strain in the radial direction;
ε_r^c	is creep strain in the radial direction;
ε_r^e	is elastic strain in the radial direction;
$\dot{\varepsilon}_r^c$	is creep strain rate in the radial direction;
$\varepsilon_{r\theta}$	is shear strain;

$\dot{\varepsilon}_s$ is a secondary creep strain rate;

$\dot{\varepsilon}_z^c$ is creep strain rate in the z direction;

ε_θ is total strain in the tangential direction;

ε_θ^c is creep strain in the tangential direction;

ε_θ^e is elastic strain in the tangential direction;

$\dot{\varepsilon}_\theta^c$ is creep strain rate in the tangential direction;

Φ_i is a value in location i in the vector of unknowns;

ϕ is an interpolation function for the transverse direction;

γ is the subgrade modulus (unit weight of water);

$\dot{\gamma}$ is minimum shear strain rate;

η is a viscosity constant (creep coefficient);

η_0 is viscosity;

η_1, η_2 are viscosity moduli (dashpot constants);

η_L is the lower bound for calibrated values of η;

η_U is the upper bound for calibrated values of η;

φ is an interpolation function for the radial direction;

κ^c is total creep curvature;

κ_r^c is creep curvature in the radial direction;

κ_θ^c is creep curvature in the tangential direction;

μ is a coefficient in the Bessel function equations (Appendix D);

ν is Poisson's ratio;

Π is the potential energy function;

θ	is an angle in Bessel function equations (Appendix D);
ρ	is a non-dimensional coordinate;
ρ_i	is density of ice;
ρ_w	is density of water;
σ	is stress (uniaxial);
σ_e	is effective shear stress;
σ_n	is a material parameter in the creep model;
σ_r	is radial stress;
σ_{rz}	is transverse shear stress;
σ_T	is tensile strength of ice;
σ_z	is normal stress;
$\sigma_{\theta z}$	is tangential shear stress;
σ_θ	is tangential stress;
σ_0	is proof stress;
$\tilde{\sigma}$	is a resultant stress (function of σ_r and σ_θ);
τ	is shear stress;
τ_c	is time required for ice deflection to reach twice the elastic deflection;
ϖ_i, ϖ_j	are weighting factor for Gaussian quadrature;
ω	is a function of y_0 used in the Bessel function equations (Appendix D);
ξ	is a coefficient in the Bessel function equations (Appendix D);
$[K]$	is the global stiffness matrix;
$[K^u]$	is the global horizontal stiffness matrix;

$[k^u]$	is the element horizontal stiffness matrix;
$[K^w]$	is the global vertical stiffness matrix;
$[k^w]$	is the element vertical stiffness matrix;
$[K_f^w]$	is the global elastic foundation stiffness matrix;
$[k_f^w]$	is the element elastic foundation stiffness matrix;
$\{P^u\}$	is the global horizontal load vector;
$\{p^u\}$	is the element horizontal load vector;
$\{P^w\}$	is the global vertical load vector;
$\{p^w\}$	is the element vertical load vector;
$\{Q^c\}$	is the global creep load vector;
$\{q^c\}$	is the element creep load vector;
$\{q^{uc}\}$	is the element horizontal creep load vector;
$\{q^{wc}\}$	is the element vertical creep load vector;
$\{R\}$	is the global mechanical load vector;
$\{\Phi\}$	is the vector of unknowns;

1.0 INTRODUCTION

The creep of materials can have a significant effect on engineering structures. Creep can be defined as the time dependent plastic deformation of a material, which is also influenced by temperature (Beer and Johnston, 1992). Since ice is a material that exists relatively close to its melting point, the effects of creep can become much more significant than the material's elastic response to loading (Ashton, 1986).

The study of creep is important because it is often necessary to be able to predict a material's response to stationary loading over time. Numerical modelling of this behaviour can be a useful tool in predicting the response of a material to loading, allowing the user to predict when failure might occur, and enabling one to remove the load before failure actually does occur. Ice is often subjected to long term loading in construction applications, as well as numerous other types of situations described below.

1.1 Construction Applications

In northern regions, ice is often used as a construction platform, and therefore it is important to be able to predict the deflection of the ice cover over time in response to long term loading. Some typical construction scenarios include cranes lifting materials, material storage, and the parking of loaded vehicles on the ice cover (Hicks and Fayek, 1999). According to Kerr (1975), logging operations use ice platforms to store materials and construction of river structures can also be performed from an ice platform.

Another common use of ice covers is as a platform on which to erect drilling rigs in the Arctic (Ekelund and Masterson, 1980; Masterson and Kivisild, 1980; Baudais *et. al.*, 1976). Sea ice is thickened by flooding or spray ice production and drilling rigs

1

weighing in the order of 845 tons (Baudais *et. al.*, 1976) to 1350 tonnes (Ekelund and Masterson, 1980) can be constructed on these ice platforms. These platforms must support their large loads for one to three months or longer (Masterson and Kivisild, 1980). It is important to be able to calculate the deflection of the platform as time progresses and to predict when the loss of freeboard will occur, as this will likely make people working on the platform uncomfortable; loss of freeboard will likely happen before the complete failure of the ice cover (Masterson and Kivisild, 1980). With deflections greater than the freeboard, allowing water to fill the deflection bowl, the bearing capacity of the ice could also be reduced (Beltaos, 1978).

1.2 Other Applications

Ice platforms can also experience long term loading in situations other than construction. Some examples include aircraft storage, temporary car parking lots, and festivals on an ice cover.

Freshwater lake or river ice, as well as sea ice, have been used as airfields in northern climates for many years (Assur, 1956; Barthelemy, 1992). After landing on an ice sheet, an aircraft may need to be parked for a period of time. Assur (1956) states that parking aircraft on an ice cover is acceptable under certain conditions, but that if deflection of the ice cover becomes noticeable, the aircraft should be moved immediately. Barthelemy (1992) developed parking curves for various weights of aircraft, giving the allowable parking time based on sea ice thickness, using the criterion that the ice sheet is allowed to deflect 10% of its thickness.

Another example of long term loading of an ice cover is the Blackstrap Lake (Saskatchewan) parking lot (Meneley, 1974). This parking lot was designed for the Canada Winter Games, as parking areas on land were insufficient for the number of spectators expected at the games. This parking lot held over 4000 parked cars at a time in February 1971 (Meneley, 1974). Keeping deflections less than the freeboard of the ice cover, and therefore keeping water from appearing on the ice surface, was considered essential in order to keep the general public feeling safe. This was accomplished by continuously measuring the ice deflection and controlling parking and traffic (Meneley, 1974), but a predictive model could have been very useful in this situation.

Ice covers have also been used as a platform on which a festival was held in February of 1985 and 1986, as described by Sinha (1990, 1992). The Winterlude festival in Ottawa, held on Dow's Lake, included a snow sculpture competition as well as a large opening ceremony on the ice cover. Each year the snow sculptures were restricted in size and shape and were distributed across the ice cover. The opening ceremony in 1985 involved a concert on two large stages placed on the ice cover near the edge of the lake, and approximately 60,000 spectators were in attendance (Sinha, 1990). For the 1986 festival the stage was constructed in the middle of the lake but, unfortunately, when the opening night concert was about to begin 40,000 people rushed to the stage causing large deflections. The ice surface became flooded with water, forcing organizers to cancel the show (Sinha, 1992). This is another situation in which the prediction of time dependent deflection could be very useful.

1.3 Organization of Thesis

This thesis contains 7 chapters. Chapter 1 contains a brief introduction. Chapter 2 describes the physical behaviour of ice under both short and long term loading. The different types of creep (primary, secondary and tertiary) are discussed. Also described are the physical properties of different types of ice. Chapter 3 describes some of the previous model studies performed on the creep of ice.

In chapter 4, the formulation of the finite element model is discussed. A rheological model for ice is described. The assumptions used in this model are discussed, followed by the Principle of Minimum Potential Energy and the Rayleigh-Ritz Method. The finite element system of equations to be solved is described along with the interpolation functions used by the model. Expressions for various model elements are developed, including the element and foundation stiffness matrices, and the mechanical load and creep load vectors. Two choices of method for estimating the creep strains over time are described: the Euler method, and the 4th Order Runge-Kutta method. Finally, the implementation of the boundary conditions through the use of the penalty method is discussed, followed by various issues pertaining to the boundary elements.

Chapter 5 contains sections on the verification of various parts of the finite element model. An analytical solution and an elastic behaviour test for a simple elastic plate are illustrated. A pure bending test and an artificial creep strain test for an elastic plate with creep are summarized. An analytical solution for an elastic plate on an elastic foundation is outlined, along with an elastic behaviour test. The spatial and temporal discretization scales for an elastic plate on an elastic foundation with creep are determined for both concentrated and distributed loading cases. Also included is a

discussion on the number of integration points required for reasonable accuracy within the numerical solution.

In chapter 6, the finite element model is applied to large scale load test data from two sources. The sources of the field data are described, along with the justification for the exclusion of certain sets of test data. A summary of the spatial and temporal discretization scales to be used for the model application is given. A brief discussion on the model calibration parameters is given. Calibration of two creep parameters and one elastic parameter is performed for various types of loading situations: constant loading, increasing loading, and other loading. An attempt to relate the calibrated parameters to ice temperature is made, and a summary of the findings from this chapter is presented.

Chapter 7 contains a summary of each chapter, and discusses the assumptions and decisions that were made as the model was developed and verified. A discussion on the conclusions obtained from the model application is presented. Some recommendations for future research are discussed.

2.0 PHYSICAL BEHAVIOUR OF ICE UNDER LOADING

2.1 Introduction

Ice exhibits different behaviour under short term loading and long term loading conditions. A long term load is considered to be any load present on a floating ice cover for longer than about ten minutes (Beltaos, 1978). According to Michel (1978a), when ice is loaded at a rapid rate, it will behave perfectly elastically; however, when ice is loaded slowly, or a static load is present, the ice will undergo creep and permanent deformation will occur. For any material, creep can depend on several factors including the magnitude and duration of loading, the temperature, and the dimensions and orientation of the ice grains (Puswewala and Rajapakse, 1993).

This chapter begins with a brief explanation of the behaviour of ice under short term and long term loading conditions, and the primary, secondary and tertiary stages of creep are explained. Some of the failure criteria used in practice are discussed. The physical properties of various types of ice (lake, river, and sea) are discussed, and some typical values of these properties are reported. Finally, a brief section on ice crystallography is presented.

2.2 Behaviour of Ice under Short Term Loading

A brief overview of the behaviour of ice under short term loading is presented here, and is summarized from Ashton (1986). Under short term loading (in the order of a few minutes or less) a floating polycrystalline ice sheet behaves elastically; it can be considered as an elastic plate on an elastic foundation.

6

When a vertical load is placed on a floating ice sheet for a short period, the elastic

deflection, w, is governed by the following equation (thin plate theory):

$$\frac{D}{\gamma}\nabla^4 w + w = \frac{q_o}{\gamma} \tag{2.2.1}$$

where D is the bending stiffness of the ice:

$$D = \frac{Eh^3}{12(1-v^2)} \tag{2.2.2}$$

and where E is Young's modulus of elasticity, h is the ice thickness, v is Poisson's ratio,

γ is the foundation modulus (in this case, the unit weight of water), and q_o is the applied

vertical load. Thus, for any load configuration the deflection is governed by D/γ which

has the units of length raised to the fourth power.

The characteristic length of the ice cover, l, is defined as:

$$l = \left(\frac{D}{\gamma}\right)^{\frac{1}{4}} \tag{2.2.3}$$

Gold (1988) reported that the characteristic length is not strongly dependent on the elastic

properties of the ice; it is much more dependent on the ice thickness. From examination

of previous observations on the deflection of ice covers under moving and static loading,

Gold (1988) observed that the characteristic length, l, for columnar freshwater ice ranged

from about $15.9h^{0.75}$ to $17.5h^{0.75}$, where both h and l are measured in metres. This range

can be extended to $12.6\ h^{0.75}$ for granular ice. Using the following empirical relationship

for l was found to be acceptable for the short term loading of freshwater ice (Gold, 1971):

$$l = 16h^{0.75} \tag{2.2.4}$$

7

The elastic deflection of an infinite ice sheet under a point load, w_e, can be calculated from:

$$w_e = \frac{P_o}{8\gamma l^2}$$ (2.2.5)

where P_o is the concentrated load. When considering a point at a distance r away from the centre of loading, thin plate theory is not valid if $r/l < 0.5$. Thin plate theory cannot accurately predict stresses in this region, and thick plate theory must be used instead (see Ashton, 1986). Hicks and Fayek (1999) have fit a polynomial to calculate the elastic deflection of an ice cover under a point load, valid for the range of $r/l < 7$ (the influence of the load is negligible beyond $r/l > 5$). The deflection, w, at any point r can be found from:

$$\frac{w}{w_e} = a_0 + a_1\left(\frac{r}{l}\right) + a_2\left(\frac{r}{l}\right)^2 + a_3\left(\frac{r}{l}\right)^3 + a_4\left(\frac{r}{l}\right)^4 + a_5\left(\frac{r}{l}\right)^5 + a_6\left(\frac{r}{l}\right)^6$$ (2.2.6)

where $a_0 = 1.00$, $a_1 = -0.195$, $a_2 = -0.315$, $a_3 = 0.171$, $a_4 = -0.0356$, $a_5 = 0.00342$, and $a_6 = -0.000126$.

Hicks and Fayek (1999) also fit a polynomial to Nevel's (1968) curve describing the stress, σ, caused by the deflections for thin plate theory, valid when $r/l > 0.5$:

$$\frac{\sigma h^2}{P_o} = \left[\frac{1.305 - 0.0522(r/l) + 0.0120(r/l)^2}{1 + 0.870(r/l) - 0.223(r/l)^2 + 0.0200(r/l)^3}\right]^2$$ (2.2.7)

2.3 Behaviour of Ice under Long Term Loading

The behaviour of ice under long term loading is briefly described here. For the purposes of this discussion, any stationary load present on an ice cover for more than

about ten minutes is considered to be a long term load. This section summarizes Michel's (1978a) description of the ductile behaviour of ice.

Ice, as a crystalline material, contains many imperfections in its lattice structure including point defects, line defects and stacking faults. A point defect occurs when an atom is missing from a lattice site, weakening the crystal. A dislocation is small compared to the size of visible crystals, but large on an atomic scale. Some types of dislocations include edge, screw and mixed dislocations.

When a crystalline material is loaded the elastic response is followed by an increase in deflection over time, known as creep. Creep deflection will not be recovered upon removal of the load as elastic deflection will. This increase beyond the elastic deflection is caused by dislocation movement through the stressed crystal. In ice, the creep mechanism is generally a climbing movement (movement perpendicular to the slip plane). Climb can only occur by thermally activated mass transport (diffusion), which is very slow compared to the slip process. Other types of creep mechanisms observed have been:

"grain boundary slip, cavity formation at the grain boundaries, formation

of low-angle boundaries, polygonization and recrystallization" (Michel,

1978a).

Recrystallization, by grain boundary migration or new crystal growth, was observed when ice deflections were large.

2.4 Types of Creep

Michel (1978a) gives a description of the types of creep mechanisms present during the primary, secondary and tertiary creep stages. These mechanisms include:

"elastic deformation and plastic deformation by climb of dislocation ...observed by grain boundary slip, cavity formation at the grain boundaries, formation of low-angle boundaries, polygonization and recrystallization. Recrystallization was noticed mainly when the ice deformations became large. It either took the form of grain boundary migration, i.e. some grains growing at the expense of others, or the formation of completely new crystals (Michel, 1978a)."

Increasing numbers of microcracks (cracks within a crystal) also formed at certain levels of compressive stress during primary creep, but stopped if the stress did not increase beyond a certain level (Michel, 1978a). This process continues at higher stresses, eventually leading to accelerated creep and failure of the ice (Michel, 1978a). According to Ashton (1986), at temperatures below -10°C the creep of polycrystalline ice is dominated by slipping along the basal planes; above -10°C, grain boundary slip and melting at joints is the dominant creep mechanism.

Figure 2-1 shows a typical creep curve for polycrystalline ice, and illustrates the three stages of creep: primary, secondary and tertiary creep. As can be seen from this figure, primary (or transient) creep begins following the elastic deformation with a decreasing strain rate. Ashton (1986) states that in this stage, the creep rate is much more dependent on the stress than on the temperature. According to Michel (1978a), primary creep is a visco-elastic process and can include an increasing number of mobile

10

dislocations or cracking. Strain hardening occurs when impurities or grain boundaries stop the dislocation movement. When loading is initially applied, or more loading is added, the creep of the ice is characterized by retarded elasticity (Michel and Gagnon, 1979).

At low stresses and temperatures secondary and tertiary creep may never be achieved, and the creep curve may appear to have a decaying form (Puswewala and Rajapakse, 1993). If the stress level is high enough, a steady state creep rate will be attained, known as secondary creep.

Secondary (or stationary) creep is characterized by an essentially constant strain rate. It is a purely viscous process and recrystallization may or may not occur during this stage (Michel, 1978a). According to Hult (1966), the strains developed in numerous materials during secondary creep are much larger than those developed during primary creep, and a straight line can be used to approximate the creep curve.

Under high stresses, after a period of steady creep, the creep rate can eventually begin to accelerate (tertiary creep) and ultimately failure will occur (Morgenstern *et. al.*, 1980). Azizi (1989) states that for ice, the secondary creep stage is often very brief and becomes an inflection point on the strain-time curve between primary and tertiary creep.

Tertiary (or accelerating) creep signals the onset of failure. Viscous strain softening occurs, and there is no elasticity remaining in the ice (Michel, 1978a). An increase in crack formation can accelerate deformation and cause the ice to rupture (Michel, 1978a).

11

2.5 Short Term Failure Criteria

Various failure criteria have been proposed for the short term loading of floating ice covers. According to Barthelemy (1992), a failure criterion is based on either stress or deflection requirements. Often it possible to keep stresses within allowable limits, but keeping deflections within safe limits can be much more difficult (Masterson and Kivisild, 1980).

Several short term failure criteria are discussed in detail by Hicks and Fayek (1999) including Gold's safe criterion, Michel's first crack criterion, the freeboard criterion, and Beltaos' strain energy criterion. For concentrated load, P_o, Gold's (1971) safe criterion suggests:

$$P_o \leq 350h^2 \tag{2.5.1}$$

where P_o is in kN and the ice thickness, h, is in metres. For any load, few failures are reported when the ice thickness is greater than that specified using equation (2.5.1); however, the data Gold examined does not extend beyond around 300 to 400 kN, and this criterion should not be extrapolated to loads greater than this.

According to Michel (1978a), one failure criterion for the short term bearing capacity of ice is to limit the load to that which produces the first radial crack in the ice cover. It is easy to verify when the first crack has occurred in the field, and this criterion provides a factor of safety of about two. Michel (1978a) proposed the following relationship between grain size, d^*, and tensile strength, σ_T, of the ice under short term loading:

$$\sigma_T = 79.4\sqrt{\frac{1 - 0.9 \times 10^{-3}T}{d^*}} \tag{2.5.2}$$

where T is temperature (°C), d^* is in mm and σ_T is in kPa. Typical values of d^* range from 1 to 4 mm for snow ice, and from 5 to 25 mm for columnar ice (Michel, 1978a).

Several researchers (e.g. Frederking and Gold, 1976) have suggested a freeboard criterion to determine the bearing capacity of ice covers. This criterion limits the maximum allowable deflection under the load to the freeboard of the ice cover. Aside from stress and strain considerations, there are several reasons which make this a practical design criterion. Once the freeboard has been exceeded, water can flow onto the ice cover through cracks; this water can:

> "interfere with operations, damage stored material, and freeze around equipment or stores, making removal difficult. If freezing does not occur, the flood water must be considered as a load effectively neutralizing part of the buoyant force over the area that it covers (Frederking and Gold, 1976)."

The additional load resulting from surface water can increase the rate at which the ice is creeping, hastening the failure of the ice cover (Michel, 1978a). This water also increases the temperature of the upper portion of the ice, which could result in a reduction in strength properties (Frederking and Gold, 1976). In order to determine the allowable concentrated load, P_o, the freeboard is set equal to the elastic deflection (equation (2.2.5)), giving:

$$P_o \leq 8\gamma l^2 \left(1 - \frac{\rho_i}{\rho_w}\right) \qquad (2.5.3)$$

where γ is the unit weight of water, l is the characteristic length of the ice cover, ρ_i is the density of the ice, and ρ_w is the density of water (Hicks and Fayek, 1999). With l

calculated from equation (2.2.4), and the density of ice assumed to be 92% of the density of water, this reduces to:

$$P_o \leq 1600 h^{10/4} \qquad (2.5.4)$$

where h is the ice thickness in metres and P_o is in kN.

Beltaos (1978) proposed the strain energy criterion as a failure criterion for long term loading; it should also be applicable for short term loading if the strain energy is independent of time and actually representative of a material property of ice. According to Beltaos (1978):

"failure occurs when the maximum work done by internal stresses on a

unit volume of material equals or exceeds a critical value."

The cumulative strain energy at the onset of tertiary creep, $300h^{5/2}$, can be equated to the product of the concentrated load, P_o (kN), and the maximum elastic deflection, w_e, ultimately giving:

$$P_o \leq 2455 h^2 \qquad (2.5.5)$$

where h is the ice thickness in metres and the characteristic length was calculated from equation (2.1.4) (Hicks and Fayek, 1999).

2.6 Long Term Failure Criteria

The strain energy criterion has been proposed by Beltaos (1978) as a failure criterion for the bearing capacity of ice under long term loading. According to Beltaos and Lipsett (1979):

14

"the onset of failure occurs when the work done by the load reaches a critical value. This value is proportional to the ice thickness raised to the power 5/2."

They analyzed bearing capacity test data obtained from 1974 to 1977 and found that an empirical relationship exists between deflection and time (for instantaneously applied constant loads) of the following form:

$$\frac{w}{w_e} = 1 + \sqrt{\frac{t}{\tau_c}} \tag{2.6.1}$$

where w is the deflection under the centre of the load, w_e is the elastic deflection (equation (2.2.5)), t is time, and τ_c is the time needed to reach twice the elastic deflection. This relationship was found to adequately represent the deflection over time for these types of loading conditions (Beltaos and Lipsett, 1979).

From the 25 sets of data analyzed by Beltaos and Lipsett (1979), τ_c was found to range from 40 to 210 minutes, and Young's modulus ranged from 1.0×10^9 to 4.8×10^9 Pascals. They believed these variations were related to load intensity and temperature dependent variations in the ice properties.

According to Beltaos (1978), the deflection at failure is smaller for concentrated loads than for distributed loads, which is believed to be a result of the failure mode; concentrated loads often experience punching failure while distributed loads experience bending failure.

15

2.7 Physical Properties of Ice

The various physical properties of ice influence the elastic and plastic behaviour of the material. Some of these properties include Young's modulus (E), Poisson's ratio (ν), grain size (d^*), and ice density (ρ_i). These properties can have different values, depending on the type of ice and the temperature at which it exists. Experimental evidence indicates that:

"the crystal structure as well as the mechanical properties are significantly affected by its temperature and stress history as well as the meteorological and hydrodynamic conditions existing at the time of its formation (Szyszkowski et. al., 1985)."

According to Ladanyi and Saint-Pierre (1978), sea ice is heterogeneous and anisotropic, and because the ice crystals can be quite large, mechanical properties can also be scale dependent.

Ice density remains relatively constant, ranging from about 917 kg/m^3 at 0 °C and varying almost linearly to about 921 kg/m^3 at -30 °C (Ashton, 1986). No significant differences could be detected between densities for single crystals and columnar grained ice samples (Ashton, 1986).

It will be shown in section 6.1.4 that the behaviour of ice is much more sensitive to changes in E than changes in ν. Ashton (1986) took values from several sources to obtain average elastic constants for lake ice, and Poisson's ratio ranged from 0.314 to 0.345. Gold (1988) obtained values ranging from 0.29 to 0.43 for ν from laboratory experiments. For most situations Poisson's ratio is taken as approximately 0.333 (Beltaos, 1978).

16

The values reported for the elastic modulus, E, of ice vary greatly in the literature. According to Michel (1978a), the higher values occur when loading is rapidly applied, and the lower values when loading is slowly applied or static. Ashton (1986) found that Young's modulus for lake ice ranged from about 8.4×10^9 to 9.5×10^9 Pa. Other researchers have determined different values for E at different temperatures. Michel (1978a) gives several equations for the elastic modulus of polycrystalline ice as a function of temperature and ice type, as well as reporting on values found by Ewing et. al. (1934), Northwood (1947) and Gold (1958). These values can be seen in Figure 2-2.

The four types of ice for which Michel (1978a) has given equations for Young's modulus are S1, S2, T1, and S4. S1 ice is columnar ice with large, irregular grains that form vertically (parallel to the flow of heat). It is found in lakes, and low flowing rivers, but not in the sea. S2 ice is similar to S1, but the grains are oriented more randomly, and the size of the crystals increases with depth more rapidly than in S1 ice. The grains of S2 ice become oriented more horizontally at increasing depths, and this type of ice can be found in Arctic sea ice. T1 ice is snow ice with fine to medium grain sizes. It is formed when snow is flooded and freezes. S4 ice is congealed frazil slush, with fine to medium grain sizes. It can be found in rivers, and lakes which have an inflow of turbulent water, as well as at sea. For horizontal S1 and vertical S2 ice:

$$E = 9.62 \times 10^9 \left(1 - 1.07 \times 10^{-3} T\right) \qquad (2.7.1)$$

For vertical S1 ice: $\qquad E = 11.79 \times 10^9 \left(1 - 1.40 \times 10^{-3} T\right) \qquad (2.7.2)$

For horizontal S2 ice: $\qquad E = 9.27 \times 10^9 \left(1 - 1.36 \times 10^{-3} T\right) \qquad (2.7.3)$

and for T1 or S4 ice, with any grain orientation:

$$E = 8.93 \times 10^9 \left(1 - 1.28 \times 10^{-3} T\right) \qquad (2.7.4)$$

17

where T is the temperature in °C, and E is in Pascals.

The data points on Figure 2-2 represent elastic modulus values found for polycrystalline ice. Gold (1988) obtained values ranging from 7.6×10^9 to 12.3×10^9 Pa for laboratory grown ice at -10 °C. Tinawi and Murat (1978) give values of E for laboratory grown saline ice at several temperatures. Barthelemy (1992) gives several values of E for sea ice at different temperatures. Masterson and Gamble (1986) report values of E for flooded ice and spray ice. From these sources, it can be seen that the value of Young's modulus ranges anywhere from around 1×10^9 to 12×10^9 Pa for different ice types at different temperatures.

2.7.1 Ice Crystallography

Work was done in a cold room at the University of Alberta to qualitatively examine the crystal structure of lake and river ice with ice samples obtained in March of 2000. The ice samples were obtained from Joseph Lake (approximately 56 km southeast of Edmonton) and from the North Saskatchewan River in Edmonton upstream of the Quesnell Bridge. The ice from Joseph Lake is of interest because that was the location of the load tests performed from November 1975 to February 1976, and the data from these will be analyzed in Chapter 6. The river ice was examined for comparison purposes.

The samples were cut from the ice covers using a chainsaw (see Plate 2-1). The river sample was taken from ice approximately 38 cm thick, but the ice cover on the lake was thicker than the length of the chainsaw, and the sample (see Plate 2-2) had to be broken off at a depth of approximately 70 cm. The samples were cut into smaller sections which were then reduced to a very thin layer, using a microtome, for observation

between crossed polarized lenses. The microtome used to reduce the ice to a single layer of crystals can be seen in Plate 2-3.

Plates 2-4 and 2-5 show vertical sections through the lake and river ice samples, respectively. For an idea of the scale of the ice crystals, the upper layer of snow ice in Plate 2-4(a) is approximately 4 cm thick, and the layer of snow ice in Plate 2-5(a) is about 5 cm thick.
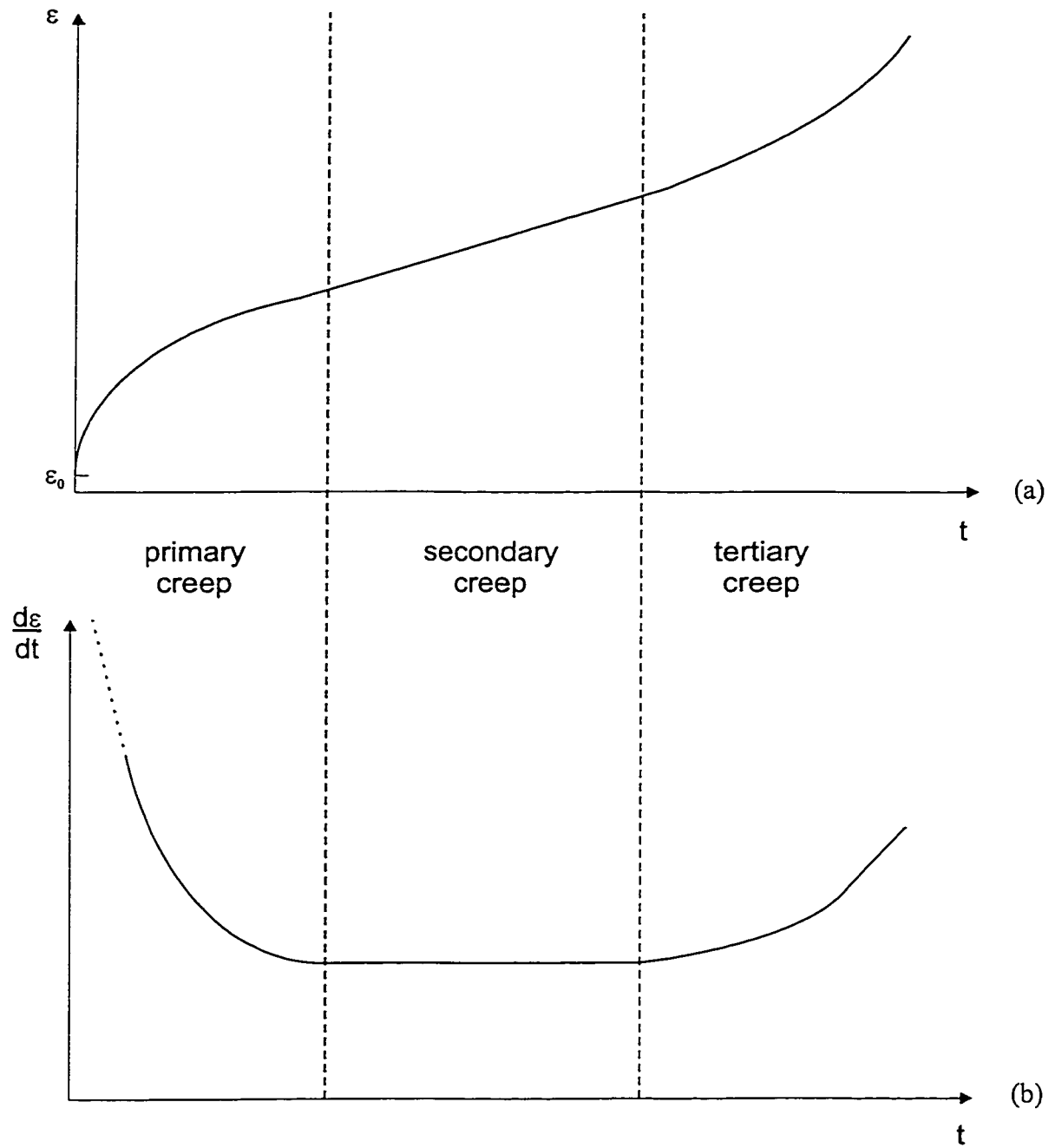
Figure 2-1: Typical creep curve for polycrystalline ice:
(a) strain, and (b) strain rate (adapted from Hult, 1966).
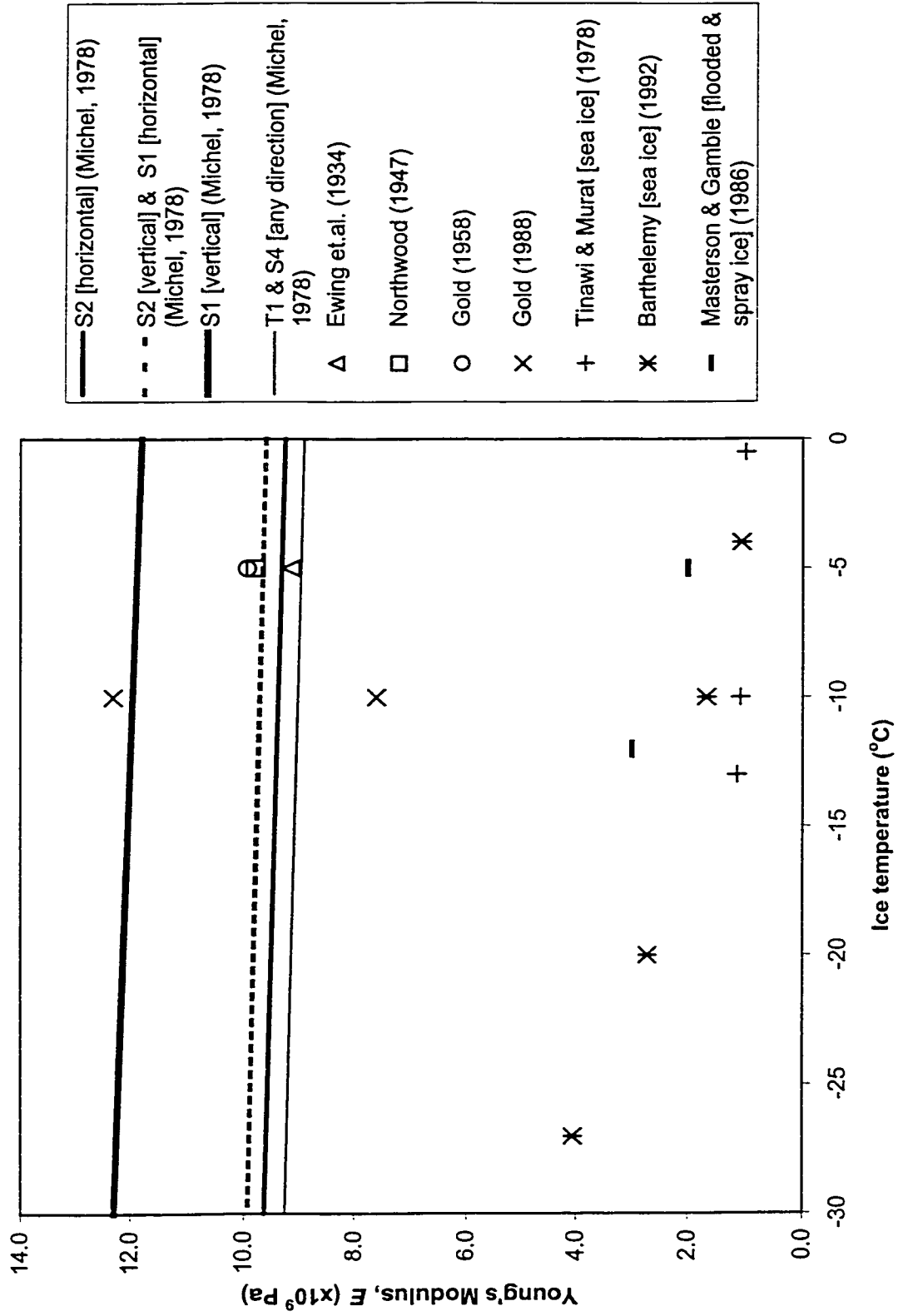
Figure 2-2: Variation in Young's modulus for different ice types as a function of ice temperature.

Plate 2-1: Cutting. an ice sample from Joseph Lake.

Plate 2-2: Ice sample from Joseph Lake.
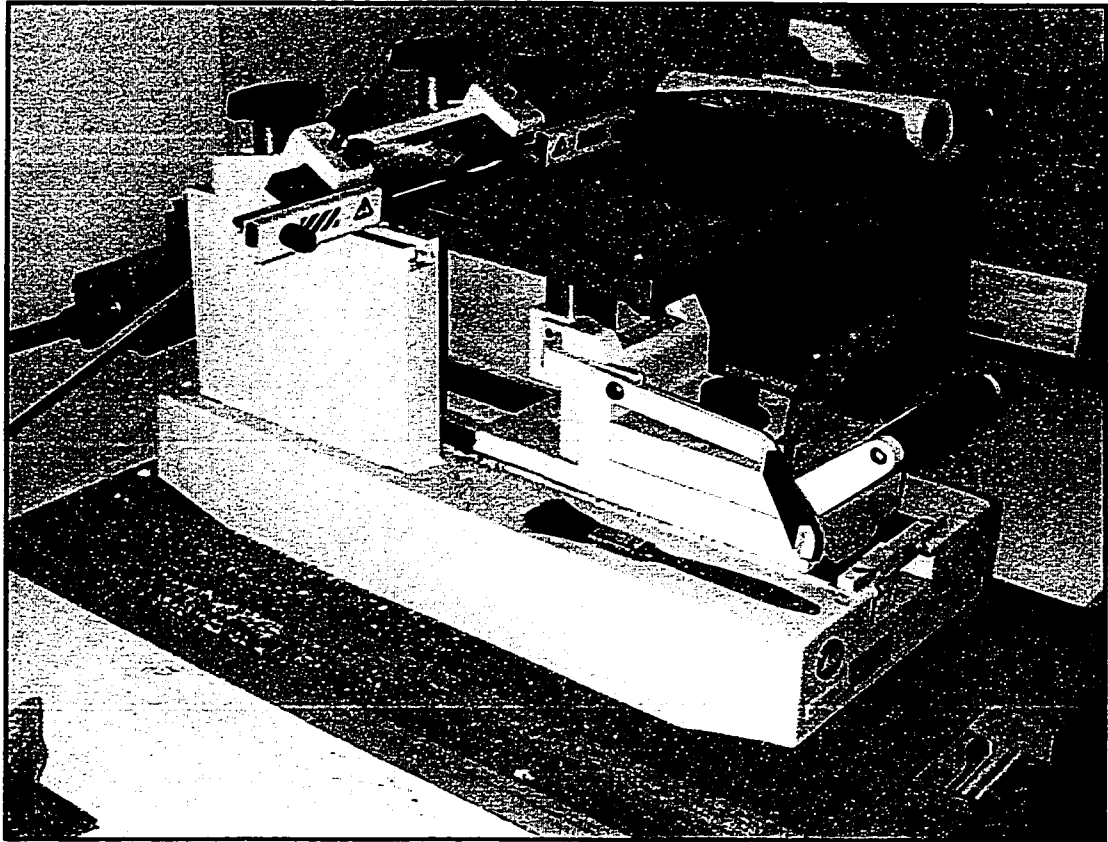
Plate 2-3: Microtome used in cold room for reducing ice samples to thin sections.
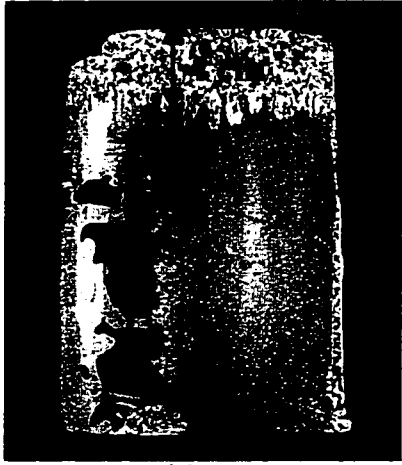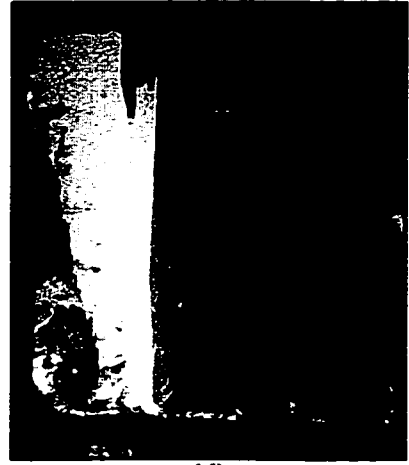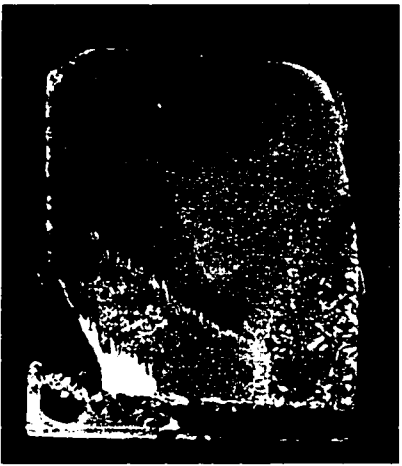
Plate 2-4: Vertical sections of ice from Joseph Lake with depth increasing from (a) to (e).
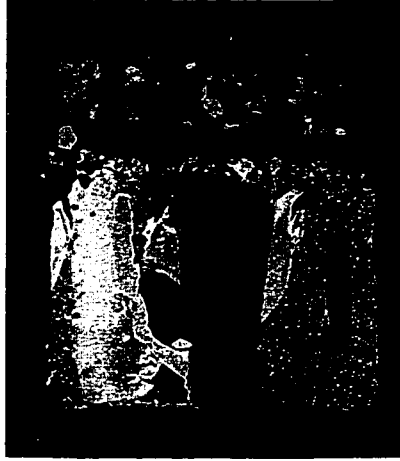
(a)
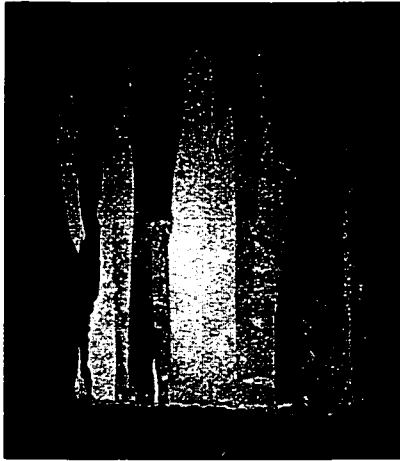
(b)

(c)

Plate 2-5: Vertical sections of ice from the North Saskatchewan River with depth increasing from (a) to (c).

3.0 PREVIOUS STUDIES MODELLING ICE CREEP

3.1 Introduction

A brief review of the literature pertaining to creep of ice and finite element modelling of this problem is presented here. Glen (1955) was one of the first to propose an empirical power law relationship between stress and strain rate for the creep of polycrystalline ice under uniaxial stress. Since then, many researchers have used the power law, or other equations, to model the creep behaviour of ice (and frozen soils) for primary and secondary creep.

Butkovich and Landauer (1959) proposed three empirical creep relationships to compare to experimental data, but found that the power law most accurately reflected their data. Mellor and Testa (1969) found that a power law relationship modelled the creep of ice under very low stresses. Barnes *et. al.* (1971) described the creep of ice using superposition. Nixon and McRoberts (1976) proposed a secondary creep power law for geotechnical applications. Tinawi and Murat (1978) performed laboratory experiments on ice beams and plates, and found that the deflection over time followed a power law. In 1979, Michel and Gagnon proposed a linear creep model, but this did not represent the behaviour of ice during primary creep very well. Masterson and Strandberg (1979) examined deflection data from an Arctic drilling platform and found that its behaviour did follow a power law. Tinawi and Murat (1979) proposed a power law for the creep behaviour of non-homogeneous floating ice sheets, and also suggested a relationship for Young's modulus as a function of location within the ice. Morgenstern *et. al.* (1980) combined the experimental data from several researchers and developed a power law relationship for ice creep. Sego and Morgenstern (1983) developed a power

law relationship for creep that was normalized to one temperature and ice grain size. Szyszkowski *et. al.* (1985) performed experiments on a simply supported rectangular column of ice, and analyzed the results using a power law. In 1989 Azizi modelled the primary creep of ice using a power law, assuming that secondary creep can be reduced to an inflection point on a deflection-time graph. Azizi and Whalley (1994) used primary creep parameters to predict secondary creep behaviour.

Other researchers have expanded these ideas to involve more complex scenarios. Michel (1978b) proposed a two dimensional model for polycrystalline ice creep which accounts for deformations within each crystal. Khoo and Hrudey (1992) examined the indentation of a floating ice sheet and the inclusion of postpeak softening. Fish (1992) and Puswewala and Rajapakse (1993) adapted models to include multiaxial states of stress. Sunder *et. al.*, (1993) examined problems which are dominated by tertiary creep. Mahrenholtz and Wu (1993) extended a one-dimensional primary creep law to three dimensions. Azuma (1995) examined the deformation of anisotropic polycrystalline ice under uniaxial loading. Meglis *et. al.* (1999) performed triaxial tests on granular ice to determine its mechanical behaviour under various confining stresses.

The remainder of this chapter will focus on research that has examined the behaviour of isotropic polycrystalline ice under uniaxial loading in the primary and secondary creep stages. For comparison purposes numerical quantities and equations have been transformed to dimensions consistent with those used in the model developed here whenever possible.

3.2 Glen (1955)

Glen believed that creep or plastic deformation of ice was primarily caused by the shear component of stress; however, as loading a specimen in uniform shear is difficult, he performed laboratory compression tests on blocks of polycrystalline ice at different stresses and at different temperatures. Stresses for these tests ranged from about 100 to 1000 kPa, and temperatures ranged from 0 to -13 °C.

In 1955, Glen proposed the following empirical power law relationship between stress and strain rate for polycrystalline ice:

$$\dot{\varepsilon} = k_1 \sigma^{n_1} \tag{3.2.1}$$

where $\dot{\varepsilon}$ is the strain rate, σ is the stress, and n_1 and k_1 are constants. Glen found that while n_1 did not vary noticeably with temperature, k_1 did vary with temperature according to an Arrhenius (Zumdahl, 1993) type of equation:

$$k_1 = B_1 \exp(-Q/RT) \tag{3.2.2}$$

where R is the universal gas constant, T is absolute temperature, Q is a heat of activation, and B_1 is a constant dependent on stress. From Glen's experiments, the value of Q was found to be 32 kcal/mol, n_1 was approximately 3.2, and B_1 was 7×10^{24} if the strain rate is measured in (years)$^{-1}$ and the stress in bars.

Combining equations (3.2.1) and (3.2.2), Glen's equation can also be written as:

$$\dot{\varepsilon} = 22.2 \exp(-16114/T) \sigma^{3.2} \tag{3.2.3}$$

where the temperature is measured in degrees Kelvin, the stress is measured in Pascals, and the strain rate is measured in (seconds)$^{-1}$.

The creep curves obtained by Glen were similar to curves obtained for other solid substances. The power law was found to be an acceptable model for primary and secondary creep between -13 °C to 0 °C, but not for tertiary (accelerating) creep of ice.

3.3 Butkovich and Landauer (1959)

Butkovich and Landauer performed laboratory creep tests on different types of ice, such as single crystals, glacier ice, and ice obtained from an ice plant (commercial ice), using both shear and uniaxial loading conditions. Tests were performed at high and low stresses. The low stress tests were performed at stresses ranging from around 49 to 294 kPa (0.5 to 3 kg/cm^2); these test durations were approximately five days, unless failure occurred sooner. The high stress tests were performed at stresses ranging from about 687 to 2747 kPa (7 to 28 kg/cm^2) at temperatures ranging from -4 to -6 °C, and the lower stresses in this range had test durations of about 2500 s.

Three empirical relationships were proposed to fit the creep data obtained from the shear tests including a hyperbolic sine function, a cubic polynomial, and a power law function. Of the three, a power law of the following form was found to fit the data the best:

$$\dot{\gamma} = k_2 \tau^{n_2} \tag{3.3.1}$$

where $\dot{\gamma}$ is the minimum shear strain rate, τ is the shear stress, and k_2 and n_2 are constants. The shear stress and shear strain rate can be related to uniaxial stress, σ, and uniaxial strain rate, $\dot{\varepsilon}$, using the following relationships:

$$\tau = \frac{\sigma}{\sqrt{3}} \tag{3.3.2}$$

and

$$\dot{\gamma} = \sqrt{3}\dot{\varepsilon}$$ (3.3.3)

The constants k_2 and n_2 had values of 0.863×10^{-8} and 2.96 respectively when τ was measured in kg/cm^2 and $\dot{\gamma}$ in (seconds)$^{-1}$.

Using equations (3.3.2) and (3.3.3), Butkovich and Landauer's equation (3.3.1) can be rewritten in terms of σ and $\dot{\varepsilon}$ as:

$$\dot{\varepsilon} = 1.646 \times 10^{-24} \sigma^{2.96}$$ (3.3.4)

where σ is measured in Pascals and $\dot{\varepsilon}$ is measured in (seconds)$^{-1}$.

3.4 Mellor and Testa (1969)

In 1969 Mellor and Testa performed experiments on polycrystalline ice at very low stresses (like those observed in glaciers) in the laboratory. They investigated the effects of long term uniaxial compression on homogeneous, isotropic samples of polycrystalline ice. Since large amounts of data already existed for stresses ranging from 100 to 2000 kN/m^2, the axial stresses used in these tests ranged from 9.1 to 42 kN/m^2.

The results from the experiments indicated that the secondary creep strain rate (using a simple power law such as equation (3.2.1)) was proportional to $\sigma^{1.8}$. This exponent is significantly lower than the values found for higher stresses, where the exponent ranged from 3 to 4.

These results did not conclusively establish a relationship between stress and strain rate for low stresses. Mellor and Testa believed that prolonged testing at the lowest stress might have produced a higher strain rate.

3.5 Barnes, Tabor and Walker (1971)

Barnes *et. al.* studied the deformation of polycrystalline ice through uniaxial compression tests with strain rates ranging from 10^{-9} to 10^{-2} s^{-1} and temperatures ranging from 0 to -48 °C. They assumed that the deformation caused by transient (primary) and steady-state (secondary) creep could be described by the superposition of two independent processes:

$$\varepsilon = \varepsilon_0 + \alpha_0 t^{1/3} + \dot{\varepsilon}_s t \qquad (3.5.1)$$

where ε is the strain at any time t, ε_0 is instantaneous strain, α_0 is a constant and $\dot{\varepsilon}_s$ is the secondary creep rate. When t is small the transient creep (i.e. the $\alpha_0 t^{1/3}$) term is dominant; $\dot{\varepsilon}_s t$ is the steady-state creep which is approached asymptotically.

According to Barnes *et. al.*, the secondary creep rate of ice can be described by an Arrhenius type of equation:

$$\dot{\varepsilon}_s = A' \sigma^{n_3} \exp(-Q/RT) \qquad (3.5.2)$$

where $\dot{\varepsilon}_s$ is the secondary creep rate, σ is the stress, Q is the activation energy, R is the universal gas constant, T is temperature, and A' and n_3 are constants. However, as this equation is only applicable over a limited range of stress, they used an empirical relationship to describe their data over the entire stress range:

$$\dot{\varepsilon}_s = A''(\sinh \alpha_0 \sigma)^{n_3} \exp(-Q/RT) \qquad (3.5.3)$$

where A'' is a constant and all other variables have been previously defined.

Over the entire range of strain rates and temperatures studied, n_3 was found to have a value close to 3 for secondary creep behaviour (i.e. equation (3.5.3)). Q had two distinct values, depending upon the temperature at which the experiment was

performed: for temperatures below -8 °C, Q was 78 kJ/mol, and for temperatures between -8 °C and -2 °C, Q was 120 kJ/mol. Values for A'' ranged from 1.88×10^{10} to 4.60×10^{18} s^{-1}, and α_0 ranged from 0.254 to 0.282 m^2/MN for experiments performed over the entire stress and temperature range.

For the temperature range of -8 to -45 °C, equation (3.5.3) can be written as:

$$\dot{\varepsilon}_s = 2.72 \times 10^{10} \exp(-9393/T)(\sinh(0.262 \times 10^{-6} \sigma))^{3.05} \tag{3.5.4}$$

where the temperature is measured in degrees Kelvin, the stress is measured in Pascals, and the strain rate is measured in (seconds)$^{-1}$.

3.6 Nixon and McRoberts (1976)

Nixon and McRoberts were interested in long term pile settlement in frozen soils; since there was little data on the creep of frozen soils at low stresses they based their analysis on the creep of ice, which would be a conservative estimate. They reviewed creep data from several sources and found that the deformation of ice consisted of a brief period of primary creep followed by constant secondary creep.

According to Nixon and McRoberts, the empirical deformation versus time relationship for any uniaxial creep test performed at low stress can be written as:

$$\varepsilon = \varepsilon_i + \dot{\varepsilon}_s t \tag{3.6.1}$$

where ε is uniaxial strain at any time t, ε_i is initial elastic settlement, and $\dot{\varepsilon}_s$ is the secondary creep rate. Since the strain occurring from the secondary creep is usually much greater than the initial elastic strain, the secondary creep rate alone may be used to represent the strain.

For geotechnical applications, Nixon and McRoberts wrote the flow law for ice as:

$$\dot{\varepsilon}_s = B_2 \sigma^{n_4} + B_3 \sigma^{n_5} \tag{3.6.2}$$

where B_2, B_3, n_4, and n_5 are constants which must be determined from tests at a stress of σ and at a constant temperature. The experimental data obtained from previous publications was plotted as $\log \sigma$ versus $\log \dot{\varepsilon}_s$, and several observations were made. While the portion of the graph below a stress of about 138 kN/m^2 was very close to a straight line, at stresses greater than this value the slope of the data showed a noticeable change. That is, the value of the creep exponent increased. As a consequence, extrapolation of results of tests performed at high stresses would underestimate the strain rates at low stresses, which is not conservative.

Nixon and McRoberts also found that for any stress level, as the test temperature is decreased the strain rates also decrease, i.e. the constants B_2, B_3, n_4, and n_5 depend on the temperature. The creep parameters were related to temperature using the following relationships:

$$B_2 = 8 \times 10^{-3} (T_o + 1)^{-2.37} \tag{3.6.3a}$$

$$n_4 = 1.35 (T_o + 1)^{0.2} \tag{3.6.3b}$$

$$B_3 = 1.0 \times 10^{-6} (T_o + 1)^{-1.9} \tag{3.6.4a}$$

$$n_5 = 4 \tag{3.6.4b}$$

where T_o is the temperature in °C below zero, the stress is measured in psi and the strain rate is measured in (years)$^{-1}$. Equations (3.6.3) and (3.6.4) can be combined with

34

equation (3.6.2) to give an empirical equation for secondary creep strain rate as a function of uniaxial stress and temperature.

3.7 Tinawi and Murat (1978)

In 1978 Tinawi and Murat performed short and long term experiments on artificially grown saline ice beams and ice plates in a laboratory cold room. Tests included instantaneous and long term flexural loading of simply supported beams and circular plates, with water underlying the ice in the beam tests. The salinity of the ice was approximately 4 to 5%. The cold room temperature was -10 °C, and the water temperature was -2 °C; the ice temperature varied linearly throughout the ice thickness in cases where water was present, and was isothermal at -10 °C in cases where water was not present. The applied stresses ranged from 276 to 552 kPa for beam tests and from 120 to 412 kPa for plate tests.

From the instantaneous flexural loading of beams, the elastic modulus, E, was found to have an average value of 3.9×10^6 kPa. The values for E obtained from the plate tests were approximately $1/3$ of the value found for the beam tests. According to Tinawi and Murat, the elastic modulus is greatly affected by the rate of loading. They state that the elastic modulus is less for plates than for beams because of the large differences in stress rate across the plate, and that the elastic modulus should be made variable across the radius of the plate.

Tinawi and Murat proposed a power law relationship to fit the creep data from the beam tests, obtaining the following empirical equation:

$$\dot{\varepsilon} = 0.269 \times 10^{-12} \sigma^{2.32} \qquad (3.7.1)$$

35

where $\dot{\varepsilon}$ is the strain rate (minutes^{-1}) and σ is the stress (in kPa). They compared this to a theoretical solution found by Hult (1966) which yields:

$$\dot{\varepsilon} = 2.305 \times 10^{-12} \sigma^{2.32} \qquad (3.7.2)$$

For the creep of simply supported ice plates with no underlying water, Tinawi and Murat found the empirical power law relationship was found to be:

$$\dot{\varepsilon} = 1.625 \times 10^{-12} \sigma^3 \qquad (3.7.3)$$

Converting these equations to units of Pascals for σ and (seconds)$^{-1}$ for $\dot{\varepsilon}$, equation (3.7.1) becomes:

$$\dot{\varepsilon} = 4.916 \times 10^{-22} \sigma^{2.32} \qquad (3.7.4)$$

and equation (3.7.3) becomes:

$$\dot{\varepsilon} = 2.708 \times 10^{-23} \sigma^3 \qquad (3.7.5)$$

3.8 Michel and Gagnon (1979)

In 1979 Michel and Gagnon developed a linear viscoelastic creep model and performed experiments on simply supported freshwater ice plates to test the validity of the model. The linear model was chosen because it was a simple representation of the secondary creep, however it did neglect part of the primary creep.

The model could be solved analytically from two differential equations. The vertical deflection over time, w, was found to be:

$$w = w_e \left(\frac{3K+G}{3K+4G} \right) \left[\frac{K+G}{K} \left(\frac{t}{T_r} \right) - \frac{G^2}{(3K+G)K} \exp\left\{ \left[\left(\frac{-3K}{3K+G} \right) \frac{t}{T_r} \right] \right\} \right] \qquad (3.8.1)$$

where w_e is the elastic deflection, K and G are the bulk modulus and the rigidity modulus, respectively, T_r is relaxation time (η_0/G), η_0 is viscosity, and t is time. This model did not predict the deflection well in the primary stages of creep, giving deflections greater than those observed during experiments.

For the secondary creep portion of the experimental curves, a power law relationship like equation (3.2.1) was fit to the data, giving:

$$\dot{\varepsilon} = B\sigma^{2.5} \qquad (3.8.2)$$

where $\dot{\varepsilon}$ is the strain rate, σ is the stress, and B is a constant. Michel and Gagnon believed that the exponent in this equation was low (it is usually around 3) because secondary creep was never actually reached in these experiments.

3.9 Masterson and Strandberg (1979)

Drilling rigs in the Arctic have been constructed on platforms of man-made ice which are built up over a natural ice cover and are in place throughout the winter season. Masterson and Strandberg (1979) took deflection data from one such ice platform, and using a finite element model, obtained creep parameters for the ice platform. They also examined the effect of having a hole (called the moonpool) in the ice cover, but determined that its effect on the overall behaviour of the platform was negligible.

The creep law used in the finite element model was Glen's power law (equation (3.2.1). The strain rate determined for this case was:

$$\dot{\varepsilon} = 164.55 \times 10^{-12} \sigma^{3.1} \qquad (3.9.1)$$

where the stress, σ, is measured in kPa and the strain rate, $\dot{\varepsilon}$, is measured in (days)$^{-1}$. The material parameters used in this analysis were: Young's modulus, $E = 690$ MPa;

Poisson's ratio, $\nu = 0.20$; and foundation modulus, $\gamma = 9.8$ kN/m^3.

This equation can be converted to units of Pascals for σ and (seconds)$^{-1}$ for $\dot{\varepsilon}$ giving:

$$\dot{\varepsilon} = 9.545 \times 10^{-25} \sigma^{3.1}$$

(3.9.2)

3.10 Tinawi and Murat (1979)

In 1979 Tinawi and Murat developed an axisymmetric solid finite element model for a non-homogeneous floating ice sheet, which could examine both short and long term loading scenarios. They used this model to solve the problem of a circular load on an infinite ice sheet, and compared their results to another model that used thin plate theory.

Tinawi and Murat proposed the following creep law:

$$\dot{\varepsilon}^c = 3.105 \times 10^{-10} \sigma^{2.53}$$

(3.10.1)

where $\dot{\varepsilon}^c$ is the creep strain rate (minutes^{-1}), and σ is the stress (kPa). They also suggested the following relationship for the variation of the elastic modulus, E, (a function of temperature and salinity), as determined from laboratory experiments:

$$E(z_0) = 1.21 \times 10^6 \left[0.572 + 0.931\left(\frac{z_0}{h}\right) - 0.655\left(\frac{z_0}{h}\right)^2 \right]$$

(3.10.2)

where E is in kPa, h is the ice thickness, and z_0 is measured up from the bottom of the ice sheet.

The stress-strain relationship of equation (3.10.1) can be converted to units of Pascals for stress and (seconds)$^{-1}$ for strain rate giving:

$$\dot{\varepsilon}^c = 1.33 \times 10^{-19} \sigma^{2.53}$$

(3.10.3)

38

After running both models and comparing the results, Tinawi and Murat found that the deflection at the centre of the plate did not change noticeably between homogeneous (E = constant) and non-homogeneous ($E = E(z_0)$) cases. They did find, however, that the stresses and strains were significantly different when comparing homogeneous and non-homogeneous cases, which will have an effect on the creep behaviour of the ice.

3.11 Morgenstern, Roggensack, and Weaver (1980)

Morgenstern et. al. performed an extensive literature review of long term creep tests on ice (and ice rich soils) and, by combining the experimental results from many researchers, proposed the following empirical power law for creep:

$$\dot{\varepsilon}_e = B_4 \sigma_e^{n_6} \tag{3.11.1}$$

where $\dot{\varepsilon}_e$ is the effective shear strain rate, σ_e is the effective shear stress, and B_4 and n_6 are constants which depend on temperature. This relationship has been suggested for temperatures colder than $-1°C$. The value of the exponent, n_6, was found to be 3, and B_4 ranged from 4.5×10^{-8} ($kPa^{-n_6} year^{-1}$) at $-1\ °C$ to 5.6×10^{-9} ($kPa^{-n_6} year^{-1}$) at $-10\ °C$.

Converting these quantities into units of Pascals and $(seconds)^{-1}$, at $-1\ °C$ equation (3.11.1) becomes:

$$\dot{\varepsilon}_e = 1.426 \times 10^{-24} \sigma^3 \tag{3.11.2}$$

and at $-10\ °C$:

$$\dot{\varepsilon}_e = 1.775 \times 10^{-25} \sigma^3 \tag{3.11.3}$$

3.12 Sego and Morgenstern (1983)

Following Glen's (1955) power law, Sego and Morgenstern proposed a form of equation more useful for geotechnical problems:

$$\frac{\dot{\varepsilon}}{\dot{\varepsilon}_0} = \left(\frac{\sigma}{\sigma_0}\right)^{n_7} \tag{3.12.1}$$

where $\dot{\varepsilon}$ is the axial strain rate, σ is axial stress, and n_7 is a constant. $\dot{\varepsilon}_0$ is defined as the proof strain rate, and σ_0 as the proof stress; the proof strain rate is a quantity against which the experimental results can be normalized, and the proof stress is the stress level which will produce this strain rate. Equation (3.12.1) can be related to Glen's (1955) equation (equation (3.2.1)) by:

$$k_1 = \dot{\varepsilon}_0 / (\sigma_0)^{n_7} \tag{3.12.2}$$

The experimental data of Sego and Morgenstern was normalized to -2 °C, and combined with data from Barnes et. al. (1971), Glen (1955), and others. A relationship for the strain rate in the stress range of 100 to 1000 kPa using this combined data was found to be:

$$\dot{\varepsilon} = 0.001\left(\frac{\sigma}{150.0}\right)^{3.0} \tag{3.12.3}$$

where the strain rate is measured in hours^{-1}, and for a grain size ratio (the average crystal diameter divided by the average sample diameter) of 0.030.

Equation (3.12.3) can also be written as:

$$\dot{\varepsilon} = 8.23 \times 10^{-23} \sigma^{3.0} \tag{3.12.4}$$

where the stress is measured in Pascals, and the strain rate is measured in (seconds)$^{-1}$.

3.13 Szyszkowski, Dost, and Glockner (1985)

According to Szyszkowski et. al., some of the factors affecting the mechanical properties of ice include crystal structure, temperature, stress history, and the meteorological and hydrodynamic conditions which were present at the time of ice formation. Therefore, while different types of ice (such as river, lake, or sea ice) have varying mechanical properties, viscoelastic models can be used to approximate the mechanical behaviour of ice.

Empirical or semi-empirical creep functions can often be expressed in the following form:

$$\dot{\varepsilon}^c = B(T)[1 + f(t)]\sigma^{n_s} \tag{3.13.1}$$

where $\dot{\varepsilon}^c$ is the creep strain rate, $B(T)$ is a function of temperature (T), $f(t)$ is a function of time (t) which defines the primary creep, σ is a stress, and n_s is a constant (ranging from 1.5 to 4.0). The six-parameter creep function used in the model developed by Szyszkowski et. al. is:

$$\dot{\varepsilon}^c = \frac{K_0}{3^{n_s+1/2}[1+|T|]}\left[1 + \frac{mb_1t'}{(1+b_1t)^{n+1}}\right]\sigma^{n_s} \tag{3.13.2}$$

where b_1, K_0, m, n_s, and t' are constants. The instantaneous elastic response of the model to loading is characterized by σ/E_T, with E_T being the sixth constant of the model. This model analyzes the primary and secondary stages of creep, but does not include tertiary creep.

To compare equation (3.13.2) with equation (3.13.1), Szyszkowski *et. al.* used the following values:

$$K_0 = 2.59 \times 10^{-4} \ °C/(\,hr(Pa)^{n_s}\,)$$
$$E_T = 4(1+0.0125|T) \ GPa$$

$$n_s = 1.8$$
$$b_l = 0.5 \ hr^{-1}$$

$$t' = 100 \ hr$$
$$m = 1.0$$

$$T = -5°C$$

The results found using equation (3.13.2) agree very well with the results found from equation (3.13.1) at stress levels of 0.5 MPa and 4.0 MPa for primary and secondary creep.

Using the above values, and converting all quantities to units of Pascals and (seconds)$^{-1}$, equation (3.13.2) becomes:

$$\dot{\varepsilon}^c = 9.583 \times 10^{-10} \left(1 + \frac{50}{\left(1 + 1.389 \times 10^{-4} t\right)^2} \right) \sigma^{1.8}$$

(3.13.3)

Szyszkowski *et. al.* tested their model on a simply supported rectangular ice column with an initial imperfection, which was subjected to a constant axial load. They concluded from their numerical results that the size of the time interval required for rapid convergence and adequate accuracy of the solution is a function of the model parameters, and not of the load conditions or geometry of the problem. This suggests that the duration of primary creep is not dependent on the stress level or the temperature.

3.14 Azizi (1989)

According to Azizi (1989), primary creep of ice is of greater importance than secondary creep since secondary creep is often reduced to an inflection point on strain

time curves, characterizing the transition between primary and tertiary creep. Compression test data was analyzed by Azizi under the assumption that the primary creep of ice can be modelled using a power law. The form of the power law used by Azizi was:

$$\varepsilon^c = K_1 \sigma^{d_1} t^{b_2} \qquad (3.14.1)$$

where ε^c is the creep strain, σ is the applied stress, t is time, and K_1, b_2 and d_1 are constants.

The uniaxial compression tests that were analyzed were performed at stresses ranging between 1 and 4 MPa, and at a temperature of -5 °C. The results of the analysis indicated that $K_f = 1.27 \times 10^{-4}$, $b_2 = {}^2\!/_3$, and $d_1 = 2.43$ when σ is measured in MPa and t in minutes. The constant b_2 was determined to be independent of stress.

Converting the units for all quantities into seconds and Pascals, equation (3.14.1) becomes:

$$\varepsilon^c = 3.63 \times 10^{-22} \sigma^{2.43} t^{2/3} \qquad (3.14.2)$$

3.15 Azizi and Whalley (1994)

In 1994 Azizi and Whalley related the secondary creep parameters of ice to the parameters determined from primary creep. They used Hult's (1966) expression for primary creep:

$$\varepsilon^c = K_2 \sigma^{d_2} t^{b_3} \qquad (3.15.1)$$

where ε^c is the creep strain, σ is the stress, and t is time. The parameters b_3, d_2 and K_2 are determined empirically. Using Glen's power law (equation (3.2.1)) to represent the secondary creep gives:

$$\dot{\varepsilon}^c = B_s \sigma^{n_s} \qquad (3.15.2)$$

43

with $$B_s = K_c \exp(-Q/RT)$$ (3.15.3)

where $\dot{\varepsilon}^c$ is the creep strain rate, n_9 is an empirical exponent, K_c is the fluidity coefficient, Q is the activation energy, R is the universal gas constant and T is temperature.

The derivative of equation (3.15.1) with respect to time is:

$$\dot{\varepsilon}^c = b_3 K_2^{1/b_3} \varepsilon_c^{(b_3-1)/b_3} \sigma^{d_2/b_3}$$ (3.15.4)

where ε_c is the average strain. According to Azizi and Whalley, the average strain, ε_c, at the minimum strain rate is 0.9%, so equation (3.15.4) can be written as:

$$\dot{\varepsilon}^c_{(min)} = A_1 \sigma^{d_2/b_3}$$ (3.15.5)

where $A_1 = b_3 K_2^{1/b_3} \varepsilon_c^{(b_3-1)/b_3}$. This is similar to equation (3.15.2), and therefore:

$$\dot{\varepsilon}^c_{(min)} = A_1 \sigma^{d_2/b_3} = B_s \sigma^{n_9}$$ (3.15.6)

The minimum creep strain rate can then be written as:

$$\dot{\varepsilon}^c_{(min)} = B_s \sigma^{n_9}$$ (3.15.7)

where $$B_s = b_3 K_2^{1/b_3} \varepsilon_c^{(b_3-1)/b_3}$$ (3.15.8)

and $$n_9 = d_2/b_3$$ (3.15.9)

with the primary creep parameters d_2, b_3, and K_2 used to predict the secondary creep minimum strain rate.

Using the results of uniaxial creep tests, the relationship between stress and minimum strain rate was found to be:

$$\dot{\varepsilon}^c_{(min)} = 1.34 \times 10^{-5} \sigma^{3.64}$$ (3.15.10)

where σ is in MPa and $\dot{\varepsilon}^c_{(min)}$ is in minutes^{-1}. Conversion of this equation to units of Pa

44

and (seconds)$^{-1}$ gives:

$$\dot{\varepsilon}^c_{(min)} = 3.88 \times 10^{-40} \sigma^{3.64}$$

(3.15.11)

3.16 Summary

A summary of the type of creep modelled by each of the studies described in this chapter, along with some of the test conditions, can be found in Table 3-1. Also shown in this table are the creep rate equations, which have been transformed to be dimensionally consistent for comparison purposes.

As can be seen from Table 3-1, several researchers have used similar equations to model the creep rate for the long term behaviour of ice. These relationships are similar to the one used in the model developed here. The differences lie in the results obtained for the creep coefficient and exponent, which are seen to be quite inconsistent. The values obtained for the creep exponent ranged from 1.8 to 3.64. In many cases, the values found for Young's modulus were not reported. It should also be noted that the majority of these results were obtained from small scale laboratory experiments rather than large scale field tests.

The purpose of this research was to perform a comprehensive analysis of large scale creep test data over a range of temperatures and stresses in order to determine if a consistent set of creep parameters (creep coefficient, exponent, and Young's modulus) can be obtained for the power law creep model. As the mechanical properties of ice can be scale dependent (Ladanyi and Saint-Pierre, 1978), small scale tests in a laboratory may not accurately represent the behaviour of a larger sheet of ice; analyzing large scale test data would be more desirable. The data sets analyzed here, from both Beltaos and

Frankenstein, are from large scale load tests on effectively infinite ice sheets. A complete range of calibrated parameters (creep coefficient, creep exponent, and Young's modulus) will be obtained and reported for each set of data. These results will also be examined to determine if any correlation can be observed between the calibrated parameters and the temperature at which the data was obtained.

Table 3-1: Summary creep model studies performed on ice.

Section	Study	Type of Creep Modelled: Primary	Secondary	Laboratory (L), Field (F), or Published (P) Data	Temperature (°C)
3.2	Glen (1955)	✓	✓	L	0 to -13
3.3	Butkovich and Landauer (1959)	✓	✓	L	-4 to -6
3.4	Mellor and Testa (1969)		✓	L	-2
3.5	Barnes et. al. (1971)		✓	L	-8 to -45
3.6	Nixon and McRoberts (1976)		✓	P	-
3.7	Tinawi and Murat (1978)	✓	✓	L	-10
3.8	Michel and Gagnon (1979)	✓	✓	L	-
3.9	Masterson and Strandberg (1979)	✓	✓	F	-
3.10	Tinawi and Murat (1979)	✓	✓	L	-10
3.11	Morgenstern et. al. (1980)	✓	✓	P	-1 to -10
3.12	Sego and Morgenstern (1983)	✓	✓	L, P	-2
3.13	Szyszkowski et. al. (1985)	✓		L	-5
3.14	Azizi (1989)	✓		L, P	-5
3.15	Azizi and Whalley (1994)		✓	L	-2 to -5
6.2	Present Study (2001): Beltaos' data		✓	F	+6 to -25
6.3	Present Study (2001): Frankenstein's data		✓	F	-0.1 to -12

Table 3-1: Summary creep model studies performed on ice (continued).

Section	Stress Range (kPa) or {Strain Rate Range, s⁻¹}	Creep Strain Rate Equation [1] (seconds⁻¹)	Creep Exponent	Young's Modulus [2] (Pa)
3.2	100 to 1000	$22.2 \exp(-16114/T)\, \sigma^{3.2}$	3.2	-
3.3	49 to 294, 687 to 2747	$1.646 \times 10^{-24}\, \sigma^{2.96}$	2.96	-
3.4	9.1 to 42	$\propto \sigma^{1.8}$	1.8	-
3.5	{10^{-9} to 10^{-2} s⁻¹}	$2.72 \times 10^{10} \exp(-9393/T)\{\sinh(0.262 \times 10^{-6}\, \sigma)\}^{3.05}$	3	-
3.6	-	see chapter 3	function of temperature	-
3.7	276 to 552 (beam test) 120 to 412 (plate test)	$4.916 \times 10^{-22}\, \sigma^{2.32}$ (beam test) $2.708 \times 10^{-23}\, \sigma^{3}$ (plate test)	2.32 (beam test) 3 (plate test)	3.9×10^{9} (beam test) 1.1×10^{9} (plate test)
3.8	-	$\propto \sigma^{2.5}$	2.5	0.38×10^{9}
3.9	-	$9.545 \times 10^{-25}\, \sigma^{3.1}$	3.1	0.69×10^{9}
3.10	-	$1.33 \times 10^{-19}\, \sigma^{2.53}$	2.53	$E = 1.21 \times 10^{6}[0.572 + 0.931(z_0/h) - 0.655(z_0/h)^2)]$
3.11	-	$1.426 \times 10^{-24}\, \sigma^{3}$ (at -1 °C) $1.775 \times 10^{-25}\, \sigma^{3}$ (at -10 °C)	3	-
3.12	100 to 1000	$8.23 \times 10^{-23}\, \sigma^{3.0}$	3.0	-
3.13	500 to 4000	$9.583 \times 10^{-10}\, (1 + 50/(1 + 1.389 \times 10^{-4}\, t)^2)\, \sigma^{1.8}$	1.8	-
3.14	1000 to 4000	$3.63 \times 10^{-22}\, \sigma^{2.43}\, t^{2/3}$ *	2.43	-
3.15	1000 to 4000	$3.88 \times 10^{-40}\, \sigma^{3.64}$ **	3.64	-
6.2	15 to 79	see chapter 6	see chapter 6	see chapter 6
6.3	15 to 1750	see chapter 6	see chapter 6	see chapter 6

Notes:

[1] stress (σ) is measured in Pascals, temperature (T) in degrees Kelvin, and time (t) in seconds.

[2] z_0 is measured from up from the bottom of the ice sheet; h is ice thickness.

* this is a relationship for creep strain, not creep strain rate.

** this is the minimum creep strain rate.

48

4.0 FINITE ELEMENT FORMULATION

4.1 Introduction

A two dimensional axisymmetric finite element model was developed to examine the time dependent deformation of an elastic plate of infinite extent, such as a floating ice cover, under a circular distributed load. The model was developed in three stages: first by examining an edge supported elastic plate; second, by adding an elastic foundation; and finally, by refining the model to allow for creep deflection over time.

In this chapter, a rheological model for ice is described, followed by the underlying theory of the finite element model and the assumptions made when implementing the model. The Principle of Minimum Potential Energy and the Rayleigh-Ritz Method are discussed, leading to the system of equations to be solved and the interpolation functions used in the solution. Expressions are obtained for the element and foundation stiffness matrices, as well as the mechanical load vector. In calculating the creep load vector, the creep strains are obtained using either the Euler method, or the 4th Order Runge-Kutta method. The boundary conditions are implemented using a penalty method, and the boundary elements are discussed.

4.2 Rheological Model

Figure 4-1 illustrates the deformation-time relationship for an ice sample which is loaded (with stress, σ) and unloaded instantaneously. This behaviour can be described using a simple rheological model consisting of a Maxwell unit in series with a Kelvin or Voight unit, such as the one seen in Figure 4-2 (Ashton, 1986). The Maxwell unit consists of a spring and dashpot in series, with the spring and the dashpot representing

49

elastic deformation and permanent viscous deformation, respectively; the Kelvin or Voight unit contains a spring in parallel with a dashpot, and represents the elastic lag, also known as retarded elasticity (Ashton, 1986). The spring constants are the elastic moduli, E_1 and E_2, while the dashpot constants are the viscosity moduli, η_1 and η_2.

The model developed here is analogous to a Maxwell unit with one elastic constant, E, and one viscosity constant, η.

4.3 Finite Element Model

For the circular load configurations to be examined here, this problem is annular in nature, as seen in Figure 4-3. The ice cover is broken down into annular elements, with the outer radius (r_2) of one element being the inner radius (r_1) of the next element. Mathematically, each element can be represented one dimensionally since the displacements are assumed to be axisymmetric. Figure 4-4 illustrates the cross sectional view of an element, where $u(r)$ and $w(r)$ are the displacements in the radial (r) and transverse (z) directions, respectively and h is the thickness of the plate.

4.3.1 Assumptions

Several assumptions are made when implementing the model developed here. Two physical properties of ice are used as parameters in this model: Poisson's ratio (ν) and Young's modulus (E). Although other properties such as ice density and ice grain size can influence the behaviour of ice, the density remains relatively constant and grain size is not often measured (Ashton, 1986), making E and ν logical choices for the physical parameters to represent the elastic behaviour of ice.

50

One assumption made is that the ice sheet is homogeneous and transversely isotropic. According to Premachandran and Horii (1994), for a single crystal of ice the elastic properties are not constant in every direction, but a polycrystalline ice sheet with random particle orientation generally has isotropic properties. Consequently, constant values can be used for E and ν, as these material parameters are assumed not to change through the depth of the ice cover or at a distance away from the load.

Another assumption made in the model application is that the ice sheet is infinite in extent. Ashton (1986) states that stresses are insignificant at distances greater than five times the characteristic length ($r > 5l$) from the centre of loading; an ice sheet larger than this can be considered infinite. Test data was obtained from S. Beltaos (National Water Research Institute) and from Frankenstein's (1963) paper. Joseph Lake (the location of Beltaos' tests) was observed to be much larger than $5l$ when ice samples were obtained from that location in March of 2000, making the assumption of an infinite ice sheet a valid one. The test locations for Frankenstein's (1963) data were not described in detail, but they are also assumed to be sufficiently large to make this a valid assumption.

A third assumption made is that the unit weight of water (γ) is 9,806 N/m^3. The density of water (and thus γ) does change with temperature; however, the temperature of the water underlying the ice cover will essentially be 0 °C. The density of water at this temperature is approximately 1,000 kg/m^3, giving a unit weight of 9,806 N/m^3.

4.3.2 Principle of Minimum Potential Energy

This model is formulated based on the Theorem of Minimum Potential Energy, which is derived from the Principle of Virtual Work (Ugural and Fenster, 1995). This

51

theorem applies to linear elasticity problems. Although the creep problem is not linear in nature, the creep strains here will be treated as initial strains, and the problem will be solved as a sequence of linear elastic problems.

The potential energy, Π, is defined as the difference between the elastic strain energy, U, of a body and the change in potential of the applied loads, F_i (Ugural and Fenster, 1995) giving:

$$\Pi = \int_V U(\varepsilon_{ij})dV - \int_V F_i \Phi_i dV$$

(4.3.1)

where ε_{ij} are elastic strains, Φ_i are components of the displacement field (the vector of unknowns), V is the volume of the body, and i and j are location indices within the vectors. This function assumes a minimum value when the displacements satisfy the boundary conditions and the equilibrium conditions, that is, the exact solution is obtained when Π is minimized (Ugural and Fenster, 1995).

For the axisymmetric problem illustrated in Figures 4-3 and 4-4, in a typical element the elastic strain energy density, U, can be written as:

$$U = \frac{1}{2}\left(\sigma_r \varepsilon_r^e + \sigma_\theta \varepsilon_\theta^e\right)$$

(4.3.2)

where σ_r and ε_r^e, and σ_θ and ε_θ^e, are the stresses and elastic strains in the radial and tangential directions, respectively. The radial and tangential directions are principal directions for stress and strain. The stress normal to the plate (σ_z) is zero, and so plane stress conditions exist. The stresses in the principal directions can be related to the strains using the following expressions:

$$\sigma_r = \frac{E}{1-\nu^2}\left(\varepsilon_r^e + \nu\varepsilon_\theta^e\right)$$

(4.3.3)

52

$$\sigma_\theta = \frac{E}{1-\nu^2}\left(\varepsilon_\theta^e + \nu\varepsilon_r^e\right) \tag{4.3.4}$$

where E is Young's modulus, and ν is Poisson's ratio.

The total radial and tangential strain components (ε_r and ε_θ) are calculated from:

$$\varepsilon_r = \frac{\partial u}{\partial r} - z\frac{\partial^2 w}{\partial r^2} \tag{4.3.5}$$

$$\varepsilon_\theta = \frac{u}{r} - \frac{z}{r}\frac{\partial w}{\partial r} \tag{4.3.6}$$

where u and w are the displacements in the radial (r) and transverse (z) directions, respectively. The shear strain $\varepsilon_{r\theta}$ is zero because of the symmetry of the problem. The total strain in each direction (ε_r and ε_θ) is a combination of the elastic (ε_r^e and ε_θ^e) and creep (ε_r^c and ε_θ^c) strains:

$$\varepsilon_r = \varepsilon_r^e + \varepsilon_r^c \tag{4.3.7}$$

and
$$\varepsilon_\theta = \varepsilon_\theta^e + \varepsilon_\theta^c \tag{4.3.8}$$

The elastic strains can then be expressed as:

$$\varepsilon_r^e = \left(\frac{\partial u}{\partial r} - z\frac{\partial^2 w}{\partial r^2}\right) - \varepsilon_r^c \tag{4.3.9}$$

and
$$\varepsilon_\theta^e = \left(\frac{u}{r} - \frac{z}{r}\frac{\partial w}{\partial r}\right) - \varepsilon_\theta^c \tag{4.3.10}$$

Equations (4.3.3) and (4.3.4) can be substituted into equation (4.3.2), giving a total strain energy, U, of:

$$U = \frac{E}{2(1-\nu^2)}\int_{-h/2}^{+h/2}\left[\int_{r=r_1}^{r=r_2}\left(\left(\varepsilon_r^e\right)^2 + \left(\varepsilon_\theta^e\right)^2 + 2\nu\varepsilon_r^e\varepsilon_\theta^e\right)2\pi r\,dr\right]dz \tag{4.3.11}$$

53

where h is the plate thickness. By substituting from (4.3.9) and (4.3.10), expanding and rearranging the terms in the integrand, (4.3.11) can be written as:

$$U = U_1 + U_2 + U_3 \tag{4.3.12}$$

where

$$U_1 = \frac{C}{2} \int_{r=r_1}^{r=r_2} \left[\left(\frac{\partial u}{\partial r} \right)^2 + \left(\frac{u}{r} \right)^2 + \frac{2v}{r} u \frac{\partial u}{\partial r} \right] 2\pi r dr$$

$$+ \frac{D}{2} \int_{r=r_1}^{r=r_2} \left[\left(\frac{\partial^2 w}{\partial r^2} \right)^2 + \left(\frac{1}{r} \frac{\partial w}{\partial r} \right)^2 + \frac{2v}{r} \frac{\partial^2 w}{\partial r^2} \frac{\partial w}{\partial r} \right] 2\pi r dr \tag{4.3.13}$$

$$U_2 = \frac{-E}{2(1-v^2)} \int_{-h/2}^{+h/2} \left[\int_{r=r_1}^{r=r_2} 2 \left(\varepsilon_r \varepsilon_r^c + \varepsilon_\theta \varepsilon_\theta^c + 2v(\varepsilon_\theta \varepsilon_r^c + \varepsilon_r \varepsilon_\theta^c) \right) 2\pi r dr \right] dz \tag{4.3.14}$$

$$U_3 = \frac{E}{2(1-v^2)} \int_{-h/2}^{+h/2} \left[\int_{r=r_1}^{r=r_2} \left((\varepsilon_r^c)^2 + (\varepsilon_\theta^c)^2 + 2v\varepsilon_r^c \varepsilon_\theta^c \right) 2\pi r dr \right] dz \tag{4.3.15}$$

with

$$C = \frac{Eh}{(1-v^2)} \quad \text{(in-plane stiffness)} \tag{4.3.16}$$

$$D = \frac{Eh^3}{12(1-v^2)} \quad \text{(bending stiffness)} \tag{4.3.17}$$

The stiffness matrix, $[K]$, will result from equation (4.3.13), and an additional load vector, $\{Q^c\}$, arising from equation (4.3.14) will include the effects of the creep strain. Equation (4.3.15) is independent of the displacement fields u and w, and as a result does not affect the finite element formulation.

4.3.3 Finite Element System of Equations

The finite element method is an application of the Rayleigh-Ritz Method (Chandrupatla and Belegundu, 1997). With this method, displacement fields

(interpolation functions) are assumed for each element which must satisfy the specified boundary conditions. The interpolation functions, which define the displacement fields for this problem, will be discussed in the next section.

Through the process of minimizing Π and applying the Rayleigh-Ritz Method, a set of finite element equations arises of the following form:

$$[K]\{\Phi\} = \{R\}$$

(4.3.18)

where $[K]$ is the global stiffness matrix, $\{\Phi\}$ is the vector of unknowns, and $\{R\}$ is the mechanical load vector.

The global stiffness matrix will be the combination of the global horizontal and vertical stiffness matrices ($[K^u]$ and $[K^w]$), as well as the global foundation stiffness matrix ($[K_f^w]$):

$$[K] = [K^u] + [K^w] + [K_f^w]$$

(4.3.19)

Three degrees of freedom are chosen for each node: displacement in the radial direction, u; displacement in the transverse direction, w; and rotation in the transverse direction, $w_r = \dfrac{\partial w}{\partial r}$. Hence, the vector of unknowns has the form:

$$\{\Phi\} = \{\ldots \ldots, u_i, w_i, w_{ri}, \ldots \ldots\}$$

(4.3.20)

where:

- u_i is the radial displacement at any node i ($1 \le i \le N_n$, where N_n is the total number of nodes);

- w_i is the vertical displacement at any node i ($1 \le i \le N_n$);

- w_{ri} is the slope at any node i ($1 \le i \le N_n$).

The mechanical load vector will be the addition of the global horizontal and vertical applied load vectors ($\{P_u\}$ and $\{P_w\}$):

$$\{R\} = \{P_u\} + \{P_w\}$$

(4.3.21)

Expressions will be developed for the components of the global stiffness matrix, $[K]$, in sections 4.4 and 4.5, and for the mechanical load vector, $\{R\}$, in section 4.6. In the next section the interpolation functions, which describe the displacement fields within each element, will be discussed.

4.3.4 Interpolation Functions

It is convenient to define a non-dimensional coordinate, ρ, for any element such that its value is zero at node 1 and its value is one at node 2 (see Figure 4-5):

$$\rho = \frac{r - r_1}{a} \quad \text{with} \quad a = (r_2 - r_1)$$

(4.3.22)

where r is the distance from the centre of the load and r_1 and r_2 are the inner and outer radii of the element, respectively. Between the nodal values, the displacements can be interpolated from the following expressions:

$$u(\rho) = u_1 \varphi_1 + u_2 \varphi_2$$

(4.3.23)

$$w(\rho) = w_1 \phi_1 + w_{r1} \phi_2 + w_2 \phi_3 + w_{r2} \phi_4$$

(4.3.24)

where u_1 and u_2 are the radial displacements, w_1 and w_2 are the vertical displacements, and w_{r1} and w_{r2} are the slopes at nodes 1 and 2, respectively. The interpolation functions for the radial displacement (φ_1 and φ_2) and the vertical (ϕ_1, ϕ_2, ϕ_3, and ϕ_4) displacement are defined respectively as:

56

$$\{\varphi\} = \left\{ \begin{array}{c} \varphi_1 \\ \varphi_2 \end{array} \right\} = \left\{ \begin{array}{c} (1-\rho) \\ \rho \end{array} \right\}$$ (4.3.25)

$$\{\phi\} = \left\{ \begin{array}{c} \phi_1 \\ \phi_2 \\ \phi_3 \\ \phi_4 \end{array} \right\} = \left\{ \begin{array}{c} (1-3\rho^2+2\rho^3) \\ a(\rho-2\rho^2+\rho^3) \\ (3\rho^2-2\rho^3) \\ a(-\rho^2+\rho^3) \end{array} \right\}$$ (4.3.26)

These interpolation functions can be seen graphically in Figure 4-5.

Letting $\quad \{u\} = \left\{ \begin{array}{c} u_1 \\ u_2 \end{array} \right\}$ and $\{w\} = \left\{ \begin{array}{c} w_1 \\ w_{r_1} \\ w_2 \\ w_{r_2} \end{array} \right\}$ (4.3.27)

the radial and vertical displacement fields (u and w) can be expressed as:

$$u = <\varphi> \{u\}$$ (4.3.28)

and $$w = <\phi> \{w\}$$ (4.3.29)

Using the various equations developed in section 4.3, expressions can now be obtained for the global horizontal and vertical stiffness matrices ($[K^u]$ and $[K^w]$), the global elastic foundation stiffness matrix ($[K_f^w]$), and global mechanical and creep load vectors ($\{R\}$ and $\{Q^c\}$).

4.4 Element Stiffness Matrix

Each element will generate a horizontal and vertical stiffness matrix ($[k^u]$ and $[k^w]$), which can then be assembled (see Appendix A) into a global horizontal and vertical stiffness matrix ($[K^u]$ and $[K^w]$). The element stiffness matrices arise from equation (4.3.13), which, after substitution of equations (4.3.28) and (4.3.29) gives:

57

$$U_1 = \frac{1}{2} < u > [k^u]\{u\} + \frac{1}{2} < w > [k^w]\{w\}$$

(4.4.1)

where

$$[k^u] = C \int_{r=r_1}^{r=r_2} \left[\{\varphi_r\} < \varphi_r > + \frac{1}{r^2}\{\varphi_r\} < \varphi_r > + \frac{v}{r}(\{\varphi_r\} < \varphi_r > + \{\varphi_r\} < \varphi_r >) \right] 2\pi r dr$$

(4.4.2)

and

$$[k^w] = D \int_{r=r_1}^{r=r_2} \left[\begin{array}{c} \{\phi_{rr}\} < \phi_{rr} > + \frac{1}{r^2}\{\phi_r\} < \phi_r > \\ + \frac{v}{r}(\{\phi_{rr}\} < \phi_{rr} > + \{\phi_r\} < \phi_r >) \end{array} \right] 2\pi r dr$$

(4.4.3)

The subscripts r and rr indicate derivatives of φ and ϕ with respect to r.

The portion of the element stiffness matrix based on the radial displacement is $[k^u]$, and the portion based on the transverse displacement is $[k^w]$. The element stiffness matrix can be evaluated in closed form from equations (4.4.2) and (4.4.3).

For any element, from equation (4.4.2):

$$k_{ij}^u = \int_{r_1}^{r_2} C \left(\frac{d\varphi_i}{dr}\frac{d\varphi_j}{dr} + \frac{1}{r^2}\varphi_i\varphi_j + \frac{v}{r}\left\{ \frac{d\varphi_i}{dr}\varphi_j + \varphi_i\frac{d\varphi_j}{dr} \right\} \right) 2\pi r dr$$

(4.4.4a)

where k_{ij}^u is located in row i and column j of the element horizontal stiffness matrix, $[k^u]$. Applying the assembly operator (see Appendix A) gives:

$$[K^u] = \underset{e=1}{\overset{N_e}{A}}[k^u]_e$$

(4.4.4b)

where the index e refers to a specific element, N_e is the total number of elements, and i and j vary from 1 to 2 (for the interpolation functions given in equation (4.3.25)).

It is necessary to change the bounds of the integral in (4.4.4a) from the global to the local coordinate system (in terms of ρ rather than r). In order to accomplish this, it is necessary to express r, dr, and $d\varphi_i/dr$ in terms of ρ:

58

$$r = \rho \cdot a + r_1 \tag{4.4.5}$$

and
$$\frac{d\varphi_i}{dr} = \frac{d\varphi_i}{d\rho} \frac{d\rho}{dr} \tag{4.4.6}$$

From equation (4.3.22), $\dfrac{d\rho}{dr} = \dfrac{1}{a}$ and therefore $dr = a \cdot d\rho$ (4.4.7)

and so,
$$\frac{d\varphi_i}{dr} = \frac{d\varphi_i}{d\rho} \frac{1}{a} \tag{4.4.8a}$$

Similarly,
$$\frac{d\varphi_j}{dr} = \frac{d\varphi_j}{d\rho} \frac{1}{a} \tag{4.4.8b}$$

Now, substituting equations (4.4.7) and (4.4.8) into equation (4.4.4a):

$$k_{ij}^u = 2\pi C \int_{\rho=0}^{\rho=1} \left(\frac{d\varphi_i}{d\rho} \frac{d\varphi_j}{d\rho} \frac{r}{a} + \frac{a}{r} \varphi_i \varphi_j + v \left\{ \frac{d\varphi_i}{d\rho} \varphi_j + \varphi_i \frac{d\varphi_j}{d\rho} \right\} \right) d\rho \tag{4.4.9}$$

For each combination of i and j (a total of four combinations), equations (4.3.25) and (4.4.5) are substituted into equation (4.4.9), which is then integrated to yield an equation in terms of r_1 and r_2.

For each element, from equation (4.4.3):

$$k_{ij}^w = \int_{r_1}^{r_2} D \left(\begin{array}{l} \dfrac{d^2\phi_i}{dr^2} \dfrac{d^2\phi_j}{dr^2} + \dfrac{1}{r^2} \dfrac{d\phi_i}{dr} \dfrac{d\phi_j}{dr} \\ + \dfrac{v}{r} \left\{ \dfrac{d^2\phi_i}{dr^2} \dfrac{d\phi_j}{dr} + \dfrac{d\phi_i}{dr} \dfrac{d^2\phi_j}{dr^2} \right\} \end{array} \right) 2\pi r \, dr \tag{4.4.10a}$$

where k_{ij}^w is located in row i and column j of the element vertical stiffness matrix, $[k^w]$.

Applying the assembly operator (see Appendix A) gives:

$$[K^w] = \mathop{A}_{e=1}^{N_e} [k^w]_e \tag{4.4.10b}$$

where the index e refers to a specific element, N_e is the total number of elements, and i

and j vary from 1 to 4 (for the interpolation functions given in equation (4.3.26)).

Equation (4.4.10) must also be modified to reflect the local coordinate system. In this case, the second derivative of ϕ is required. Replacing φ with ϕ in equation (4.4.8a) and taking the derivative again with respect to r (using the product rule):

$$\frac{d^2\phi_i}{dr^2} = \frac{d}{dr}\left(\frac{d\phi_i}{d\rho}\frac{1}{a}\right) = \frac{d\phi_i}{d\rho}\cdot 0 + \frac{1}{a}\frac{d}{dr}\left(\frac{d\phi_i}{d\rho}\right) =$$
$$\frac{1}{a}\frac{d}{d\rho}\left(\frac{d\phi_i}{d\rho}\right)\frac{d\rho}{dr} = \frac{d^2\phi_i}{d\rho^2}\frac{1}{a^2} \tag{4.4.11}$$

A similar result is found for ϕ_j. Using the results of equations (4.4.7), (4.4.8), and (4.4.11), equation (4.4.10a) becomes:

$$k_{ij}^w = 2\pi D \int_{\rho=0}^{\rho=1}\left(\begin{array}{c}\dfrac{d^2\phi_i}{d\rho^2}\dfrac{d^2\phi_j}{d\rho^2}\dfrac{r}{a^3} + \dfrac{1}{r\cdot a}\dfrac{d\phi_i}{d\rho}\dfrac{d\phi_j}{d\rho} \\[2mm] + \dfrac{v}{a^2}\left\{\dfrac{d^2\phi_i}{d\rho^2}\dfrac{d\phi_j}{d\rho} + \dfrac{d\phi_i}{d\rho}\dfrac{d^2\phi_j}{d\rho^2}\right\}\end{array}\right)d\rho \tag{4.4.12}$$

For each combination of i and j (a total of 16 combinations), equations (4.4.6) and (4.3.26) are substituted into equation (4.4.12), which is then integrated.

The results of the integration of equations (4.4.9) and (4.4.12) can be found in Appendix B.

4.5 Elastic Foundation Stiffness Matrix

In cases concerning the creep of ice, water is invariably supporting the elastic plate (ice cover). The water is considered to be a linear elastic foundation with the foundation modulus equal to the unit weight of water, γ(Ashton, 1986).

60

The deflection of the foundation beneath one element yields the following strain energy, U_f:

$$U_f = \frac{\gamma}{2} \int_{r_1}^{r_2} 2\pi r w^2 dr$$

(4.5.1)

Substitution of equation (4.3.29) gives:

$$U_f = \frac{1}{2} < w > [k_f^w]\{w\}$$

(4.5.2)

where

$$[k_f^w] = \int_{r_1}^{r_2} 2\pi r \gamma \{\phi\} < \phi > dr$$

(4.5.3)

For each element, from equation (4.5.3):

$$k_{f_{ij}}^w = \int_{r_1}^{r_2} \gamma \phi_i \phi_j 2\pi r dr$$

(4.5.4a)

where $k_{f_{ij}}^w$ is located in row i and column j of the element foundation stiffness matrix, $[k_f^w]$. Applying the assembly operator (see Appendix A) gives:

$$[K_f^w] = \underset{e=1}{\overset{N_e}{A}} [k_f^w]_e$$

(4.5.4b)

where $[K_f^w]$ is the global foundation stiffness matrix, the index e refers to a specific element, N_e is the total number of elements, and i and j vary from 1 to 4 (for the interpolation functions given in equation (4.3.26)). Substituting expressions for r and dr, equations (4.4.5) and (4.4.7), into equation (4.5.4a) gives:

$$k_{f_{ij}}^w = \int_{\rho=0}^{\rho=1} \gamma \phi_i \phi_j 2\pi r a d\rho = 2\pi \gamma \int_0^1 \phi_i \phi_j (\rho \cdot a + r_1) a d\rho$$

(4.5.5)

For each combination of i and j, equation (4.5.5) was integrated and the results can be found in Appendix B.

61

4.6 Mechanical Load Vector

The mechanical load vector $\{R\}$ is also developed from a potential energy perspective. The work done is the change in potential of the applied loads as they move through the displacements (Ugural and Fenster, 1995). In the case of a distributed load, this is the integral of force multiplied by displacement, integrated over the entire area of loading.

Certain elements of the load vector arise as a result of vertical loading (the elements corresponding to w_i and w_{ri} in the vector of unknowns, $\{\varPhi\}$), and others arise as a result of horizontal loading (the elements corresponding to u_i in $\{\varPhi\}$). The loads corresponding to u_i and w_i are force loads, and the loads corresponding to w_{ri} are moment loads. The global mechanical load vector $\{R\}$ is the assembly of the global load matrices from both vertical and horizontal loading ($\{P^w\}$ and $\{P^u\}$).

4.6.1 Vertical Loading

The type of load considered by this model is a circular vertical load of uniform magnitude q_o applied to the elastic plate over an area, A. This load can have a constant value, or a magnitude that changes over time. The work done by this vertical load in moving through displacement, w, is:

$$work = \int q_o w \cdot dA = q_o \int_A < w > \{\phi\} 2\pi r dr = < w > \{p_w\}$$

(4.6.1)

where

$$\{p_w\} = q_o \int_A \{\phi\} 2\pi r dr$$

(4.6.2)

For each element, from equation (4.6.2):

$$p_i^w = q_o \int_{r_1}^{r_2} \phi_i 2\pi r \, dr \qquad (4.6.3a)$$

where p_i^w is located in row i of the element vertical load vector, $\{p^w\}$. Applying the assembly operator (see Appendix A) gives:

$$\{P^w\} = \overset{N_e}{\underset{e=1}{A}} \{p^w\}_e \qquad (4.6.3b)$$

where the index e refers to a specific element, and i varies from 1 to 4 (for the interpolation functions given in equation (4.3.26)). Substituting expressions for r and dr, equations (4.4.5) and (4.4.7), into (4.6.3) gives the following for any element:

$$p_i^w = q_o \int_{\rho=0}^{\rho=1} \phi_i 2\pi(\rho \cdot a + r_1) a \, d\rho = 2\pi q_o \int_{\rho=0}^{\rho=1} \phi_i (\rho \cdot a + r_1) a \, d\rho \qquad (4.6.4)$$

For each interpolation function, expressions for ϕ_i are substituted into equation (4.6.4), which is then integrated, and the resulting equations can be found in Appendix B.

4.6.2 Horizontal Loading

As the solutions for vertical and horizontal displacements are not coupled (because Young's modulus, E, is constant throughout the thickness of the ice sheet), it is not necessary to include a horizontal load vector in order to solve for the vertical deflection of the ice sheet. The global horizontal load vector, $\{P^u\}$, has been set to zero for all of the cases considered here. Should a situation arise which requires the inclusion of a horizontal load vector, this finite element model would only require expressions for the components of the element horizontal load vector, $\{p^u\}$, to be derived and implemented (in a similar fashion to those expressions found for $\{p^w\}$).

4.7 Creep Load Vector

The vertical deflection of ice over time has been shown experimentally to be a nonlinear relationship. One version of a constitutive model used to represent the viscous creep of ice under uniaxial loading conditions is:

$$\dot{\varepsilon}^c = \frac{\dot{\varepsilon}_n}{\sigma_n} \left| \frac{\sigma}{\sigma_n} \right|^{(n-1)} \sigma$$

(4.7.1)

where $\dot{\varepsilon}^c$ is the creep strain rate, σ is the stress, $\dot{\varepsilon}_n$ and σ_n and n are material parameters. Equation (4.7.1) reduces to:

$$\dot{\varepsilon}^c = \eta \sigma^n$$

(4.7.2)

with the constant, η taking the form:
$$\eta = \frac{\dot{\varepsilon}_n}{\sigma_n^n}$$

(4.7.3)

Considering ice to be an isotropic material, the plane stress version of this constitutive equation (4.7.1) becomes:

$$\dot{\varepsilon}_r^c = \frac{d\varepsilon_r^c}{dt} = \eta \tilde{\sigma}^{(n-1)} \left(\sigma_r - \frac{1}{2} \sigma_\theta \right)$$

(4.7.4)

$$\dot{\varepsilon}_\theta^c = \frac{d\varepsilon_\theta^c}{dt} = \eta \tilde{\sigma}^{(n-1)} \left(\sigma_\theta - \frac{1}{2} \sigma_r \right)$$

(4.7.5)

with
$$\tilde{\sigma} = \sqrt{\sigma_r^2 - \sigma_r \sigma_\theta + \sigma_\theta^2}$$

(4.7.6)

where σ_r and $\dot{\varepsilon}_r^c$, and σ_θ and $\dot{\varepsilon}_\theta^c$, are the stresses and creep strain rates in the radial and tangential directions, respectively, and $\tilde{\sigma}$ is a resultant stress.

It is commonly assumed that the volume of ice does not vary during creep (Khoo and Hrudey, 1992), and therefore the creep strain rate in the z direction, $\dot{\varepsilon}_z^c$, is:

$$\dot{\varepsilon}_z^c = -\dot{\varepsilon}_r^c - \dot{\varepsilon}_\theta^c$$

(4.7.7)

or

$$\dot{\varepsilon}_z^c = -\frac{1}{2}\eta\tilde{\sigma}^{(n-1)}(\sigma_\theta + \sigma_r)$$

(4.7.8)

The transverse shear stress, σ_{rz}, is ignored because of the plane stress assumption, and the tangential shear stress, $\sigma_{\theta z}$, is zero due to axisymmetry.

At any given time, the creep strain rates (which are used to estimate the creep strain increments) can be calculated at any location within an element from the current stress solution, using equations (4.7.4) and (4.7.5). The strain rates will actually be calculated at a number of integration points within each element and will be used to calculate the horizontal and vertical components ($\{q^{uc}\}$ and $\{q^{wc}\}$) of the element creep load vector, $\{q^c\}$. From equations (4.3.5), (4.3.6), and (4.3.14):

$$U_2 = -\frac{E}{2(1-v^2)}\int_{-h/2}^{+h/2}\left[\int_{r_1}^{r_2}2\left(\frac{\partial u}{\partial r}\varepsilon_r^c + \frac{u}{r}\varepsilon_\theta^c + v\left(\frac{u}{r}\varepsilon_r^c + \frac{\partial u}{\partial r}\varepsilon_\theta^c\right)\right)2\pi r dr\right]dz$$

$$+\frac{E}{2(1-v^2)}\int_{-h/2}^{+h/2}\left[\int_{r_1}^{r_2}2\left(z\frac{\partial^2 w}{\partial r^2}\varepsilon_r^c + \frac{z}{r}\frac{\partial w}{\partial r}\varepsilon_\theta^c + v\left(\frac{z}{r}\frac{\partial w}{\partial r}\varepsilon_r^c + z\frac{\partial^2 w}{\partial r^2}\varepsilon_\theta^c\right)\right)2\pi r dr\right]dz$$

(4.7.9)

or

$$U_2 = -<u>\{q^{uc}\}-<w>\{q^{wc}\}$$

(4.7.10)

where

$$\{q^{uc}\} = \frac{E}{2(1-v^2)}\int_{-h/2}^{+h/2}\left[\int_{r_1}^{r_2}2\left(\begin{array}{c}\{\varphi_r\}\varepsilon_r^c + \frac{1}{r}\{\varphi\}\varepsilon_\theta^c \\ +v\left(\frac{1}{r}\{\varphi\}\varepsilon_r^c + \{\varphi_r\}\varepsilon_\theta^c\right)\end{array}\right)2\pi r dr\right]dz$$

(4.7.11)

$$\left\{q^{wc}\right\} = -\frac{E}{2(1-v^2)} \int\limits_{-h/2}^{+h/2} \left[\int\limits_{r_1}^{r_2} 2 \left(\begin{array}{l} z\{\phi_{rr}\}\varepsilon_r^c + \dfrac{z}{r}\{\phi_r\}\varepsilon_\theta^c + \\[2mm] v\left(\dfrac{z}{r}\{\phi_r\}\varepsilon_r^c + z\{\phi_{rr}\}\varepsilon_\theta^c \right) \end{array} \right) 2\pi r dr \right] dz \qquad (4.7.12)$$

In order to evaluate these components of the element creep load vector, the creep strains in the radial and tangential directions, ε_r^c and ε_θ^c (equations (4.7.4) and (4.7.5)), are calculated at a set of integration points at each time step. Once these values have been obtained, $\{q^{uc}\}$ and $\{q^{wc}\}$ can be evaluated, and added together to form the element creep load vector $\{q^c\}$:

$$\{q^c\} = \{q^{uc}\} + \{q^{wc}\} \qquad (4.7.13)$$

These element creep load vectors are then assembled (see Appendix A) into the global creep load vector, $\{Q^c\}$, giving:

$$\{Q^c\} = \mathop{A}\limits_{e=1}^{N_e} \{q^c\}_e \qquad (4.7.14)$$

where the index e refers to a specific element. This global creep load vector is then added to the mechanical load vector $\{R\}$. The new system to be solved at each time step is:

$$[K]\{\Phi\} = \{R\} + \{Q^c\} \qquad (4.7.15)$$

4.7.1 Numerical Integration

The integration in equations (4.7.11) and (4.7.12) is performed using a common method of numerical integration known as Gaussian quadrature (Stasa, 1985). The integrand is evaluated at a number of sampling points, and the value at each sampling

66

point is multiplied by a weighting factor. For example, for a two dimensional (p, s) integration the integrand, I, can be written as:

$$I = \int\limits_{-1}^{+1}\int\limits_{-1}^{+1} f(p,s)dpds = \sum_{j=1}^{m_2}\sum_{i=1}^{m_1} \varpi_i \varpi_j f(p_i, s_j)$$

(4.7.16)

where $f(p,s)$ is any function, p_i and s_j are sampling points, ϖ_i and ϖ_j are weighting factors, and m_1 and m_2 are the number of sampling points chosen in the p and s directions, respectively (Stasa, 1985). These sampling points and weighting factors can be seen in Table 4-1. The number of integration (Gauss) points chosen within each element will affect the accuracy of the solution. According to Stasa (1985), a Gaussian quadrature routine using m_1 sampling points will integrate a polynomial of the order $2m_1-1$ exactly, therefore a greater number of Gauss points will produce a more accurate solution.

To implement this numerical integration, the limits of integration must range from -1 to $+1$ for each variable (Stasa, 1985). As the limits of integration in equations (4.7.11) and (4.7.12) do not meet this requirement, the equations are transformed into functions of a non-dimensional coordinate, x $(-1 \le x \le +1)$, where:

$$r = \frac{a}{2}(x+1)+r_1 \quad \text{and} \quad dr = \frac{a}{2}dx$$

(4.7.17)

In the z direction, another transformation takes place, changing z to a non-dimensional coordinate, y $(-1 \le y \le +1)$, where:

$$z = \frac{h}{2}y \quad \text{and} \quad dz = \frac{h}{2}dy$$

(4.7.18)

Equations (4.7.11) and (4.7.12) can now be expressed in terms of x and y, giving the following expressions for the element horizontal and vertical creep load vectors (which must be evaluated for each value of i):

67

$$\{q^{uc}\} = \frac{Eh}{(1-v^2)} \int\limits_{y=-1}^{y=1} \left[\int\limits_{x=-1}^{x=1} \left(\begin{array}{c} \dfrac{2}{a}\dfrac{d\varphi_i}{dx}\varepsilon_r^c + \dfrac{1}{x_o}\varphi_i\varepsilon_\theta^c + \\ v\left(\dfrac{1}{x_o}\varphi_i\varepsilon_r^c + \dfrac{2}{a}\dfrac{d\varphi_i}{dx}\varepsilon_\theta^c\right) \end{array} \right) \frac{\pi a}{2} x_o dx \right] dy \qquad (4.7.19)$$

$$\{q^{wc}\} = \frac{-Eh}{(1-v^2)} \int\limits_{y=-1}^{y=1} \left[\int\limits_{x=-1}^{x=1} \left(\begin{array}{c} \dfrac{2hy}{a^2}\dfrac{d^2\phi_i}{dx^2}\varepsilon_r^c + \dfrac{hy}{ax_o}\dfrac{d\phi_i}{dx}\varepsilon_\theta^c + \\ v\left(\dfrac{hy}{ax_o}\dfrac{d\phi_i}{dx}\varepsilon_r^c + \dfrac{2hy}{a^2}\dfrac{d^2\phi_i}{dx^2}\varepsilon_\theta^c\right) \end{array} \right) \frac{\pi a}{2} x_o dx \right] dy \qquad (4.7.20)$$

where x_o is defined as:
$$x_o = \frac{1}{2}(x+1)a + r_1 \qquad (4.7.21)$$

Evaluation of the creep strains, ε_r^c and ε_θ^c (with equations (4.7.4) and (4.7.5)), requires the elastic strains (ε_r^e and ε_θ^e) at each integration point, as well as radial and tangential stresses (σ_r and σ_θ) at each point. Transforming equations (4.3.10) and (4.3.11) from functions of r to x, the elastic strains in the radial and tangential directions can be calculated from:

$$\varepsilon_r^e = \frac{2}{a}\left(\frac{du}{dx} - \frac{hy}{a}\frac{d^2w}{dx^2}\right) - \varepsilon_r^c \qquad (4.7.22)$$

$$\varepsilon_\theta^e = \frac{1}{x_o}\left(u - \frac{hy}{a}\frac{dw}{dx}\right) - \varepsilon_\theta^c \qquad (4.7.23)$$

The radial and tangential stresses (σ_r and σ_θ) can be calculated from equations (4.3.3) and (4.3.4).

As equations (4.7.4) and (4.7.5) are ordinary differential equations, the creep strains in the radial and tangential directions can be estimated at each time step using one of several common methods. These include the *Euler* and the *4th Order Runge-Kutta* methods.

4.7.2 Estimating Creep Strains Using an Euler Method

One method for solving first order ordinary differential equations is the Euler method (Gerald and Wheatley, 1984). In this model, the Euler method can be used to evaluate the creep strains, ε_r^c and ε_θ^c. The Euler method is an explicit method, and so the solution for the current time step, t_{i+1}, is based entirely upon the solution from the previous time step, t_i (where $\Delta t = t_{i+1} - t_i$). The creep strain rates can be approximated as:

$$\frac{d\varepsilon_r^c}{dt} \approx \frac{\varepsilon_{r_{t_{i+1}}}^c - \varepsilon_{r_{t_i}}^c}{\Delta t} \tag{4.7.24}$$

$$\frac{d\varepsilon_\theta^c}{dt} \approx \frac{\varepsilon_{\theta_{t_{i+1}}}^c - \varepsilon_{\theta_{t_i}}^c}{\Delta t} \tag{4.7.25}$$

where the subscripts t_{i+1} and t_i denote the time step at which the various quantities are being evaluated. Substitution into (4.7.4) and (4.7.5) yields:

$$\varepsilon_{r_{t_{i+1}}}^c = \varepsilon_{r_{t_i}}^c + \Delta t \left[\eta \tilde{\sigma}^{(n-1)} \left(\sigma_r - \frac{1}{2} \sigma_\theta \right) \right] \tag{4.7.26}$$

$$\varepsilon_{\theta_{t_{i+1}}}^c = \varepsilon_{\theta_{t_i}}^c + \Delta t \left[\eta \tilde{\sigma}^{(n-1)} \left(\sigma_\theta - \frac{1}{2} \sigma_r \right) \right] \tag{4.7.27}$$

Equations (4.7.26) and (4.7.27) are used with equations (4.7.19) and (4.7.20) to evaluate the creep load vector at each time step. A flowchart of the solution procedure using the Euler method can be found in Figure 4-6, with T_e being the time at the end of the test.

4.7.3 Estimating Creep Strains Using a 4th Order Runge-Kutta Method

Another method for solving first order ordinary differential equations is the 4th Order Runge-Kutta Method (Gerald and Wheatley, 1984). It is often advantageous to

69

use this method as it is more accurate than the Euler method (for four times the computational effort), as well as being more numerically stable (and therefore a larger time step can be used). This method takes the solution from the previous time step (t_i) and makes intermediate calculations at the centre and end of the time step before yielding a final solution for the current time step (t_{i+1}).

There are four intermediate calculation steps involved in solving this problem using the 4th Order Runge-Kutta method, as illustrated for the radial equations in Figure 4-7. The equations to be solved are (4.7.4) and (4.7.5), and slope functions in the radial and tangential directions (f_r and f_θ) can be defined as:

$$f_r = \eta \tilde{\sigma}^{(n-1)}\left(\sigma_r - \frac{1}{2}\sigma_\theta\right)$$

(4.7.28)

$$f_\theta = \eta \tilde{\sigma}^{(n-1)}\left(\sigma_\theta - \frac{1}{2}\sigma_r\right)$$

(4.7.29)

For each intermediate calculation, f_r and f_θ can be calculated using equations (4.3.3), (4.3.4), (4.7.6), (4.7.22) and (4.7.23).

For the first stage of the intermediate calculations, the quantities in equations (4.7.28) and (4.7.29) are calculated from the solution at the previous time step, t_i:

Stage 1:
$$f_{r1} = f_r\left(t_i, \varepsilon^c_{r_{t_i}}, \varepsilon^c_{\theta_{t_i}}\right)$$

(4.7.30a)

$$f_{\theta1} = f_\theta\left(t_i, \varepsilon^c_{\theta_{t_i}}, \varepsilon^c_{r_{t_i}}\right)$$

(4.7.30b)

$$\varepsilon^c_{r1} = \varepsilon^c_{r_{t_i}} + \frac{\Delta t}{2}f_{r1}$$

(4.7.31a)

$$\varepsilon^c_{\theta1} = \varepsilon^c_{\theta_{t_i}} + \frac{\Delta t}{2}f_{\theta1}$$

(4.7.31b)

70

where the numerical subscripts on f_r, f_θ, ε_r^c and ε_θ^c indicate the stage of the calculations. These quantities are used to evaluate the global creep load vector $\{Q^c\}$, which is then added to the mechanical load vector and the system in equation (4.7.15) is solved for $\{\Phi\}$.

· This process is repeated for intermediate calculation stages 2 through 4, with the following expressions used to evaluate the creep strains at each stage (each being based on the solution from the previous stage):

Stage 2:

$$f_{r2} = f_r\left(t_i + 0.5\Delta t, \varepsilon_{r1}^c, \varepsilon_{\theta1}^c\right) \qquad (4.7.32a)$$

$$f_{\theta2} = f_\theta\left(t_i + 0.5\Delta t, \varepsilon_{\theta1}^c, \varepsilon_{r1}^c\right) \qquad (4.7.32b)$$

$$\varepsilon_{r2}^c = \varepsilon_{r t_i}^c + \frac{\Delta t}{2} f_{r2} \qquad (4.7.33a)$$

$$\varepsilon_{\theta2}^c = \varepsilon_{\theta t_i}^c + \frac{\Delta t}{2} f_{\theta2} \qquad (4.7.33b)$$

Stage 3:

$$f_{r3} = f_r\left(t_i + 0.5\Delta t, \varepsilon_{r2}^c, \varepsilon_{\theta2}^c\right) \qquad (4.7.34a)$$

$$f_{\theta3} = f_\theta\left(t_i + 0.5\Delta t, \varepsilon_{\theta2}^c, \varepsilon_{r2}^c\right) \qquad (4.7.34b)$$

$$\varepsilon_{r3}^c = \varepsilon_{r t_i}^c + \Delta t \cdot f_{r3} \qquad (4.7.35a)$$

$$\varepsilon_{\theta3}^c = \varepsilon_{\theta t_i}^c + \Delta t \cdot f_{\theta3} \qquad (4.7.35b)$$

Stage 4:

$$f_{r4} = f_r\left(t_i + \Delta t, \varepsilon_{r3}^c, \varepsilon_{\theta 3}^c\right)$$

(4.7.36a)

$$f_{\theta 4} = f_\theta\left(t_i + \Delta t, \varepsilon_{\theta 3}^c, \varepsilon_{r3}^c\right)$$

(4.7.36b)

$$\varepsilon_{r4}^c = \varepsilon_{r t_i}^c + \frac{\Delta t}{6}\cdot\left(f_{r1} + 2f_{r2} + 2f_{r3} + f_{r4}\right)$$

(4.7.37a)

$$\varepsilon_{\theta 4}^c = \varepsilon_{\theta t_i}^c + \frac{\Delta t}{6}\cdot\left(f_{\theta 1} + 2f_{\theta 2} + 2f_{\theta 3} + f_{\theta 4}\right)$$

(4.7.37b)

These last values for the creep strains, ε_{r4}^c and $\varepsilon_{\theta 4}^c$, are used to calculate the final creep load vector for this time step and solve for the deflections and rotations, $\{\Phi\}$, at the end of the time interval, t_{i+1}. A flowchart describing the entire solution process using the 4th Order Runge-Kutta method can be found in Figure 4-8, where T_e is the time at the end of the test.

4.8 Boundary Conditions

The boundary conditions were imposed upon the matrix system by the use of a penalty method (Chandrupatla and Belegundu, 1997). In order to implement this, the system of equations was prepared as if all degrees of freedom at each node were unknown, and then the system was forced to the boundary condition values by introducing a penalty, P. For example, in a simple system like the following (where S is the total number of equations):

$$\begin{bmatrix} K_{11} & K_{12} & \cdots & K_{1S} \\ K_{21} & K_{22} & \cdots & K_{2S} \\ \vdots & \vdots & \ddots & \vdots \\ K_{S1} & K_{S2} & \cdots & K_{SS} \end{bmatrix} \begin{Bmatrix} \Phi_1 \\ \Phi_2 \\ \vdots \\ \Phi_S \end{Bmatrix} = \begin{Bmatrix} R_1 \\ R_2 \\ \vdots \\ R_S \end{Bmatrix}$$

(4.8.1)

where K_{ij} are stiffness matrix values, Φ_i are unknown values, and R_i are load vector values (with $1 \le i \le S$ and $1 \le j \le S$). If Φ_l is known to have a value of Φ_o, then the penalty and known boundary condition are included to give the following system:

$$
\begin{bmatrix}
(K_{11} + P) & K_{12} & \cdots & K_{1S} \\
K_{21} & K_{22} & \cdots & K_{2S} \\
\vdots & \vdots & \ddots & \vdots \\
K_{S1} & K_{S2} & \cdots & K_{SS}
\end{bmatrix}
\begin{Bmatrix}
\Phi_1 \\
\Phi_2 \\
\vdots \\
\Phi_S
\end{Bmatrix}
=
\begin{Bmatrix}
R_1 + \Phi_o \cdot P \\
R_2 \\
\vdots \\
R_S
\end{Bmatrix}
\tag{4.8.2}
$$

where Φ_l is now forced to the value of Φ_o and the system is solved for the remaining unknowns. If more than one boundary condition is specified, the penalty is imposed on each location in the load and stiffness matrices corresponding to that boundary condition.

4.8.1 Penalty Size

The size of the penalty, P, imposed on the matrix system can affect the accuracy of the solution obtained. According to Chandrupatla and Belegundu (1997), an acceptable approach for choosing the value of P is:

$$
P = \max|K_{ij}| \times 10^4
\tag{4.8.3}
$$

with $1 \le i \le S$ and $1 \le j \le S$, that is, P is 10^4 times the largest absolute value in the stiffness matrix. As the magnitude of the penalty approaches infinity, the solution for Φ_l will approach the exact value of Φ_o (Rao, 1989).

A simple test was performed to determine the sensitivity of the model to the size of the penalty. The elastic solution of the model for both a simply supported beam and a clamped edge beam was compared to an analytical solution (see section 5.2) for various penalty numbers. The maximum absolute value of the stiffness matrix was multiplied by three different values: 10^3, 10^4, and 10^5 to obtain the penalty, P. A slight improvement

73

was seen in the model solution when increasing the multiplier from 10^3 and 10^4, but no noticeable improvement was found between 10^4 and 10^5. To be conservative, the penalty was set at:

$$P = \max\left|K_{ij}\right| \times 10^5$$

(4.8.4)

4.8.2 Boundary Elements

Since the situations considered by this model are axisymmetric, the first node of the interior element is directly below the centre of the load and therefore the inner radius, $r_I = 0$. This presents a problem when calculating the stiffness matrices, as certain equations used in these calculations contain terms involving the natural logarithm, $ln(r_I)$, which is undefined when $r_I = 0$. These stiffness matrix equations can be found in Appendix B.

Within the horizontal and vertical element stiffness matrices, $[k^u]$ and $[k^w]$, the terms in equations (B.1), (B.3), and (B.8) which contain the natural logarithm can be set to zero (for the first element only). These locations in the matrices correspond to specified boundary conditions ($u_I = 0$, $w_{rI} = 0$, and $u_{Nn} = 0$, where N_n is total the number of nodes) for all cases considered here, and these terms will become insignificant once the penalty is added. The other terms in $[k^u]$ and $[k^w]$ which contain $ln(r_I)$ will approach zero as r_I approaches zero. This can be shown by taking the limit as r_I approaches zero using l'Hospital's Rule (Stewart, 1991). As a result, for the first element, these terms can also be set to zero.

The distance from the load to the farthest element will be discussed in the spatial discretization analysis of section 5.5.1.

74

4.9 Summary

The finite element model described in this chapter was developed into a computer application using Visual Basic. A brief explanation of the program and interface can be found in Appendix C; a more detailed explanation of the model inputs, outputs and general information can be found in the *Readme* file accompanying the program.

Table 4-1: Sampling points and weighting factors for Gaussian quadrature. (adapted from Zienkiewicz, 1977)

Number of sampling points, n	Sampling point $\pm p_i$	Weighting factor ϖ_i
1	0.000000000000000	2.000000000000000
2	0.577350269189626	1.000000000000000
3	0.774596669241483	0.555555555555556
	0.000000000000000	0.888888888888889
4	0.861136311594053	0.347854845137454
	0.339981043584856	0.652145154862546
5	0.906179845938664	0.236926885056189
	0.538469310105683	0.478628670499366
	0.000000000000000	0.568888888888889
6	0.932469514203152	0.171324492379170
	0.661209386466265	0.360761573048139
	0.238619186083197	0.467913934572691
7	0.949107912342759	0.129484966168870
	0.741531185599394	0.279705391489277
	0.405845151377397	0.381830050505119
	0.000000000000000	0.417959183673469
8	0.960289856497536	0.101228536290376
	0.796666477413627	0.222381034453374
	0.525532409916329	0.313706645877887
	0.183434642495650	0.362683783378362
9	0.968160239507626	0.081274388361574
	0.836031107326636	0.180648160694857
	0.324253423403809	0.312347077040003
	0.000000000000000	0.330239355001260
10	0.973906528517172	0.066671344308688
	0.865063366688985	0.149451349150581
	0.679409568299024	0.219086362515982
	0.433395394129247	0.269266719309996
	0.148874338981631	0.295524224714753

ε_0 = elastic deformation
ε_1 = transient creep
ε_2 = elastic deformation recovery
ε_3 = elastic lag
ε_4 = permanent viscous deformation
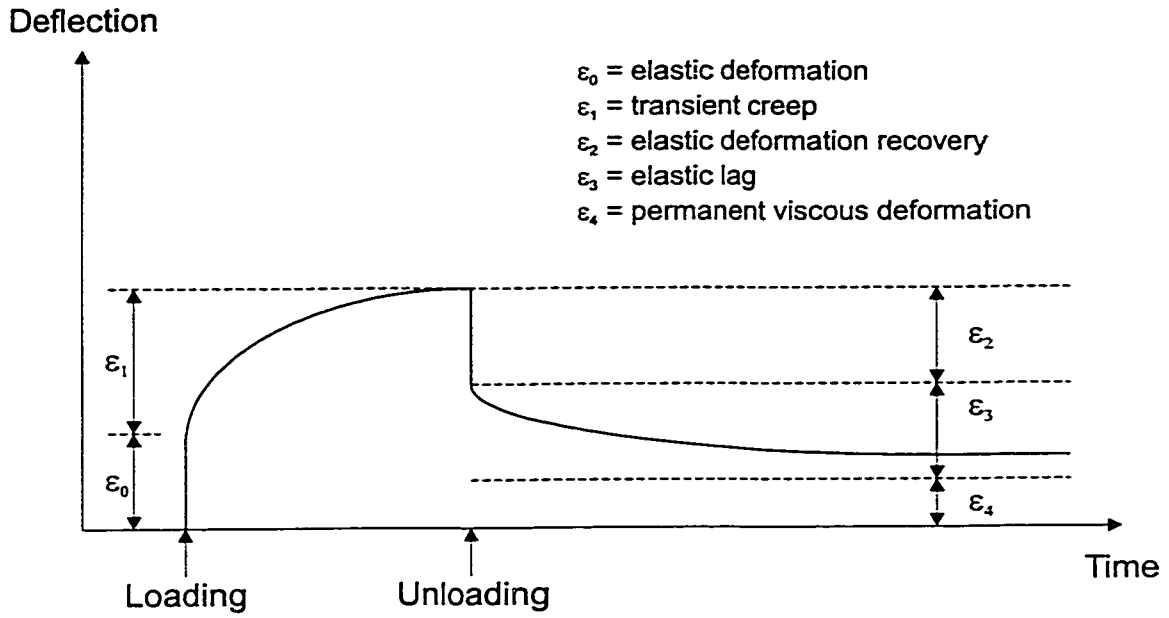
Figure 4-1: Deflection-time relationship for an ice sample subjected to instantaneous loading and unloading (adapted from Ashton, 1986).
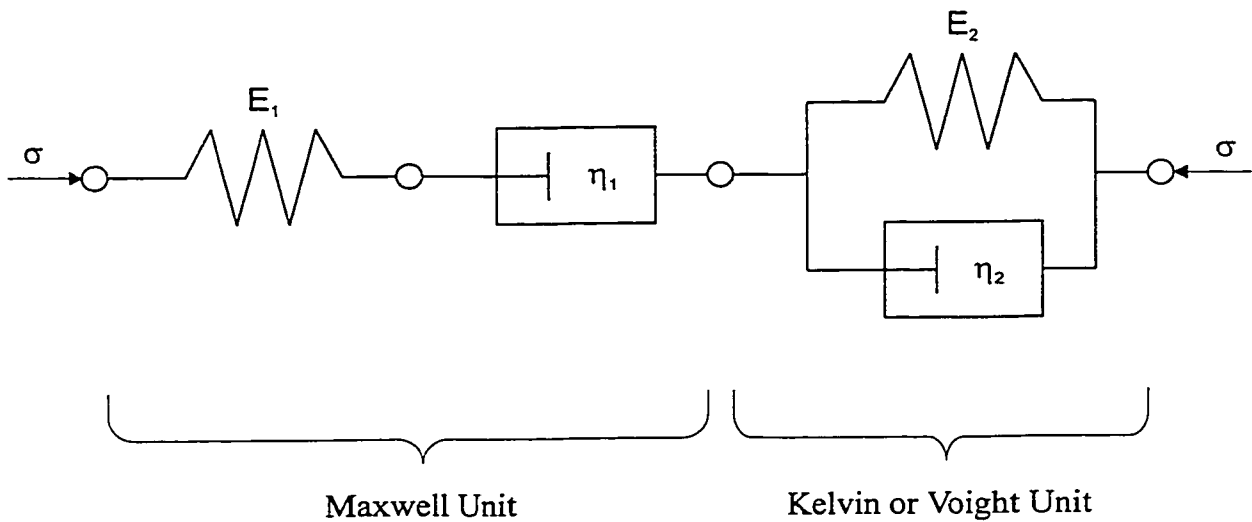

Maxwell Unit   Kelvin or Voight Unit

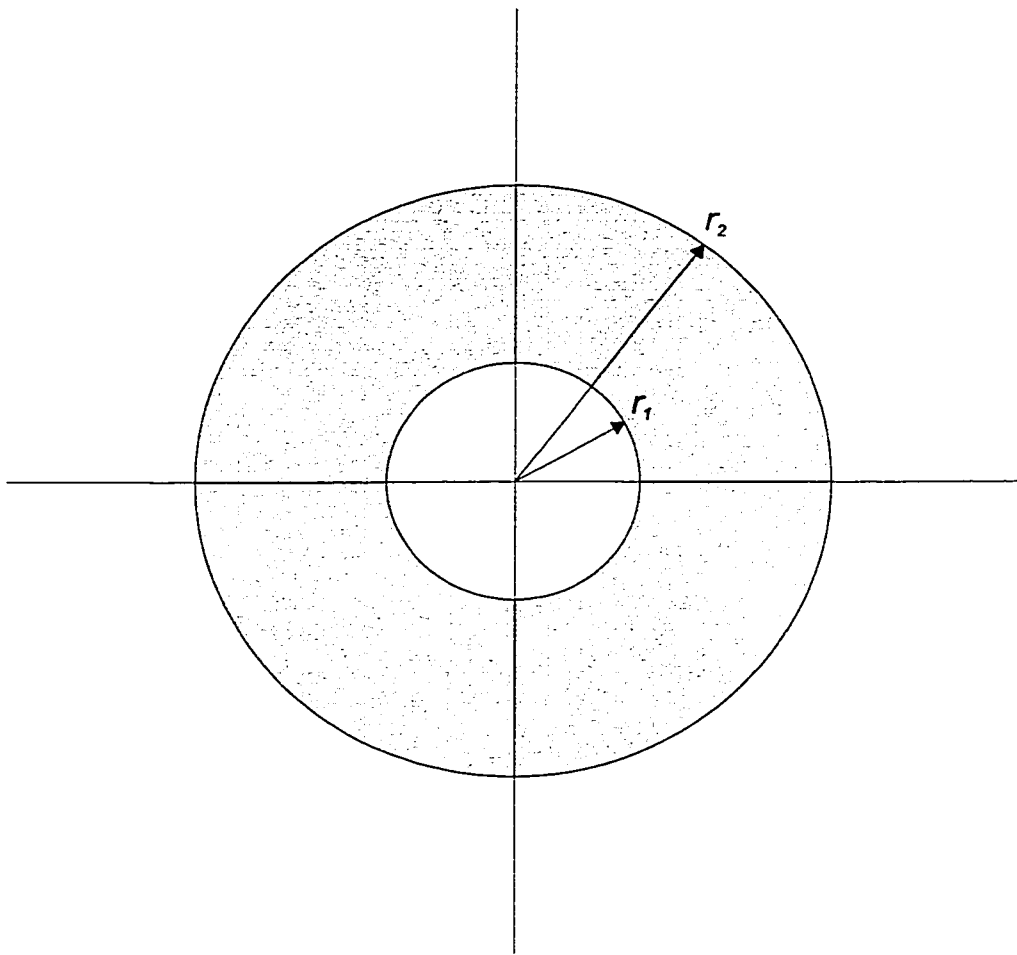Figure 4-2: Composite rheological model of ice (adapted from Ashton, 1986).

Figure 4-3: Plan view of one element.

Figure 4-4: Element cross section.
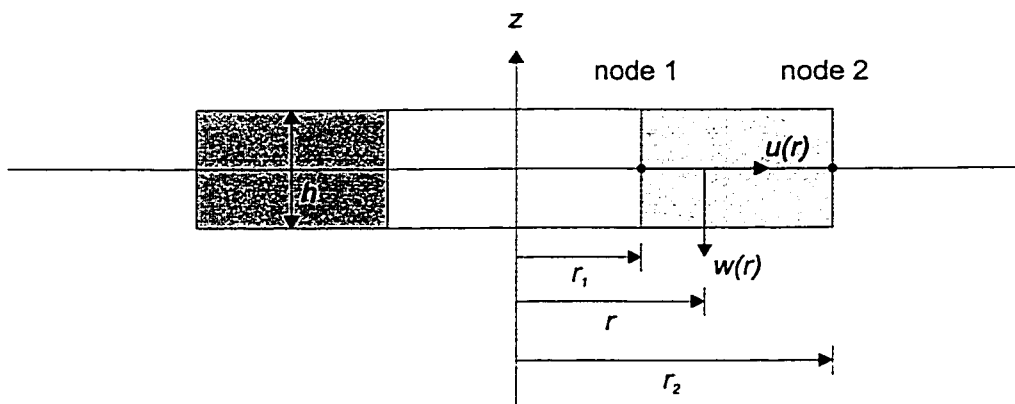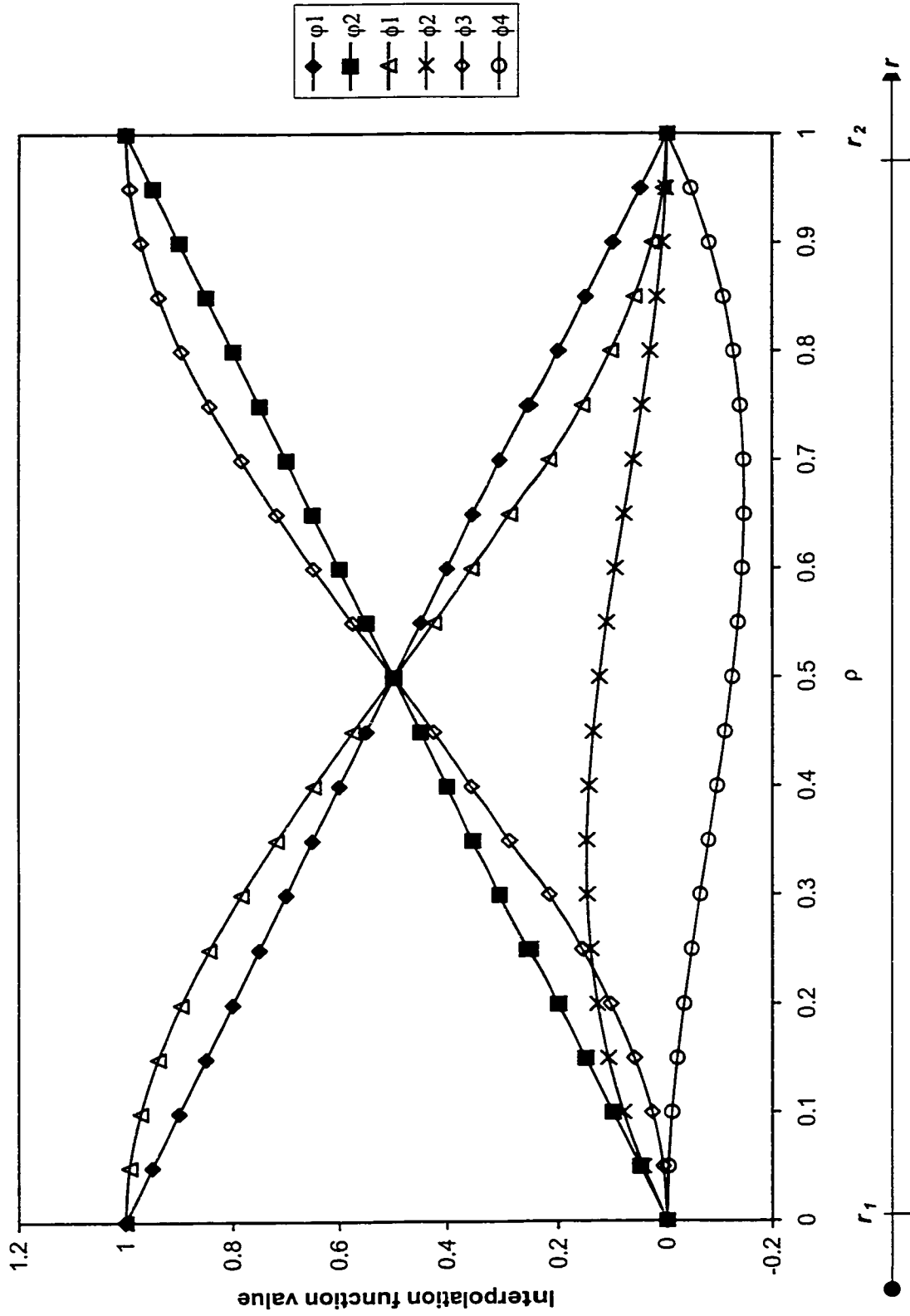
Figure 4-5: Interpolation functions.

79

Have the solution from the previous time step, t_i
Loop over time steps, t [Do While $t <= T_e$]

Loop over elements, n

Loop over integration points (radial direction), i

Loop over integration points (vertical direction), j

Calculate elastic strains $\varepsilon_r^e(n,i,j)$ and $\varepsilon_\theta^e(n,i,j)$ {equations 4.7.22 and 4.7.23}

Calculate stresses $\sigma_r(n,i,j)$, $\sigma_\theta(n,i,j)$, and $\sigma_\sim(n,i,j)$ {equations 4.3.3, 4.3.4, and 4.7.6}

Calculate creep strains $\varepsilon_r^c(n,i,j)$ and $\varepsilon_\theta^c(n,i,j)$ {equations 4.7.26 and 4.7.27}

Calculate creep load vectors $\{q^{uc}\}$ and $\{q^{wc}\}$ {equations 4.7.11 and 4.7.12}

next integration point (vertical), j

next integration point (radial), i

next element, n

Assemble creep load vector $\{Q^c\}$ and add to mechanical load vector $\{R\}$

Solve $[K]\{\Phi\} = \{R\} + \{Q^c\}$ {equation 4.7.15}

Reset variables for the next time step (e.g. u_i, w_i, w_{ri})
Increment the time ($t = t + \Delta t$)

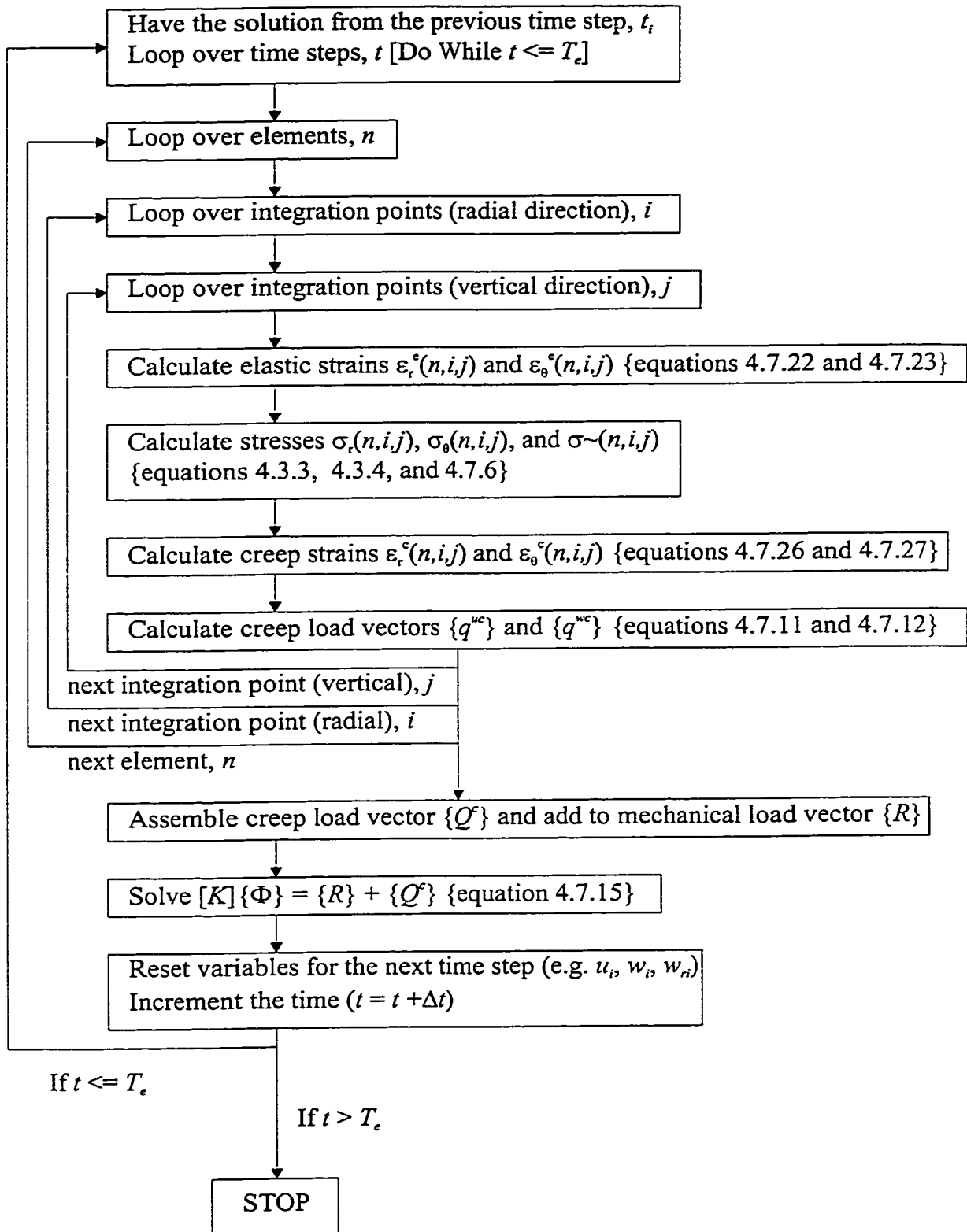If $t <= T_e$

If $t > T_e$

STOP

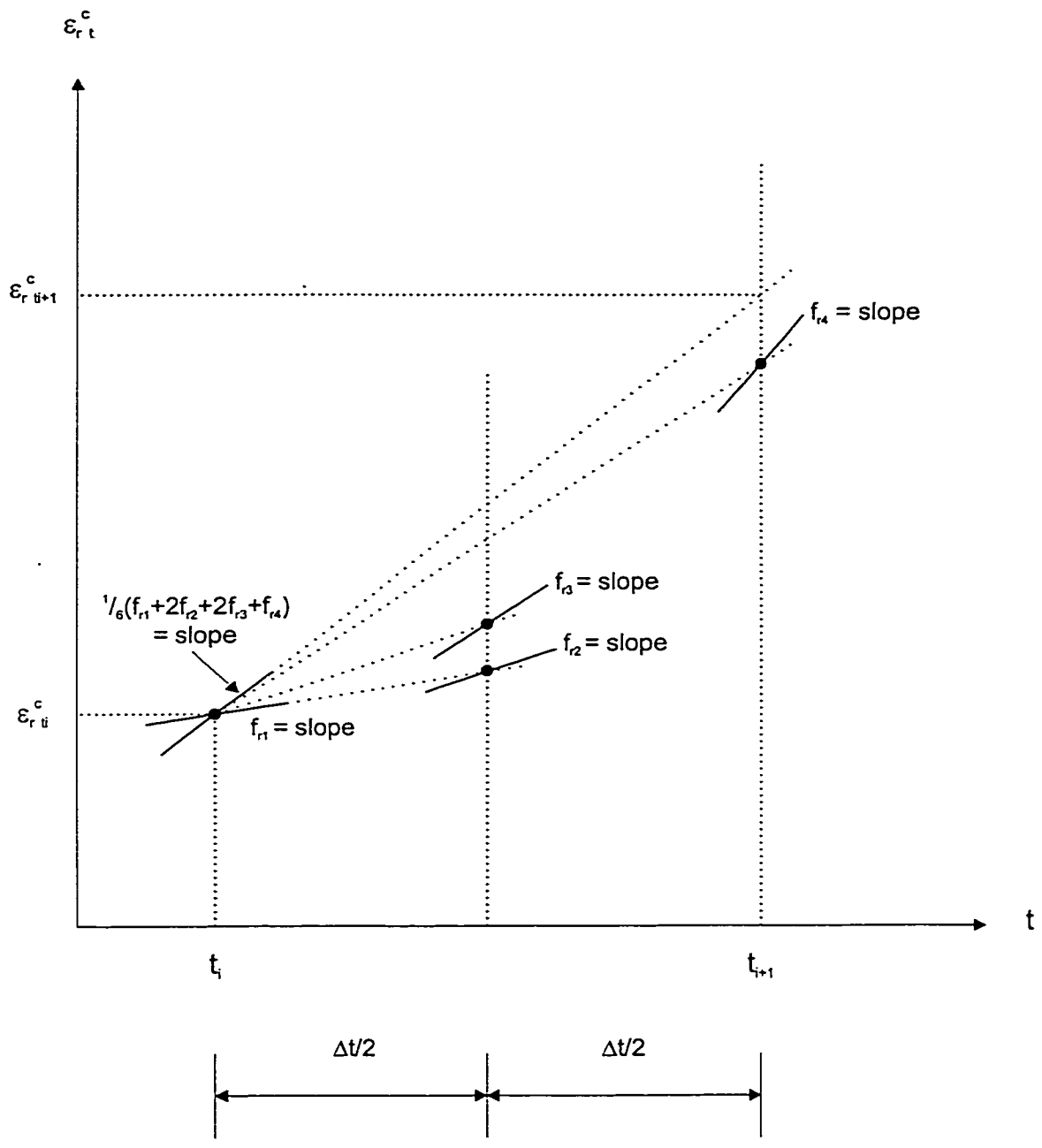Figure 4-6: Flowchart for Euler method of solution.

80

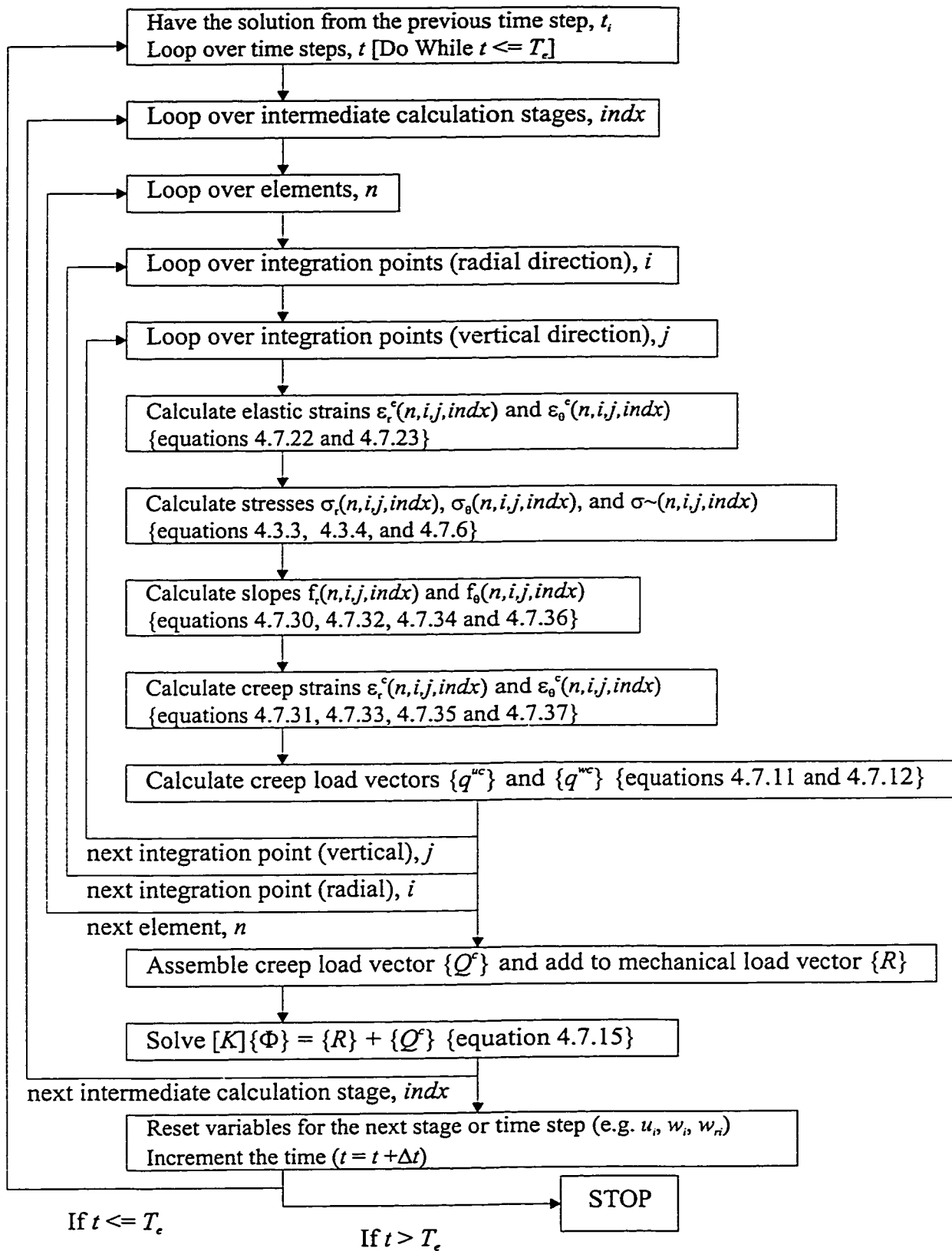Figure 4-7: 4th Order Runge-Kutta Method.

Figure 4-8: Flowchart for 4th Order Runge-Kutta method of solution.

5.0 MODEL VERIFICATION

5.1 Introduction

In order to verify the finite element model, the solutions found for several test problems were compared to analytical solutions. For elastic behaviour, analytical solutions exist for several cases including vertical loading of a simply supported or clamped edge plate, as well as vertical loading of an elastic plate on an elastic foundation.

Situations involving the creep of ice are very complex and therefore an analytical solution has not yet been developed for the long term deflection of an ice beam or plate on an elastic foundation. This model predicts the time dependent ice deflection using a numerical method such as the Euler method or the 4th Order Runge-Kutta method. The creep calculations of the model will be tested for some simple cases.

This chapter contains a section on the analytical solution for an elastic plate with no elastic foundation and describes a test case. Another section deals with two test cases involving an elastic plate with no elastic foundation that is experiencing creep. The next section describes an analytical solution and test case for an elastic plate on an elastic foundation. Finally, appropriate spatial and temporal discretization scales for an elastic plate on an elastic foundation with creep are examined, and values to be used for the model application in the following chapter are decided.

5.2 Elastic Plate

5.2.1 Analytical Solution

Timoshenko (1959) derived an analytical solution for uniform vertical loading of a circular elastic plate with no elastic foundation. For the case of a plate with simply

supported edges (see Figure 5-1), the expression for vertical deflection, w, is:

$$w = \frac{q_o(\alpha^2 - r^2)}{64D}\left(\frac{5+\nu}{1+\nu}\alpha^2 - r^2\right) \tag{5.1.1}$$

and the slope, w_r, can be calculated from:

$$w_r = -\frac{2rq_o}{64D}\left[\left(\frac{5+\nu}{1+\nu}\alpha^2 - r^2\right) + \left(\alpha^2 - r^2\right)\right] \tag{5.1.2}$$

where α is the radius of the load (and in this case the radius of the plate as well), q_o is the uniform applied load, D is bending stiffness, ν is Poisson's ratio, and r is the distance from the centre of the plate. If the edges of the plate are clamped (see Figure 5-2), the equation for deflection is:

$$w = \frac{q_o}{64D}\left(\alpha^2 - r^2\right)^2 \tag{5.1.3}$$

and the slope can be found from:

$$w_r = -\frac{4rq_o}{64D}\left(\alpha^2 - r^2\right) \tag{5.1.4}$$

5.2.2 Elastic Behaviour Test

A simple example was designed to test the elastic response of the model to the loading of a simply supported or clamped edge plate, and to compare this to the analytical solution derived by Timoshenko (1959).

The simply supported elastic plate is illustrated in Figure 5-1. In this example the plate thickness $h = 0.10$ m, Young's modulus $E = 9\times10^9$ Pa, $\nu = 0.333$ and $q_o = 18000$ Pa. Because of the axisymmetry of the problem, the elements extended from $r = 0$ to $r = L/2$, where L is the diameter of the plate. Ten elements were used in this analysis (each 0.5 m

long). The deflected shape of the plate, as calculated by the model and by Timoshenko's equation (5.1.1), can be seen in Figure 5-3. The two solutions are in excellent agreement with a maximum percent difference of approximately 0.002%.

The clamped edge plate (Figure 5-2) example also uses $h = 0.10$ m, $E = 9 \times 10^9$ Pa, $\nu = 0.333$ and $q_o = 18000$ Pa. The same element discretization was used as in the simply supported case. Figure 5-4 shows the deflected shape of the plate as computed by the model and Timoshenko's equation (5.1.3). The two methods produce results that agree very well, with the maximum percent difference of about 0.3%.

5.3 Elastic Plate with Creep

Two simple examples were formulated to test the model calculations for the vertical creep load vector for a case in which no elastic foundation is present. The first example examines a pure bending situation in which the creep load vector contains only moment loads; the second examines vertical loading in which "artificial" creep strains are imposed on the system to obtain deflections directly proportional to these creep strains.

5.3.1 Pure Bending Test

The pure bending example can be solved analytically, and assumes that the deflected shape of the plate (due to creep only) is spherical. This situation would cause each element's creep load vector to contain values in the moment locations only with no vertical forces present (i.e. loads corresponding to the local w_{r1} and w_{r2} positions of the creep load vector only). When the element creep load vectors are assembled, the moment values at the adjoining ends of elements will be equal in magnitude but opposite in

direction, cancelling each other out, and leaving loads in the first and last global moment positions. The innermost moment will be proportional to the inner radius of the first element ($r_1 = 0$) leaving only one load in the last moment position of the creep load vector.

Looking at the element vertical creep load vector, $\{q^{wc}\}$, equation (4.7.12) can be rewritten as:

$$\{q^{wc}\} = -\frac{E}{(1-\nu^2)} \int_{-h/2}^{h/2} \int_{r_1}^{r_2} z\left[\{\phi_{rr}\}(\varepsilon_r^c + \nu\varepsilon_\theta^c) + \frac{1}{r}\{\phi_r\}(\varepsilon_\theta^c + \nu\varepsilon_r^c)\right] 2\pi r\, dr\, dz \qquad (5.3.1)$$

or $$\{q^{wc}\} = -\frac{2\pi E}{(1-\nu^2)} \int_{-h/2}^{h/2} \int_{r_1}^{r_2} z\left[r\{\phi_{rr}\}(\varepsilon_r^c + \nu\varepsilon_\theta^c) + \{\phi_r\}(\varepsilon_\theta^c + \nu\varepsilon_r^c)\right] dr\, dz \qquad (5.3.2)$$

Transforming this relationship into a function of non-dimensional coordinates ρ and y (where $0 \le \rho \le 1$ and $-1 \le y \le 1$), using equations (4.4.5), (4.4.7) and (4.4.13) gives:

$$\{q^{wc}\} = -\frac{2\pi E}{(1-\nu^2)}\left(\frac{h}{2}\right)^2 a \int_{-1}^{1}\int_{0}^{1} y\left[\begin{array}{c}\left(\rho+\dfrac{r_1}{a}\right)\dfrac{1}{a}\{\phi_{\rho\rho}\}(\varepsilon_r^c + \nu\varepsilon_\theta^c) \\[2mm] +\dfrac{1}{a}\{\phi_\rho\}(\varepsilon_\theta^c + \nu\varepsilon_r^c)\end{array}\right] d\rho\, dy \qquad (5.3.3)$$

or $$\{q^{wc}\} = -\frac{\pi E h^2}{2(1-\nu^2)} \int_{-1}^{1}\int_{0}^{1} y\left[\left(\rho+\frac{r_1}{a}\right)\{\phi_{\rho\rho}\}(\varepsilon_r^c + \nu\varepsilon_\theta^c) + \{\phi_\rho\}(\varepsilon_\theta^c + \nu\varepsilon_r^c)\right] d\rho\, dy \qquad (5.3.4)$$

where the subscripts ρ and $\rho\rho$ denote derivatives with respect to ρ.

Next, a "spherical" creep shape is assumed, such that the curvature in the radial and tangential directions (κ_r^c and κ_θ^c) are equal to the total creep curvature, κ^c:

$$\kappa^c = \kappa_r^c = \kappa_\theta^c \qquad (5.3.5)$$

Therefore, the creep strains in both directions are equal and can be written as:

$$\varepsilon^c = -z\kappa^c = -\frac{hy}{2}\kappa^c \qquad (5.3.6)$$

Substitution of this relationship into equation (5.3.4) gives:

$$\{q^{wc}\} = -\frac{\pi E h^2}{2(1-\nu^2)} \int\limits_{-1}^{1}\int\limits_{0}^{1} \left(-\frac{h}{2}\right) y^2 (1+\nu)\kappa^c \left[\left(\rho + \frac{r_1}{a}\right)\{\phi_{\rho\rho}\} + \{\phi_\rho\}\right] d\rho \, dy \qquad (5.3.7)$$

which can be reduced to:

$$\{q^{wc}\} = \frac{\pi E h^3 \kappa^c}{6(1-\nu)} \int\limits_{0}^{1} \left[\frac{r_1}{a}\{\phi_{\rho\rho}\} + \rho\{\phi_{\rho\rho}\} + \{\phi_\rho\}\right] d\rho \qquad (5.3.8)$$

Evaluation of the integral yields:

$$\{Q^{wc}\} = \frac{\pi E h^3 \kappa^c}{6(1-\nu)} \begin{Bmatrix} 0 \\ -r_1 \\ 0 \\ r_2 \end{Bmatrix} \qquad (5.3.9)$$

This equation is used to evaluate the element creep load vectors which will then be assembled into the global creep load vector.

It was found while running the model that certain combinations of integration points gave identical results to the values from the analytical solution, while other combinations of integration points did not. Using the same plate characteristics as the simply supported case of section 5.2.2, the assembled analytical creep load vector contains all zero values, except for the moment at $r = 5$ m which is 1.77×10^7 Nm. The model was run using, for example, four integration points in the radial direction and six in the vertical direction, giving the same results as the analytical solution. However, when the number of integration points was changed to, say, three and five in the radial and vertical directions, respectively, the model gave slightly different results for the creep load vector. The effect that the number of integration points chosen has on the solution is investigated further in the section on spatial discretization (5.5.1.3).

5.3.2 Artificial Creep Strain Test

A second simple test of the creep load vector involves the use of "artificial" creep strains. Based on the elastic solution, the elastic strains are calculated. Rather than calculating the creep strains using the Euler or the 4th Order Runge-Kutta method, the creep strains are replaced by "artificial" creep strains set equal to 50% of the elastic strains. Once the creep load vector is added to the mechanical load vector and the system of equations is solved, the deflections should be 50% larger than the deflections of the elastic solution.

Using the same inputs as for the simply supported example of section 5.2.2, the model found the deflection bowl, which included the creep load vector effects, to be 50% greater than the elastic deflection bowl, as can be seen in Figure 5-5.

5.4 Elastic Plate on Elastic Foundation

5.4.1 Analytical Solution

Wyman (1950) obtained a solution for the instantaneous deflection of an infinite elastic plate on an elastic foundation under uniform loading. In the case of uniform circular loading (see Figure 5-6), two equations are required to define the deflection over the entire radial extent of interest. For a point internal to the load, (i.e. $0 \le r \le \alpha$, where α is the radius of the load), the deflection of the plate, w, is calculated by:

$$w = \frac{q_o}{\gamma} + \frac{q_o b}{\gamma} \left[\text{ker}'(b)\,\text{ber}(r/l) - \text{kei}'(b)\,\text{bei}(r/l) \right] \qquad (5.4.1)$$

and for a point external to the load ($r > \alpha$) the deflection is found from:

$$w = \frac{q_o b}{\gamma} \left[\text{ber}'(b)\,\text{ker}(r/l) - \text{bei}'(b)\,\text{kei}(r/l) \right] \qquad (5.4.2)$$

where $b = a/l$, l is the characteristic length of the ice cover, q_o is the uniform applied load, and γ is the unit weight of water. The functions *ber*, *bei*, *ber'*, *bei'*, *ker*, *kei*, *ker'*, and *kei'* are Bessel functions for which expressions can be found in Appendix D.

5.4.2 Elastic Behaviour Test

A second example was designed to test the elastic response of the model to loading on an infinite elastic plate supported by an elastic foundation in order to compare the model results to Wyman's (1950) analytical solution.

The finite element solution for the elastic plate supported by an elastic foundation (Figure 5-6) was compared to the analytical solution using the following parameters: ice thickness $h = 0.10$ m, Young's modulus $E = 9 \times 10^9$ Pa, Poisson's ratio $\nu = 0.333$ and $q_o = 18000$ Pa. The load radius was 5 m, and the model solved the problem up to a radius of 50 m from the centre of the load. From $r = 0$ to 10 m the elements were each 0.5 m long, and from $r = 10$ to 50 m the elements were each 1.0 m long. A plot of the deflected shapes from the model and from Wyman's equations (5.4.1) and (5.4.2) can be seen in Figure 5-7. From this figure, it can be observed that the two solutions are virtually indistinguishable ($< 1\%$ difference).

5.5 Elastic Plate on Elastic Foundation with Creep

In the next chapter, several sets of test data from actual field measurements will be analyzed using the finite element model developed here. In order to maintain consistency between different tests, standards need to be set for spatial and temporal

discretization, after which the creep parameters n and η, along with the material parameters ν and E, can be calibrated.

5.5.1 Spatial Discretization

The number and size of element chosen, as well as the number of integration points used within each element affects the accuracy of the solution found by the finite element model. For both concentrated and distributed loading scenarios a sensitivity analysis was performed to determine an appropriate element discretization. The number of integration points was chosen based on testing of the pure bending example described in section 5.3.1.

Masterson and Strandberg (1979) state that the radial extent of modelling can end at three to four times the characteristic length of the ice from the centre of the load. According to Tinawi and Murat (1979), modelling four times the characteristic length of the ice cover in the radial direction is sufficient. Beyond this radius, the load has a negligible effect on the ice cover. The characteristic length, l, of the ice cover is defined by Gold (1971) as:

$$l = 16h^{0.75} \qquad (5.5.1)$$

where h is the ice thickness, and both h and l are given in metres. The outside radius of the farthest element from the load, r_o, to be used in this model, therefore, will be:

$$r_o = 64h^{0.75} \qquad (5.5.2)$$

For each test, the ice thickness, calculated value of r_o, and a summary of other test conditions can be found in Tables 5-1 and 5-2 for Beltaos' data and for Frankenstein's

data, respectively. Since the largest value of r_o from all of the tests is approximately 50 m, this will be used as the outside radius for all tests.

5.5.1.1 Concentrated Loading

Data set C04 (see Table 5-1) was used to determine the number of elements to be used in all concentrated load cases (defined here as load radius ≤ 0.3 m). It has a relatively long test duration and any errors that are propagated will be most noticeable near the end of the test. Therefore, if acceptable accuracy is achieved with this data set, the shorter duration tests should also have acceptable accuracy.

In order to determine the number of elements necessary for suitable accuracy, all other model parameters were kept constant between runs. The values used for the other model parameters can be found in Table 5-3. First, a very dense grid with 71 elements was created, in order to have a conservative solution with which to compare all other discretization schemes. In this grid, the first element was 5 mm long, with each subsequent element 10% larger than the previous element. The other grids contained 40, 33, 20, and 14 elements. The radius at each node can be seen in Table 5-4 for each grid.

On the deflection-time plot (Figure 5-8), the upper line represents the solutions for 71, 40, 33, and 20 elements, while the lower line is the solution using 14 elements. Based on these results, using 20 elements for the concentrated load cases would be considered acceptable (as it is indistinguishable from the 71 element case), however, 33 elements were chosen to be more conservative. The maximum percent difference between the 71 and 33 element solutions was approximately 0.4% at 235 minutes.

5.5.1.2 Distributed Loading

Data set C16 (see Table 5-1) was used to determine the number of elements to be used for all distributed load cases (defined here as load radius > 0.3 m). Similar grids were used as in the concentrated load cases, with the 71 element case being the most conservative. The other grids created contained 40, 33, 20, 13, 9, and 6 elements. The nodes and radii for data set C16 can be seen in Table 5-5.

Figure 5-9 shows the deflection-time results for the distributed load cases. The upper line encompasses the results for 71, 40, 33, 20, 14, and 9 element grids. The lower line shows the solution found using 6 elements. Using only 9 elements would give results very close to the 71 element solution, however, 20 elements were chosen to be more conservative. The maximum percent difference between the 71 and 20 element cases was approximately 0.007%.

5.5.1.3 Integration Points

The number of integration (or Gauss) points chosen within each element affects the accuracy of the model solution. As a greater number of Gauss points is used, the stress and strain situation within each element can be represented more realistically; however, the time required to run the model also increases as the computations become more involved. The model is configured to allow the number of Gauss points to be input by the user; the same number of Gauss points can be specified in the radial and vertical directions but it is not required that they be equal. The model can calculate a maximum of ten Gauss points in each direction (for a total of 100 integration points within the element).

The pure bending test (section 5.3.1) was used to determine the number of integration points to use in all final calibration runs. Both data sets C04 (concentrated loading) and C16 (distributed loading) were examined. The solutions calculated using ten integration points in each direction were taken as the "exact" solutions, as this was the maximum number of points given by Zienkiewicz (1977); all other solutions were judged based on these. Other solutions were compared to the exact solution using a least squares analysis on the deflection values over time, with:

$$\delta = \sqrt{\sum_{t=0}^{T_e} \left(w_{10,10} - w_{x,y}\right)^2}$$
(5.5.3)

where δ is the least squares value for the solution, T_e is the time at the end of the solution (which approaches zero as the solution approaches the exact solution), and $w_{10,10}$ and $w_{x,y}$ are the deflection values for the exact solution and any other solution at time t, respectively. The results for data set C04 can be found in see Table 5-6.

From Table 5-6, it can be seen that several combinations of Gauss points give the exact solution. In general, using even numbers of Gauss points in the vertical direction gave better results than using odd numbers; for example, using 6 and 8 points in the radial and vertical directions, respectively, gave a smaller value for δ than using 6 and 9 points. Using 5 Gauss points in the radial direction and 10 in the vertical direction is the combination that uses the fewest number of integration points (and therefore takes the least computational time) while still producing a solution identical to that found with 10 Gauss points in each direction. The same process was repeated for data set C16, and it was found that 5 points in the radial direction and 10 points in the vertical direction was sufficient to reproduce the exact solution for this case.

5.5.2 Temporal Discretization

The size of the time step increment (Δt) used in the model also has a significant effect on the accuracy of the solution. Since a numerical method like the Euler or the 4th Order Runge-Kutta method is used to predict strains over time, the larger the time step increment is, the less accurate the predicted strain is likely to be. However, as the size of the time step increment decreases, the time required to run the model increases. A balance must be reached between accuracy of the solution and computational efficiency.

5.5.2.1 Distributed Loading

For the distributed loading case (data set C16: increasing load magnitude) all parameters except Δt were kept constant (see Table 5-7). The time step was varied from 5 s to 10, 30, 60, 120, 240, and 360 s. The solution found using $\Delta t = 5$ s was taken as the "exact" solution for comparison purposes. As less than 0.5% difference was found between the deflection at the end of the tests when using $\Delta t = 10$ s and $\Delta t = 5$ s, decreasing the time step increment any further would not significantly increase the accuracy of the solution.

At the end of the test duration (about 60 minutes), the deflection found using $\Delta t = 360$ s was 3 mm larger than the "exact" solution (about 2.5% difference), and using $\Delta t = 30$ s gave results only 1 mm different from the "exact" solution (0.9% difference). As even the largest difference was insignificant, it is apparent that any of these time steps would give acceptable accuracy.

5.5.2.2 Concentrated Loading

As with the distributed loading case of the previous section, for the concentrated loading case (data set C04: constant load magnitude) all model parameters were kept constant while Δt was varied (see Table 5-7). Since a time step of 30 s was found to be quite accurate in the distributed loading case, it was taken as the "exact" solution for comparison with the other time step sizes in this case. The time step for distributed loading was varied from 30 s to 60, 120, 240, 360, and 480 s.

At the end of this test duration (about 235 minutes), the deflection found using $\Delta t = 480$ s was 0.1 mm larger than the "exact" solution (0.7% difference), using $\Delta t = 240$ s gave a deflection 0.02 mm larger than the exact solution (0.1% difference), and using $\Delta t = 120$ s gave results only 0.01 mm larger than the "exact" solution (0.06% difference). These differences are even less significant than those from the concentrated loading case are; any of these time steps should give an acceptable result when used in the model.

One thing that became apparent with this case (since a brief period of increasing load was followed by constant loading for the remainder of the test) was that the size of the time step did affect the solution near the transition between increasing and constant loading. It can be seen from Figure 5-10 that as the size of the time step increases, the deflection deviates somewhat from the "exact" solution in this transitional region. Consequently, the size of the time step should be kept quite small until the full load is applied (while the plate is responding rapidly), at which point Δt can be increased, decreasing the overall computational time required to run the model.

95

Several different combinations of time steps were examined. It was found that a sudden change in Δt created an abrupt jump in the deflection-time graph, and that the larger the difference in the size of the time steps, the larger this jump became. Instead of having a sudden change from say, Δt_1 to Δt_2 (where Δt_1 and Δt_2 are unequal time step increments), a transitional region was created. In this region, the size of the time step was increased by a percentage of the current time step size, until the new time step size (Δt_2) was reached. After trying several different percentages (e.g. 33%, 16.7%, 10%), it was found that increasing Δt by 10% each time gave a smooth transition from Δt_1 to Δt_2.

5.6 Summary

The results of the elastic analyses (with comparisons to analytical solutions) and simple creep tests indicate that this model performs with acceptable accuracy in these cases. The model will next be extended to more complex loading situations in the following chapter.

Table 5-1: Summary of test conditions for Beltaos' data.

Test #	Date	Air Temperature (°C)*	Ice thickness (m)	Load Radius (m)	Test Duration (minutes)	Outside radius r_o (m)
C01	14-11-1975	6.1	0.076	0.292	22	9.3
C02	17-11-1975	-8.3	0.058	0.292	34	7.6
C03	17-11-1975	-8.3	0.067	0.292	11	8.4
C04	17-11-1975	-8.3	0.069	0.292	235	8.6
C05	18-11-1975	-4.5	0.076	0.292	131	9.3
C06	18-11-1975	-4.5	0.089	0.292	25	10.4
C07	19-11-1975	-6.5	0.089	0.292	300	10.4
C08	19-11-1975	-6.5	0.086	0.292	187	10.2
C09	20-11-1975	-6.4	0.124	0.292	124	13.4
C10	26-11-1975	-11.1	0.178	0.915	25	17.5
C11	27-11-1975	-11.2	0.191	0.915	300	18.5
C12	(27-28)-11-1975	-13.1	0.216	0.915	64	20.3
C13	(2-5)-12-1975	-16.9	0.274	0.915	4264	24.3
C14	(3-4)-12-1975	-17.9	0.305	0.915	1619	26.3
C15	09-12-1975	-3.8	0.348	0.915	338	29.0
C16	11-12-1975	-25.4	0.363	2.195	58	29.9
C19	23-01-1976	-3.1	0.640	1.753	30	45.8
C20	27-01-1976	4.1	0.671	1.753	47	47.4
C21	29-01-1976	0.4	0.648	1.753	70	46.2
C22	03-02-1976	-14.4	0.747	1.753	98	51.4

* taken at Edmonton International Airport (average of hourly readings)

Table 5-2: Summary of test conditions for Frankenstein's data.

Test #	Date	Temperature (°C)			Ice thickness (m)	Load radius (m)	Test Duration (minutes)	Outside radius r_o (m)
		Air	Surface	Ice				
F01	04-01-1956	-7.8	-4.6	-1.2	0.279	1.829	65.8	24.6
F02	13-01-1956	-6	-4	-3	0.361	1.829	102.0	29.8
F03	03-02-1956	-12.2	-6.3	-1	0.330	1.829	39.8	27.9
F04	28-02-1956	-9.6	-0.2	-0.7	0.480	1.829	88.3	36.9
F05	20-03-1956	-1.3	0	-0.2	0.584	1.829	282.6	42.8
F06	22-03-1956	-11.3	0	-0.4	0.597	1.829	159.5	43.5
F07	28-03-1956	-2.4	-2.6	-0.4	0.500	1.829	204.0	38.1
F08	18-01-1957	-4.8	-4	-4.2	0.556	0.220	230.5	41.2
F09	23-01-1957	-20.1	-15.1	-12	0.592	0.220	33.0	43.2
F10	17-02-1959	-10.1	-6.1	-4.8	0.511	0.220	32.6	38.7
F11	10-03-1959	-1.8	-3.2	-3.7	0.544	0.220	31.5	40.5
F12	13-03-1959	-6.3	-4	-5	0.589	0.220	49.5	43.0
F13	19-03-1959	4.4	0	-0.1	0.538	0.220	28.5	40.2

Table 5-3: Parameters used for determination of spatial discretization.

	Concentrated Load Case	Distributed Load Case
Young's modulus, E (Pa)	9×10^9	9×10^9
Poisson's ratio, v	0.333	0.333
Creep exponent, n	3.0	3.0
Creep coefficient, η	2×10^{-25}	2×10^{-25}
# of Gauss points in radial direction	2	2
# of Gauss points in vertical direction	5	4
Size of time step, Δt (s)	240	120
Numerical method	4th Order Runge-Kutta	4th Order Runge-Kutta

Table 5-4: Grid nodes and radii for concentrated loading.

71 element case		40 element case		33 element case		20 element case		14 element case	
Node	Radius (m)	Node	Radius (m)	Node	Radius (m)	Node	Radius (m)	Node	Radius (m)
1	0	1	0	1	0	1	0	1	0
2	0.005	2	0.1	2	0.292	2	0.292	2	0.292
3	0.011	3	0.2	3	0.5	3	0.5	3	2
4	0.017	4	0.292	4	1	4	1	4	4
5	0.023	5	0.4	5	1.5	5	2	5	6
6	0.031	6	0.5	6	2	6	3	6	8
7	0.039	7	0.6	7	2.5	7	4	7	10
8	0.047	8	0.7	8	3	8	5	8	15
9	0.057	9	0.8	9	3.5	9	6	9	20
10	0.068	10	0.9	10	4	10	7	10	25
11	0.08	11	1	11	4.5	11	8	11	30
12	0.093	12	1.5	12	5	12	9	12	35
13	0.107	13	2	13	5.5	13	10	13	40
14	0.123	14	2.5	14	6	14	15	14	45
15	0.14	15	3	15	6.5	15	20	15	50
16	0.159	16	3.5	16	7	16	25		
17	0.18	17	4	17	7.5	17	30		
18	0.203	18	4.5	18	8	18	35		
19	0.228	19	5	19	8.5	19	40		
20	0.256	20	5.5	20	9	20	45		
21	0.292	21	6	21	9.5	21	50		
22	0.332	22	6.5	22	10				
23	0.376	23	7	23	11				
24	0.424	24	7.5	24	12				
25	0.477	25	8	25	13				
26	0.535	26	8.5	26	14				
27	0.599	27	9	27	15				
28	0.67	28	9.5	28	20				
29	0.747	29	10	29	25				
30	0.833	30	11	30	30				
31	0.927	31	12	31	35				
32	1.03	32	13	32	40				
33	1.144	33	14	33	45				
34	1.269	34	15	34	50				
35	1.406	35	20						
36	1.557	36	25						
37	1.724	37	30						
38	1.907	38	35						
39	2.108	39	40						
40	2.329	40	45						
41	2.573	41	50						
42	2.841								
43	3.136								
44	3.46								
45	3.816								
46	4.209								
47	4.64								
48	5.115								
49	5.637								
50	6.211								
51	6.843								
52	7.538								
53	8.302								
54	9.143								
55	10.068								
56	11.086								
57	12.205								
58	13.436								
59	14.79								
60	16.28								
61	17.918								
62	19.721								
63	21.703								
64	23.884								
65	26.283								
66	28.922								
67	31.825								
68	35.018								
69	38.531								
70	42.395								
71	46.645								
72	51.32								

Table 5-5: Grid nodes and radii for distributed loading.

71 element case		40 element case		33 element case		20 element case		13 element case		9 element case		6 element case	
Node	Radius (m)	Node	Radius (m)	Node	Radius (m)	Node	Radius (m)	Node	Radius (m)	Node	Radius (m)	Node	Radius (m)
1	0	1	0	1	0	1	0	1	0	1	0	1	0
2	0.005	2	0.1	2	0.5	2	0.5	2	2.195	2	2.195	2	2.195
3	0.011	3	0.2	3	1	3	1	3	4	3	5	3	10
4	0.017	4	0.3	4	1.5	4	2	4	6	4	10	4	20
5	0.023	5	0.4	5	2	5	2.195	5	8	5	15	5	30
6	0.031	6	0.5	6	2.195	6	3	6	10	6	20	6	40
7	0.039	7	0.6	7	2.5	7	4	7	15	7	30	7	50
8	0.047	8	0.7	8	3	8	5	8	20	8	40		
9	0.057	9	0.8	9	3.5	9	6	9	25	9	50		
10	0.068	10	0.9	10	4	10	7	10	30				
11	0.08	11	1	11	4.5	11	8	11	35				
12	0.093	12	1.5	12	5	12	9	12	40				
13	0.107	13	2.195	13	5.5	13	10	13	45				
14	0.123	14	2.5	14	6	14	15	14	50				
15	0.14	15	3	15	6.5	15	20						
16	0.159	16	3.5	16	7	16	25						
17	0.18	17	4	17	7.5	17	30						
18	0.203	18	4.5	18	8	18	35						
19	0.228	19	5	19	8.5	19	40						
20	0.256	20	5.5	20	9	20	45						
21	0.292	21	6	21	9.5	21	50						
22	0.332	22	6.5	22	10								
23	0.376	23	7	23	11								
24	0.424	24	7.5	24	12								
25	0.477	25	8	25	13								
26	0.535	26	8.5	26	14								
27	0.599	27	9	27	15								
28	0.67	28	9.5	28	20								
29	0.747	29	10	29	25								
30	0.833	30	11	30	30								
31	0.927	31	12	31	35								
32	1.03	32	13	32	40								
33	1.144	33	14	33	45								
34	1.269	34	15	34	50								
35	1.406	35	20										
36	1.557	36	25										
37	1.724	37	30										
38	1.907	38	35										
39	2.195	39	40										
40	2.329	40	45										
41	2.573	41	50										
42	2.841												
43	3.136												
44	3.46												
45	3.816												
46	4.209												
47	4.64												
48	5.115												
49	5.637												
50	6.211												
51	6.843												
52	7.538												
53	8.302												
54	9.143												
55	10.068												
56	11.086												
57	12.205												
58	13.436												
59	14.79												
60	16.28												
61	17.918												
62	19.721												
63	21.703												
64	23.884												
65	26.283												
66	28.922												
67	31.825												
68	35.018												
69	38.531												
70	42.395												
71	46.645												
72	51.32												

Table 5-6: Summary of least squares analysis for data set C04.

Number of Gauss Points Radially (x)	Number of Gauss Points Vertically (y)	Least Squares Value (δ)
2	2	0.00783460
2	3	0.00444926
2	4	0.00133398
2	5	0.00110111
2	6	0.00039194
2	7	0.00045920
2	8	0.00012920
2	9	0.00025405
2	10	0.00002963
3	3	0.00448980
3	4	0.00130952
3	5	0.00113260
3	6	0.00036530
3	7	0.00048897
3	8	0.00010161
3	9	0.00028330
3	10	0.00000116
4	4	0.00130851
4	5	0.00113384
4	6	0.00036423
4	7	0.00049014
4	8	0.00010050
4	9	0.00028445
4	10	0.00000005
5	5	0.00113387
5	6	0.00036420
5	7	0.00049018
5	8	0.00010046
5	9	0.00028449
5	10	0
6	6	0.00036420
6	7	0.00049018
6	8	0.00010046
6	9	0.00028449
6	10	0
7	7	0.00049018
7	8	0.00010046
7	9	0.00028449
7	10	0
8	8	0.00010046
8	9	0.00028449
8	10	0
9	9	0.00028449
9	10	0

Table 5-7: Parameters used for determination of temporal discretization.

	Concentrated Load Case	Distributed Load Case
Young's modulus, E (Pa)	9×10^9	9×10^9
Poisson's ratio, v	0.333	0.333
Creep exponent, n	3.0	3.0
Creep coefficient, η	2×10^{-25}	2×10^{-25}
# of Gauss points in radial direction	5	5
# of Gauss points in vertical direction	10	10
Number of elements	33	20
Numerical method	4th Order Runge-Kutta	4th Order Runge-Kutta
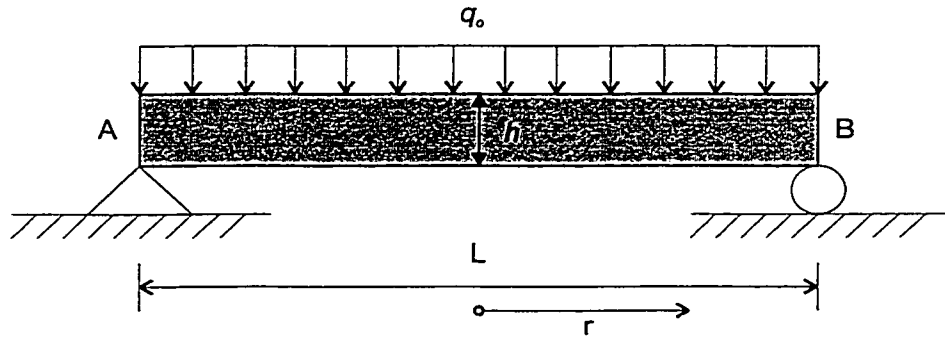
Figure 5-1: Cross section of a vertically loaded simply supported elastic plate.
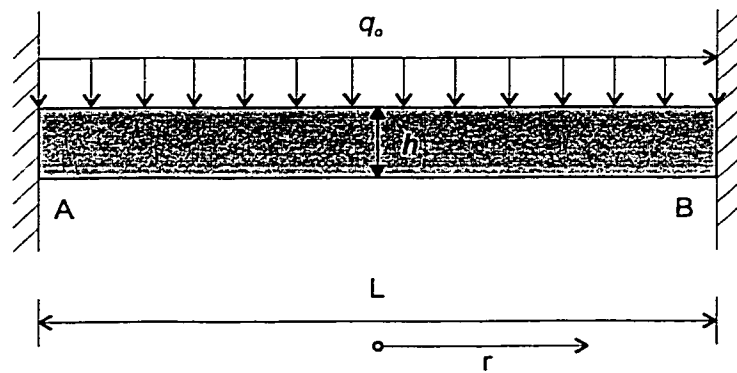
Figure 5-2: Cross section of a vertically loaded clamped edge elastic plate.
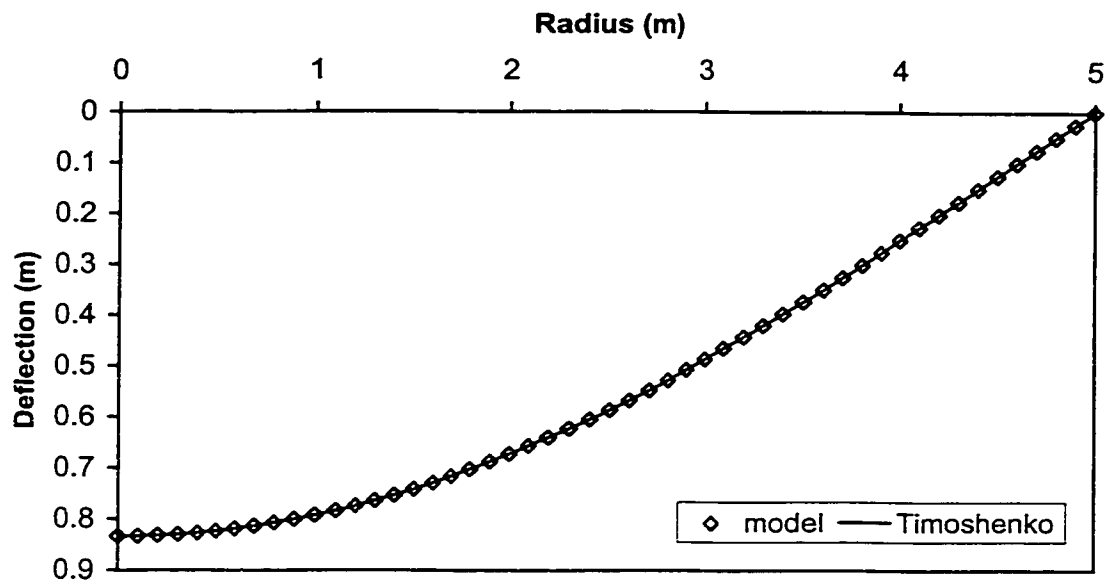
Figure 5-3: Deflected shape from model and Timoshenko for a simply supported elastic plate.
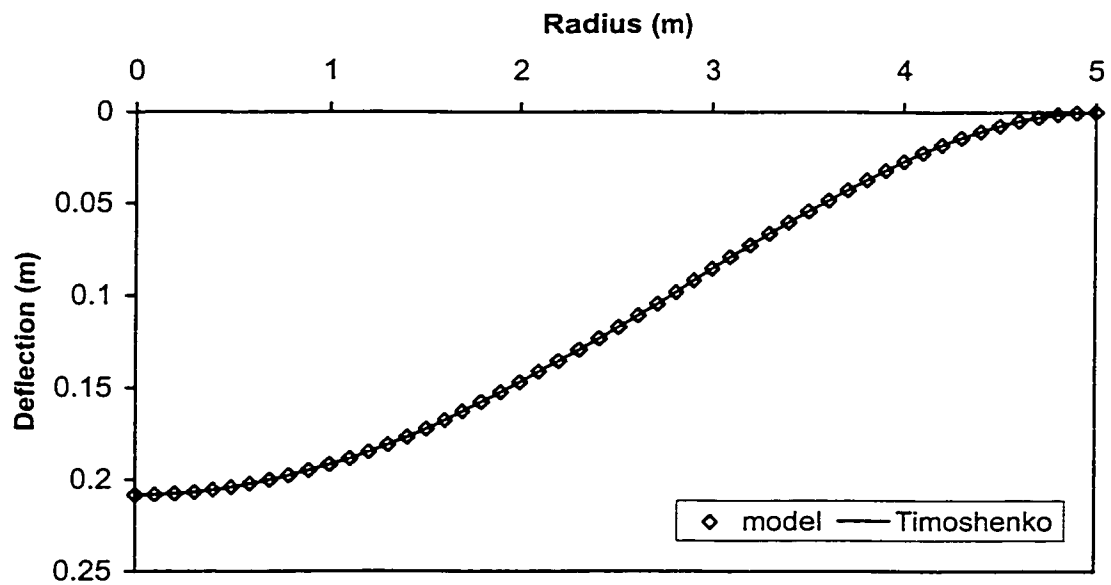
Figure 5-4: Deflected shape from model and Timoshenko for a clamped edge elastic plate.
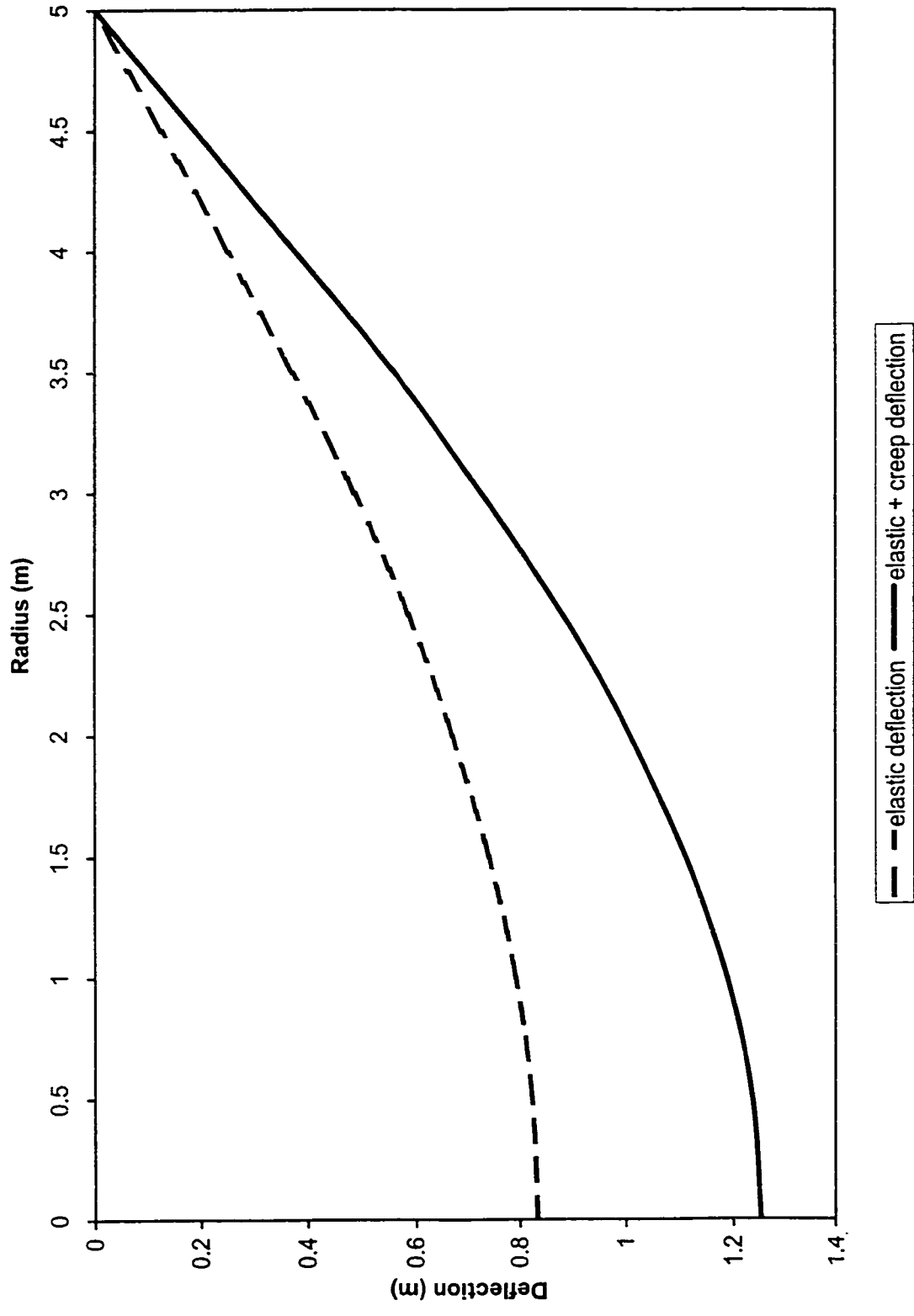
Figure 5-5: Deflected shape for artificial creep strain test.
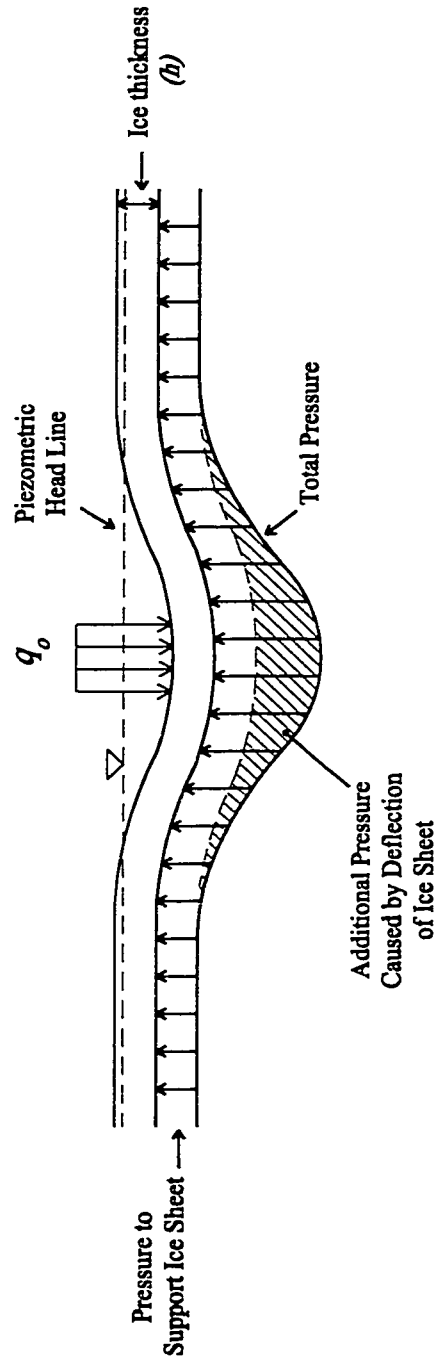
Figure 5-6: Pressure balance in an ice sheet between load, ice deflection and supporting pressure (adapted from Ashton, 1986).
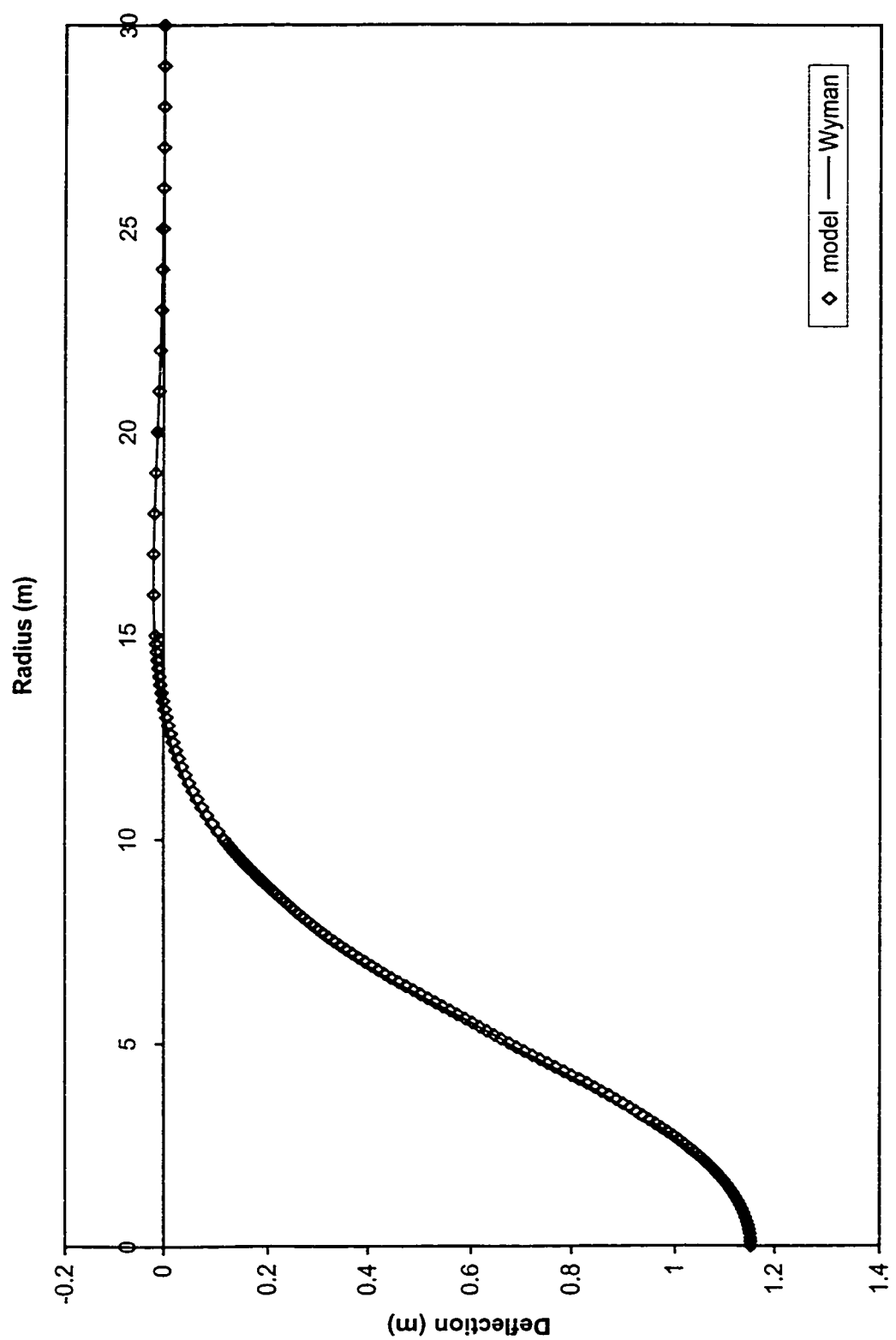
Figure 5-7: Deflected shape from model and Wyman for an elastic plate on an elastic foundation.
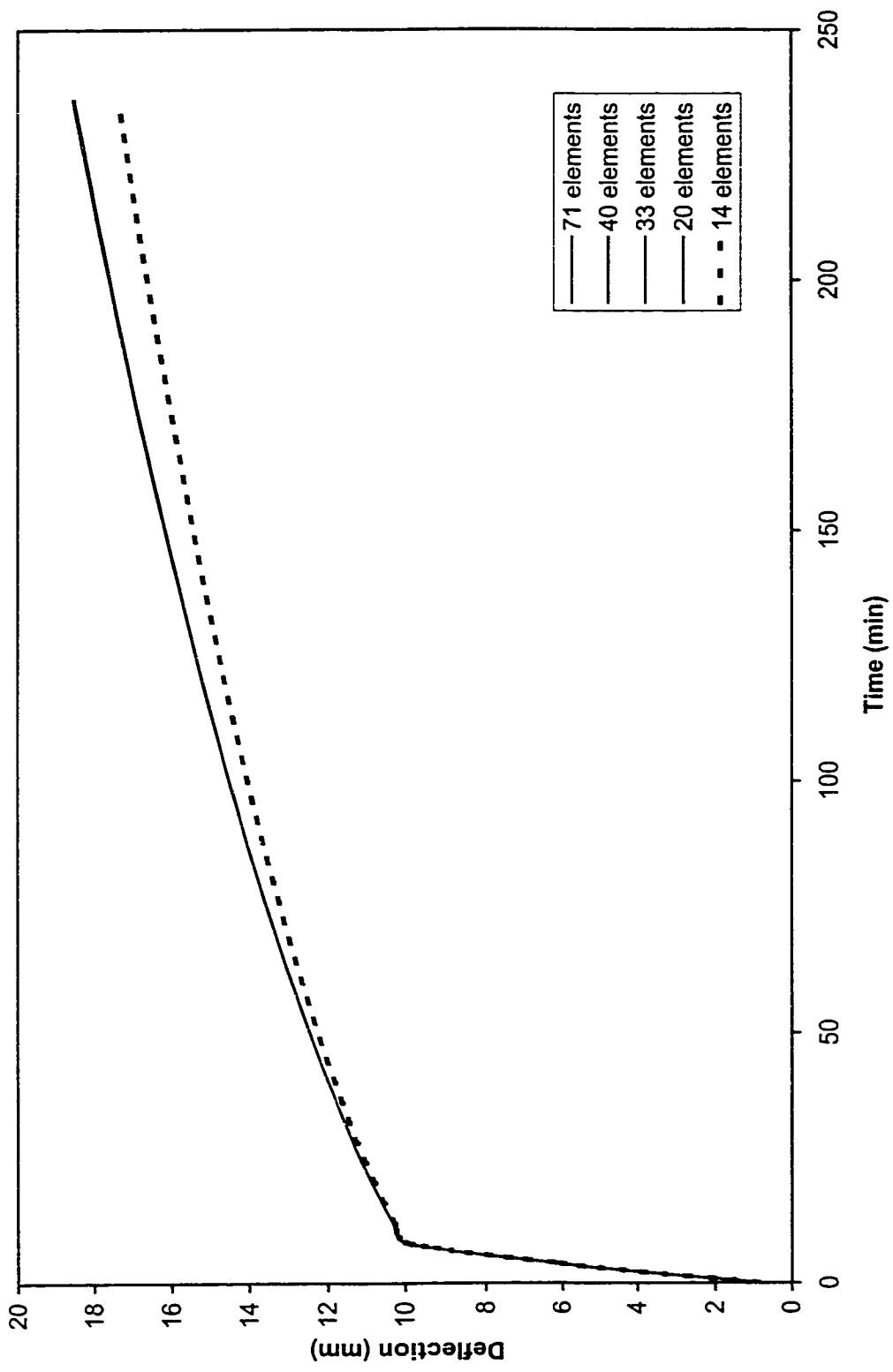
Figure 5-8: Determination of element discretization for concentrated loading.
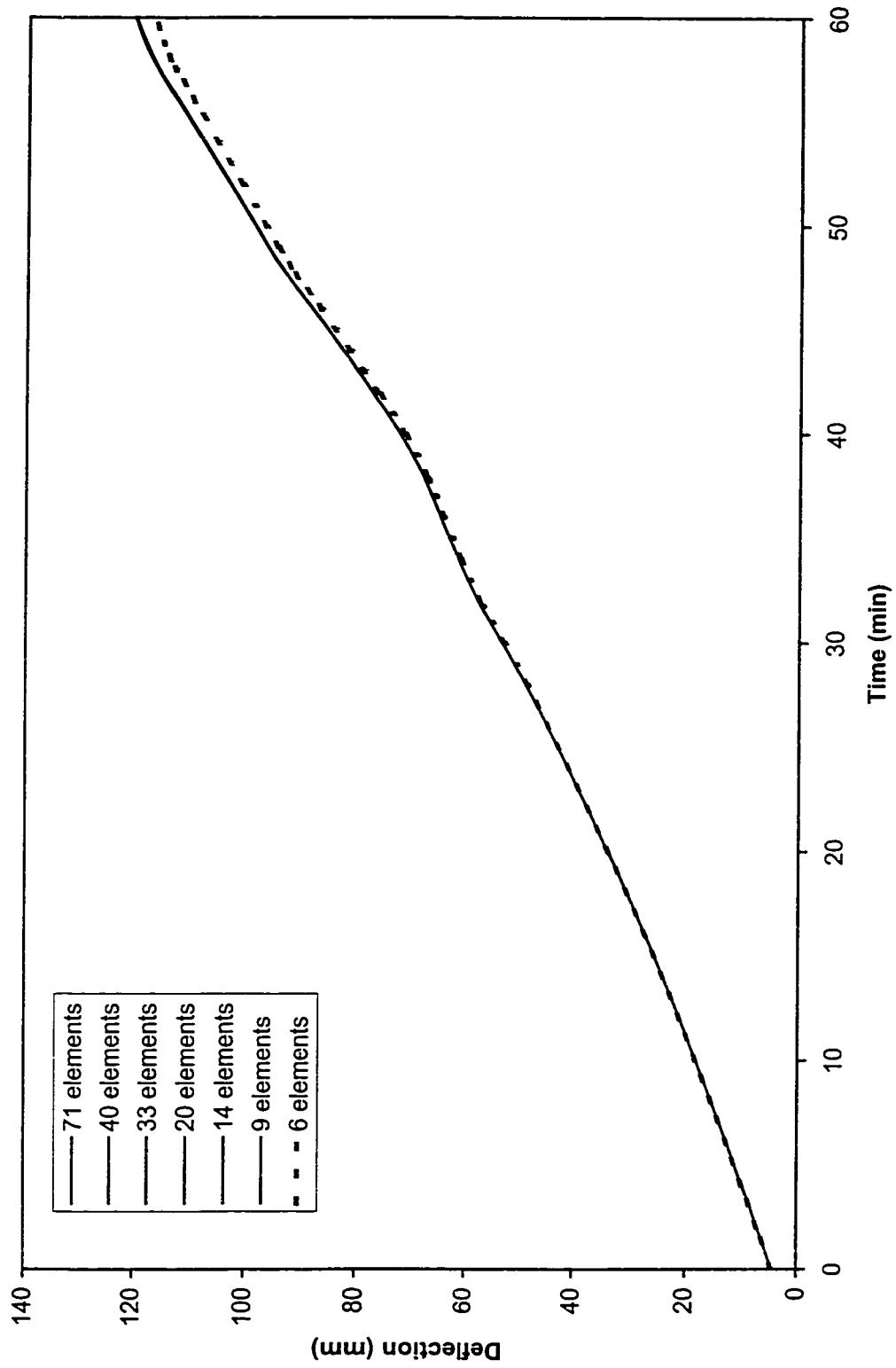
Figure 5-9: Determination of element discretization for distributed loading.

Legend:
- 71 elements
- 40 elements
- 33 elements
- 20 elements
- 14 elements
- 9 elements
- 6 elements
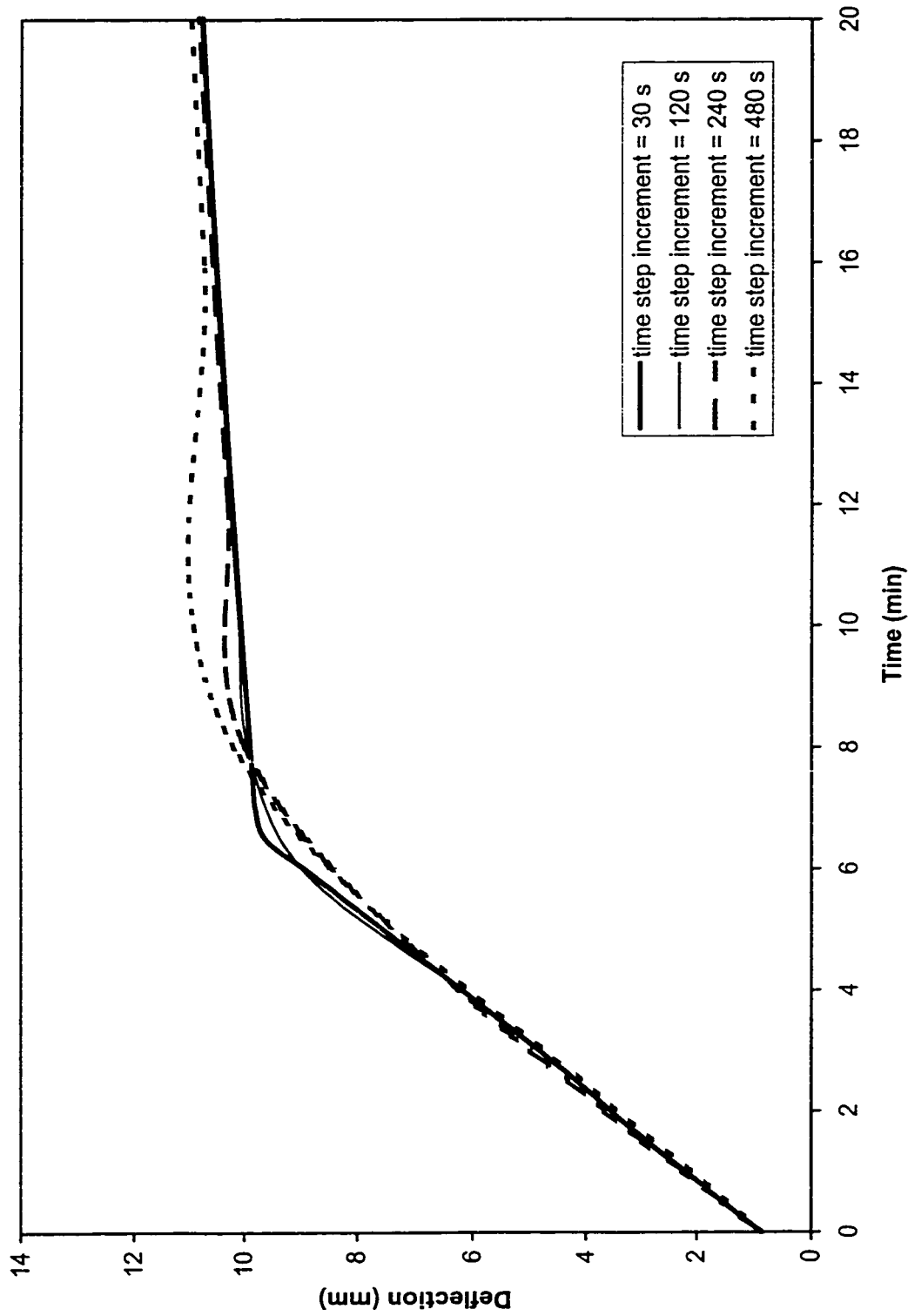
Figure 5-10: Deviation of finite element solution with increasing time step increment.

6.0 MODEL APPLICATION

6.1 Introduction

The response of the model to elastic loading was verified and some simplified creep scenarios were examined in chapter 5. In this chapter, the model is tested on more complex situations involving the creep of ice, for which analytical solutions do not exist. The secondary creep behaviour predicted by the model (using a power law) is compared to large scale experimental data. The 4th Order Runge-Kutta method is used to predict the creep strain increments for all the cases described in this chapter.

This chapter contains a section describing the sources of the large scale experimental field data used to verify the model developed here, and a brief justification for the exclusion of certain sets of data. A discussion on the calibration parameters is presented. The results of the model calibration runs, which are grouped according to the type of loading applied, are compared with the field data. An attempt to correlate the calibrated parameters to ice temperature is presented. Finally, the results obtained in this study are summarized.

6.1.1 Sources of Experimental Data

The model developed here will be verified using data obtained from two sources. A total of 22 sets of long term deflection data were acquired from S. Beltaos (National Water Research Institute). This data is from large scale load tests performed by the Alberta Research Council on the ice cover at Joseph Lake (near Edmonton) during November 1975 to February 1976, and has not been previously analyzed with any creep model. The ice thickness in these tests ranged from approximately 6 cm to 75 cm (see

Table 5-1). These tests were performed at stresses ranging from approximately 15 to 79 kPa, with air temperatures ranging from about +6 to -26 °C. Various tank diameters were used to distribute the load, with water being pumped in from the lake to load the tanks (Beltaos, 1978). Of the 22 sets of load-deflection-time data obtained, 9 were from concentrated load tests and 13 were from distributed load tests.

The second source of load test data was Frankenstein's (1963) paper, which includes load and deflection data for 13 large scale tests. This data was obtained from load tests performed on the ice covers on a lake and a bay in Michigan, as well as a reservoir in North Dakota from January to March of 1956, 1957, and 1959. The ice thickness for these tests ranged from about 28 cm to 60 cm (see Table 5-2). The stresses in these tests ranged from about 15 to 1750 kPa, and the ice temperatures ranged from -0.1 to -12 °C. For the seven distributed load tests, a 3.66 m (12 ft) diameter tank was placed on the ice surface and water was pumped in from the lake; for the six concentrated load tests, this tank was balanced on a 0.44 m (17.3 in) diameter cylinder.

For both sources of data, the deflection measurements were taken with surveying levels and rods.

6.1.2 Exclusion of Test Data

In total, 35 sets of field data were available for comparison with the model. Of these, two sets of Beltaos' data were discarded. Data set C17 was not used because the loading curve was in question. According to the loading curve most of the load was removed early in the test, but this is believed to be due to a leak of some sort (personal communication: Beltaos, January 2001). The magnitude of the load was calculated based

on the water level in the tank, and while the leaked water may have remained on the ice surface (as a much more distributed load), it would no longer be accounted for by the loading curve. Data set C18 was also discarded because the load configuration was rectangular rather than circular; this model only deals with circular loads.

6.1.3 Spatial and Temporal Discretization

From the results of the model verification discussed in the previous chapter it was decided that 33 and 20 elements would be used for the spatial discretization of the concentrated and distributed loading cases, respectively, for the model applications in this chapter. Five integration points in the radial direction and ten integration points in the vertical direction were chosen, producing a total of 50 integration points within each element.

The choice of time step increment(s), Δt, to be used depended on the loading configuration and the total duration of each individual test. For any tests less than 5,000 seconds (about 83 minutes), a time step increment of 30 seconds was used. If the test duration was longer than 5,000 seconds, a 30 second time step increment was used until after full loading was applied, followed by a transition to a time step increment of 120 seconds. In most cases, if the test lasted longer than about 10,000 seconds (167 minutes), another transition was implemented to a time step increment of 240 seconds. Test C13 is a notable exception to this, with a transition to $\Delta t = 240$ seconds occurring earlier (at 167 minutes) since the duration of this test is relatively long (over 4,000 minutes). Test C03 is also an exception and $\Delta t = 15$ seconds is used for the 640 second duration of the test. A summary of the time step increments and their

durations for each test can be found in Table 6-1(a) for Beltaos' data, and Table 6-1(b) for Frankenstein's data.

6.1.4 Calibration Parameters

Four parameters can be calibrated using this model: Young's modulus, E; Poisson's ratio, ν; the creep exponent, n; and the creep coefficient, η. In the early stages of model verification, it was discovered that the model results were not very sensitive to changes in Poisson's ratio, ν, that is, the other three parameters were found to have a much greater effect on the creep behaviour of ice. As a result, Poisson's ratio was set at the typical value of $1/3$ for ice (Beltaos, 1978) for all cases, and the three remaining parameters were calibrated for each set of data.

While any one parameter was being calibrated, all other parameters were kept constant. The parameters were generally calibrated in the following order: n, followed by E, and finally η. The creep exponent, n, was modified first to approximate the correct shape of the deflection-time curve. Next, E was adjusted to obtain the proper order of magnitude for the deflection. Finally, η was varied to fine-tune the model results. The goodness of fit of the model to the experimental data was judged by visual inspection.

Various combinations of the three calibration parameters could be found to give similar deflection-time curves, and so a range of values for each parameter is reported, rather than trying to choose the "best" value for each parameter.

6.2 Calibration of Beltaos' Data

The results obtained from the calibration of Beltaos' test data are discussed here. The results have been grouped according to the type of loading applied. Beltaos' tests have been separated into groups of constant loading, increasing loading, and other loading (see Table 6-2). For each test, the figures described in the following sections contain one graph for each of the calibrated parameters. Graph (a) shows the upper and lower bounds (E_U and E_L) found for Young's modulus, graph (b) shows the upper and lower bounds (η_U and η_L) for the creep coefficient (denoted as *eta* in the figure legend), and graph (c) shows the upper and lower bounds (n_U and n_L) for the creep exponent. The majority of these graphs show an average value for each parameter. These figures also illustrate the magnitude of loading over time.

6.2.1 Constant Load Tests

The tests in which the load increased until a certain magnitude was reached, and the load was then kept at that magnitude for the remainder of the test were classified as constant load tests here. Some of the test durations were not very long; the time required to apply the load in some cases was approximately as long as the period of constant loading, but these were still grouped with the constant load tests.

The results for the calibration of the fifteen constant load tests can be seen in Figures 6-1 through 6-15. The values obtained for Young's modulus, E, ranged from 0.6×10^9 to 2.4×10^9 Pa. The creep coefficient, η, ranged from 1.5×10^{-25} to 3.0×10^{-25} s^{-1}Pa^{-n} and the creep exponent, n, ranged from 3.02 to 3.43. A summary of the results can be found in Table 6-2.

116

The model predicts the deflection of the ice cover very well during secondary (steady state) creep for the tests shown in Figures 6-1 through 6-8 and 6-10. As the model approaches a steady state, the solution begins to deviate from the deflection data at the onset of tertiary (accelerated) creep, as expected. In Figures 6-9 and 6-11, the model is seen to overpredict the deflection as the load is being applied and during the early stages of secondary creep, but matches the data more closely as secondary creep progresses. For the tests shown in Figures 6-12, 6-14 and 6-15, the predicted deflection is higher than that observed during load application, but matches the data quite well during secondary creep. The deflection data in Figure 6-13 does not seem to have a significant period of steady state creep. The model deflections are high as the load is being applied and fit the data acceptably from a time of approximately 15 to 25 minutes; this is followed by accelerated creep which this model cannot predict.

For the tests in which the model overpredicts the deflection as the load is being applied, the elastic modulus needed to match the secondary creep data is too low to match this initial data. According to Ashton (1986), Young's modulus for ice can be dependent on several factors including temperature, density, type and purity of ice, stress (time or frequency, and history), and grain size. Some of these parameters may change as the ice deforms, causing Young's modulus to change as well. This could explain the apparent need for different values of E at various stages of the test.

6.2.2 Increasing Load Tests

Three tests were performed with linearly increasing loading. The results of these calibration runs can be seen in Figures 6-16 through 6-18, and are summarized in

Table 6-2. For these cases E ranged from 3.0×10^9 to 5.0×10^9 Pa, η ranged from 1.5×10^{-25} to 2.5×10^{-25} $s^{-1}Pa^{-n}$, and n ranged from 3.15 to 3.28.

The model results match the deflection data quite well for these three tests. The predicted deflections are slightly higher than the actual deflections in the early stages of tests C10 and C16 (Figures 6-17 and 6-18), which could be due to the fact that Young's modulus for the ice could be changing as the test progresses. Again, as accelerated creep begins, the model cannot predict the behaviour of ice and the model deflections remain less than the observed deflections.

6.2.3 Other Loading Scenarios

Two of the loading scenarios did not fit the constant or increasing load descriptions. Test C13 was conducted using a step function type of loading, and test C12 consisted of a constant load followed by a linearly increasing load. For test C13, E varied from 1.3×10^9 to 1.7×10^9 Pa, η ranged from 1.9×10^{-25} to 2.1×10^{-25} $s^{-1}Pa^{-n}$, and n ranged from 3.07 to 3.09. For test C12, E ranged from 2.5×10^9 to 4.0×10^9 Pa, η varied from 1.8×10^{-25} to 2.2×10^{-25} $s^{-1}Pa^{-n}$, and n ranged from 3.34 to 3.36. These calibration results can be found in Figures 6-19 and 6-20, with the findings also summarized in Table 6-2.

The model predicted the deflection for test C13 (Figure 6-19) reasonably well for the first half of the test, but at later times, the predicted deflection was higher than the measured values. This could be due in part to the long duration of test C13 and error propagation (resulting from the use of the 4th Order Runge-Kutta method) may have occurred near the end of the test. This error was thought to be due partly to the fact that a large time step increment ($\Delta t = 240$ s) was implemented quite early in this test in order to

decrease computational time. However, when this test was run again with $\Delta t = 30$ s for the entire duration, no noticeable difference ($< 0.2\%$) in the deflection-time graph resulted.

With test C12 (Figure 6-20) the model predicts the deflection of the ice very well up to the time when the load changes from a constant magnitude to a linearly increasing magnitude (occurring at about 35 minutes). At this point, it appears from the deflection data that accelerated creep is beginning, and this model cannot predict the deflection beyond this point.

6.3 Calibration of Frankenstein's Data

The results obtained from the calibration of Frankenstein's test data are discussed next. These results have been separated into groups of constant loading and increasing loading (see Table 6-3). For each test, the figures discussed in the following sections contain one graph for the calibration of each parameter, in the same manner as described earlier in section 6.2.

6.3.1 Constant Load Tests

The results of the model calibration for the four constant load tests can be found in Figures 6-21 through 6-24. For these cases Young's modulus, E, ranged from 0.1×10^9 to 1.4×10^9 Pa. The creep coefficient, η, ranged from 1.5×10^{-25} to 2.5×10^{-25} $s^{-1}Pa^{-n}$ and the creep exponent, n, ranged from 3.29 to 3.50. The results from each test are summarized in Table 6-3.

119

For tests F05 and F07 (Figures 6-21 and 6-23) the model predicted the observed deflections quite well, with model values only slightly larger than the measured values during the stage of load application. Test F06 does not have a lengthy secondary creep stage, but the model seems to fit the data very closely until the onset of tertiary creep. The model does not fit the data from test F08 well (Figure 6-24); the predicted deflections are significantly larger than the measured deflections. In tests F05, F06 and F07 the loads are distributed (load radius = 1.829 m) and the three tests have similar rates of loading (the load is fully applied in the order of 45 to 60 minutes). Test F08 had a concentrated load (load radius = 0.22 m) which was fully applied after about 20 minutes. The ice was deforming rapidly as the load was quickly applied; the elastic modulus may have been changing rapidly in this region as well, and may have been quite different from the elastic modulus reached in the secondary creep stage.

6.3.2 Increasing Load Tests

Nine tests were performed with increasing loading. The results of the calibration for these tests can be seen in Figures 6-25 through 6-33, with a summary in Table 6-3. For this group E ranged from 0.4×10^9 to 3.5×10^9 Pa, η ranged from 1.5×10^{-25} to 2.5×10^{-25} $s^{-1}Pa^{-n}$, and n ranged from 3.20 to 3.40. These findings are also summarized in Table 6-3.

Of the increasing load tests, four had a distributed load configuration and five had a concentrated load configuration. Tests F01 through F04 (Figures 6-25 through 6-28) were the distributed load tests; the model predicted the deflection quite well, except near the beginning of each test (and at the end during tertiary creep). However, the measured

data in these tests is somewhat questionable as the deflections remained at zero for several minutes even though there was an increasing magnitude of load applied.

For the remaining five concentrated load tests (Figures 6-29 through 6-33), the model deflections matched the measured deflections quite well. Again, during the early stages of load application, some of the predicted deflections are slightly higher than the observed deflections. As discussed earlier, this could be due to the fact that the actual value of Young's modulus was changing throughout the test.

6.4 Model Parameters vs. Temperature

The calibrated model parameters were plotted against temperature to determine if any type of correlation was present. For each test, the upper, lower and average values of Young's modulus (E), the creep coefficient (η), and the creep exponent (n) (see Table 6-4) were plotted against the temperature, and can be seen in Figures 6-34, 6-35 and 6-36, respectively. Frankenstein's data was plotted against the measured ice temperature. Since the ice temperature was not measured in Beltaos' tests, it was taken as one half of the air temperature. The temperature at the bottom of the ice sheet will be very close to the water temperature (which is approximately 0 °C directly beneath the ice), and the temperature at the top of the ice sheet will be near to the air temperature. As a result, the average of the water and air temperatures can give an approximate average temperature for the ice sheet.

For Young's modulus, it can be seen from Figure 6-34 that there is a great deal of scatter in the results, reinforcing the belief that E is a function of more than just temperature. The creep coefficient (η) values (see Figure 6-35) lie in a band between

1.5×10^{-25} and 2.5×10^{-25} $s^{-1}Pa^{-n}$, but this does not necessarily imply any temperature dependence. The creep exponent (n) data is also quite scattered (Figure 6-36), suggesting that no real correlation exists between n and temperature. All of the calibration parameters here appear to be functions of more than temperature alone.

6.5 Summary

Of the three calibrated parameters (E, η, and n), the model seemed most sensitive to changes in Young's modulus, and then to changes in the creep exponent. It seemed to be the least sensitive to changes in the creep coefficient. The minimum, average, and maximum values for E, η, and n can be seen in Table 6-4 for constant, increasing, and all types of loading combined.

Table 6-1(a): Summary of time step increments and durations for Beltaos' data.

Test #	Δt_1 (seconds)	Δt_2 (seconds)	Δt_3 (seconds)	Duration of Δt_1 up to (seconds)	Duration of Δt_2 up to (seconds)	Duration of Δt_3 up to (seconds)
C01	30	-	-	1340	-	-
C02	30	-	-	2040	-	-
C03	15	-	-	640	-	-
C04	30	120	-	500	10880	-
C05	30	120	-	800	7860	-
C06	30	-	-	1500	-	-
C07	30	120	240	700	10000	18000
C08	30	120	-	1000	11220	-
C09	30	120	-	1500	7000	-
C10	30	-	-	1450	-	-
C11	30	120	240	1100	10000	18000
C12	30	-	-	3894	-	-
C13	30	120	240	1000	5000	255825
C14	30	120	240	1500	10000	98157
C15	30	120	240	2700	10000	20282
C16	30	-	-	3473	-	-
C19	30	-	-	1810	-	-
C20	30	-	-	2830	-	-
C21	30	-	-	4202	-	-
C22	30	-	-	5890	-	-

Table 6-1(b): Summary of time step increments and durations for Frankenstein's data.

Test #	Δt_1 (seconds)	Δt_2 (seconds)	Δt_3 (seconds)	Duration of Δt_1 up to (seconds)	Duration of Δt_2 up to (seconds)	Duration of Δt_3 up to (seconds)
F01	30	-	-	3948	-	-
F02	30	-	-	6120	-	-
F03	30	-	-	2388	-	-
F04	30	-	-	5298	-	-
F05	30	120	240	2700	10000	16956
F06	30	120	-	3700	9570	-
F07	30	120	240	3100	10000	12240
F08	30	120	240	1300	10000	13830
F09	30	-	-	1980	-	-
F10	30	-	-	1956	-	-
F11	30	-	-	1890	-	-
F12	30	-	-	2970	-	-
F13	30	-	-	1710	-	-

Table 6-2: Summary of calibration results for Beltaos' data.

| Test # | Creep Exponent | | Creep Coefficient | | Young's Modulus | | Type of Loading |
	n_L	n_U	η_L $(s^{-1}Pa^{-n})$ $(x10^{-25})$	η_U $(s^{-1}Pa^{-n})$ $(x10^{-25})$	E_L (Pa) $(x10^9)$	E_U (Pa) $(x10^9)$	
C01	3.21	3.23	1.7	2.4	1.55	1.75	1
C02	3.08	3.11	1.8	3.0	1.50	1.65	1
C03	3.27	3.28	1.7	2.1	3.00	3.50	2
C04	3.08	3.12	1.5	2.2	1.30	1.50	1
C05	3.11	3.14	1.8	2.2	0.90	1.05	1
C06	3.32	3.34	1.8	2.2	1.40	1.65	1
C07	3.18	3.20	1.8	2.2	0.90	1.20	1
C08	3.02	3.04	1.8	2.5	1.90	2.40	1
C09	3.12	3.14	1.7	2.3	1.30	1.50	1
C10	3.24	3.26	1.5	2.5	3.50	4.50	2
C11	3.15	3.17	1.8	2.2	1.30	2.00	1
C12	3.34	3.36	1.8	2.2	2.50	4.00	4
C13	3.07	3.09	1.9	2.1	1.30	1.70	3
C14	3.11	3.13	1.9	2.1	0.78	0.84	1
C15	3.11	3.13	1.8	2.2	0.90	1.20	1
C16	3.14	3.16	1.8	2.5	3.00	5.00	2
C19	3.37	3.39	1.9	2.3	1.00	1.40	1
C20	3.37	3.43	1.5	2.5	0.80	1.10	1
C21	3.24	3.26	1.9	2.1	1.80	2.10	1
C22	3.37	3.39	1.7	2.1	0.55	0.65	1

Table 6-3: Summary of calibration results for Frankenstein's data.

| Test # | Creep Exponent | | Creep Coefficient | | Young's Modulus | | Type of Loading |
	n_L	n_U	η_L $(s^{-1}Pa^{-n})$ $(x10^{-25})$	η_U $(s^{-1}Pa^{-n})$ $(x10^{-25})$	E_L (Pa) $(x10^9)$	E_U (Pa) $(x10^9)$	
F01	3.24	3.27	1.8	2.2	2.50	3.50	2
F02	3.20	3.25	1.5	2.5	1.30	2.00	2
F03	3.25	3.28	1.8	2.5	2.50	3.50	2
F04	3.23	3.27	1.5	2.5	1.50	2.50	2
F05	3.29	3.31	1.8	2.2	1.00	1.40	1
F06	3.35	3.37	1.5	2.5	0.50	1.00	1
F07	3.33	3.35	1.8	2.2	0.80	1.00	1
F08	3.47	3.50	1.8	2.5	0.10	0.20	1
F09	3.30	3.40	1.5	2.5	0.40	0.60	2
F10	3.35	3.40	1.5	2.5	1.00	1.50	2
F11	3.31	3.33	1.5	2.5	1.50	2.00	2
F12	3.25	3.27	1.5	2.5	0.90	1.10	2
F13	3.31	3.35	1.5	2.3	1.50	2.50	2

Type of Loading:
1 = constant loading
2 = increasing loading
3 = stepped loading
4 = constant loading, followed by increasing loading

Table 6-4: Minimum, average and maximum values for calibrated parameters.

		Constant Loading Tests		Increasing Loading Tests		All Tests	
		Beltaos' data	Frankenstein's data	Beltaos' data	Frankenstein's data	Beltaos' data	Frankenstein's data
E $\times 10^9$ (Pa)	minimum	0.6	0.1	3.0	0.4	0.6	0.1
	average	1.3	0.8	3.8	1.8	1.8	1.5
	maximum	2.4	1.4	5.0	3.5	5.0	3.5
η $\times 10^{-25}$ ($s^{-1}Pa^{-n}$)	minimum	1.5	1.5	1.5	1.5	1.5	1.5
	average	2.0	2.0	2.0	2.0	2.0	2.0
	maximum	3.0	2.5	2.5	2.5	3.0	2.5
n	minimum	3.02	3.29	3.15	3.20	3.02	3.20
	average	3.20	3.37	3.23	3.29	3.21	3.32
	maximum	3.43	3.50	3.28	3.40	3.43	3.50
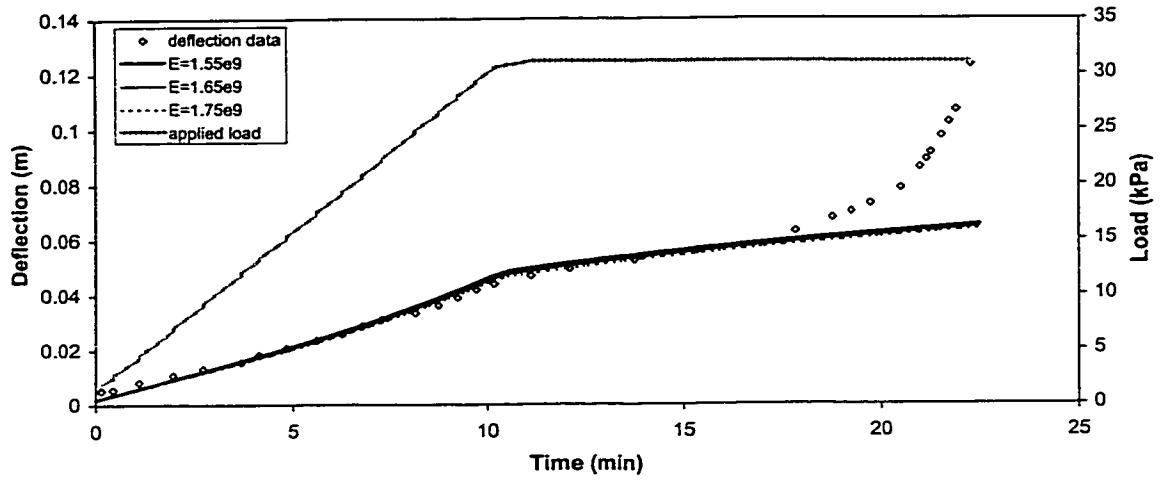
Figure 6-1(a): Range for Young's modulus, E (Test C01: n = 3.22, η = 2.0e-25).
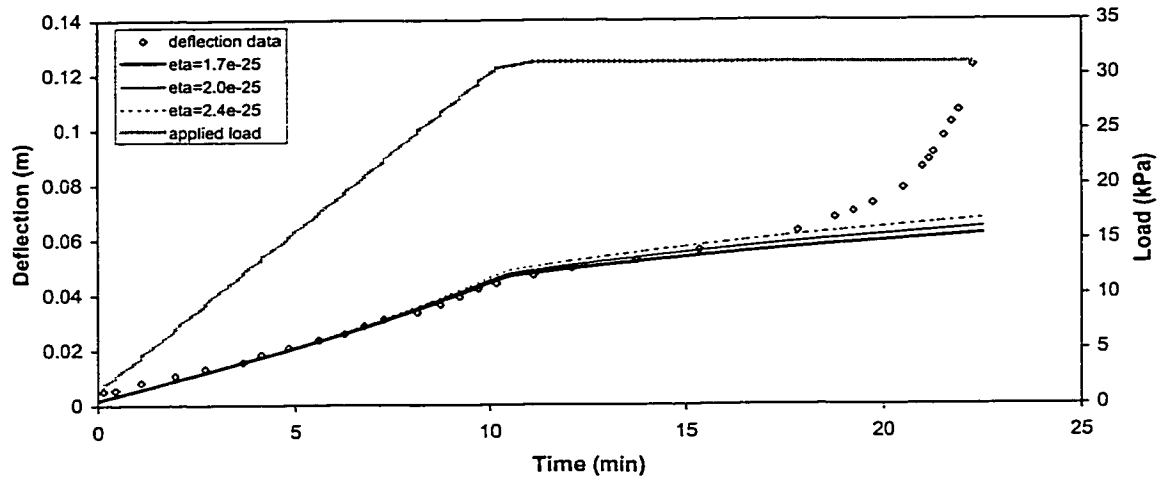
Figure 6-1(b): Range for creep coefficient, η (Test C01: n = 3.22, E = 1.65e9).
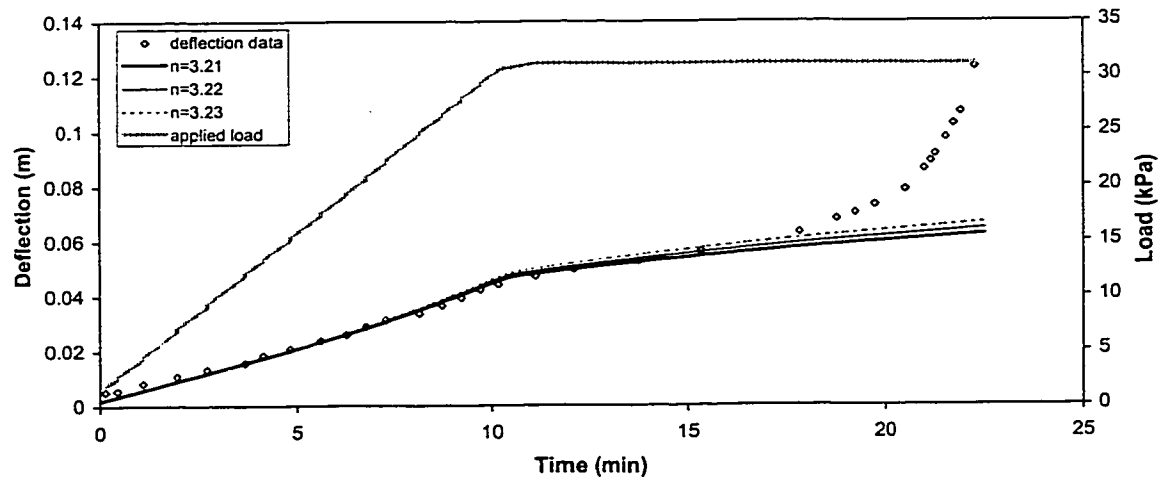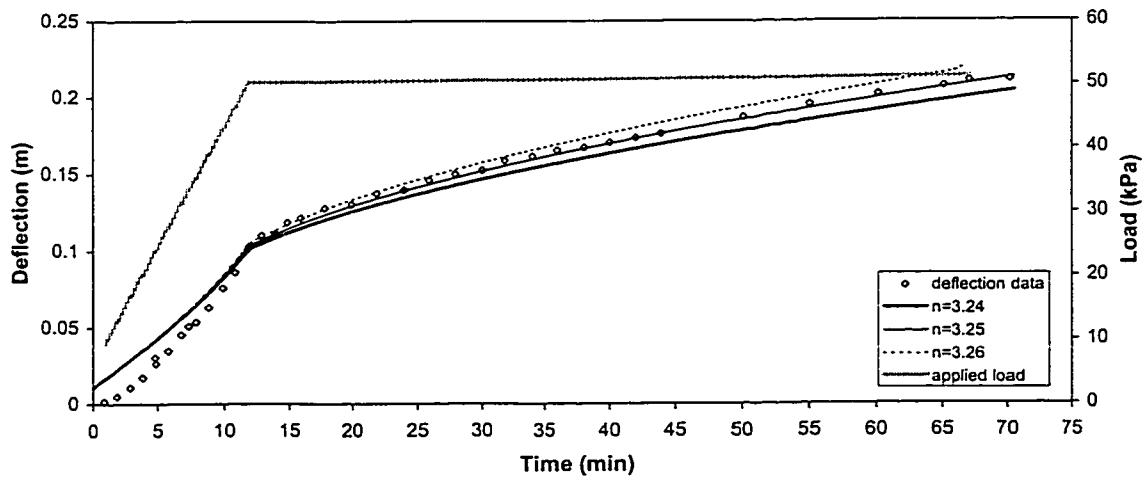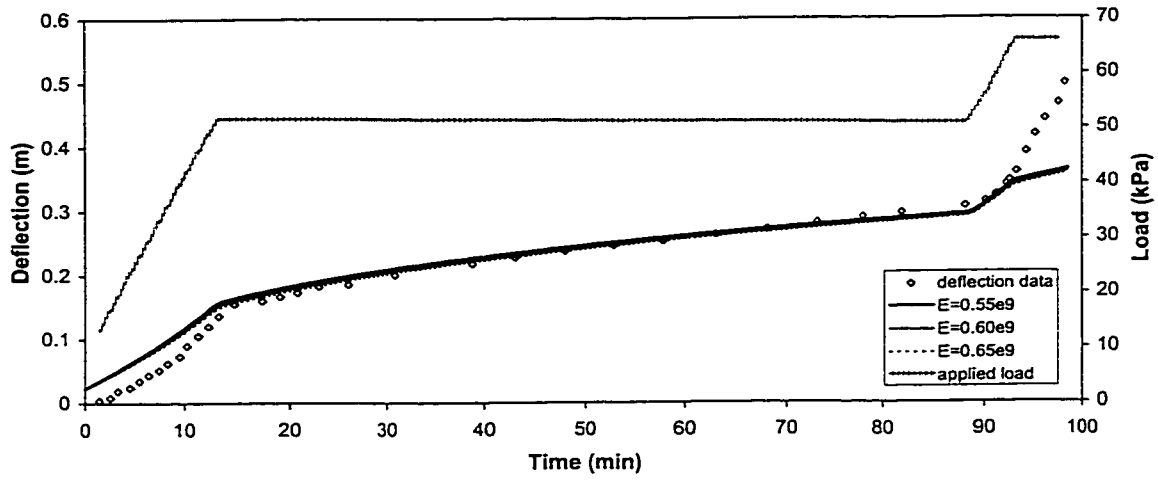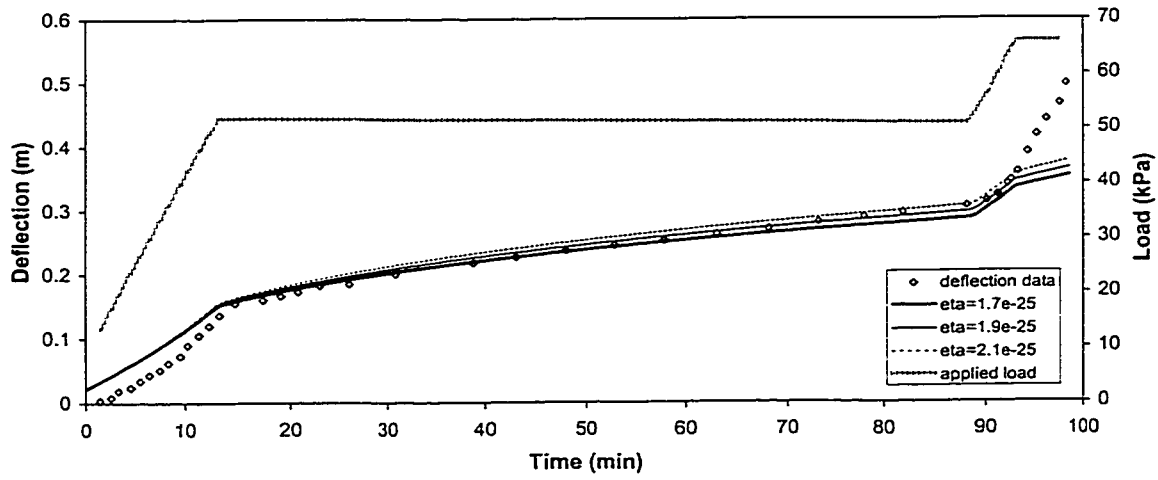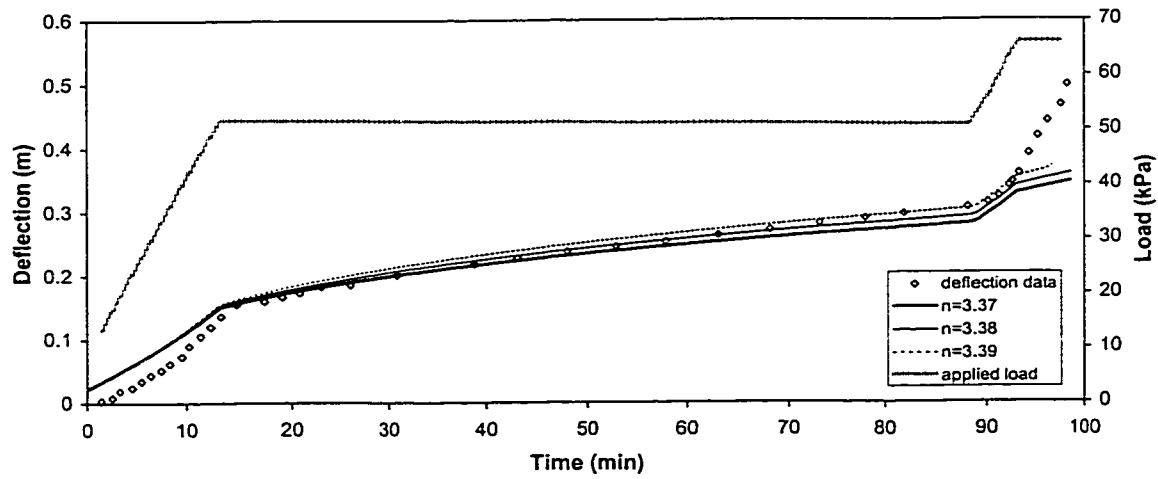

Figure 6-1(c): Range for creep exponent, n (Test C01: η = 2.0e-25, E = 1.65e9).
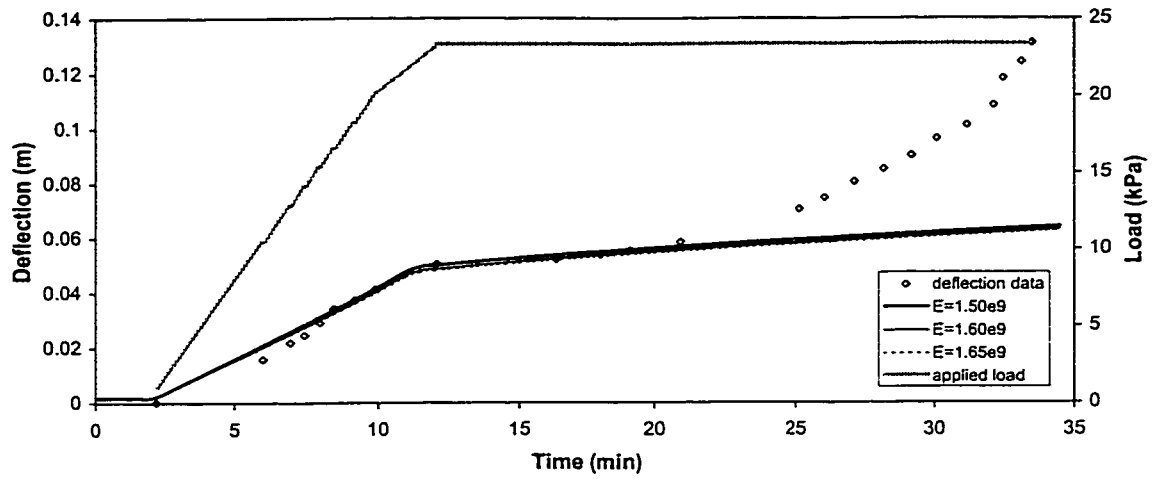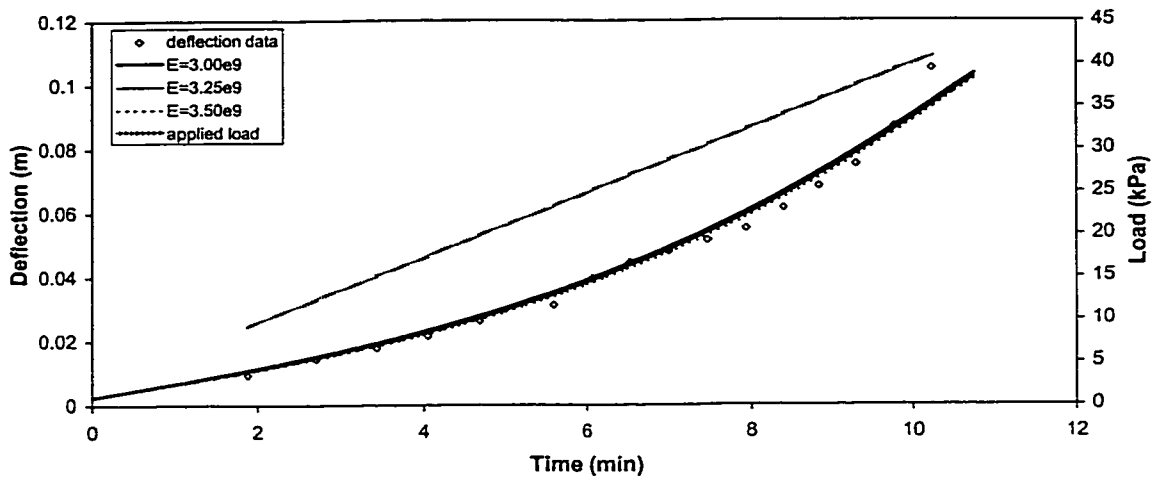
Figure 6-2(a): Range for Young's modulus, E (Test C02: n = 3.10, η = 2.0e-25).
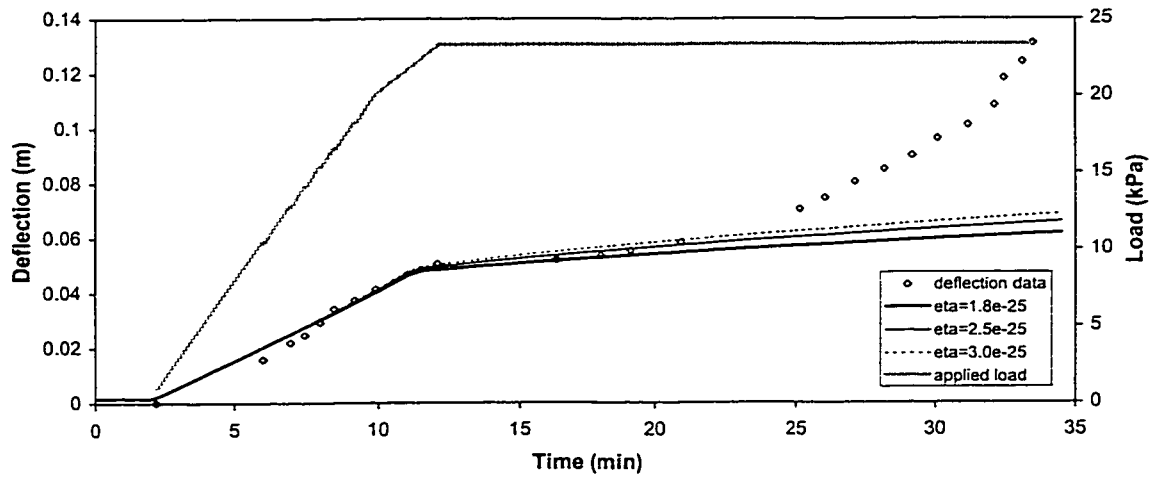
Figure 6-2(b): Range for creep coefficient, η (Test C02: n = 3.10, E = 1.60e9).
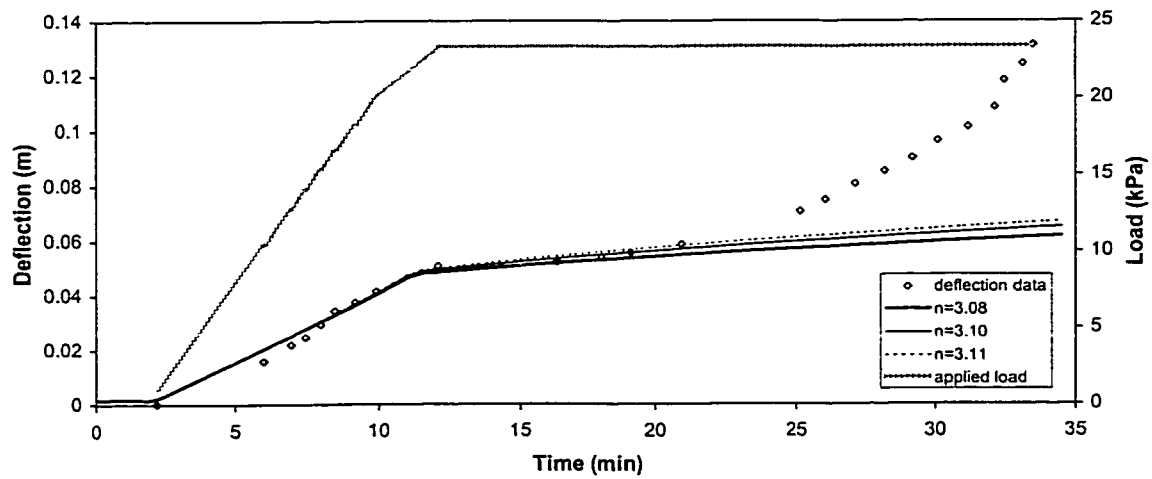
Figure 6-2(c): Range for creep exponent, n (Test C02: η = 2.3e-25, E = 1.60e9).

127
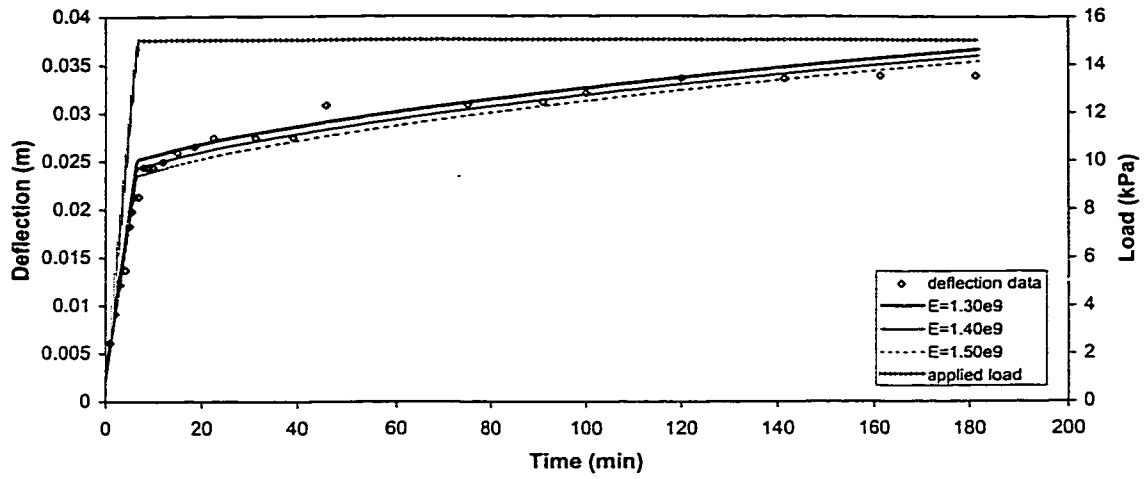
Figure 6-3(a): Range for Young's modulus, E (Test C04: n = 3.11, η = 2.0e-25).
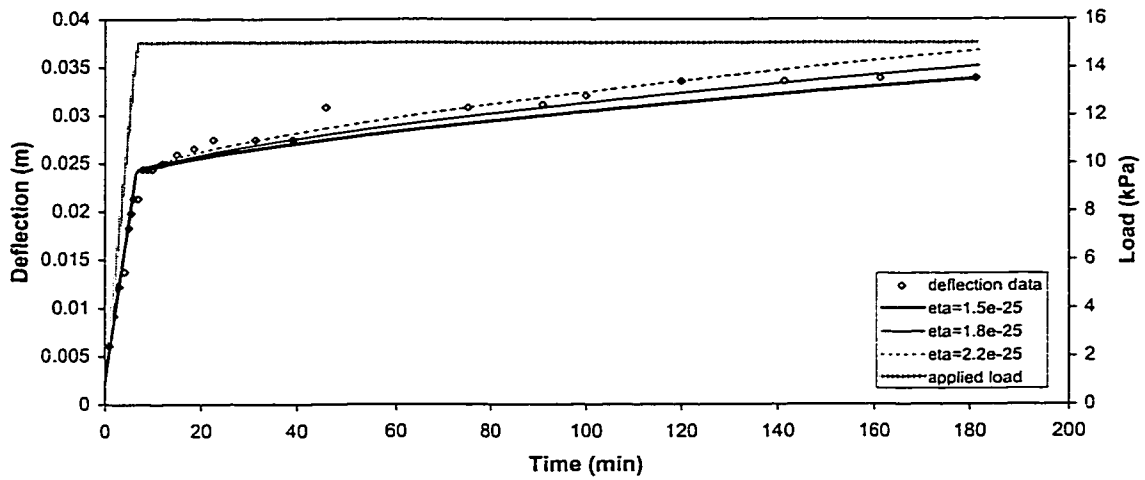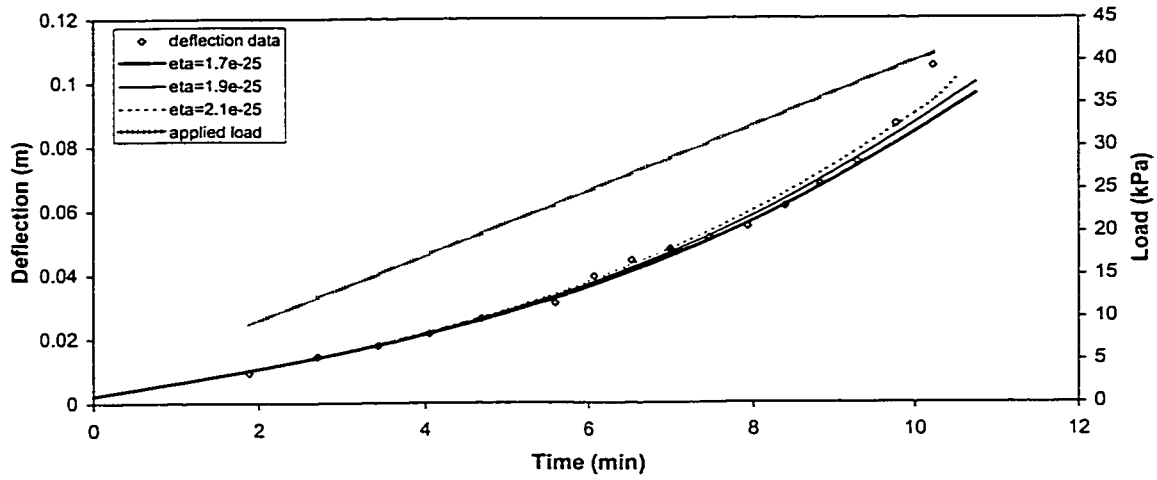

Figure 6-3(b): Range for creep coefficient, η (Test C04: n = 3.11, E = 1.40e9).
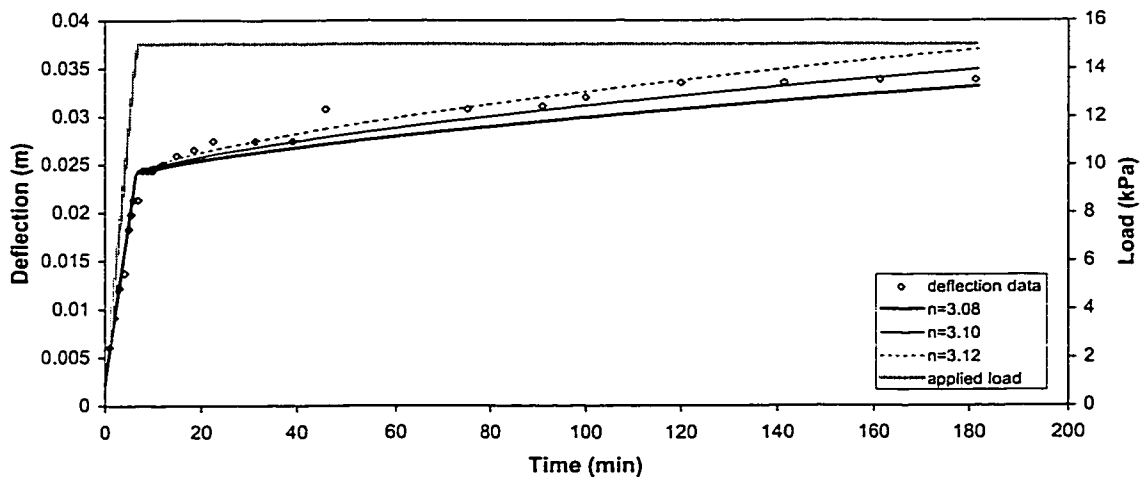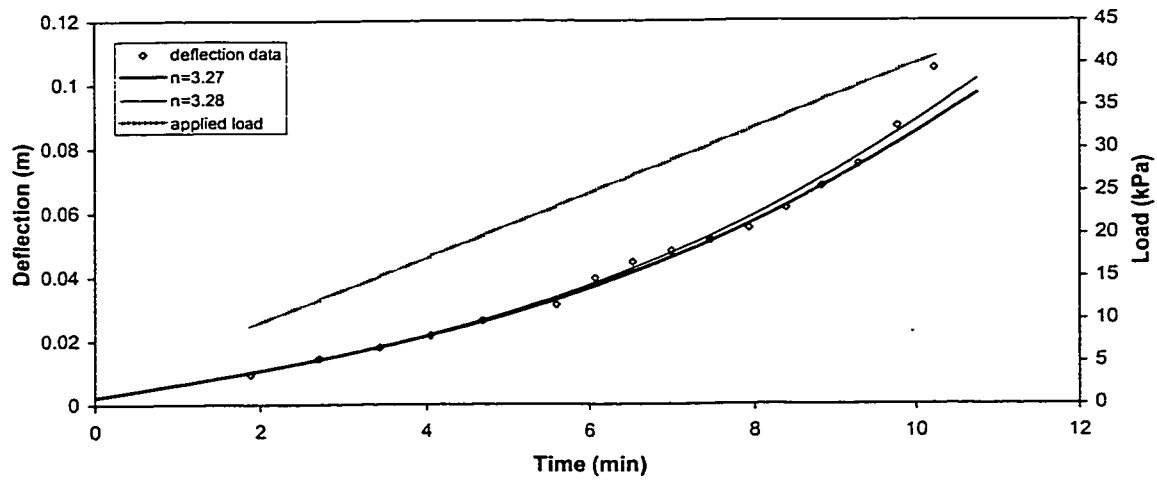

Figure 6-3(c): Range for creep exponent, n (Test C04: η = 2.0e-25, E = 1.40e9).
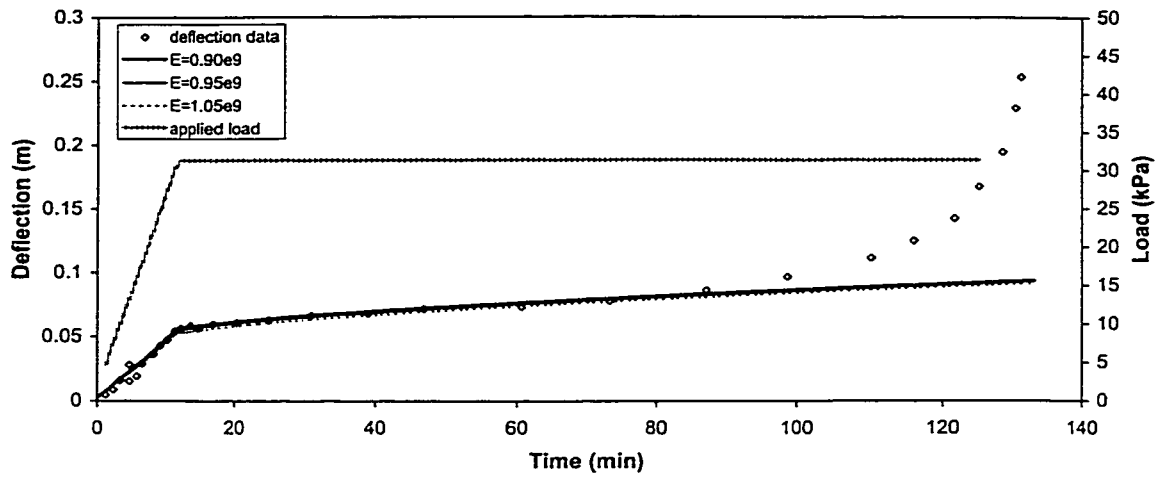
Figure 6-4(a): Range for Young's modulus, E (Test C05: n = 3.13, η = 2.0e-25).
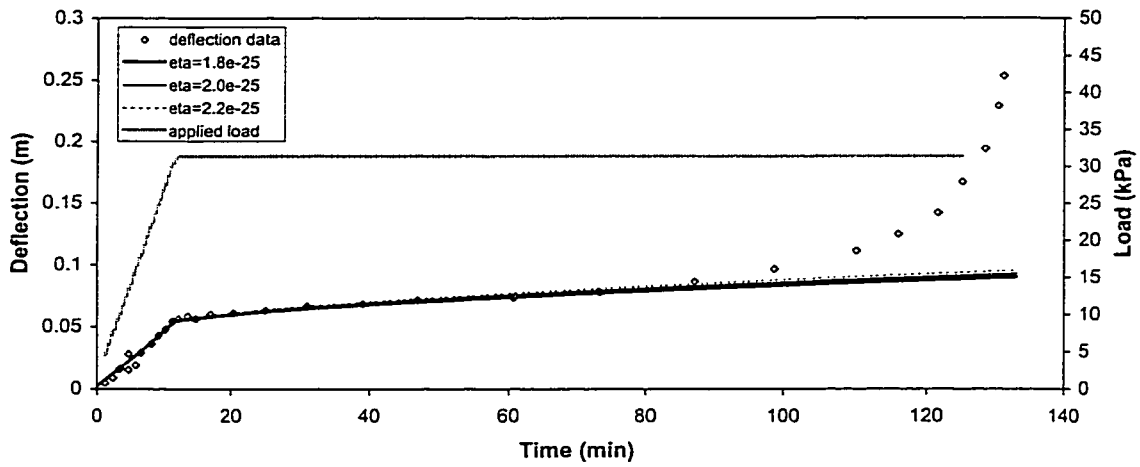
Figure 6-4(b): Range for creep coefficient, η (Test C05: n = 3.13, E = 0.95e9).
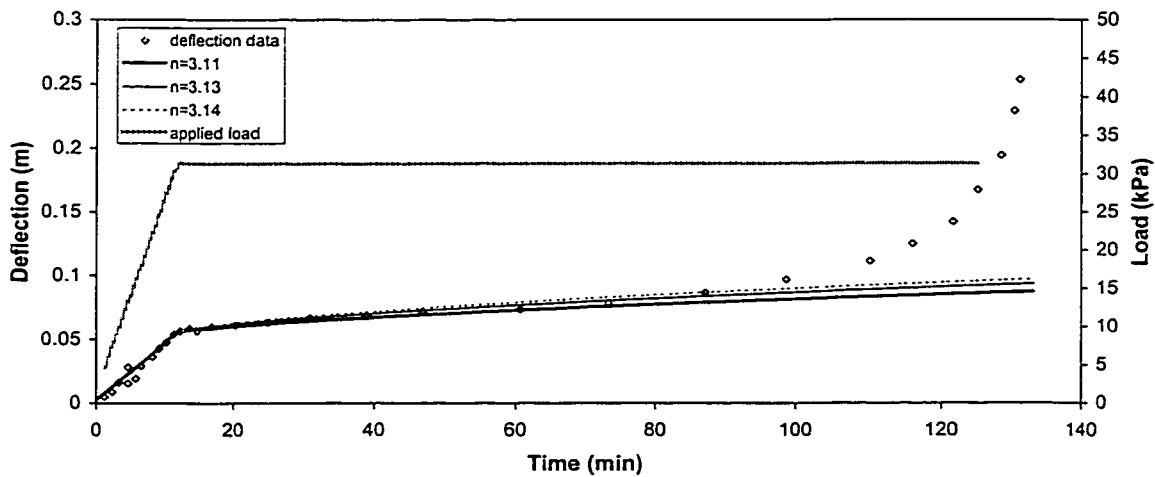
Figure 6-4(c): Range for creep exponent, n (Test C05: η = 2.0e-25, E = 0.90e9).

129
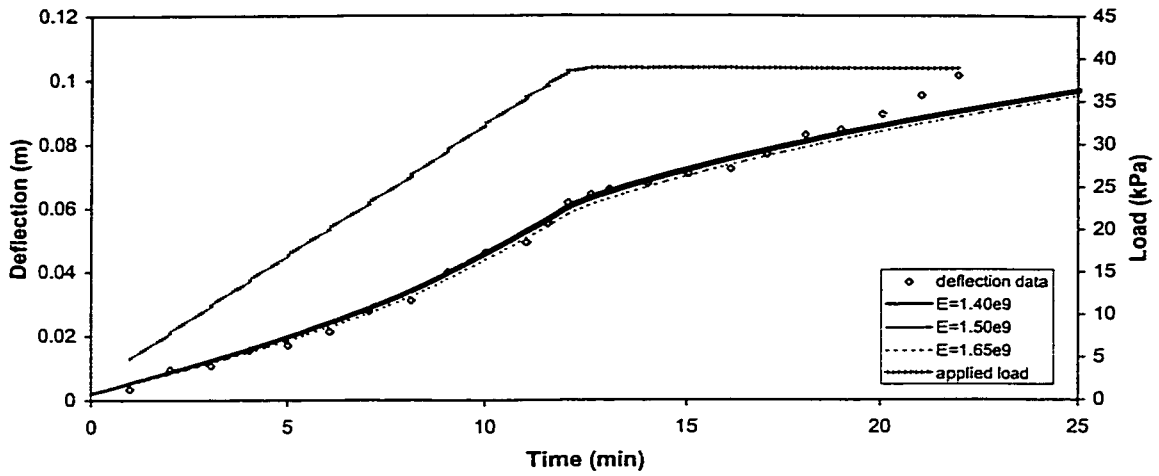
Figure 6-5(a): Range for Young's modulus, E (Test C06: n = 3.33, η = 2.0e-25).
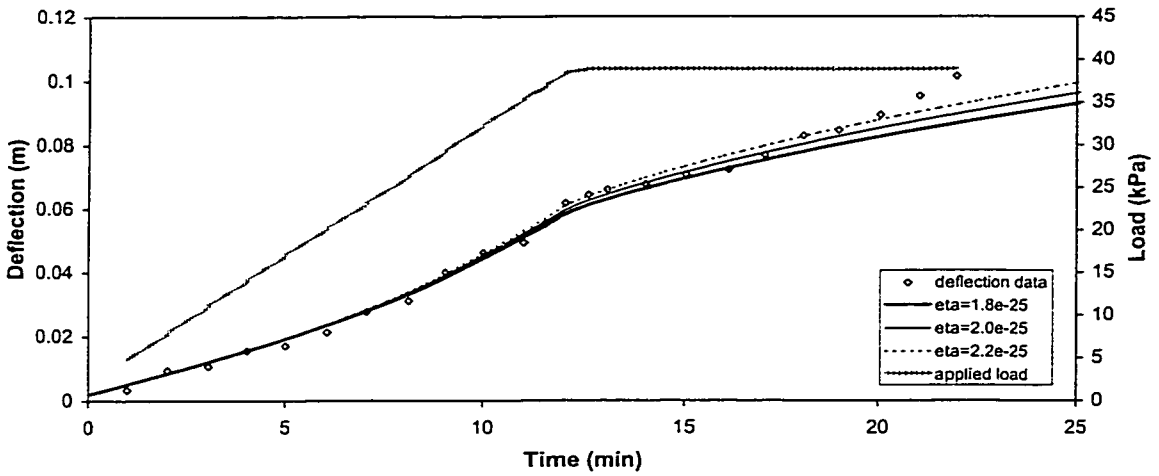
Figure 6-5(b): Range for creep coefficient, η (Test C06: n = 3.33, E = 1.50e9).
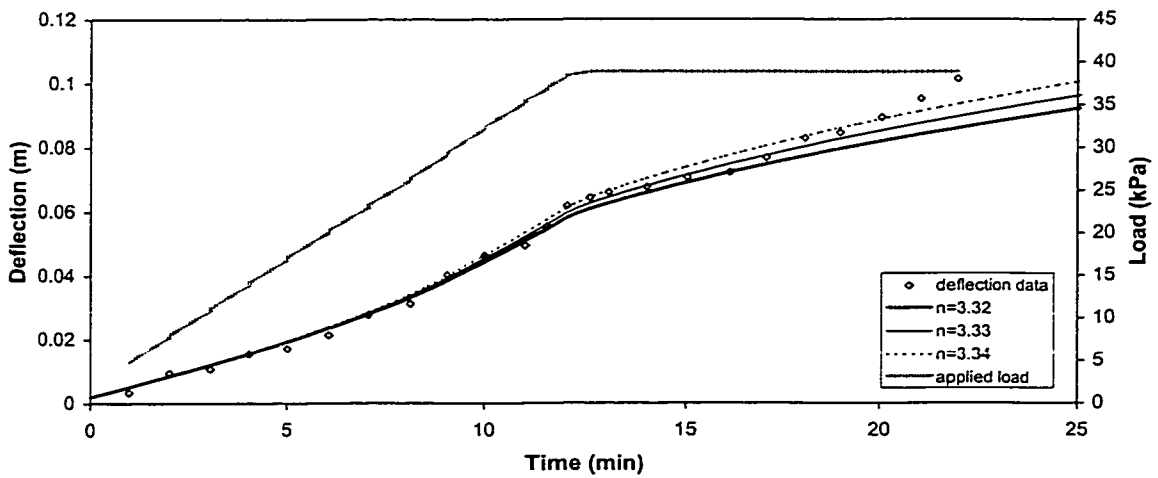
Figure 6-5(c): Range for creep exponent, n (Test C06: η = 2.0e-25, E = 1.50e9).
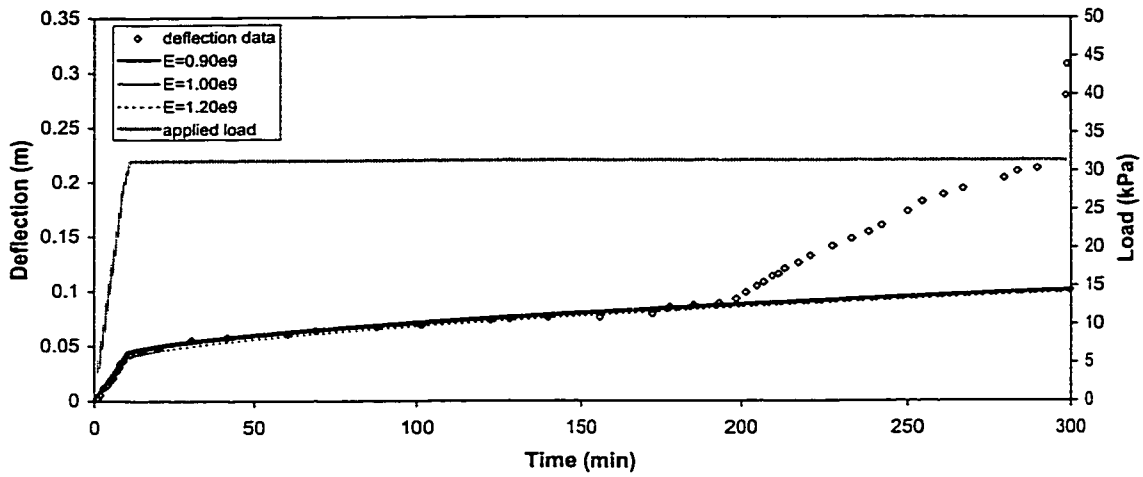
Figure 6-6(a): Range for Young's modulus, E (Test C07: n = 3.19, η = 2.0e-25).
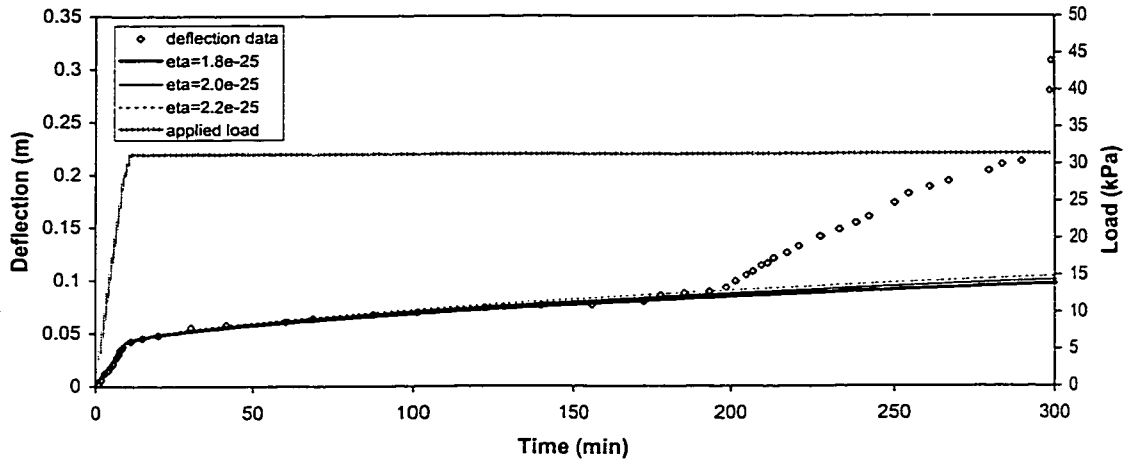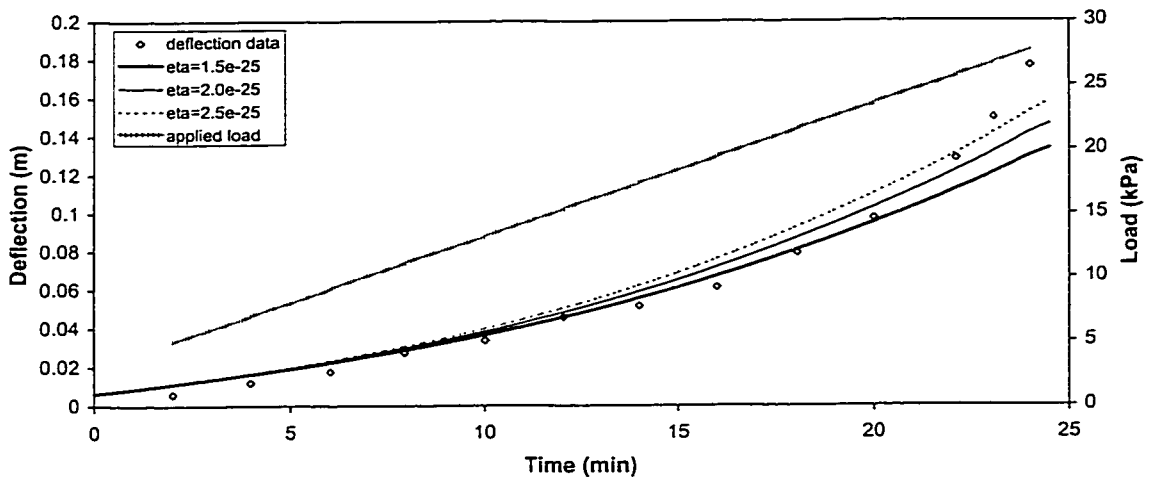

Figure 6-6(b): Range for creep coefficient, η (Test C07: n = 3.19, E = 1.00e9).
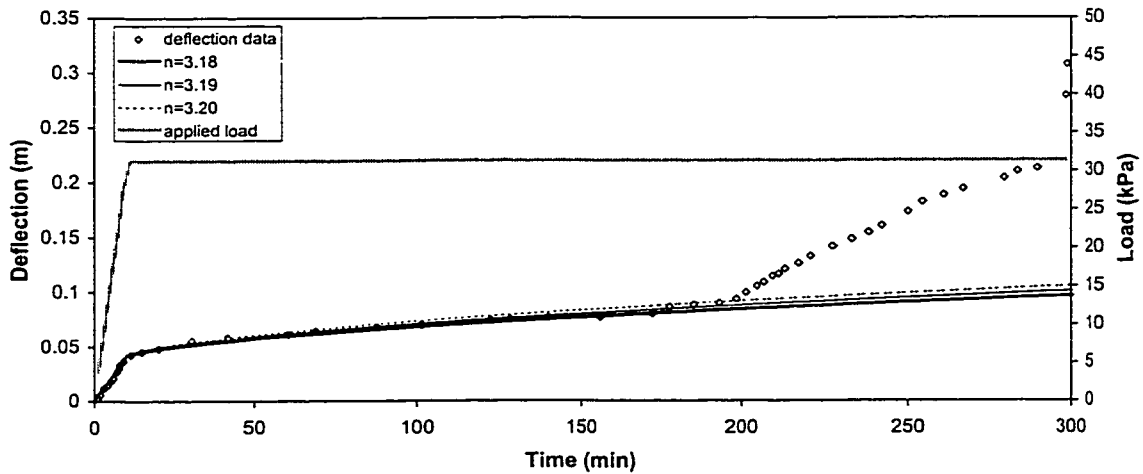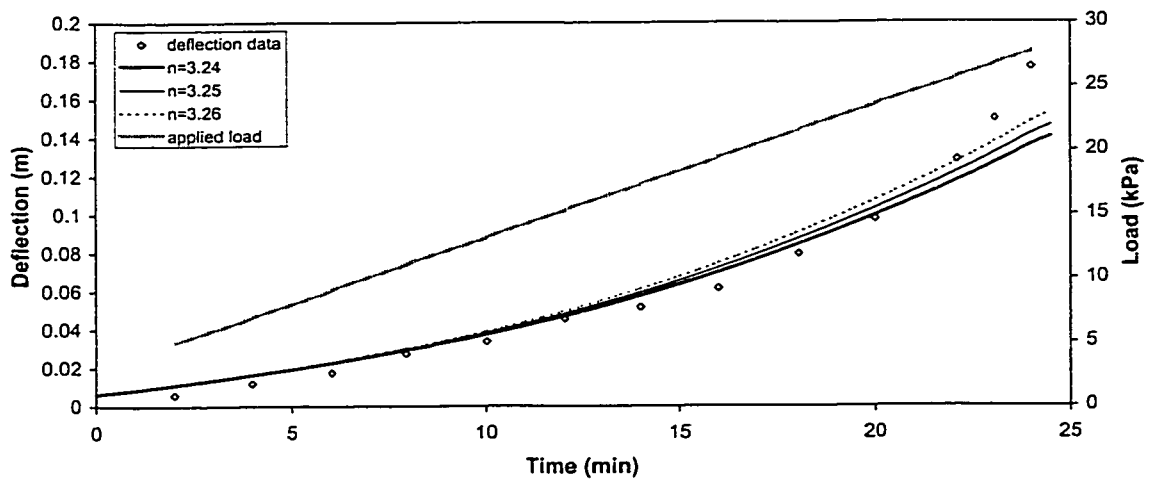

Figure 6-6(c): Range for creep exponent, n (Test C07: η = 2.0e-25, E = 1.00e9).
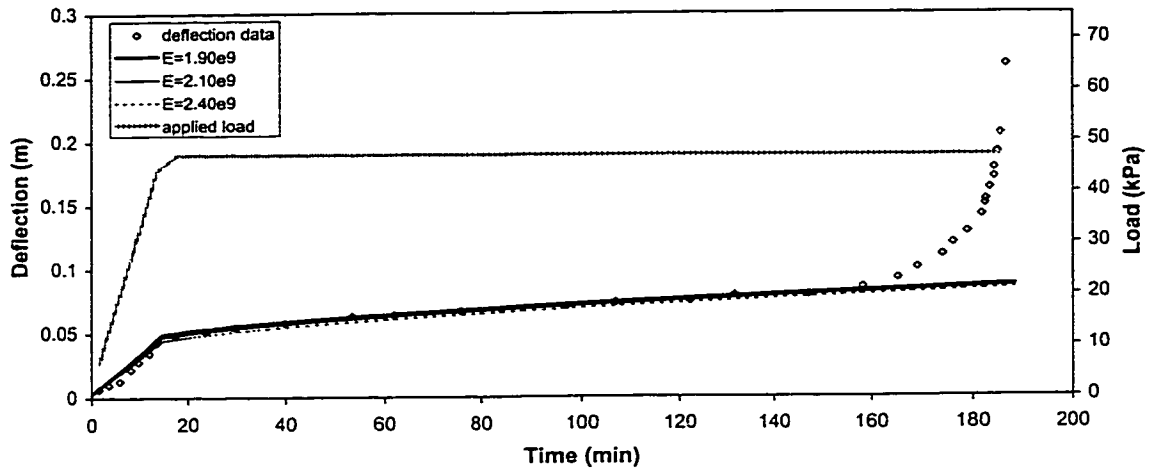
Figure 6-7(a): Range for Young's modulus, E (Test C08: $n = 3.03$, $\eta = 2.0\text{e-}25$).
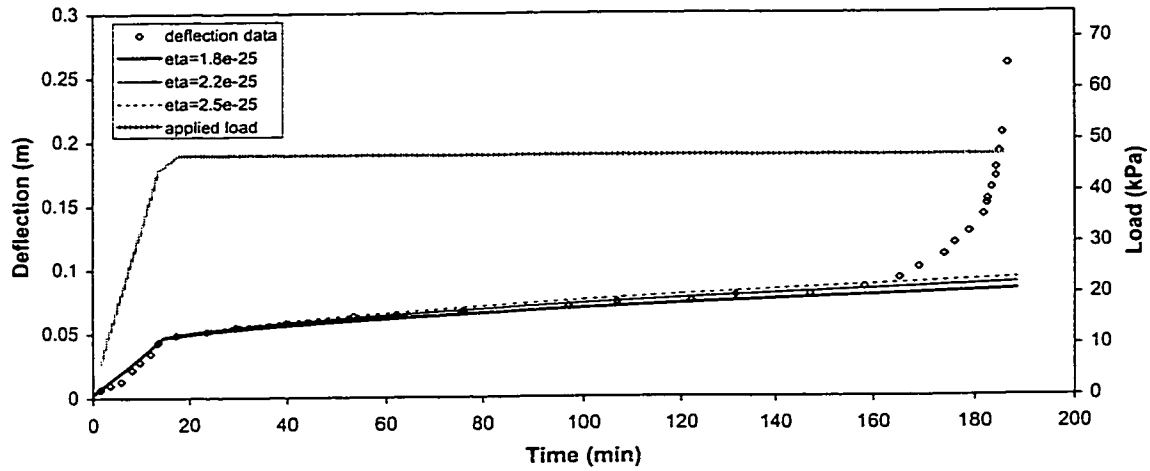
Figure 6-7(b): Range for creep coefficient, η (Test C08: $n = 3.03$, $E = 2.10\text{e}9$).
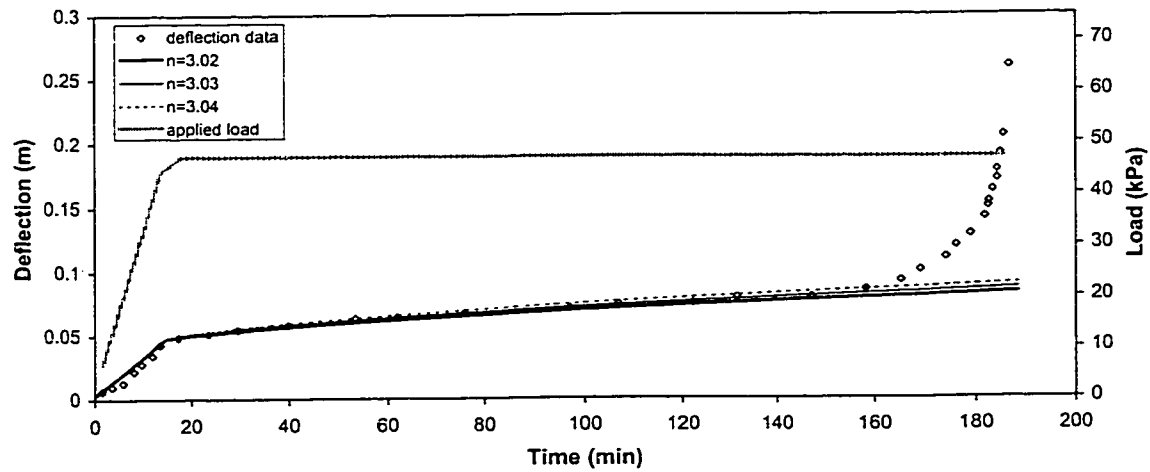
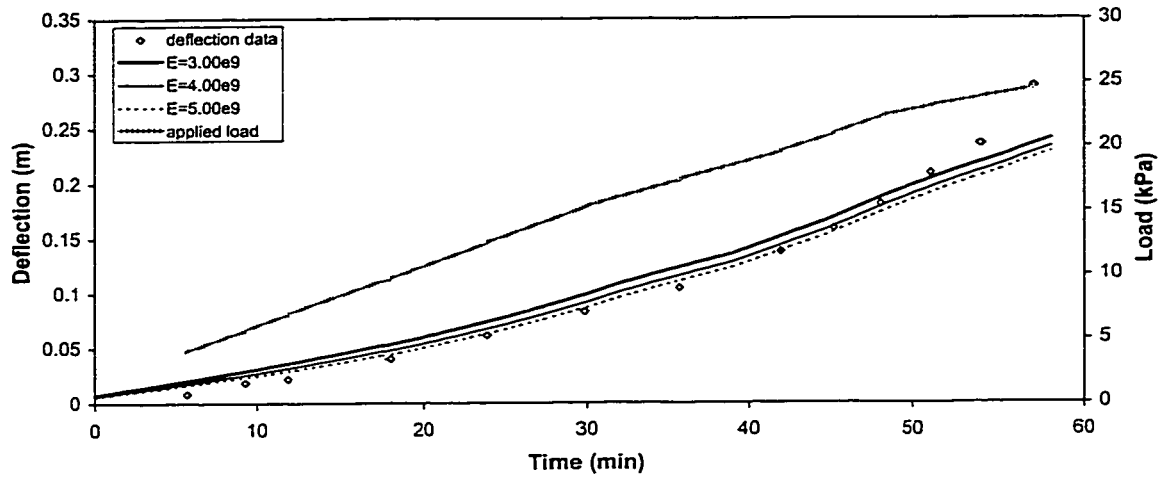Figure 6-7(c): Range for creep exponent, n (Test C08: $\eta = 2.0\text{e-}25$, $E = 2.00\text{e}9$).

132
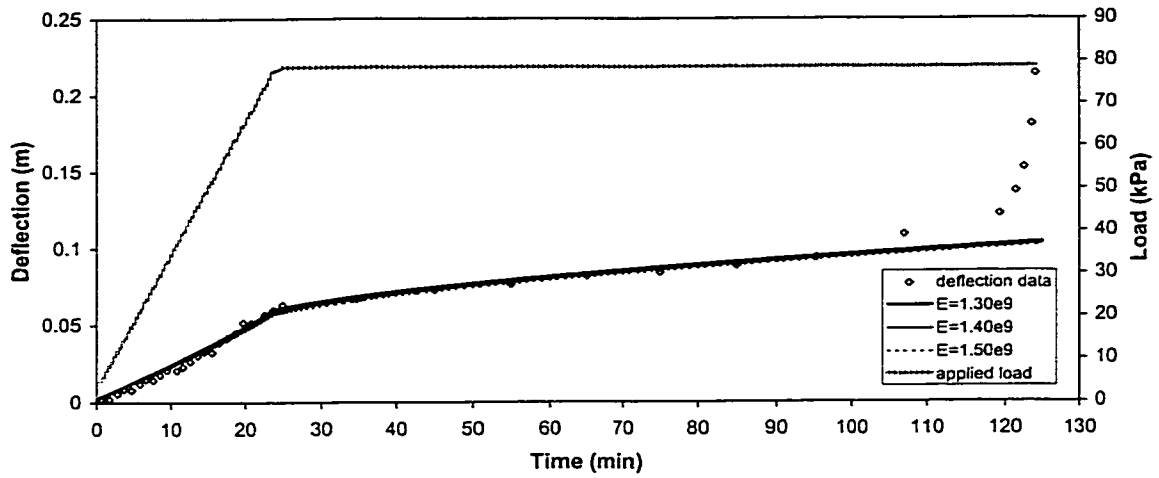
Figure 6-8(a): Range for Young's modulus, E (Test C09: n = 3.13, η = 2.0e-25).
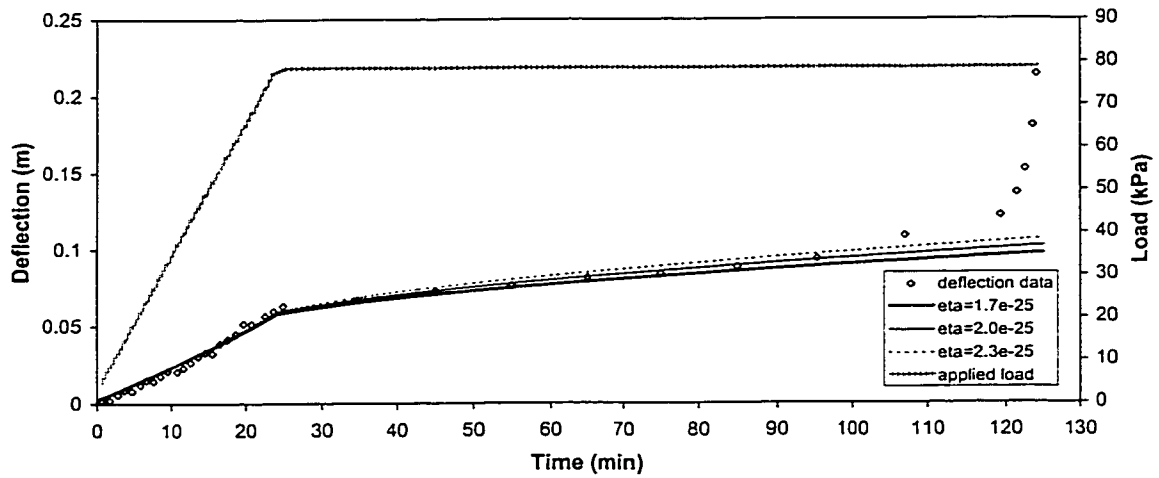
Figure 6-8(b): Range for creep coefficient, η (Test C09: n = 3.13, E = 1.40e9).
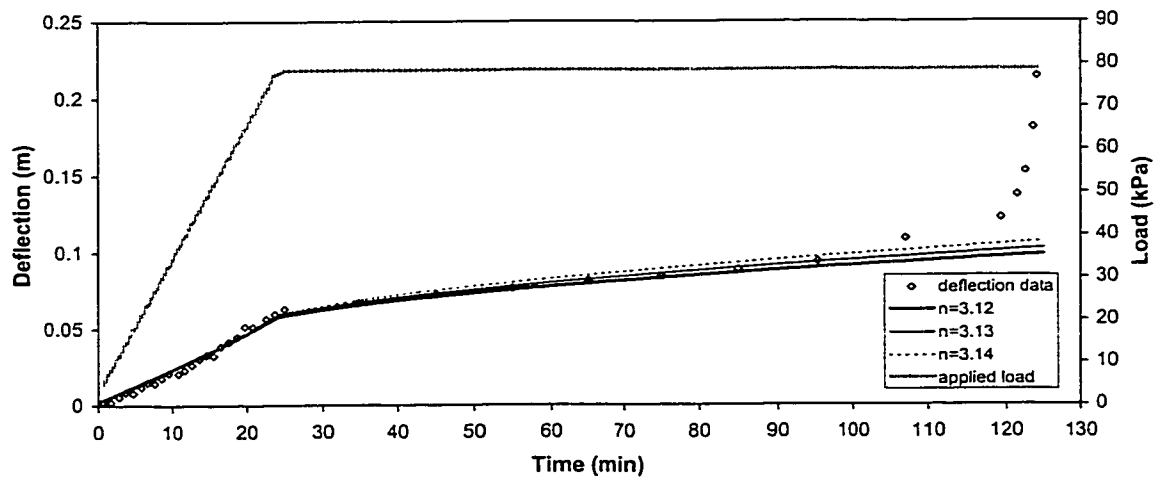
Figure 6-8(c): Range for creep exponent, n (Test C09: η = 2.0e-25, E = 1.40e9).
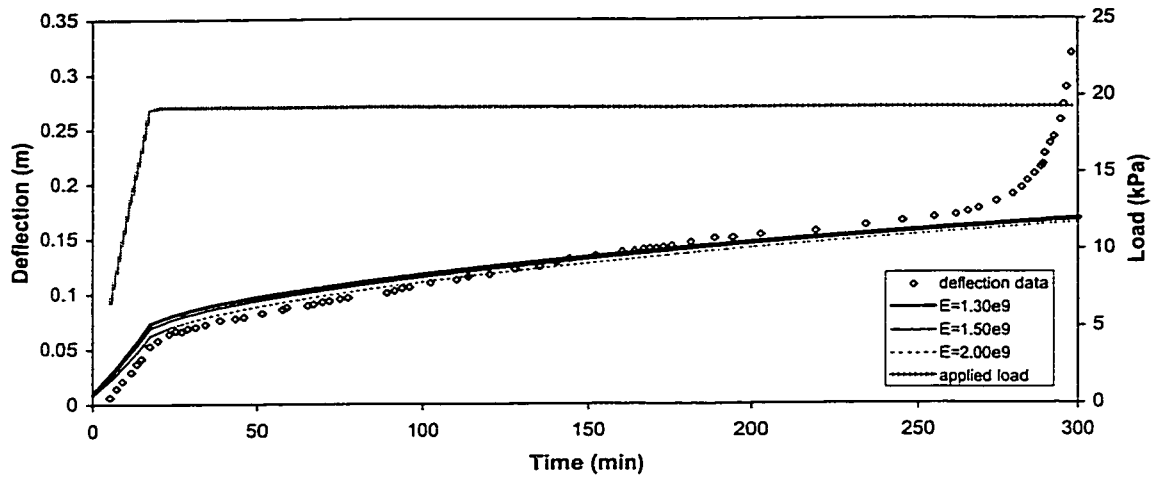
Figure 6-9(a): Range for Young's modulus, E (Test Cl1: n = 3.16, η = 2.0e-25).
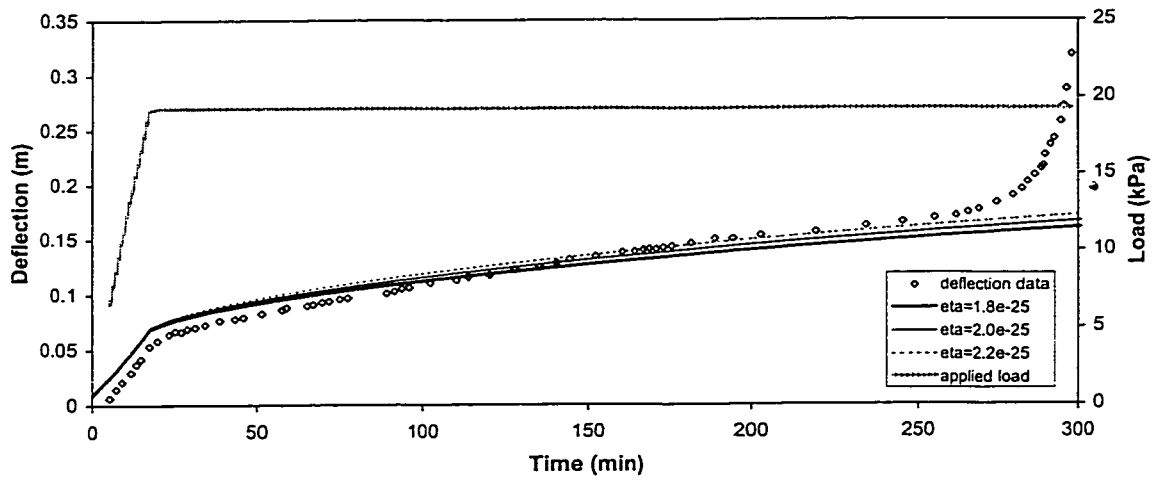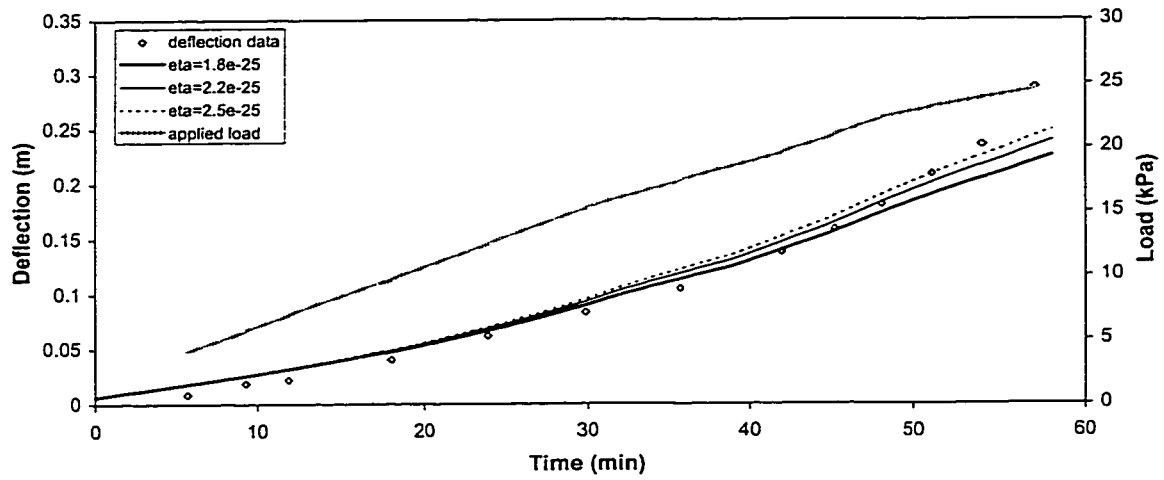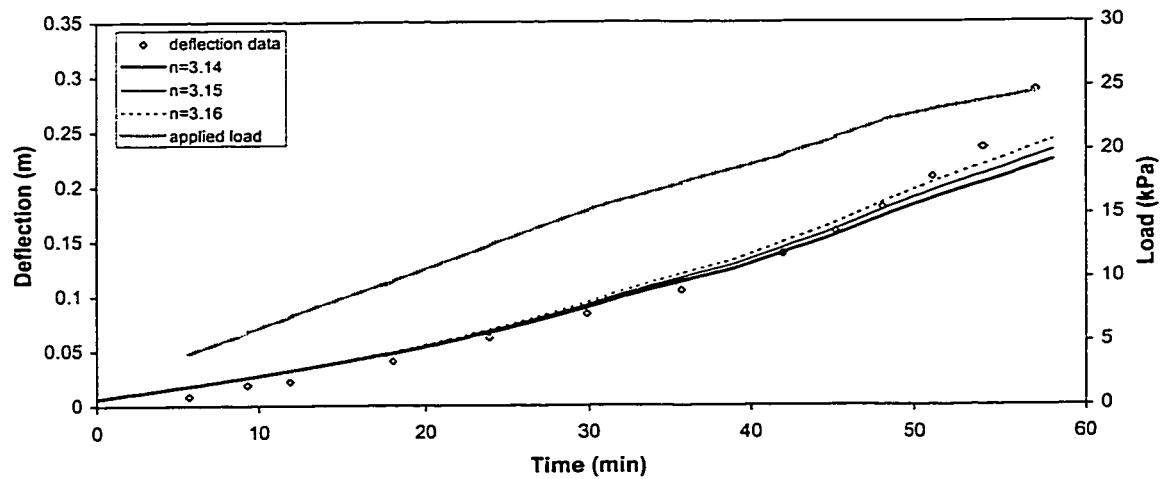

Figure 6-9(b): Range for creep coefficient, η (Test Cl1: n = 3.16, E = 1.50e9).
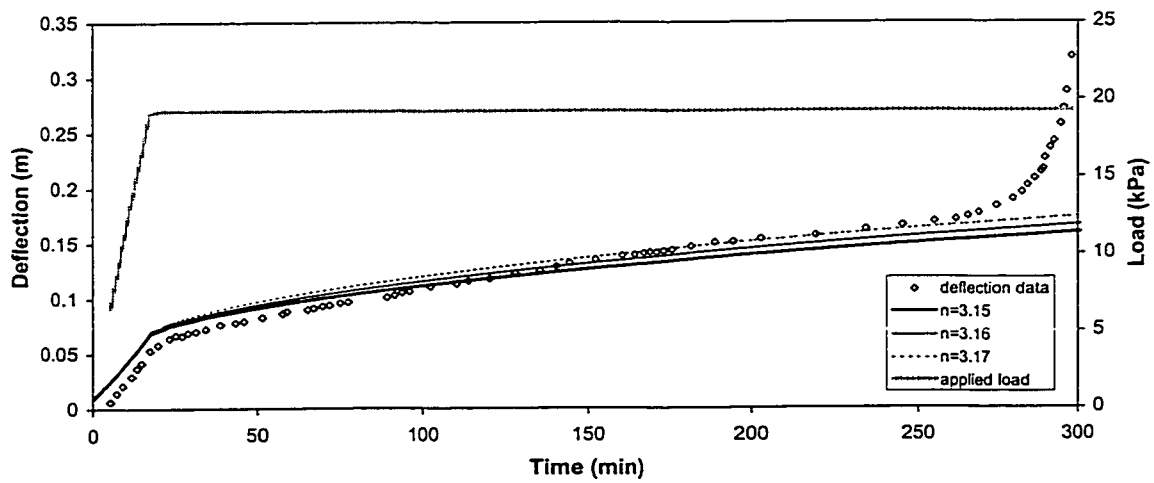
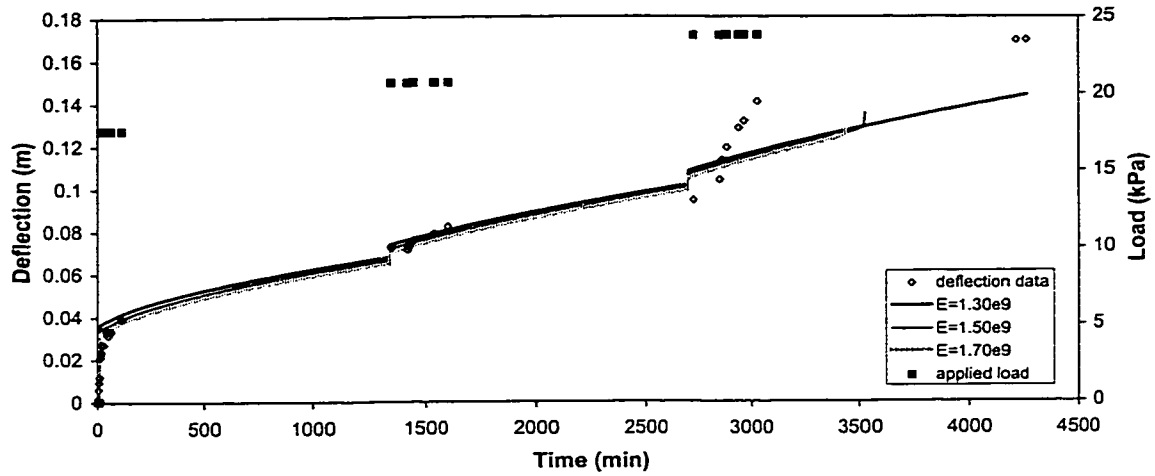Figure 6-9(c): Range for creep exponent, n (Test Cl1: η = 2.0e-25, E = 1.50e9).
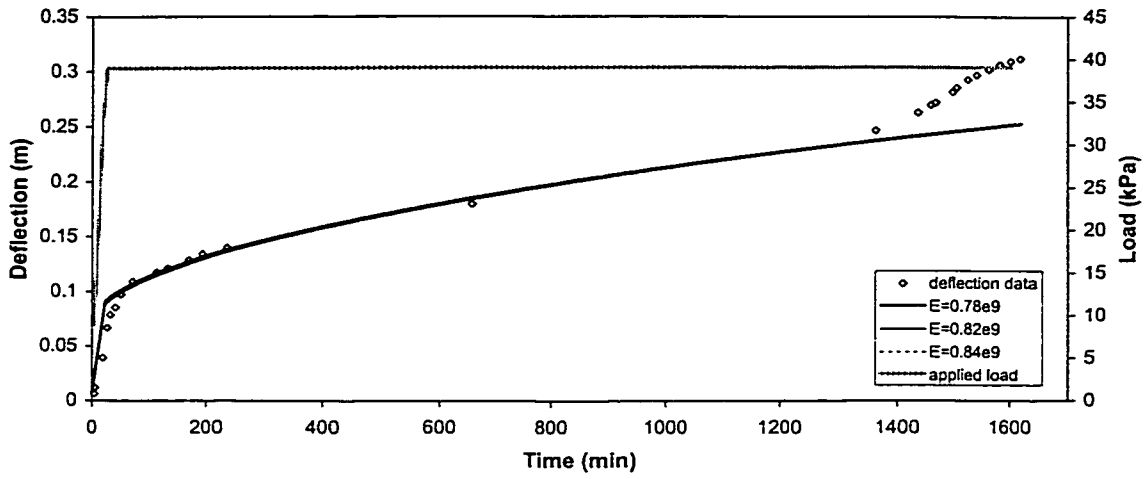
Figure 6-10(a): Range for Young's modulus, E (Test C14: $n = 3.12$, $\eta = 2.0e\text{-}25$).
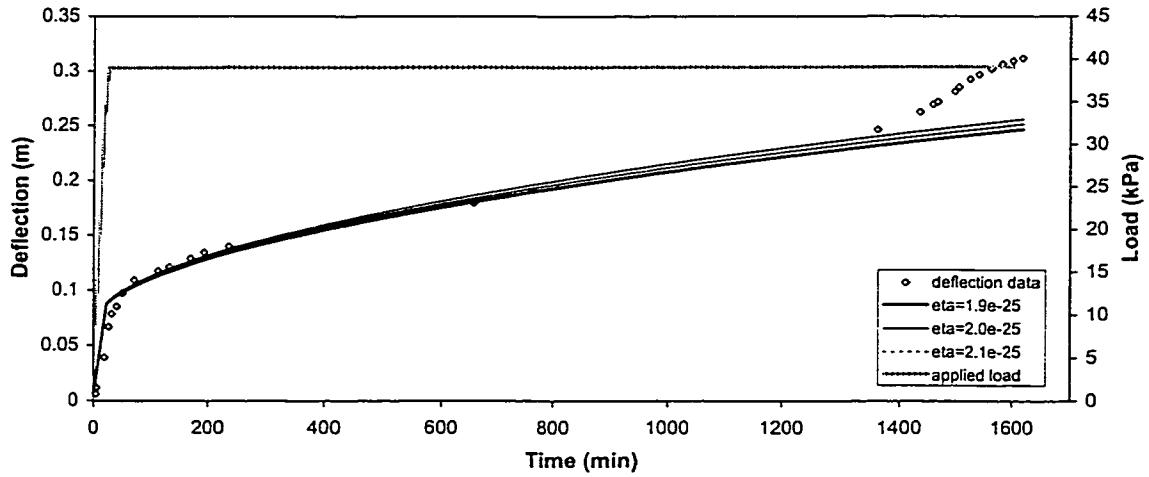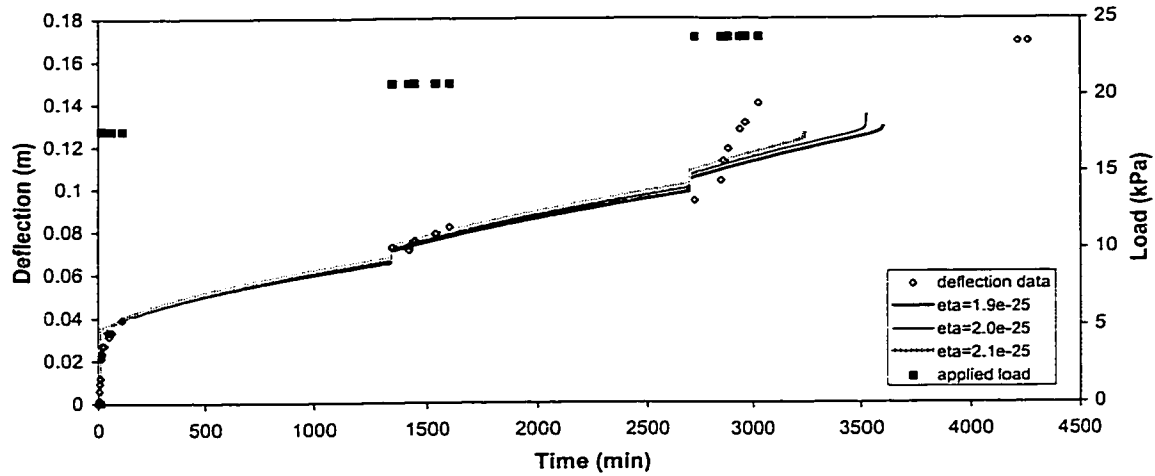

Figure 6-10(b): Range for creep coefficient, η (Test C14: $n = 3.12$, $E = 0.84e9$).
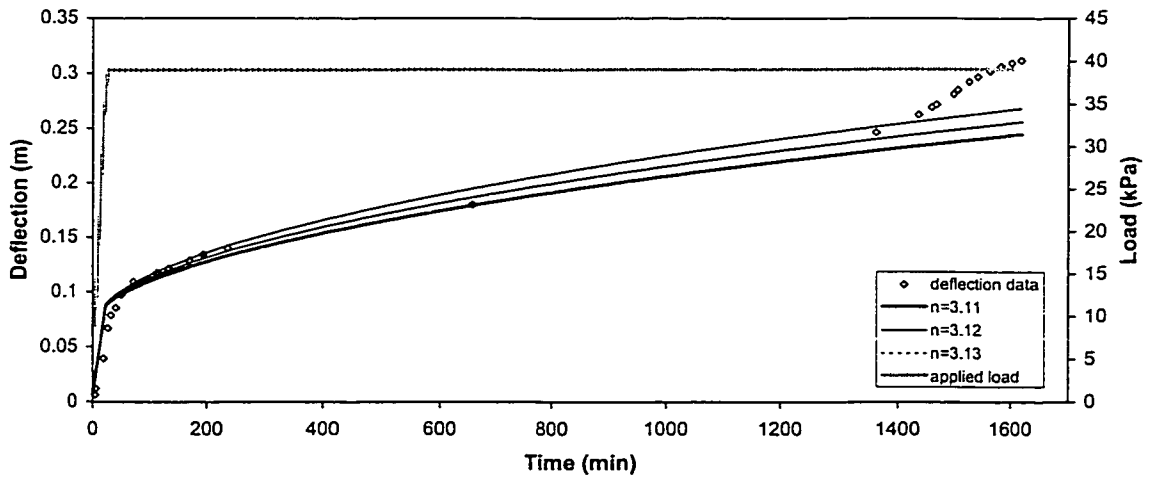
Figure 6-10(c): Range for creep exponent, n (Test C14: $\eta = 2.1e\text{-}25$, $E = 0.84e9$).

135
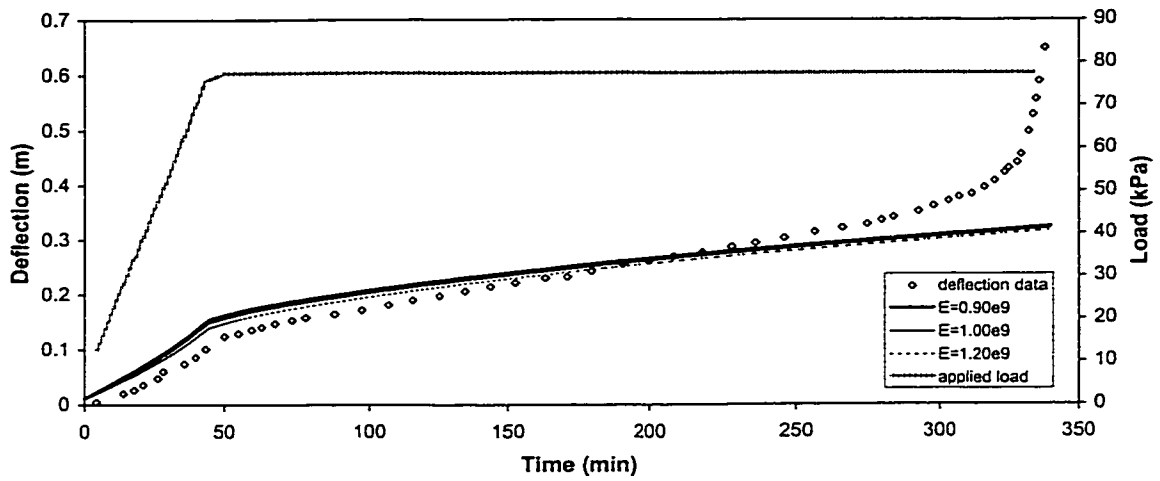
Figure 6-11(a): Range for Young's modulus, E (Test C15: n = 3.12, η = 2.0e-25).
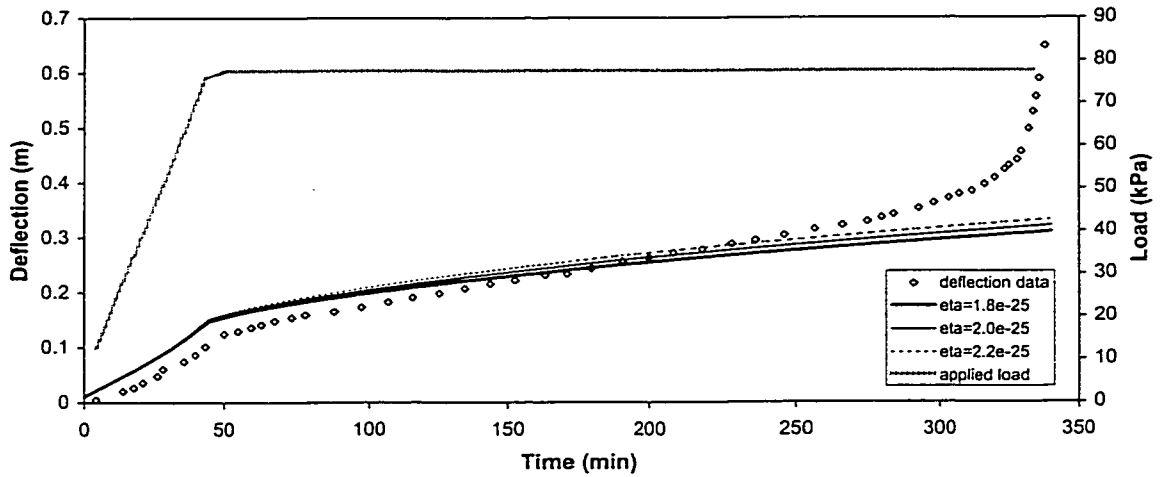
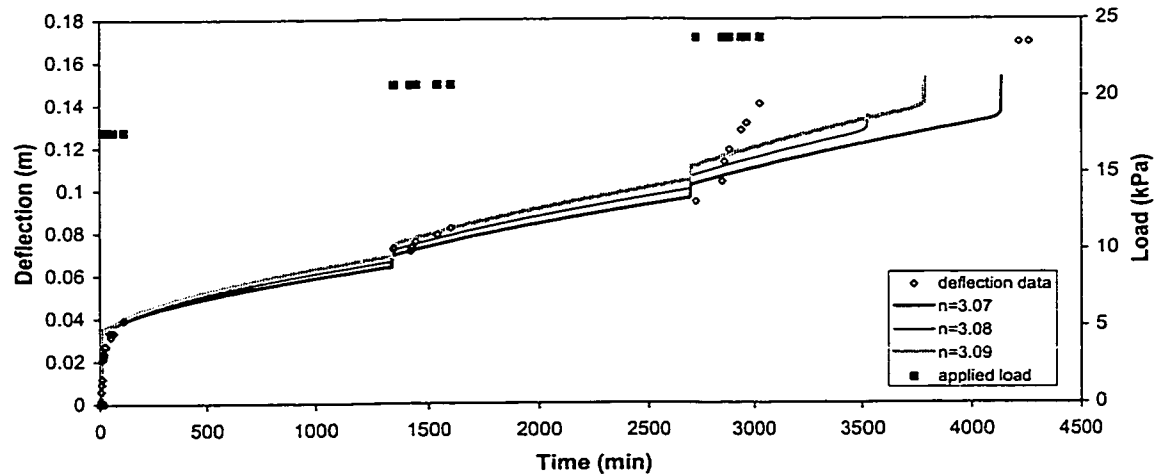Figure 6-11(b): Range for creep coefficient, η (Test C15: n = 3.12, E = 1.00e9).
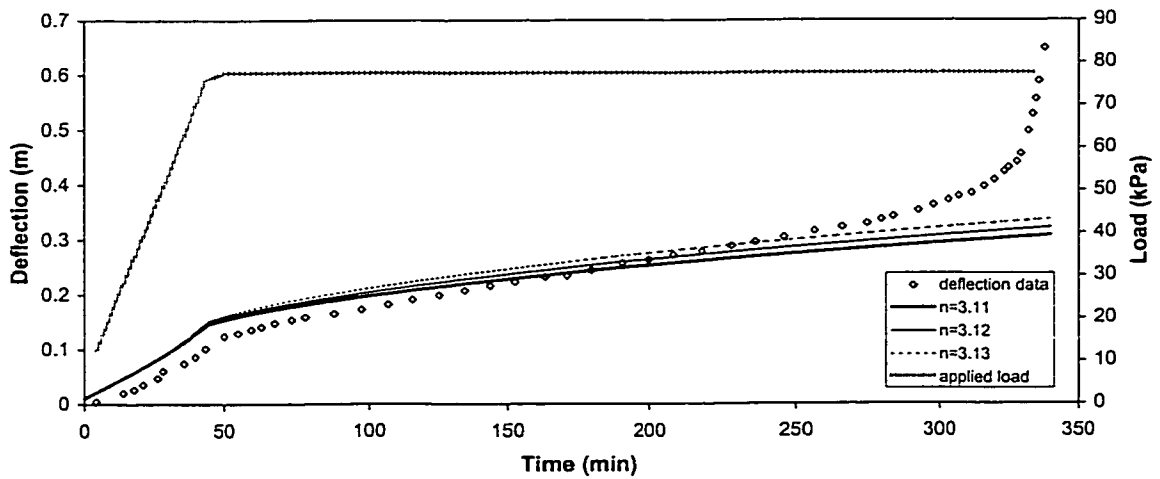
Figure 6-11(c): Range for creep exponent, n (Test C15: η = 2.0e-25, E = 1.00e9).

136
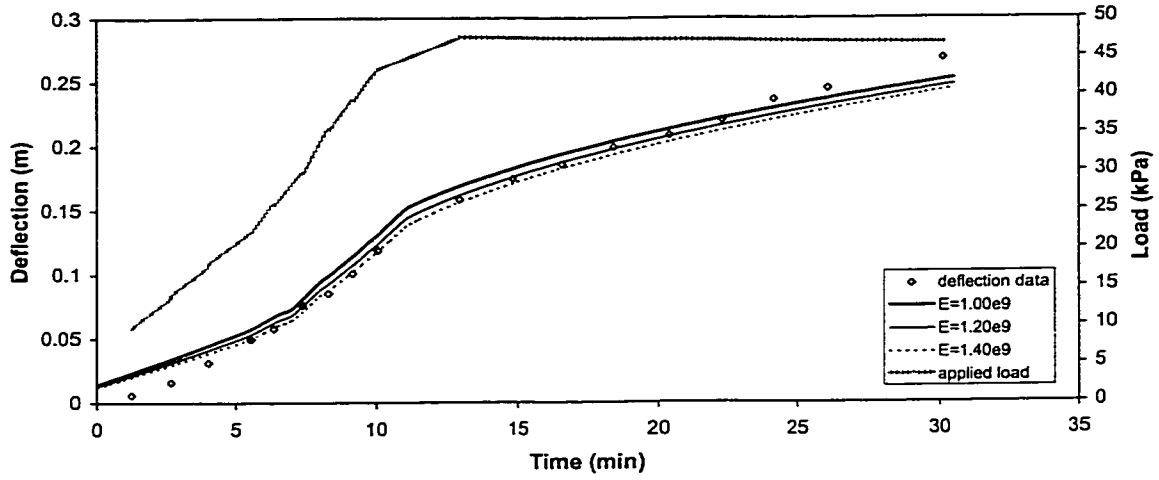
Figure 6-12(a): Range for Young's modulus, E (Test C19: n = 3.38, η = 2.0e-25).
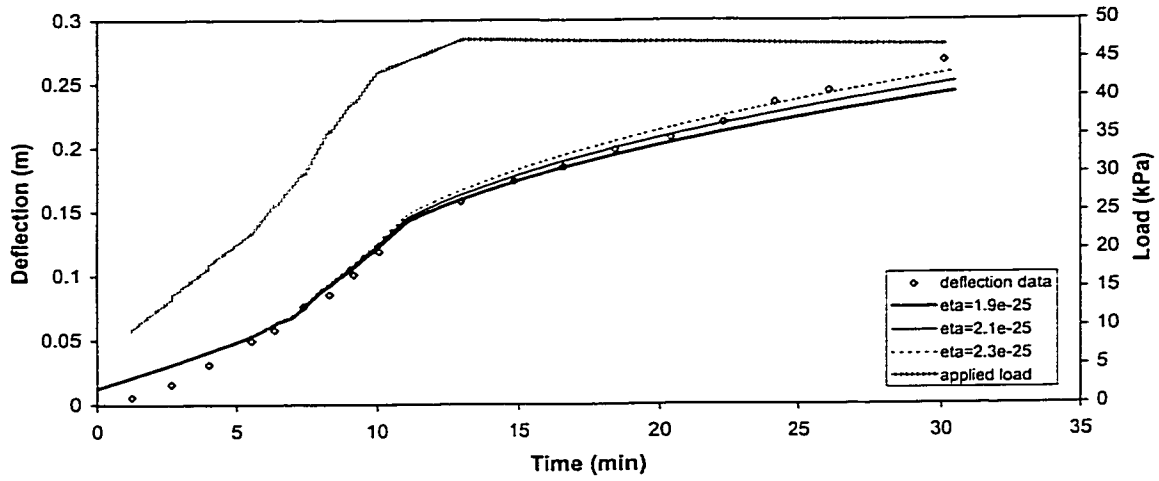
Figure 6-12(b): Range for creep coefficient, η (Test C19: n = 3.38, E = 1.20e9).
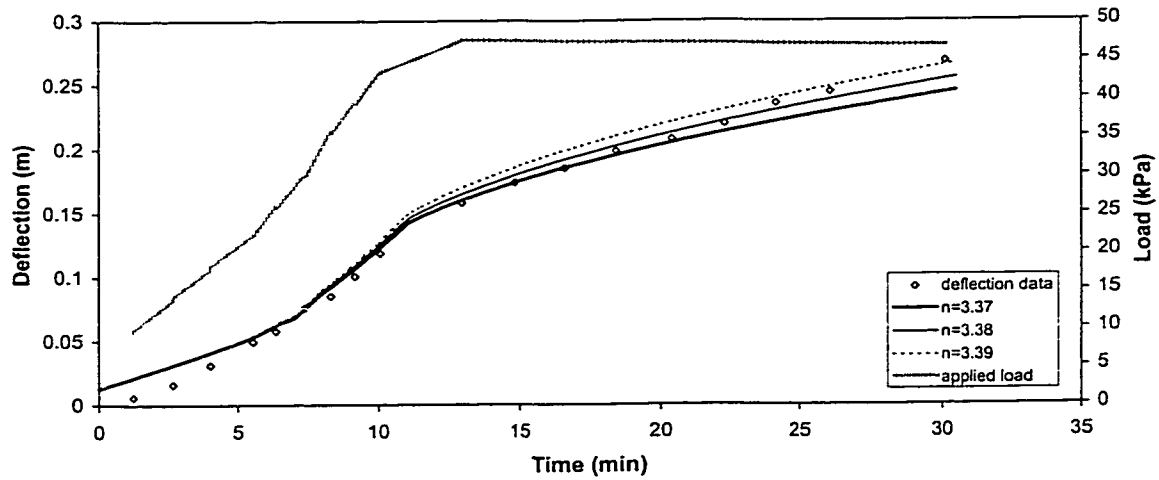
Figure 6-12(c): Range for creep exponent, n (Test C19: η = 2.2e-25, E = 1.20e9).
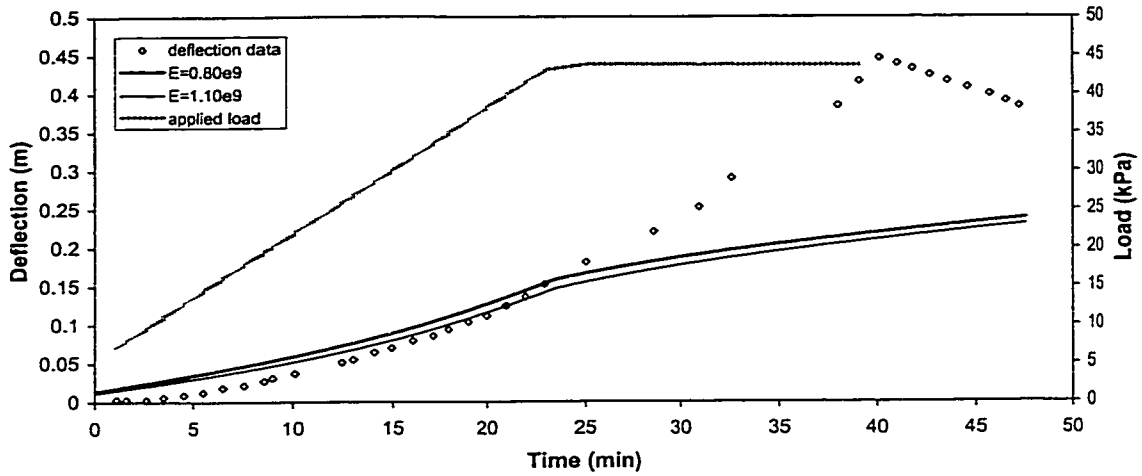
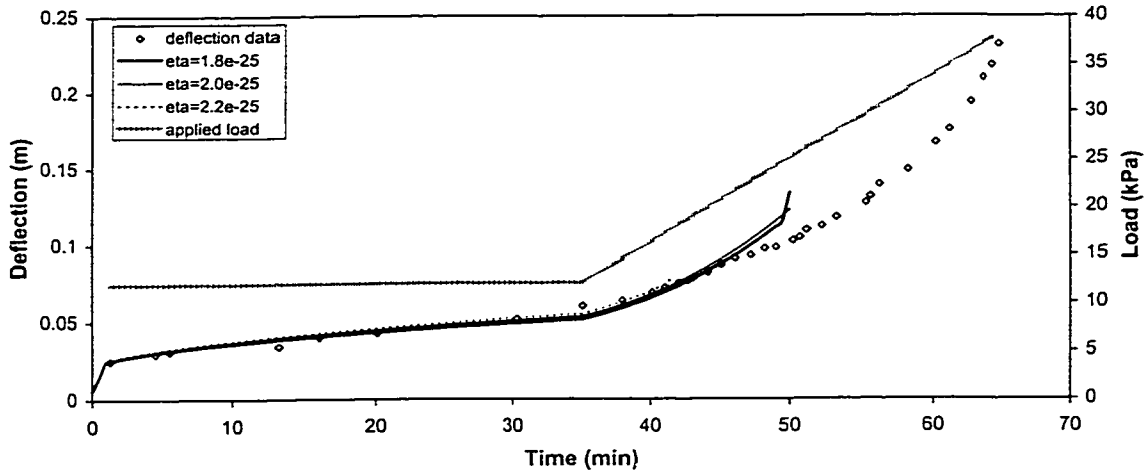Figure 6-13(a): Range for Young's modulus, E (Test C20: $n = 3.40$, $\eta = 2.0e\text{-}25$).
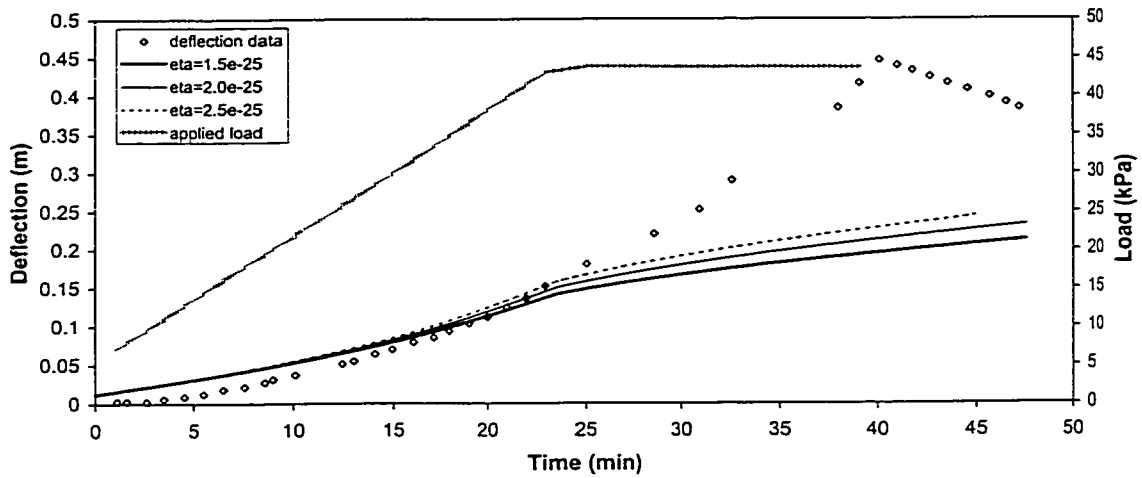
Figure 6-13(b): Range for creep coefficient, η (Test C20: $n = 3.40$, $E = 1.00e9$).
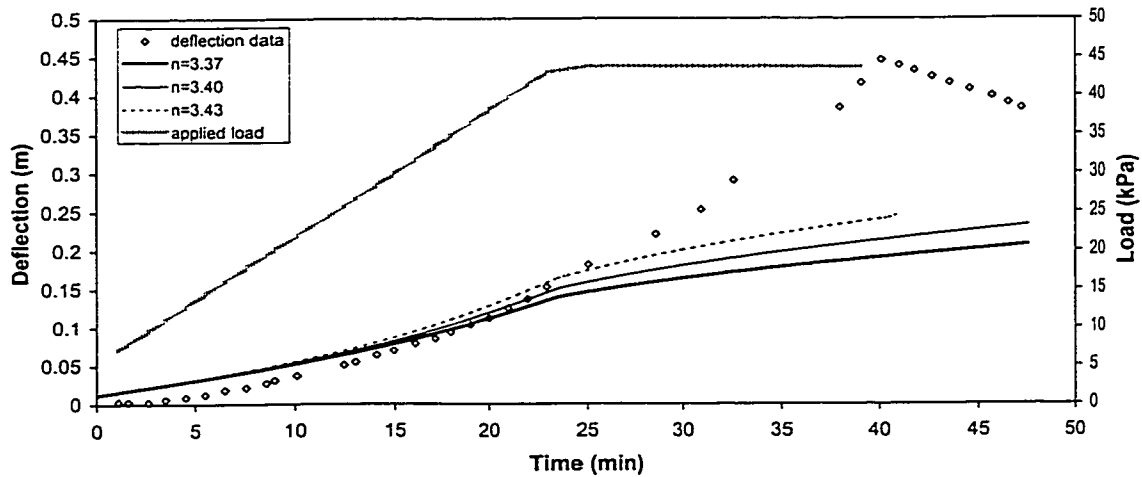
Figure 6-13(c): Range for creep exponent, n (Test C20: $\eta = 2.0e\text{-}25$, $E = 1.00e9$).

138
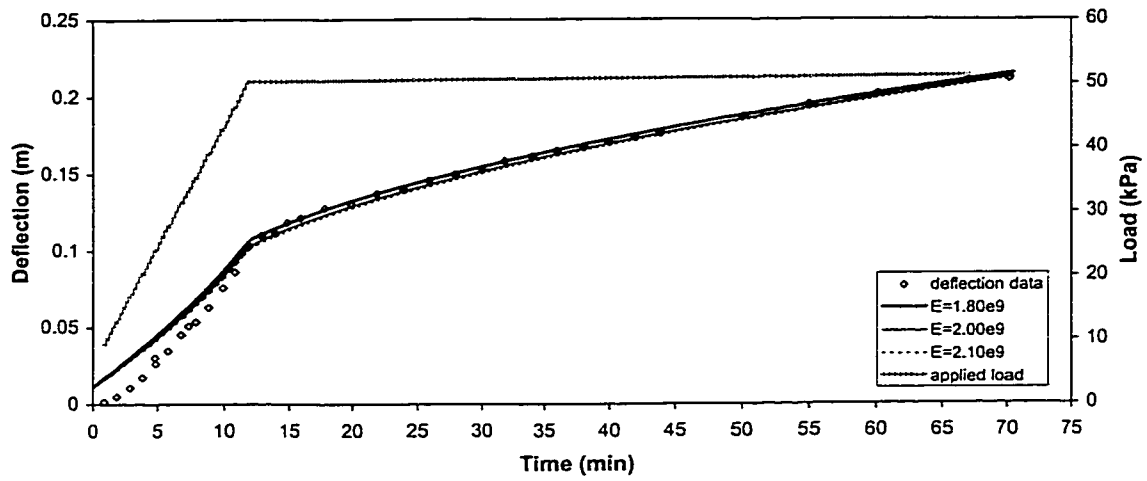
Figure 6-14(a): Range for Young's modulus, E (Test C21: n = 3.25, η = 2.0e-25).
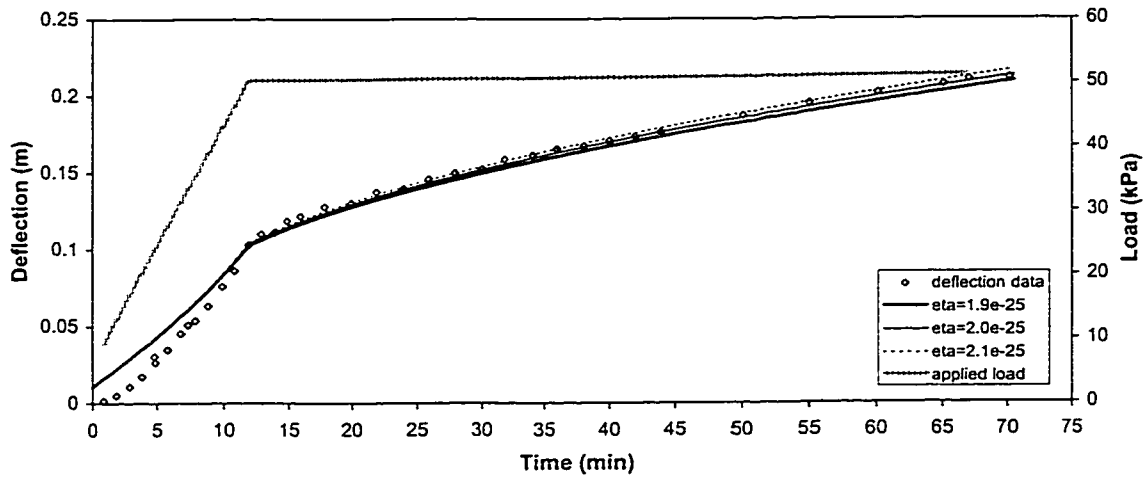
Figure 6-14(b): Range for creep coefficient, η (Test C21: n = 3.25, E = 2.00e9).
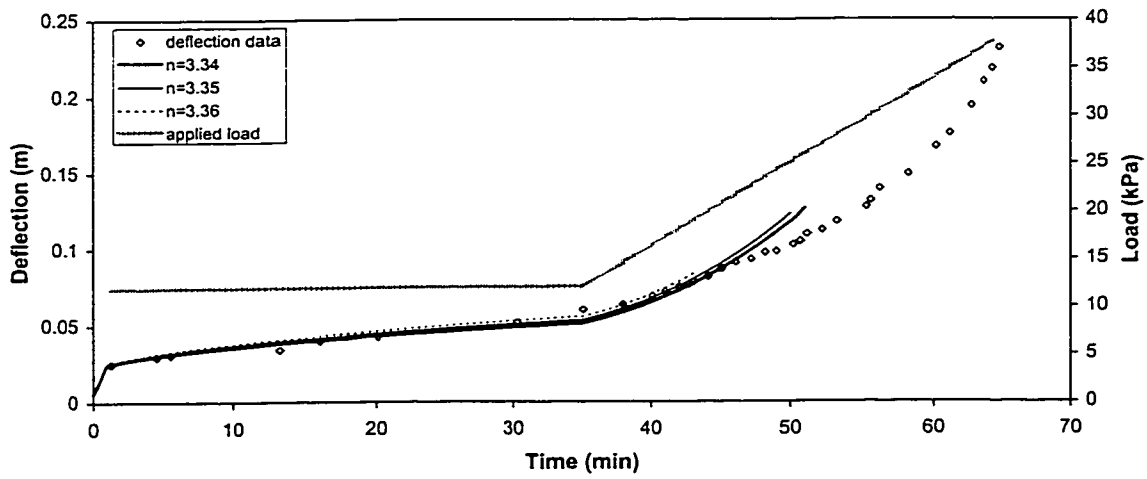

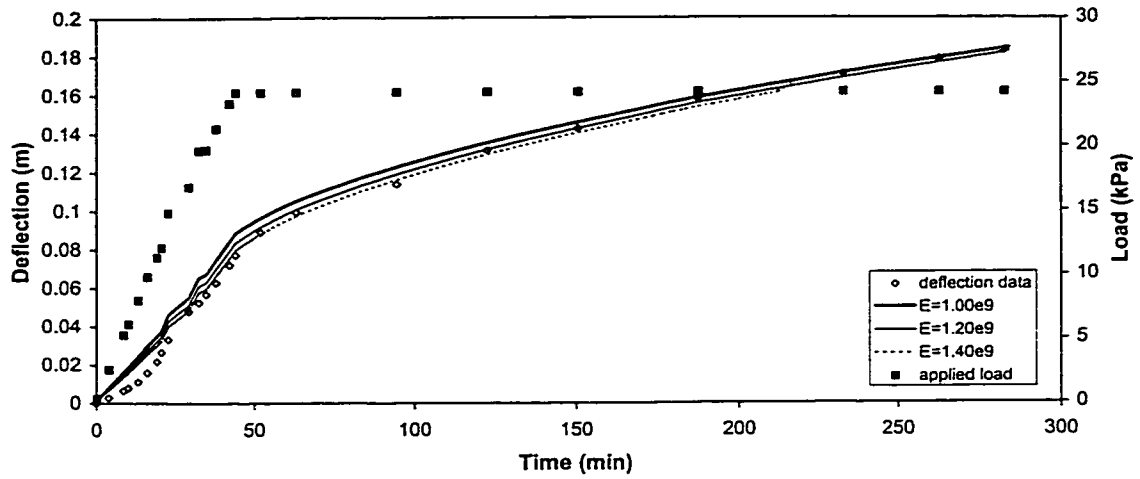Figure 6-14(c): Range for creep exponent, n (Test C21: η = 2.0e-25, E = 2.00e9).

Figure 6-15(a): Range for Young's modulus, E (Test C22: n = 3.38, η = 1.8e-25).

Figure 6-15(b): Range for creep coefficient, η (Test C22: n = 3.38, E = 0.60e9).

Figure 6-15(c): Range for creep exponent, n (Test C22: η = 1.8e-25, E = 0.60e9).

140

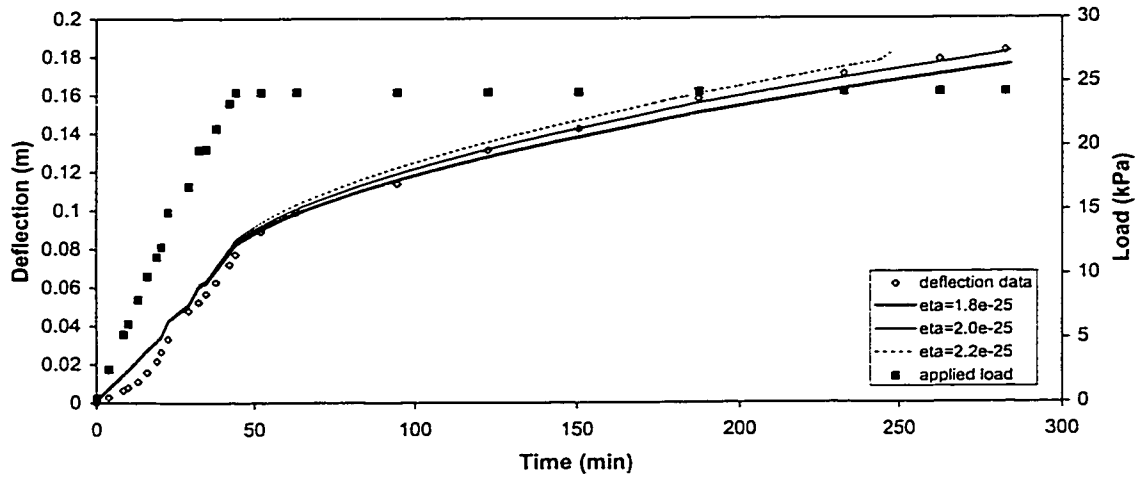Figure 6-16(a): Range for Young's modulus, E (Test C03: $n = 3.28$, $\eta = 2.0e\text{-}25$).

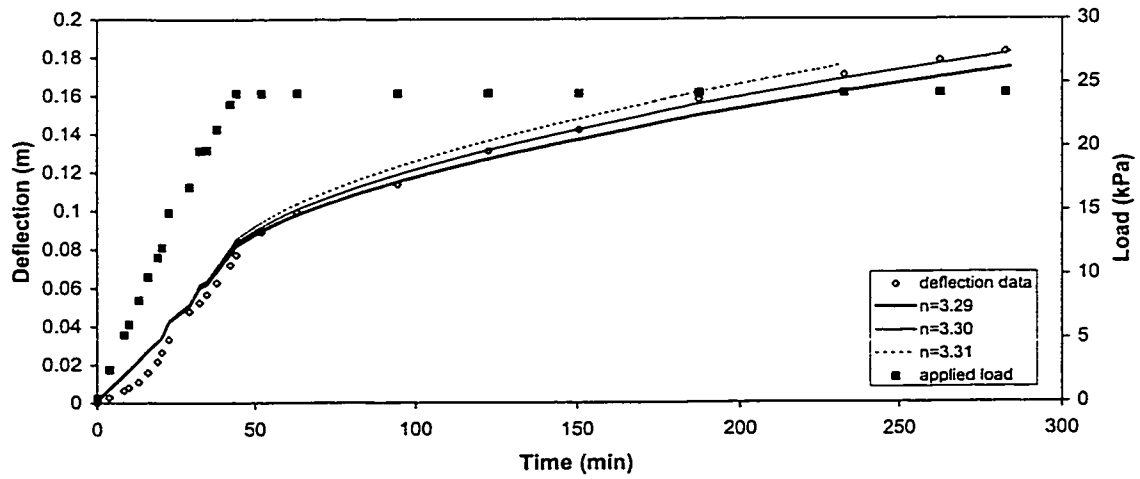Figure 6-16(b): Range for creep coefficient, η (Test C03: $n = 3.28$, $E = 3.50e9$).

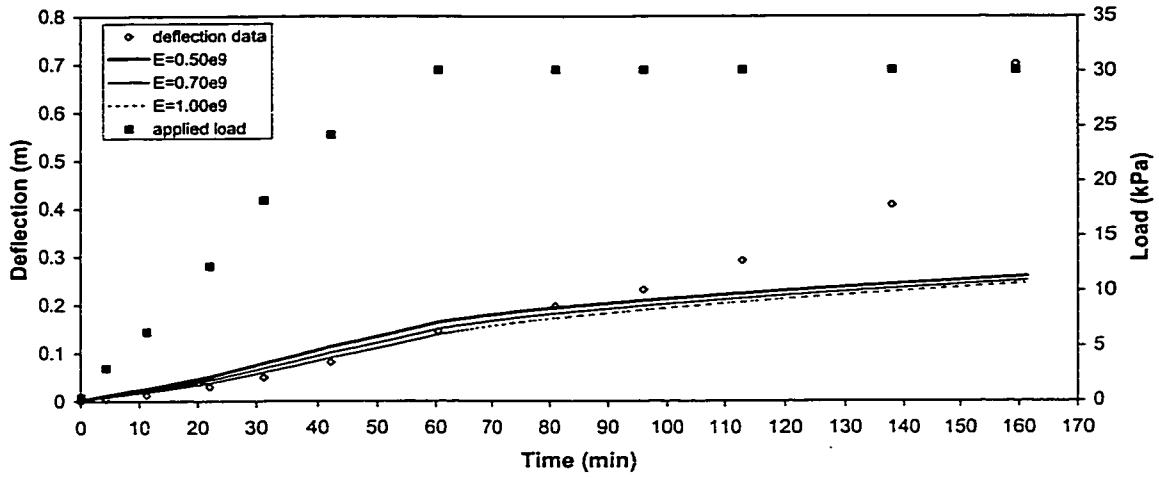Figure 6-16(c): Range for creep exponent, n (Test C03: $\eta = 2.0e\text{-}25$, $E = 3.50e9$).

141
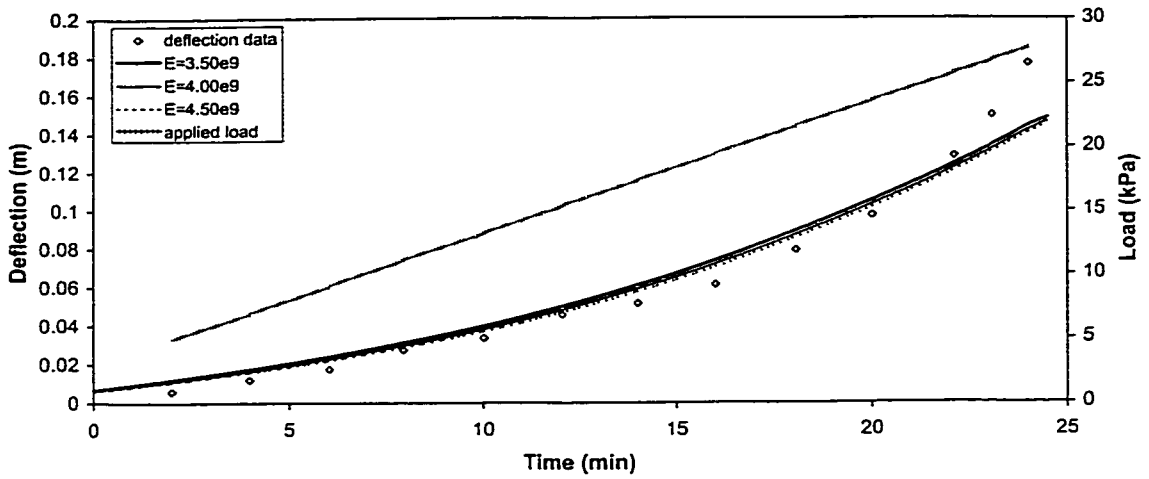
Figure 6-17(a): Range for Young's modulus, E (Test C10: $n = 3.25$, $\eta = 2.0e\text{-}25$).

Figure 6-17(b): Range for creep coefficient, η (Test C10: $n = 3.25$, $E = 4.00e9$).

Figure 6-17(c): Range for creep exponent, n (Test C10: $\eta = 2.0e\text{-}25$, $E = 4.00e9$).

142

Figure 6-18(a): Range for Young's modulus, E (Test C16: $n = 3.15$, $\eta = 2.0e\text{-}25$).
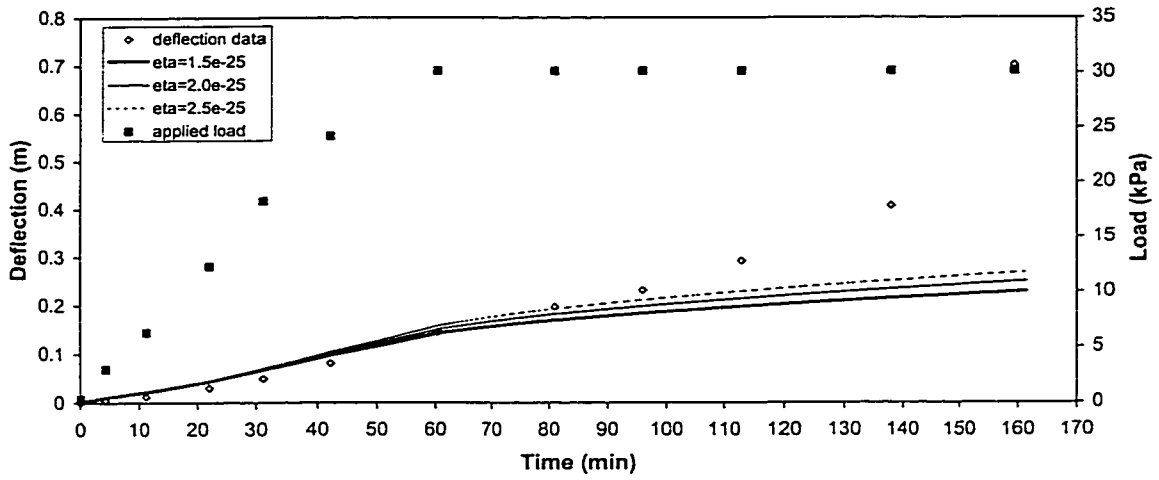

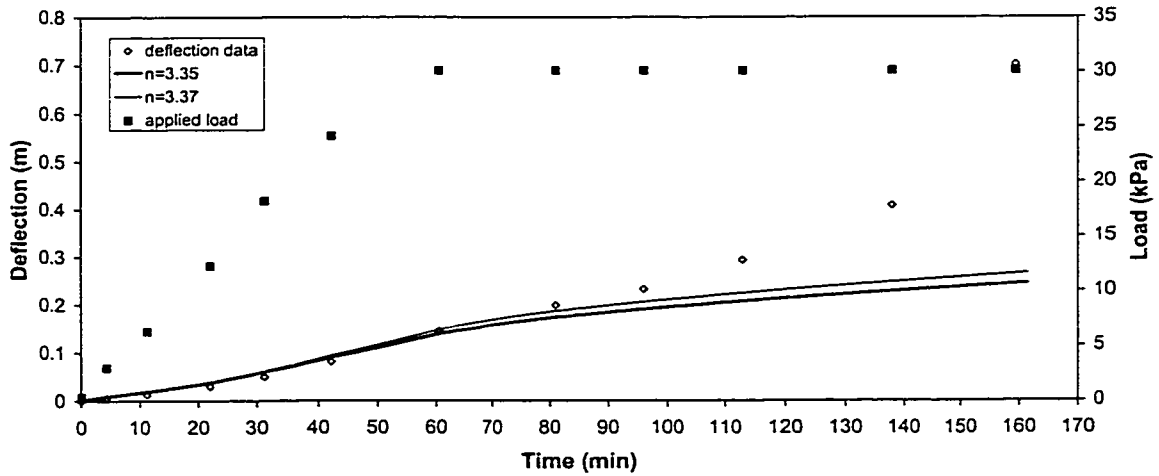Figure 6-18(b): Range for creep coefficient, η (Test C16: $n = 3.15$, $E = 4.00e9$).

Figure 6-18(c): Range for creep exponent, n (Test C16: $\eta = 2.0e\text{-}25$, $E = 4.00e9$).

Figure 6-19(a): Range for Young's modulus, E (Test C13: n = 3.08, η = 2.0e-25).

Figure 6-19(b): Range for creep coefficient, η (Test C13: n = 3.08, E = 1.50e9).

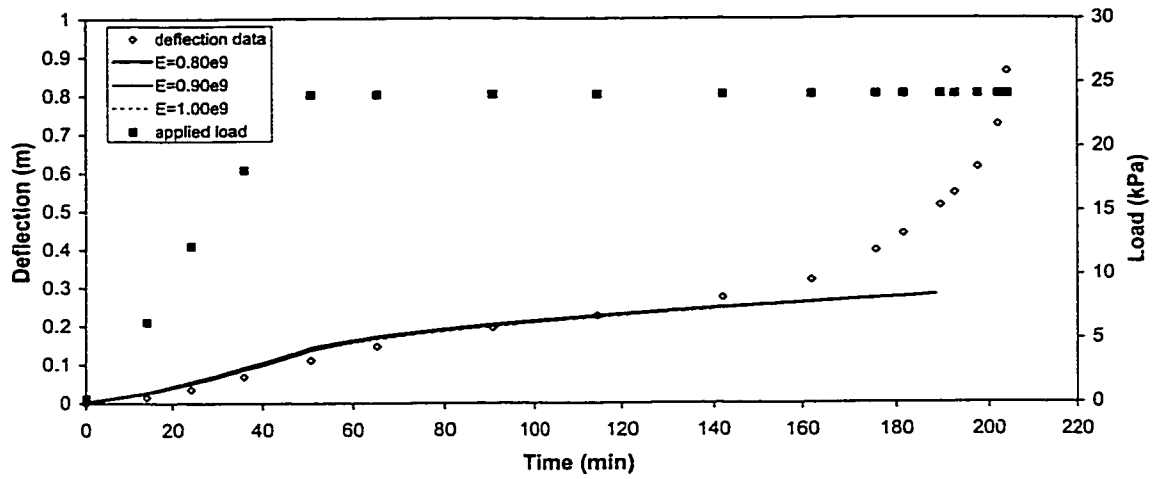Figure 6-19(c): Range for creep exponent, n (Test C13: η = 2.0e-25, E = 1.50e9).

144
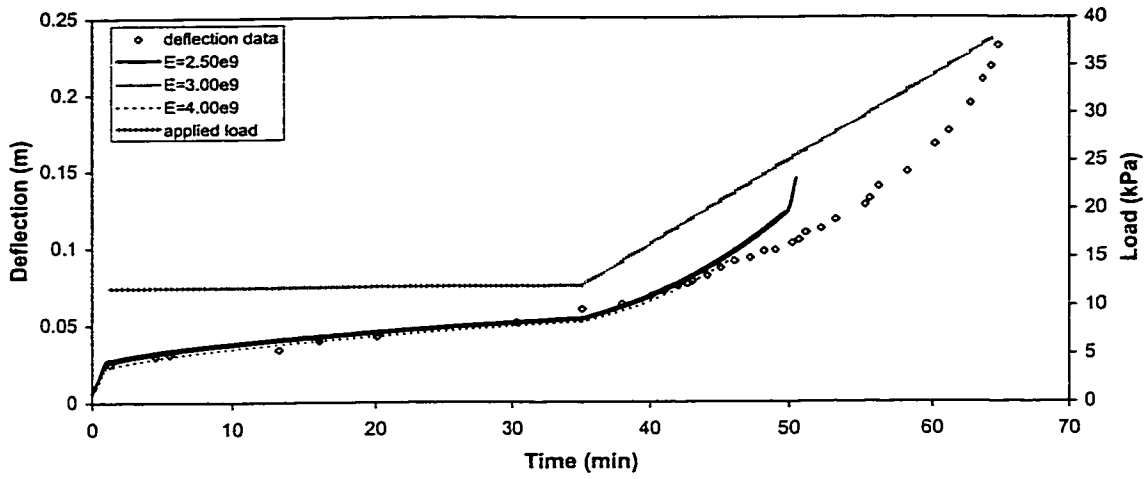
Figure 6-20(a): Range for Young's modulus, E (Test C12: $n = 3.35$, $\eta = 2.0e\text{-}25$).
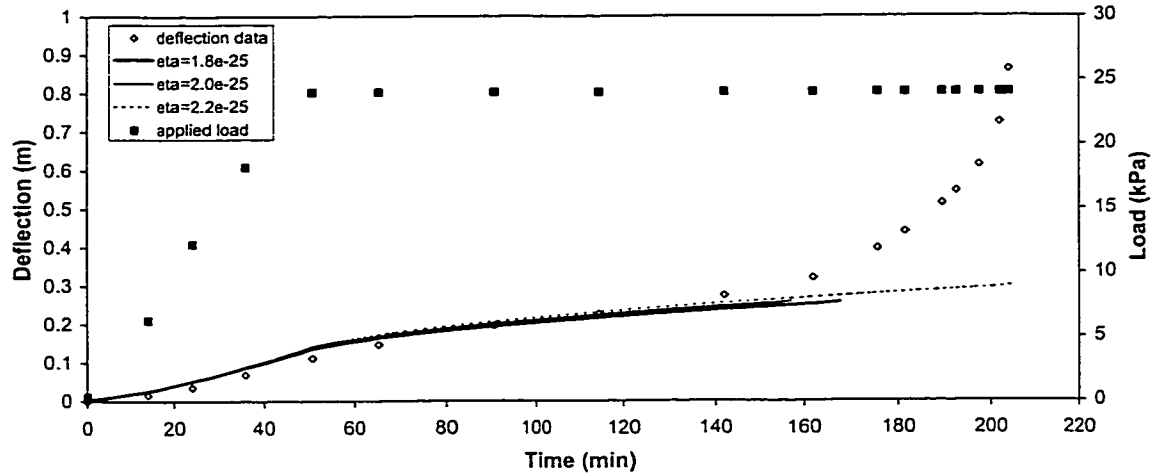

Figure 6-20(b): Range for creep coefficient, η (Test C12: $n = 3.35$, $E = 3.00e9$).

Figure 6-20(c): Range for creep exponent, n (Test C12: $\eta = 2.0e\text{-}25$, $E = 3.00e9$).

145

Figure 6-21(a): Range for Young's modulus, E (Test F05: n = 3.30, η = 2.0e-25).

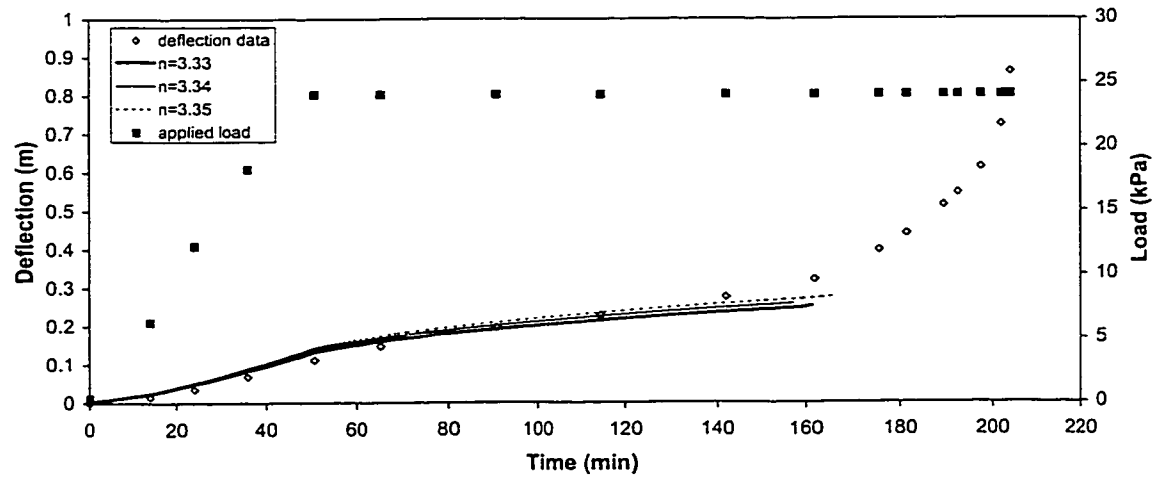Figure 6-21(b): Range for creep coefficient, η (Test F05: n = 3.30, E = 1.20e9).

Figure 6-21(c): Range for creep exponent, n (Test F05: η = 2.0e-25, E = 1.20e9).

146

Figure 6-22(a): Range for Young's modulus, E (Test F06: n = 3.35, η = 2.0e-25).

Figure 6-22(b): Range for creep coefficient, η (Test F06: n = 3.35, E = 0.70e9).

Figure 6-22(c): Range for creep exponent, n (Test F06: η = 2.0e-25, E = 1.00e9).

147

Figure 6-23(a): Range for Young's modulus, E (Test F07: n = 3.34, η = 2.0e-25).

Figure 6-23(b): Range for creep coefficient, η (Test F07: n = 3.34, E = 0.90e9).

Figure 6-23(c): Range for creep exponent, n (Test F07: η = 2.0e-25, E = 0.90e9).

148
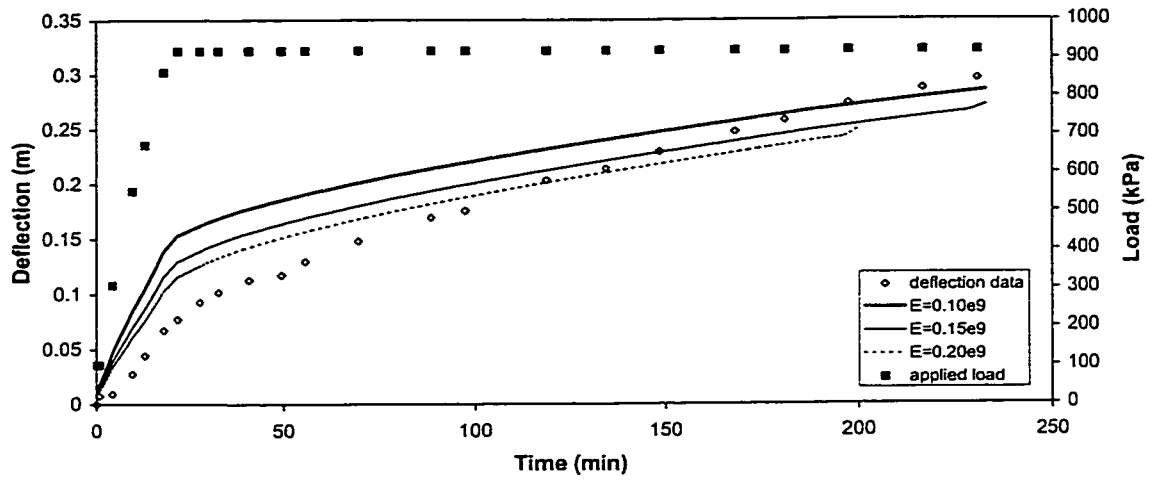
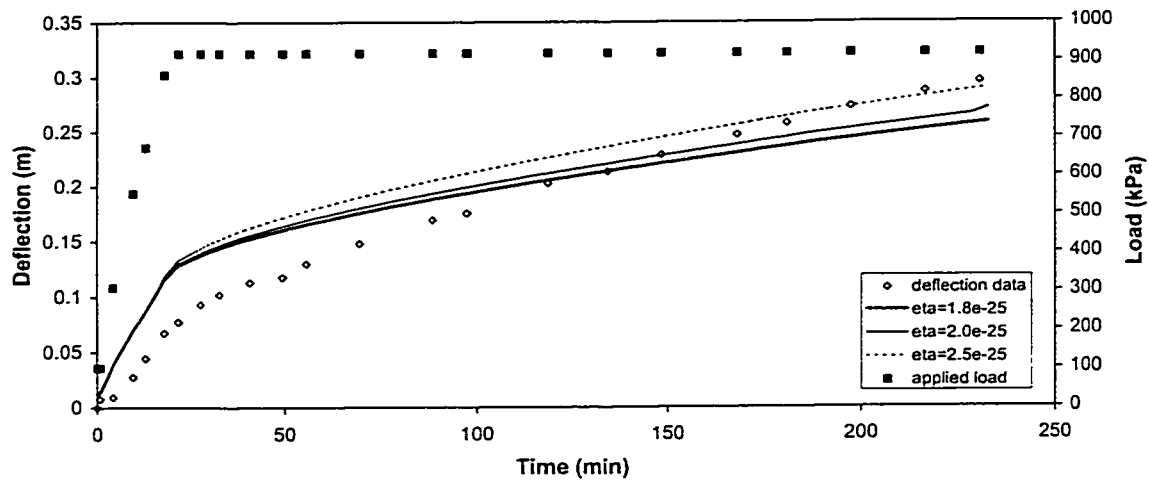Figure 6-24(a): Range for Young's modulus, E (Test F08: n = 3.48, η = 2.0e-25).

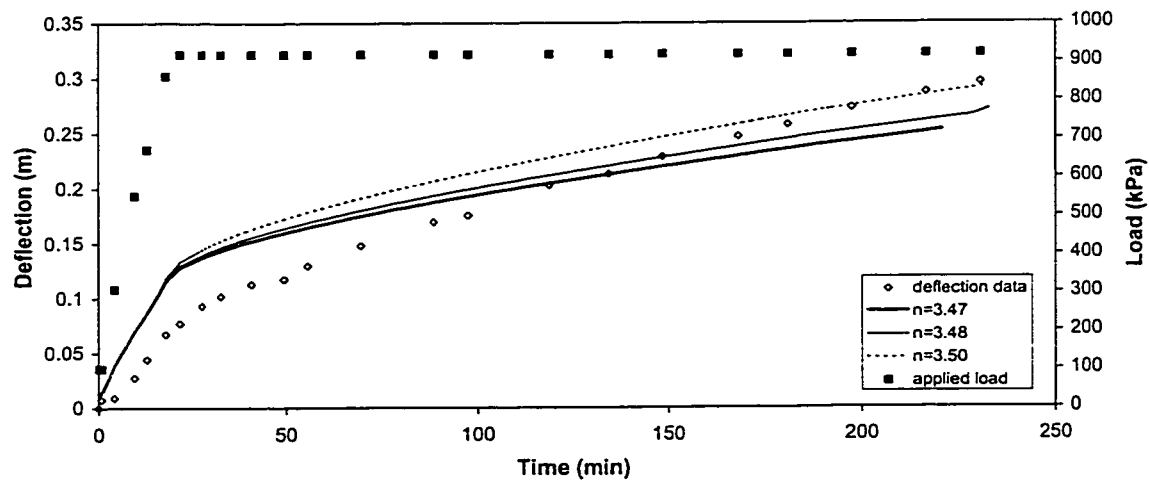Figure 6-24(b): Range for creep coefficient, η (Test F08: n = 3.48, E = 0.15e9).

Figure 6-24(c): Range for creep exponent, n (Test F08: η = 2.0e-25, E = 0.15e9).
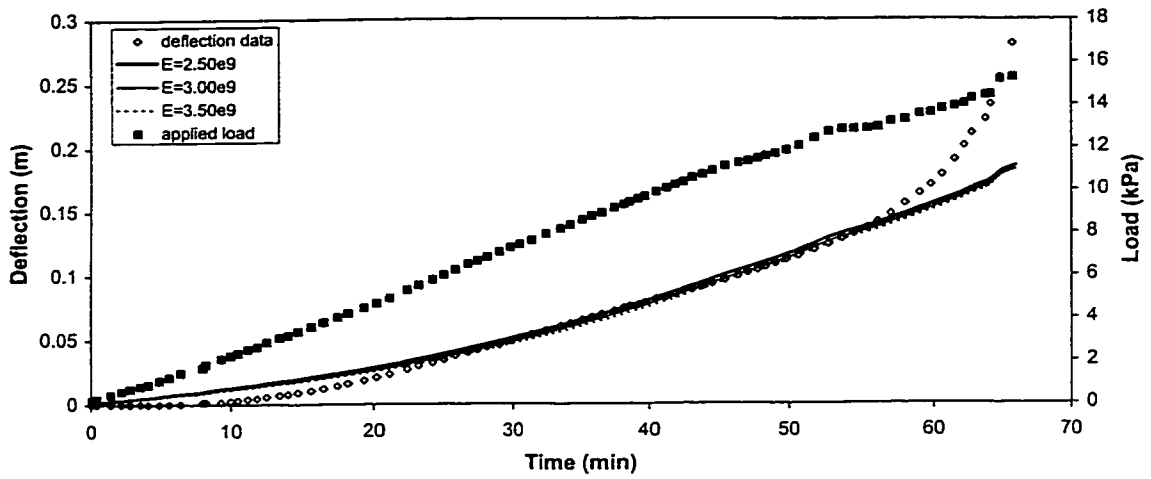
149

Figure 6-25(a): Range for Young's modulus, E (Test F01: n = 3.26, η = 2.0e-25).
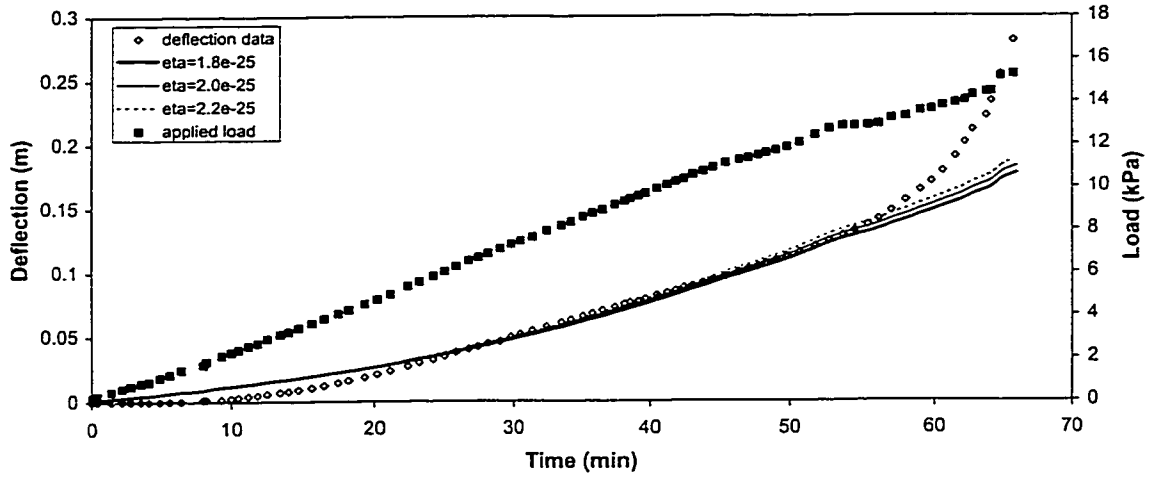

Figure 6-25(b): Range for creep coefficient, η (Test F01: n = 3.26, E = 3.00e9).

Figure 6-25(c): Range for creep exponent, n (Test F01: η = 2.0e-25, E = 3.00e9).

Figure 6-26(a): Range for Young's modulus, E (Test F02: n = 3.23, η = 2.0e-25).

Figure 6-26(b): Range for creep coefficient, η (Test F02: n = 3.23, E = 1.50e9).

Figure 6-26(c): Range for creep exponent, n (Test F02: η = 2.0e-25, E = 1.50e9).

151

Figure 6-27(a): Range for Young's modulus, E (Test F03: n = 3.26, η = 2.0e-25).

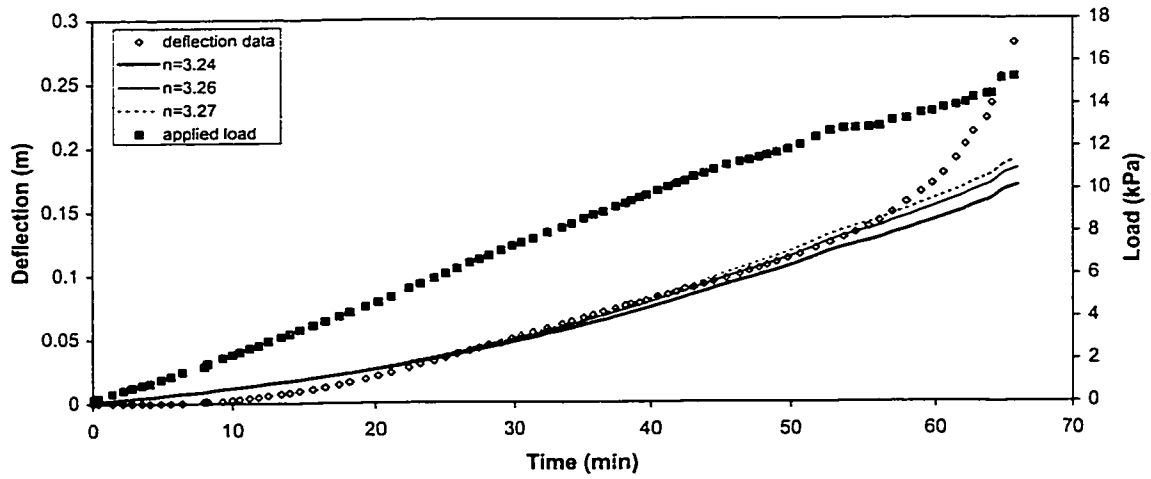Figure 6-27(b): Range for creep coefficient, η (Test F03: n = 3.26, E = 3.00e9).

Figure 6-27(c): Range for creep exponent, n (Test F03: η = 2.0e-25, E = 3.00e9).
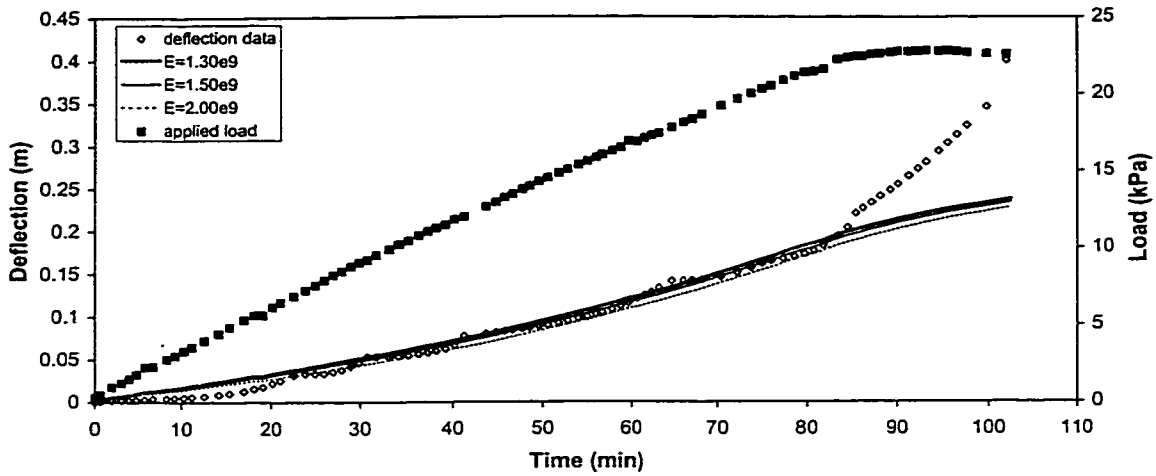
Figure 6-28(a): Range for Young's modulus, E (Test F04: n = 3.25, η = 2.0e-25).

Figure 6-28(b): Range for creep coefficient, η (Test F04: n = 3.25, E = 2.00e9).

Figure 6-28(c): Range for creep exponent, n (Test F04: η = 2.0e-25, E = 2.00e9).
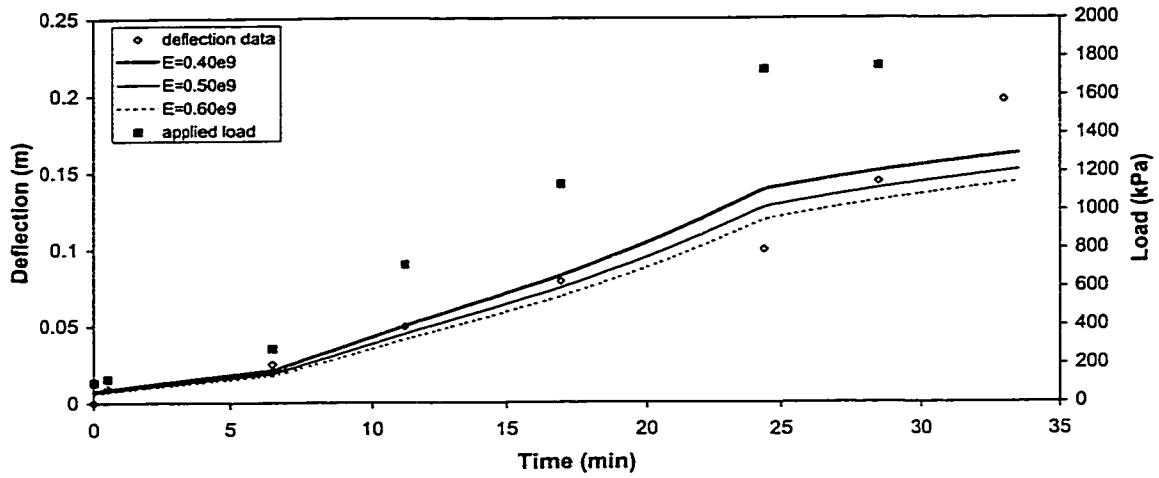
Figure 6-29(a): Range for Young's modulus, E (Test F09: n = 3.35, η = 2.0e-25).
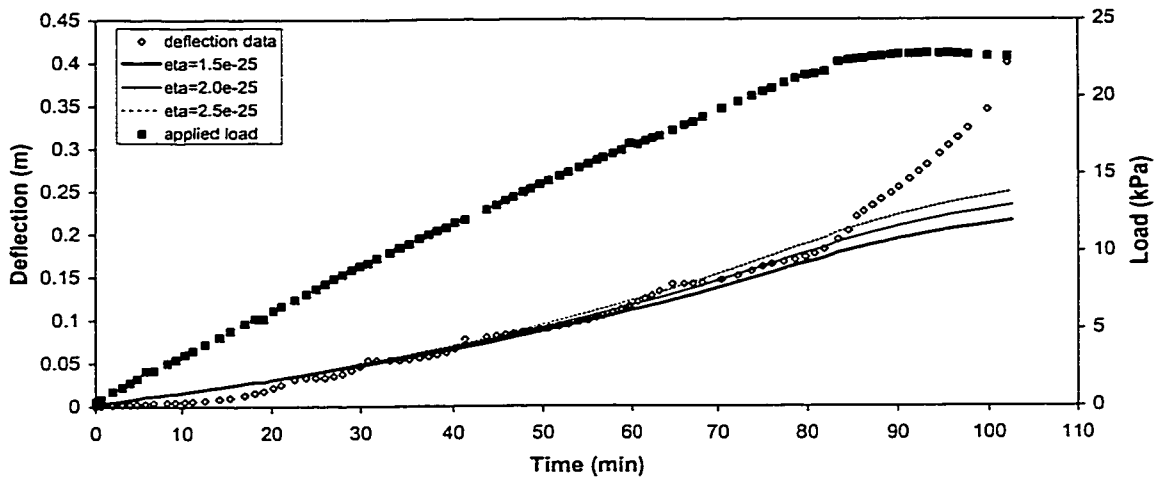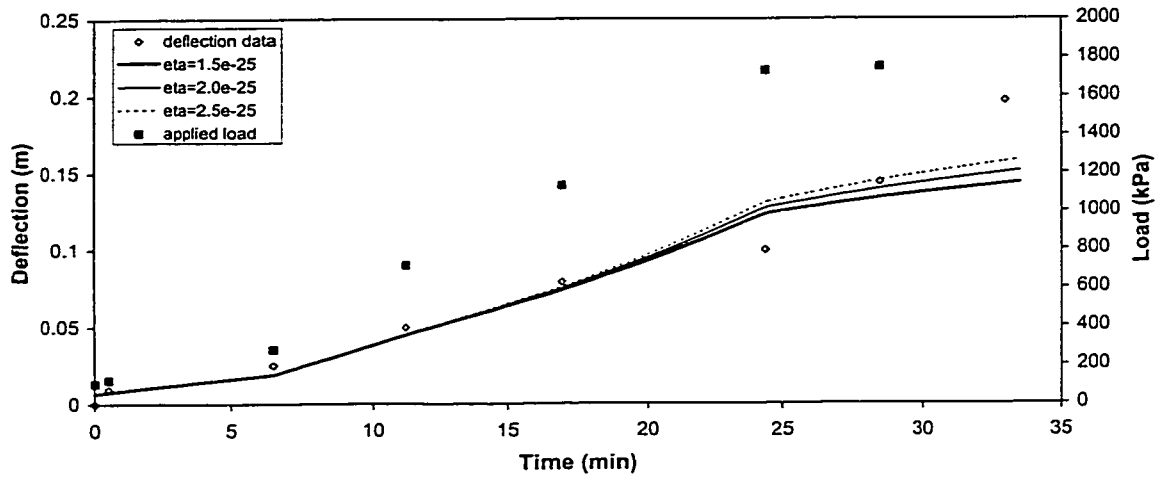

Figure 6-29(b): Range for creep coefficient, η (Test F09: n = 3.35, E = 0.50e9).
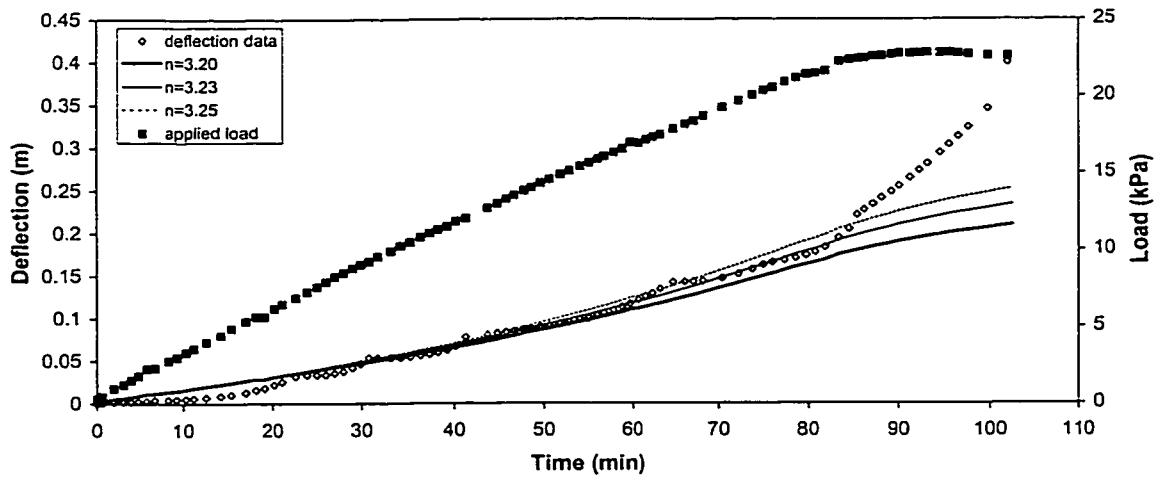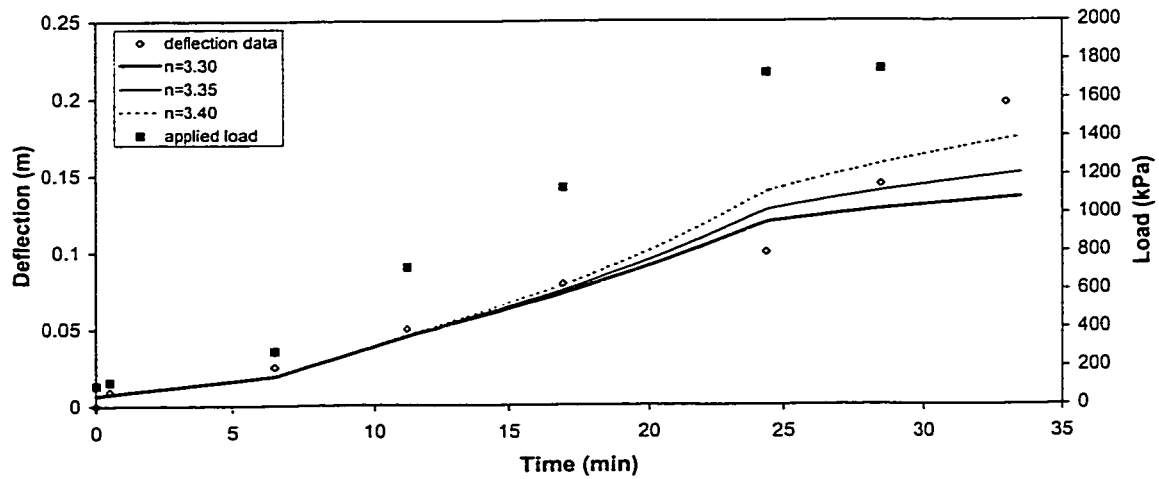

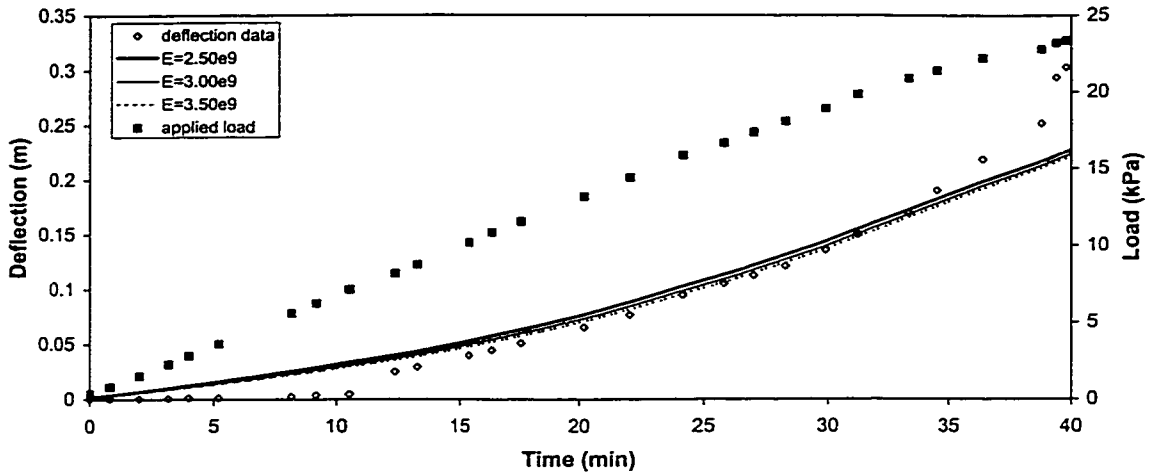Figure 6-29(c): Range for creep exponent, n (Test F09: η = 2.0e-25, E = 0.50e9).

154
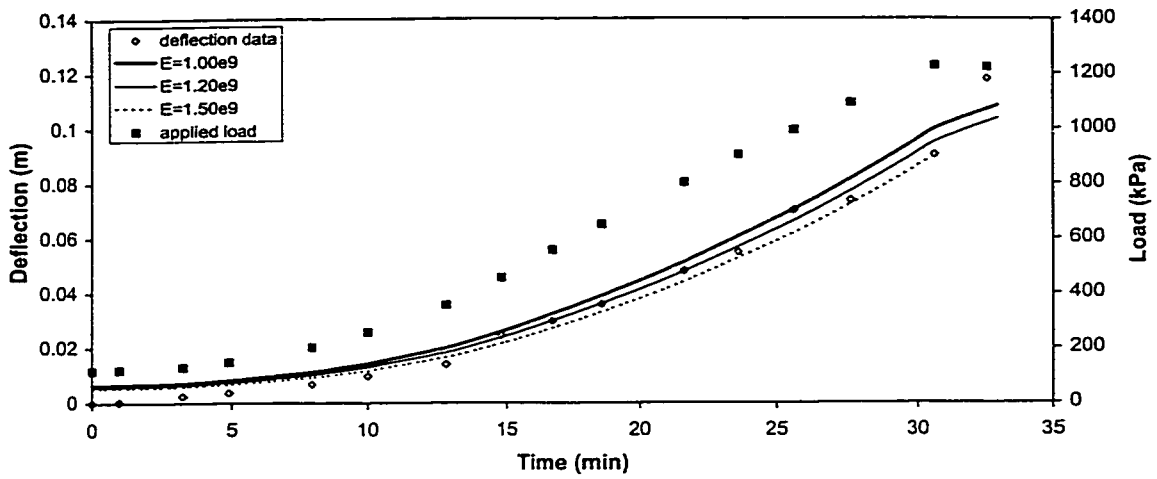
Figure 6-30(a): Range for Young's modulus, E (Test F10: n = 3.40, η = 2.0e-25).
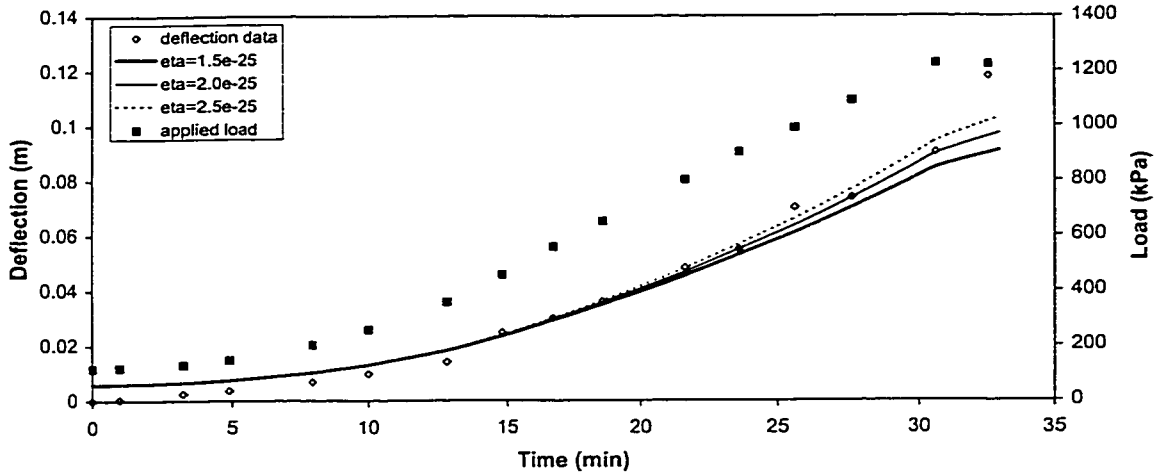
Figure 6-30(b): Range for creep coefficient, η (Test F10: n = 3.38, E = 1.20e9).
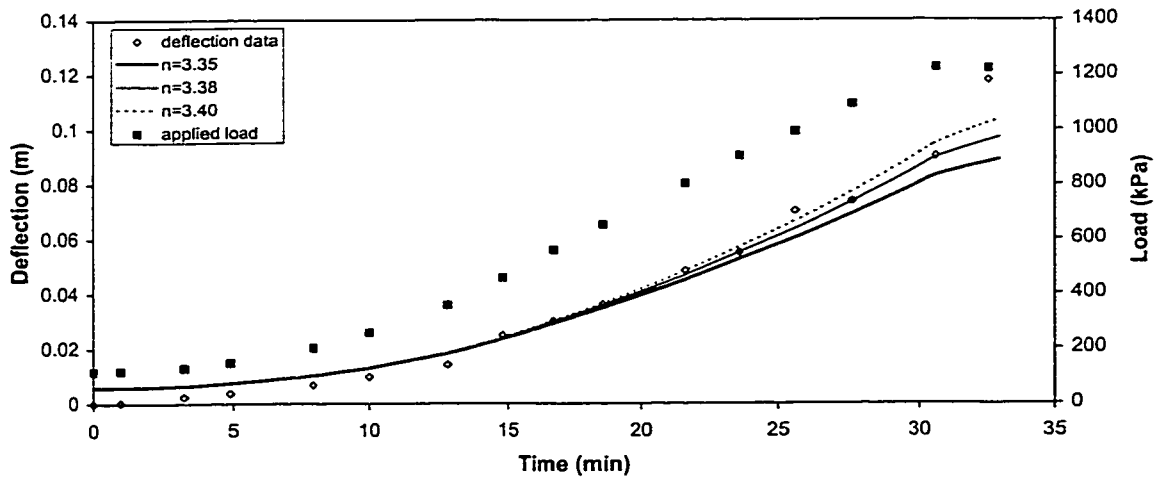
Figure 6-30(c): Range for creep exponent, n (Test F10: η = 2.0e-25, E = 1.20e9).
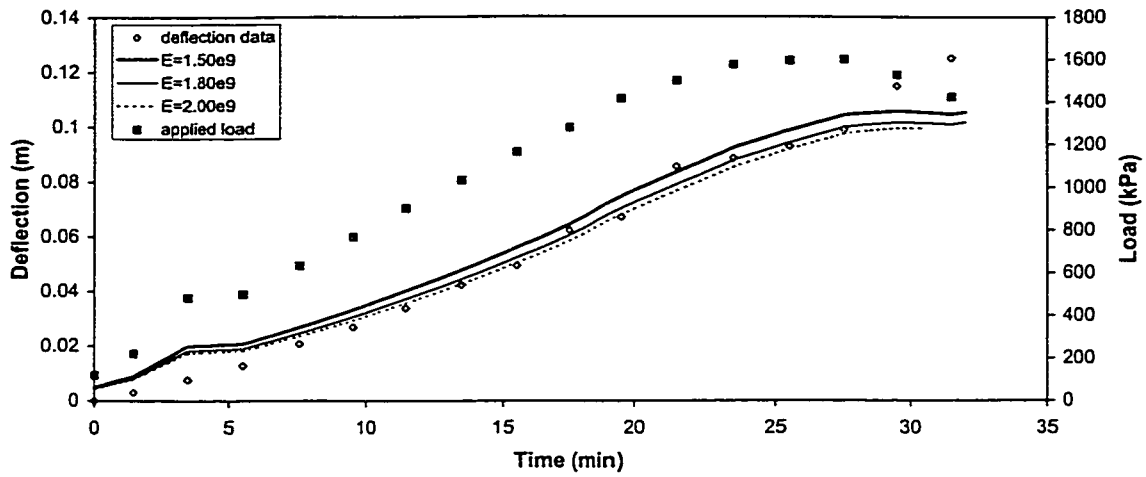
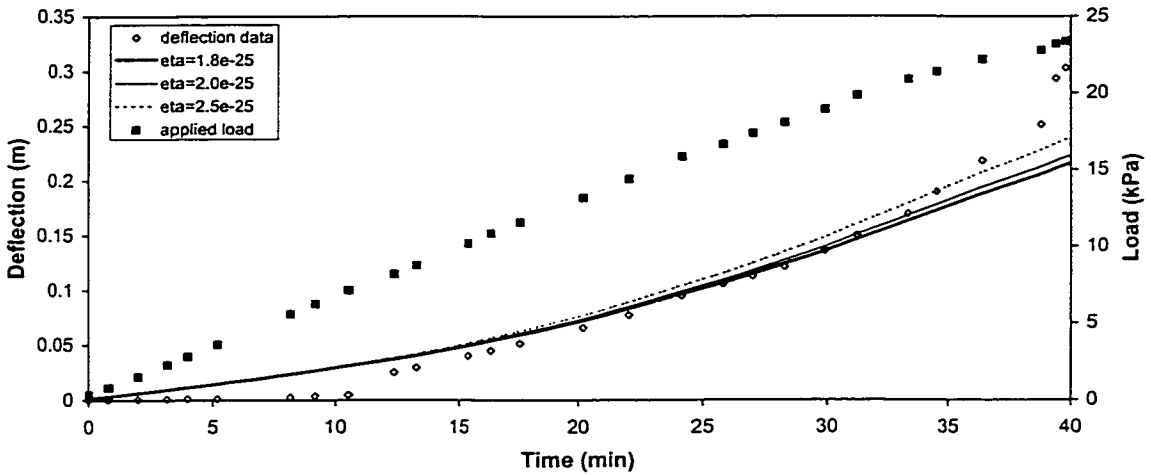Figure 6-31(a): Range for Young's modulus, E (Test F11: n = 3.32, η = 2.0e-25).
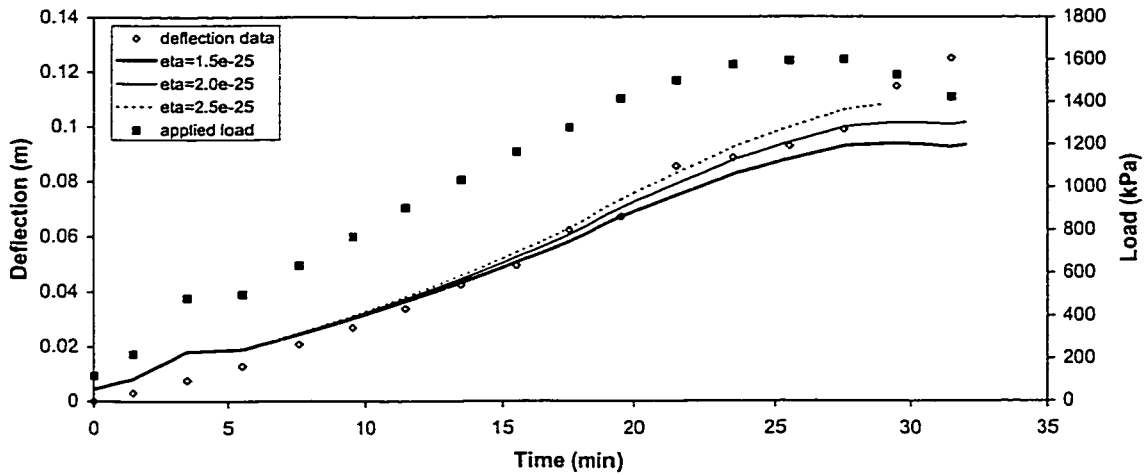
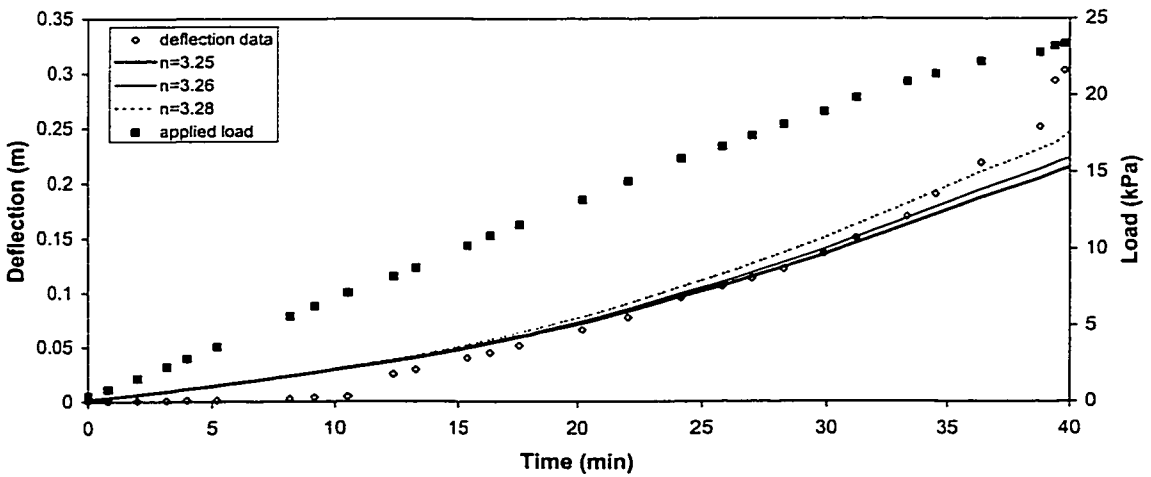Figure 6-31(b): Range for creep coefficient, η (Test F11: n = 3.32, E = 1.80e9).
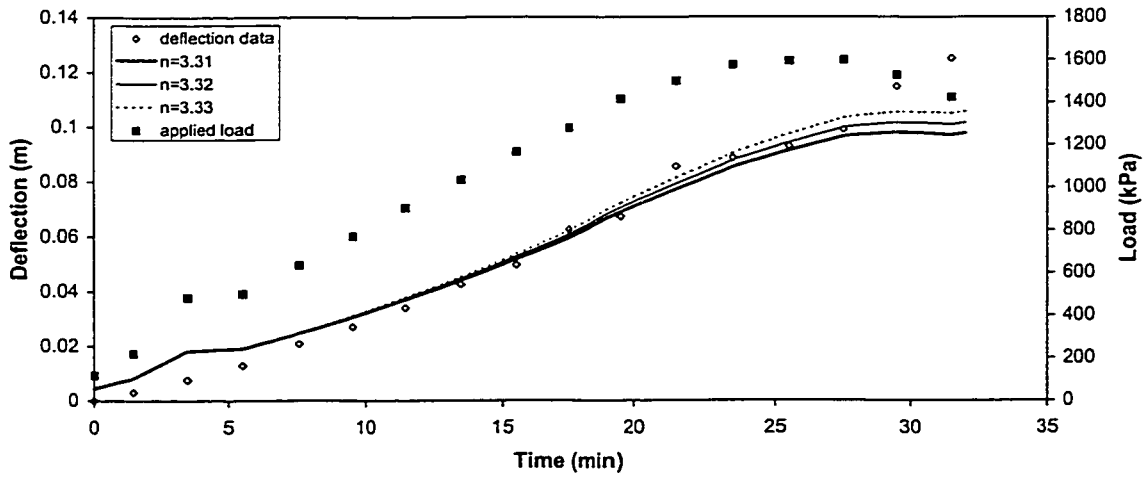
Figure 6-31(c): Range for creep exponent, n (Test F11: η = 2.0e-25, E = 1.80e9).

156
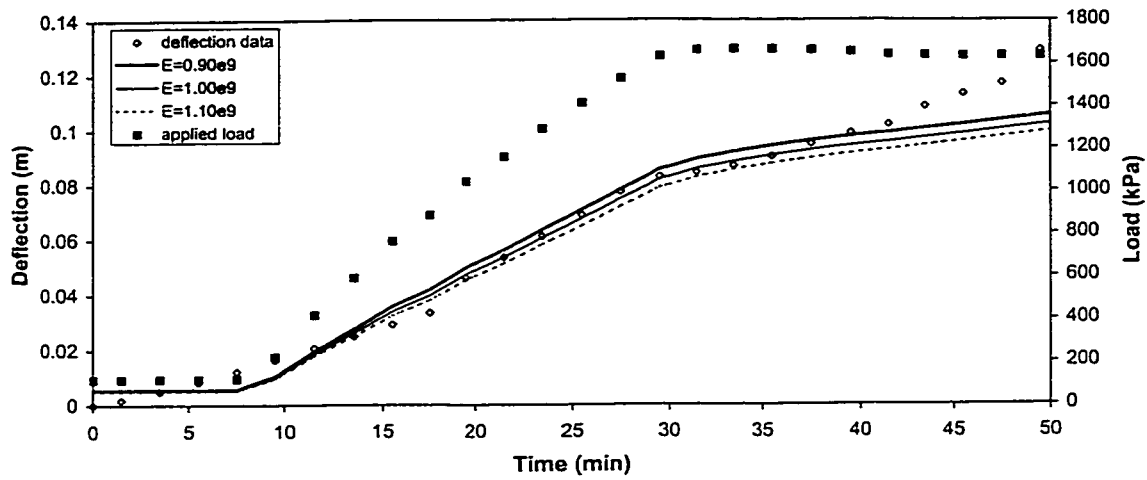
Figure 6-32(a): Range for Young's modulus, E (Test F12: n = 3.26, η = 2.0e-25).
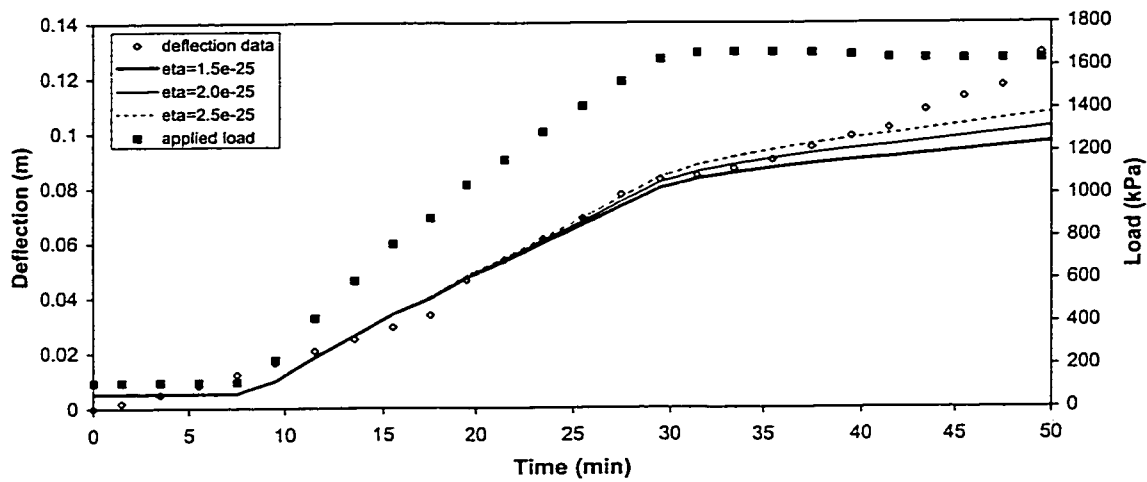
Figure 6-32(b): Range for creep coefficient, η (Test F12: n = 3.26, E = 1.00e9).
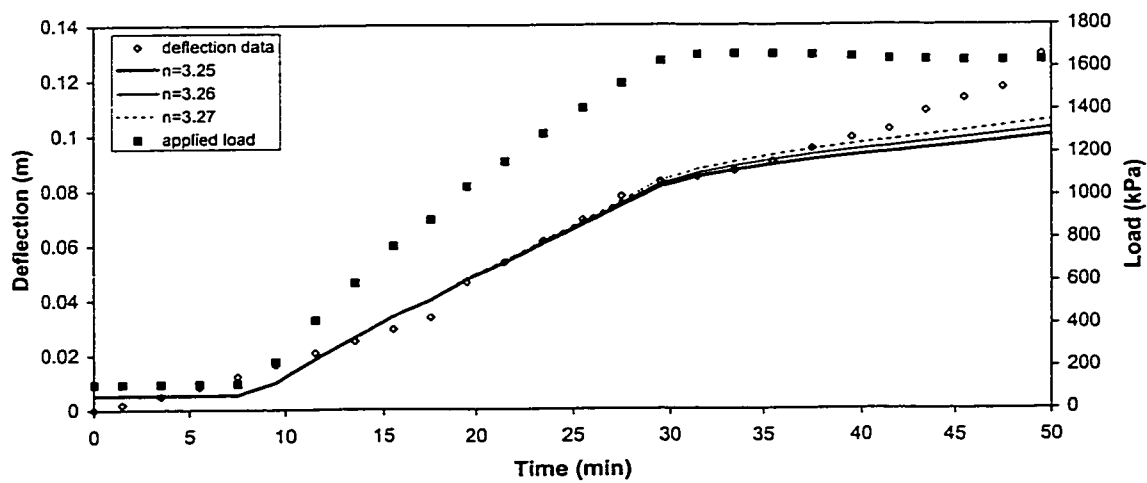
Figure 6-32(c): Range for creep exponent, n (Test F12: η = 2.0e-25, E = 1.00e9).
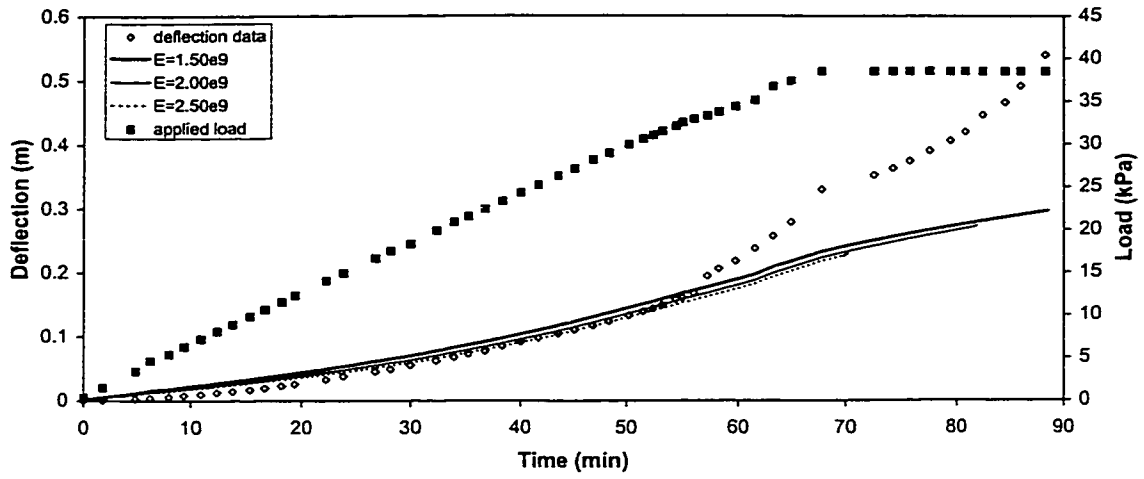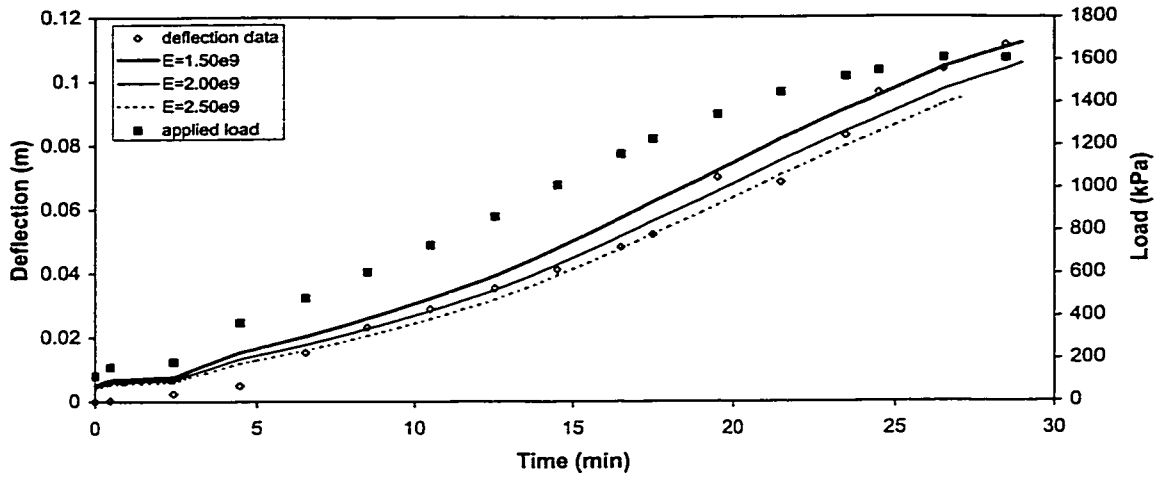
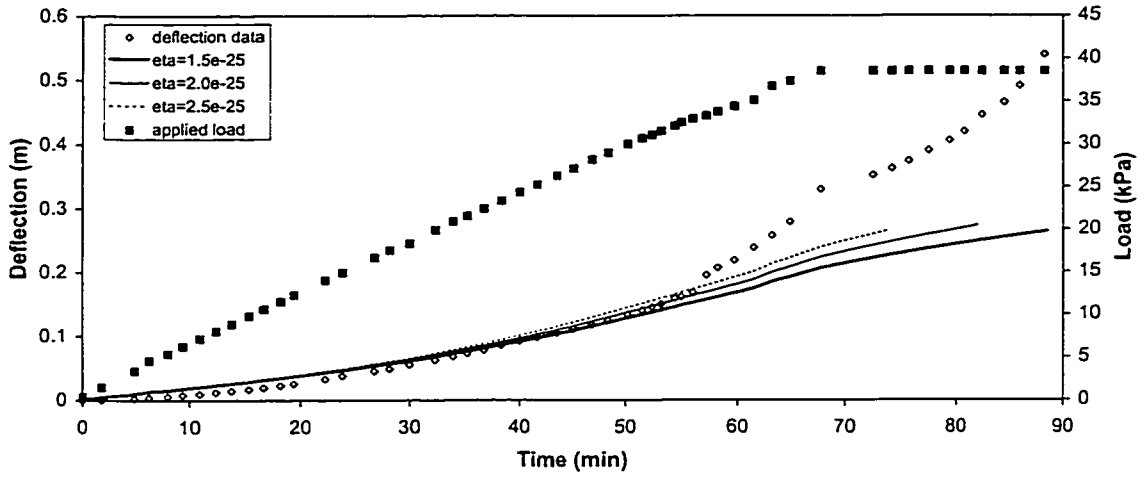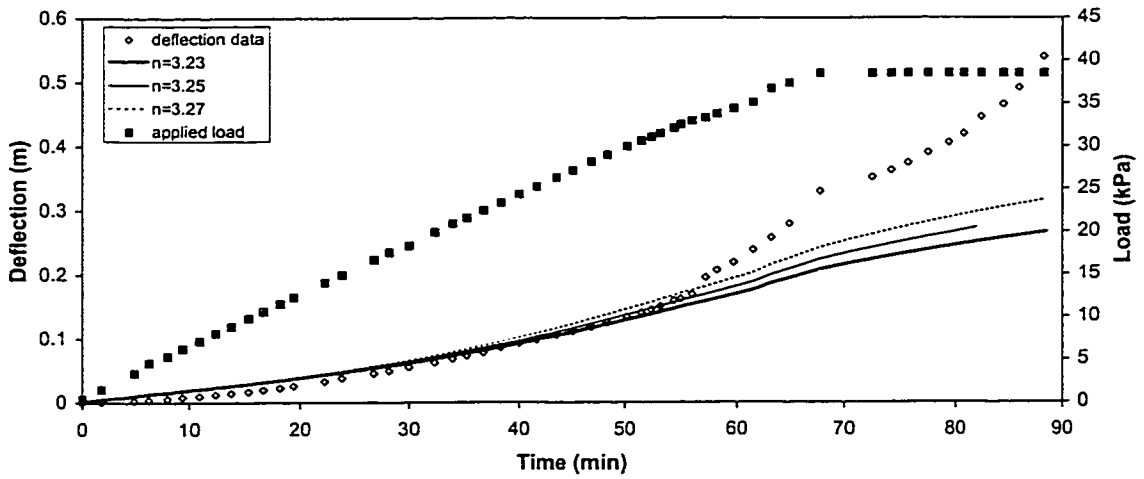Figure 6-33(a): Range for Young's modulus, E (Test F13: $n = 3.33$, $\eta = 2.0e\text{-}25$).
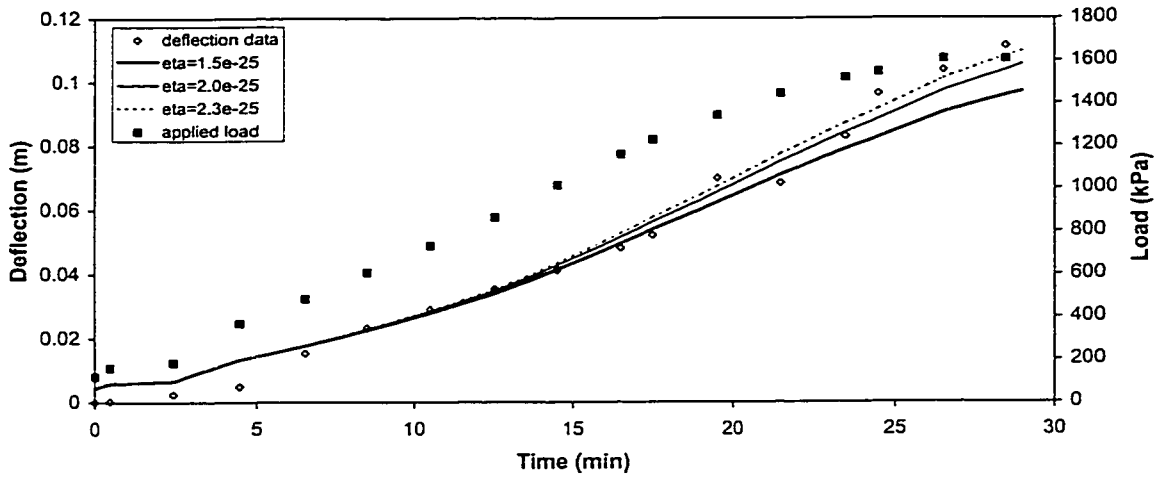
Figure 6-33(b): Range for creep coefficient, η (Test F13: $n = 3.33$, $E = 2.00e9$).
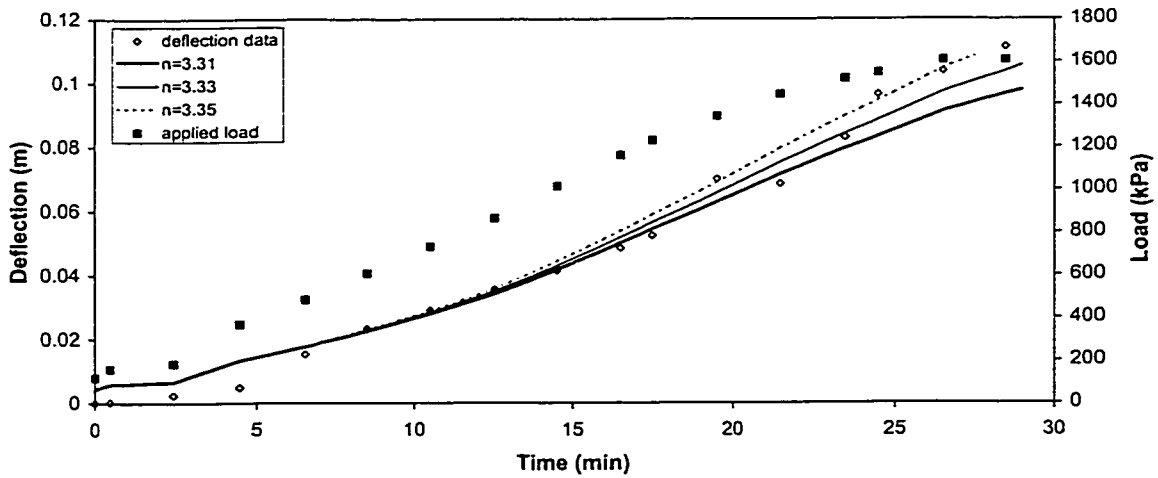
Figure 6-33(c): Range for creep exponent, n (Test F13: $\eta = 2.0e\text{-}25$, $E = 2.00e9$).

158
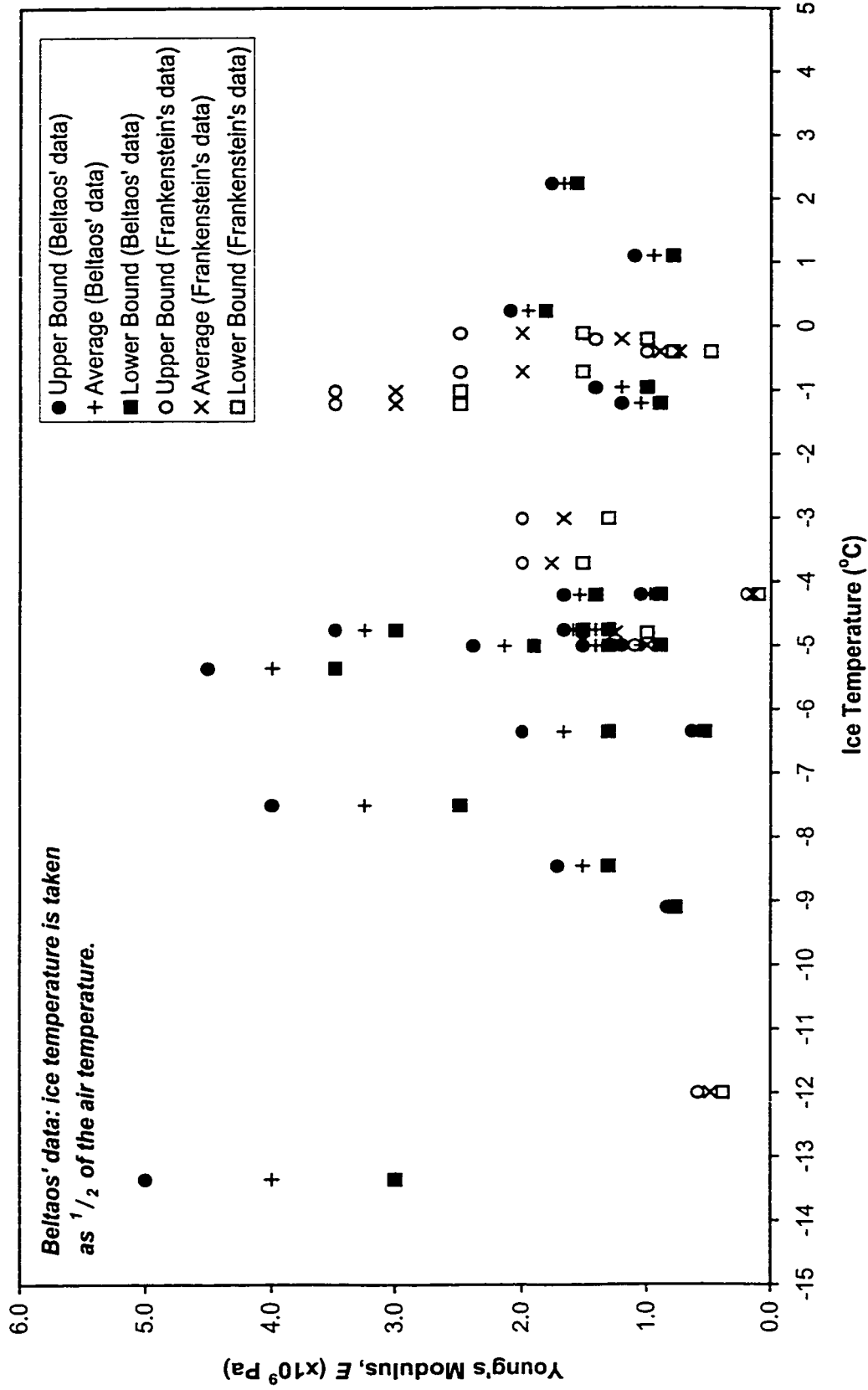
Figure 6-34: Variation of Young's modulus with temperature.
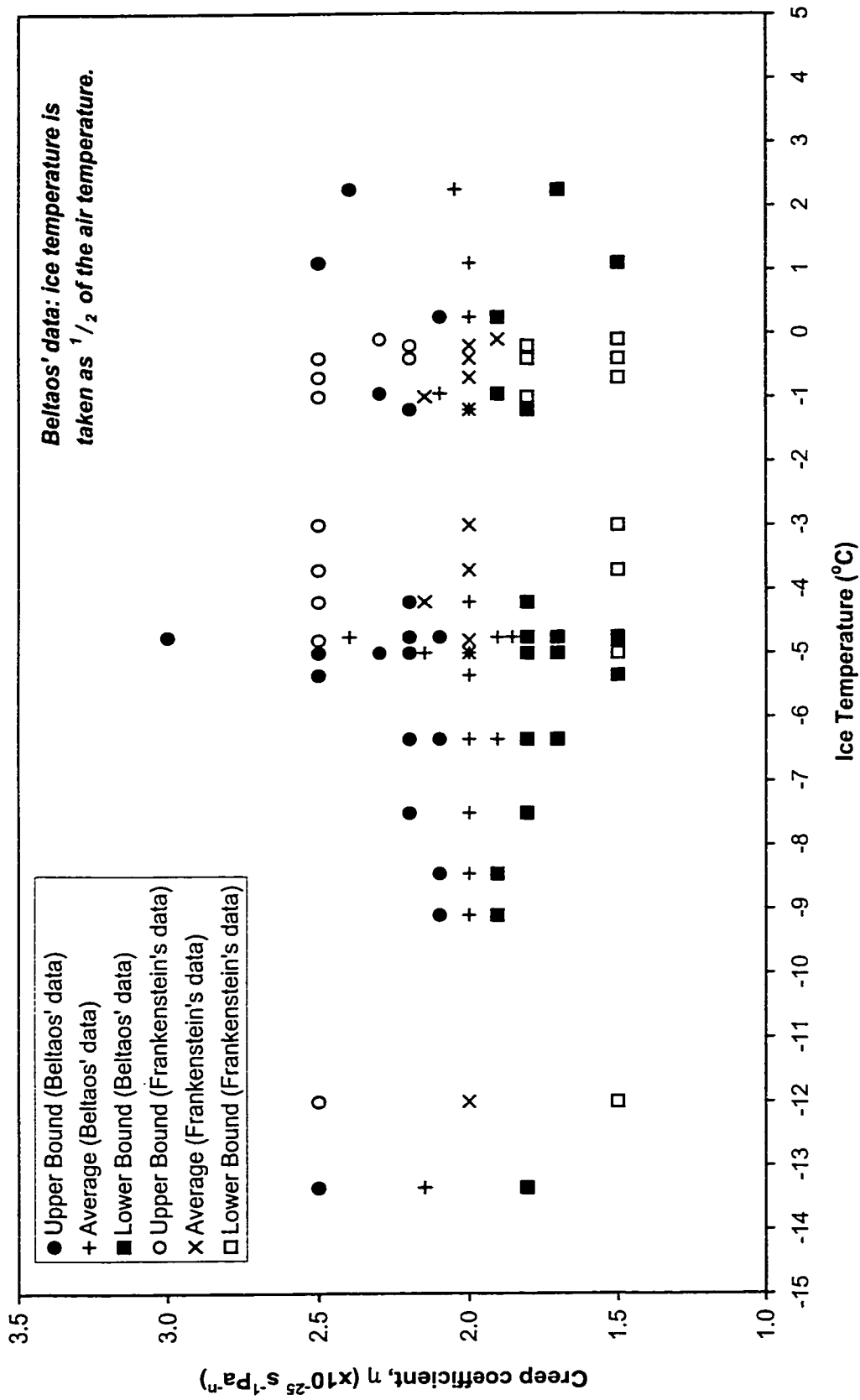
Figure 6-35: Variation of creep coefficient with ice temperature.

160
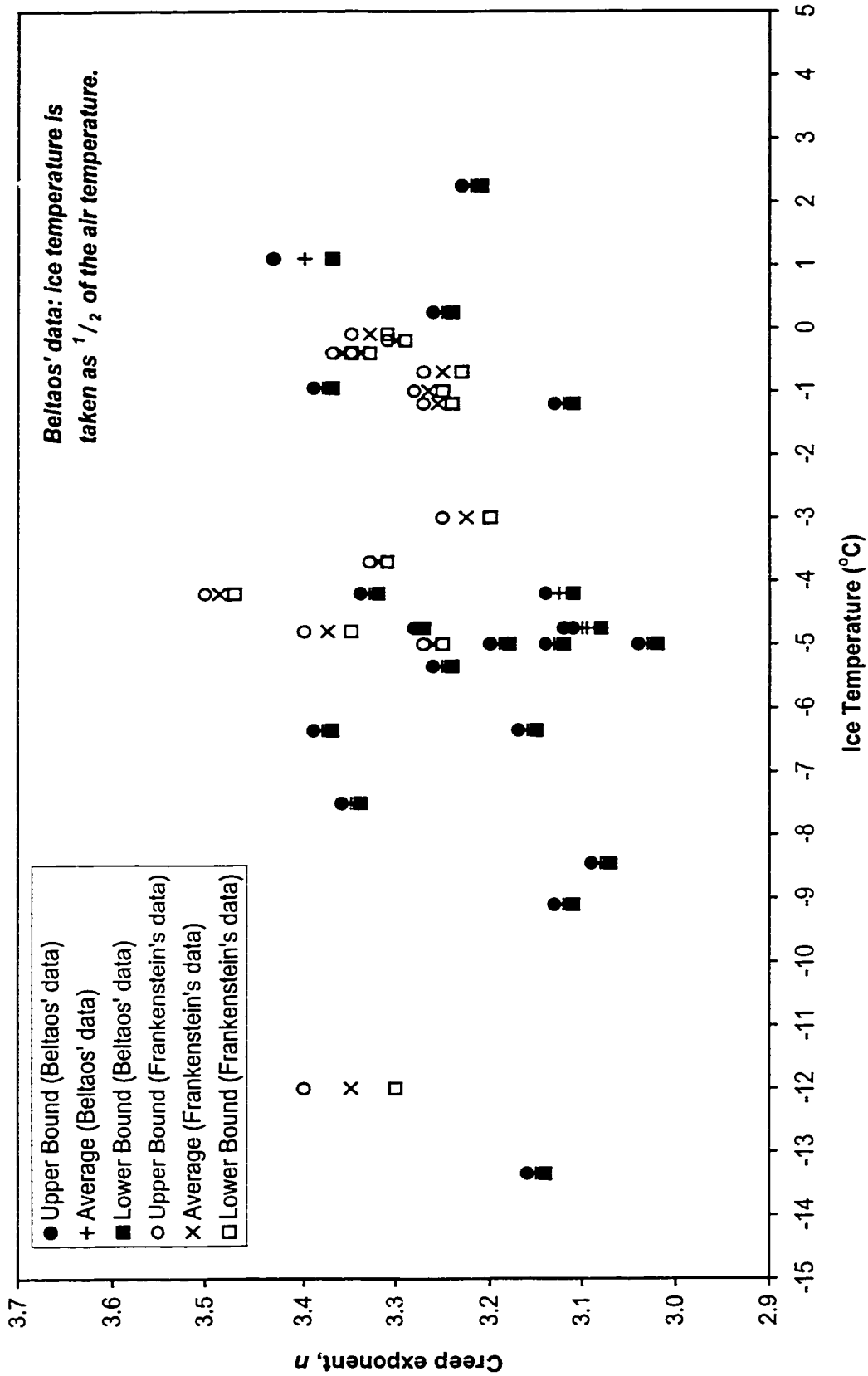
Figure 6-36: Variation of creep exponent with ice temperature.

7.0 CONCLUSION

7.1 Summary and Conclusions

The ability to predict the response of an ice sheet to long term loading is important in many situations. Ice sheets have been used as construction platforms, drilling rig platforms, airfields, parking lots, and festival platforms. Numerical models can be used to predict the deflection of an ice sheet over time, essentially allowing the load to be removed prior to the ultimate failure of the ice.

In this thesis a brief description of the behaviour of ice under both short and long term loading was given. Under short term loading ice behaves elastically, and any deflection resulting from the load is recovered upon removal of the load. Under long term loading permanent deformation (creep) occurs, caused by the movement of imperfections in the crystal structure. A typical creep curve for polycrystalline ice was described, differentiating between the three stages of creep: primary (transient), secondary (steady state) and tertiary (accelerating). Various short term failure criteria for ice were discussed, and the strain energy criterion was presented as a failure criterion for the long term loading of ice. Physical properties of ice, including Young's modulus, Poisson's ratio, ice grain size and ice density were discussed and some typical values found in the literature were presented. Ice crystallography was briefly discussed, and some photographs of thin sections of lake and river ice were shown.

A review of several previous model studies performed relating to the creep of ice was presented. Most of these studies involved modelling data obtained from small scale laboratory experiments conducted at various temperatures with various applied stresses. A power law relationship was used to model the creep behaviour of ice, with the creep

162

exponents ranging from about 1.8 to 3.64. The creep coefficient was given as a function of temperature or time in several instances; in other cases, the coefficient reported ranged from about 3.9×10^{-40} to 1.3×10^{-19} (when stresses were measured in Pascals and strains were measured in seconds^{-1}).

A rheological model for ice was described and a two dimensional, axisymmetric finite element model was developed to examine the time dependent deflection of a floating ice cover under a distributed load. Several assumptions were made during the model development: the ice sheet was homogeneous and transversely isotropic; the ice sheet was infinite in extent; and the unit weight of water was 9,806 N/m^3. The derivation of the finite element equations was presented, and brief discussions on the Theorem of Minimum Potential Energy and the Rayleigh-Ritz method were included. Equations, which could be evaluated in closed form, were derived for the stiffness matrices and mechanical load vector. A power law type of relationship was used to predict the creep strain rate. The effects of creep were incorporated into the system of equations by means of an additional creep load vector. In order to evaluate the creep load vector, creep strain increments could be estimated using either the Euler or the 4th Order Runge-Kutta method. The 4th Order Runge-Kutta method was used for all cases considered here because it is more numerically stable, and a larger time step increment can be used than with the Euler method. The creep load vector was evaluated numerically, using Gaussian quadrature. A penalty method was used to impose the boundary conditions on the system of equations, with the penalty being set equal to 10^5 times the largest value in the global stiffness matrix, based on a sensitivity analysis.

The elastic solution of the model was verified using existing analytical solutions (from technical literature), and the creep calculations were checked against simple analytical solutions that have been derived and presented here. The effects of changes in spatial and temporal discretization on the results from the model were examined for both concentrated (radius of load ≤ 0.3 m) and distributed (radius of load > 0.3 m) loading cases. For concentrated loading cases, it was found that using 33 elements (of varying size) over a 50 m extent gave acceptable accuracy for the deflection of the ice cover over time; for distributed loading cases, 20 elements gave acceptable accuracy. Changing the number of integration points within each element also had an effect on accuracy. Using 5 integration points in the radial direction and 10 in the vertical direction (for each element) was found to produce results that were identical to using 10 points in each direction (the maximum possible for this model, and therefore the most accurate). The time step increments (Δt) were chosen by comparing the solution using each Δt to an "exact" solution (using a very small Δt). The time step increments chosen were 30 s, 120 s and 240 s (or a combination), depending on the total duration of the test.

The model was applied to 33 sets of long term load test data from large scale field experiments performed on lake, bay, and reservoir ice. Three parameters were calibrated for each test: Young's modulus, E; the creep exponent, n; and the creep coefficient, η. The model results were found to be relatively insensitive to changes in Poisson's ratio (ν), therefore ν was kept constant at $1/3$ (a typical value for ice).

The model predicted the deflection of an infinite ice sheet under constant loading and under increasing loading very well, as verified by numerous tests. In several of these tests, Young's modulus appeared to be changing as the test progressed; different values

of E were needed to match the predicted model deflection to the measured data at different times. For the step function type of loading the model results were quite accurate for the first half of the test, but less accuracy was obtained near the end of the test. This was determined not to be a result of the size of the time step increment used. In the one case of constant loading followed by increasing loading, the predicted deflection during constant loading was quite good, but the model solution became unstable during the increasing loading phase.

The values obtained for the creep exponent, n, in all of the cases examined here ranged between 3.02 and 3.50, with an average of $n = 3.25$. These results are more consistent (the range of exponents is significantly smaller) than the results found from earlier researchers, as discussed in chapter 3, which varied from about 1.8 to 3.64. The creep coefficient, η, consistently ranged from about 1.5×10^{-25} to 2.5×10^{-25} $s^{-1}Pa^{-n}$, with an average value of 2.0×10^{-25} $s^{-1}Pa^{-n}$. These values for η are all in the same order of magnitude; previous researchers reported coefficients varying from the order of 10^{-40} to 10^{-19}. Young's modulus, E, showed the greatest variation here; for Beltaos' data, E ranged from about 0.6×10^9 to 5.0×10^9 Pa (average $E = 1.8 \times 10^9$ Pa) and for Frankenstein's data E ranged from 0.1×10^9 to 3.5×10^9 Pa (average $E = 1.5 \times 10^9$ Pa). However, the majority of these values for E fall within the range of previously reported results (Figure 2-1).

Each calibrated creep parameter (E, η, and n) was plotted against temperature, but no correlation was found. These parameters appear to be dependent on more than temperature alone.

Based on the results given here, the power law creep model seems to be an acceptable method for predicting the time dependent deflection of an infinite floating ice cover during primary and secondary creep, for both constant and increasing loading situations. A set of relatively consistent creep parameters was obtained. As expected, this model cannot predict the deflection of an ice cover during tertiary (accelerated) creep; the model solution approaches a steady state. Before using this type of model to predict the deflection of an ice cover under loading, the model should be calibrated using as much site specific historical and field test data as there is available.

7.2 Recommendations for Future Research

As this model only considers secondary creep, it would be beneficial to extend the scope of the model to include tertiary creep as well. The ability to identify the time at which tertiary creep begins would be helpful as this signals the onset of failure of the ice cover. An examination of the stresses and strains (elastic and creep) within the ice cover at the onset of tertiary creep might be useful in this regard, and the model has been modified to allow the output of these values along with the deflection at each time step.

It might also be interesting to model a non-homogeneous, anisotropic ice cover, to determine if any more accuracy can be obtained than when assuming a homogeneous, isotropic ice cover. This would require an expression for Young's modulus as a function of depth in the ice. Ice grain size could also be examined quantitatively rather than qualitatively (as described in chapter 2), and incorporated into the model as input.

REFERENCES

Ashton, G.D. (editor). 1986. River and Lake Ice Engineering. Water Resources Publications, Littleton, Colorado.

Assur, A. 1956. Airfields on Floating Ice Sheets for Regular and Emergency Operations. SIPRE Report 36, Corps of Engineers, U.S. Army.

Azizi, F. 1989. Primary creep of polycrystalline ice under constant stress. Cold Regions Science and Technology, v16, n2: pp159-165.

Azizi, F., and W.B. Whalley. 1994. Constitutive Modelling of the Visco-Plastic Behaviour of Ice. Proceedings, Fourth International Offshore and Polar Engineering Conference, v2: pp449-454.

Azuma, N. 1995. A flow law for anisotropic polycrystalline ice under uniaxial compressive deformation. Cold Regions Science and Technology, v23: pp137-147.

Barnes, P., D. Tabor, and J.C.F. Walker. 1971. The friction and creep of polycrystalline ice. Proceedings of the Royal Society of London, Series A, v324: pp127-155.

Barthelemy, J.L. 1992. Nomographs for operating wheeled aircraft on sea-ice runways: McMurdo Station, Antarctica. Proceedings of the International Offshore Mechanics and Arctic Engineering Symposium, v4: pp27-33.

Baudais, D.J., J.S. Watts, and D.M. Masterson. 1976. A System for Offshore Drilling in the Arctic Islands. Offshore Technology Conference, Dallas, TX, Paper Number OTC2622.

Beer, F.P., and E.R. Johnston, Jr. 1992. Mechanics of Materials. McGraw-Hill, Inc.

Beltaos, S. 1978. A strain energy criterion for failure of floating ice sheets. Canadian Journal of Civil Engineering, v5: pp352-361.

Beltaos, S., and A.W. Lipsett. 1979. An empirical analysis of the creep of floating ice sheets. Proceedings, Workshop on Bearing Capacity of Ice Covers. Associate Committee on Geotechnical Research, National Research Council of Canada, Technical Memorandum No. 123: pp124-138.

Butkovich, T.R., and J.K. Landauer. 1959. The flow law for ice. U.S. Army Corps of Engineers Snow, Ice and Permafrost Research Establishment, Research Report No. 56, Wilmette, IL.

Chandrupatla, T.R. and A.D. Belegundu. 1997. Introduction to Finite Elements in Engineering, 2nd Edition. Prentice-Hall, Inc.

Ekelund, M.J., and D.M. Masterson. 1980. Floating ice platforms for oil exploration in the Arctic Islands. Arctic, v33, n1: pp168-183.

Fish, A.M. 1992. Combined creep and yield model of ice under multiaxial stress. Proceedings, Second International Offshore and Polar Engineering Conference, San Francisco, USA, 14-19 June 1992: pp740-749.

Frankenstein, G.E. 1963. Load test data for lake ice sheets. U.S. Army Cold Regions Engineering Laboratory Technical Report 89, Hanover, New Hampshire.

Frederking, R.M.W., and L.W. Gold. 1976. The bearing capacity of ice covers under static loads. Canadian Journal of Civil Engineering, v3: pp288-293.

Gerald, C.F. and P.O. Wheatley. 1984. Applied Numerical Analysis, 3rd Edition. Addison-Wesley Publishing Company, Inc.

Glen, J.W. 1955. The creep of polycrystalline ice. Proceedings, Royal Society of London, Series A, v228: pp519-538.

Gold, L.W. 1988. On the elasticity of ice plates. Canadian Journal of Civil Engineering, v15, n6: pp1080-1084.

Gold, L.W. 1971. Use of Ice Covers for Transportation. Canadian Geotechnical Journal, v8: pp170-181.

Hicks, F., and A. Fayek. 1999. Design Considerations for the use of Ice as a Construction Platform. Proceedings of the 10th Workshop on River Ice-River Ice Management With A Changing Climate: Dealing with Extreme Events, June 8-11, 1999, Winnipeg, MB: pp346-360.

Hult, J.A. 1966. Creep in Engineering Structures. Blaisdell Publishing Company.

Kerr, A.D. 1975. The bearing capacity of floating ice plates subjected to static or quasi-static loads-a critical survey. U.S. Army Cold Regions Research and Engineering Laboratory, Research Report 333.

Khoo, H.A., and T.M. Hrudey. 1992. Constitutive model for ice. Journal of Engineering Mechanics, v118, n2: pp259-279.

Ladanyi, B., and R. Saint-Pierre. 1978. Evaluation of creep properties of sea ice by means of a borehole dilatometer. Proceedings (part 1), IAHR Symposium on Ice Problems, Lulea, Sweden, 7-9 August 1978: pp97-115.

Mahrenholtz, O., and Z. Wu. 1993. Primary creep of ice plate under constant loading. Proceedings, International Conference on Offshore Mechanics and Arctic Engineering, v4: pp97-104.

Masterson, D.M., and R.P. Gamble. 1986. Current Ice Road and Structure Design and Construction Procedures. International Polar Transportation Conference, Vancouver, BC: pp602-648.

Masterson, D.M., and H.R. Kivisild. 1980. Floating Ice Platforms: Offshore Oil Exploration. Journal of the Structural Division, Proceedings of the American Society of Civil Engineers, v106, nST1: pp133-143.

Masterson, D.M., and A.G. Strandberg. 1979. Long-term loading analysis of floating ice platforms using finite element techniques. Proceedings, Workshop on Bearing Capacity of Ice Covers. Associate Committee on Geotechnical Research, National Research Council of Canada, Technical Memorandum No. 123: pp159-182.

McLachlan, N.W. 1955. Bessel Functions for Engineers, 2nd Edition. Oxford University Press.

Meglis, I.L., P.M. Melanson, and I.J. Jordan. 1999. Microstructural change in ice: II, Creep behavior under triaxial stress conditions. Journal of Glaciology, v45, n151: pp438-448.

Mellor, M., and R. Testa. 1969. Effect of temperature on the creep of ice. Journal of Glaciology, v8, n52: pp131-145.

Meneley, W.A. 1974. Blackstrap Lake ice cover parking lot. Canadian Geotechnical Journal, v11: pp490-508.

Michel, B. 1978a. Ice Mechanics. Les Presses de l'Universite Laval, Quebec.

Michel, B. 1978b. A mechanical model of creep of polycrystalline ice. Canadian Geotechnical Journal, v15: pp155-170.

Michel, B., and L. Gagnon. 1979. Time-dependent deflection of an ice plate. Proceedings, Workshop on Bearing Capacity of Ice Covers. Associate Committee on Geotechnical Research, National Research Council of Canada, Technical Memorandum No. 123: pp80-97.

Morgenstern, N.R., W.D. Roggensack, and J.S. Weaver. 1980. The behaviour of friction piles in ice and ice-rich soils. Canadian Geotechnical Journal, v17: pp405-415.

Nevel, D.E., 1968. Bearing capacity of floating ice sheets. U.S. Army Cold Regions Research and Engineering Laboratory, Terrestrial Science Centre.

Nixon, J.F., and E.C. McRoberts. 1976. A design approach for pile foundations in permafrost. Canadian Geotechnical Journal, v13, n40: pp40-57.

Premachandran, R., and H. Horii. 1994. A micromechanics-based constitutive model for polycrystalline ice. Journal of Engineering Materials and Technology—Transactions of the ASME, v116: pp392-397.

Puswewala, U.G.A., and R.K.N.D. Rajapakse. 1993. Computational analysis of creep in ice and frozen soil based on Fish's unified model. Canadian Journal of Civil Engineering, v20: pp120-132.

Rao, S.S. 1989. The Finite Element Method in Engineering, 2nd Edition. Pergamon Press.

Sego, D.C., and N.R. Morgenstern. 1983. Deformation of ice under low stresses. Canadian Geotechnical Journal, v20: pp587-602.

Sinha, N.K. 1992. Winterlude 1986-Dows Lake ice loading test. Proceedings, International Conference on Offshore Mechanics and Arctic Engineering, v4: pp303-310.

Sinha, N.K. 1990. Crowd induced deflection of Dow's Lake ice cover during Winterlude Festival-1985. Proceedings, 9th International Conference on Offshore Mechanics and Arctic Engineering, v4: pp161-167.

Stasa, F.L. 1985. Applied Finite Element Analysis for Engineers. CBS Publishing.

Stewart, J. 1991. Calculus, 2nd Edition, Early Transcendentals. Brooks/Cole Publishing Company.

Sunder, S.S., A. Elvin, and S. Nanthikesan. 1993. Numerical modeling of transient creep in polycrystalline ice. Journal of Engineering Mechanics: v119, n10: pp2011-2035.

Szyszkowski, W., S. Dost and, P.G. Glockner. 1985. A nonlinear constitutive model for ice. International Journal of Solids and Structures, v21, n3: pp307-321.

Timoshenko, S. and S. Woinowsky-Krieger. 1959. Theory of Plates and Shells, 2nd Edition. McGraw-Hill Book Company.

Tinawi, R., and J.R. Murat. 1979. Creep of floating sea-ice sheets-a finite element formulation. 5th International Conference on Port and Ocean Engineering Under Arctic Conditions: pp779-795.

Tinawi, R., and J.R. Murat. 1978. Sea ice-flexural creep. Proceedings (part 1), IAHR Symposium on Ice Problems, Lulea, Sweden, 7-9 August 1978: pp49-75.

Ugural, A.C., and S.K. Fenster. 1995. Advanced Strength and Applied Elasticity, 3rd Edition. Prentice-Hall, Inc.

Wyman, M. 1950. Deflections of an infinite plate. Canadian Journal of Research, Volume 28, Section A: pp293-302.

Zienkiewicz, O.C. 1977. The Finite Element Method. McGraw-Hill Book Company.

Zumdahl, Steven S. 1993. Chemistry, 3rd Edition. D.C. Heath and Company.

APPENDIX A: THE "ASSEMBLY" OPERATOR

In a finite element model, the governing equations to be solved can be reduced to equations for each element. After these equations are evaluated on an element by element basis using local coordinates (forming an element matrix), they must be accumulated to solve the global system. This procedure of combining the element matrices into a global matrix system to be solved is called *assembly*.

Each element consists of two nodes, described locally as node 1 and node 2. Every one of these nodes is also assigned a global index ($1..N_n$, where N_n is the total number of nodes in the finite element formulation). The assembly procedure takes the values computed in each element matrix, local index location ($1..2$), and stores it in its position in the global matrix, adding the contributions from overlapping nodes on adjoining elements.

For example, in a system with three elements (see Figure A-1), the following type of element matrices may be formed:

$$\text{Element 1:} \quad \begin{bmatrix} A_a & B_a \\ C_a & D_a \end{bmatrix} \quad\quad\quad (A.1)$$

$$\text{Element 2:} \quad \begin{bmatrix} E_a & F_a \\ G_a & H_a \end{bmatrix} \quad\quad\quad (A.2)$$

$$\text{Element 3:} \quad \begin{bmatrix} I_a & J_a \\ K_a & L_a \end{bmatrix} \quad\quad\quad (A.3)$$

172

where A_a through L_a represent a numerical value. The assembly procedure would combine the above element matrices into a global matrix:

$$\begin{bmatrix} A_a & B_a & 0 & 0 \\ C_a & D_a + E_a & F_a & 0 \\ 0 & G_a & H_a + I_a & J_a \\ 0 & 0 & K_a & L \end{bmatrix} \tag{A.4}$$

The position (2,2) in element 1 and position (1,1) in element 2 are both at global node 2, and the position (2,2) in element 2 and position (1,1) in element 3 are both at global node 3, therefore the contributions from both elements are combined at these locations.

The assembly operator shall be denoted as:

$$\underset{e=1}{\overset{N_e}{A}}$$

where e is the element number, and N_e is the total number of elements.
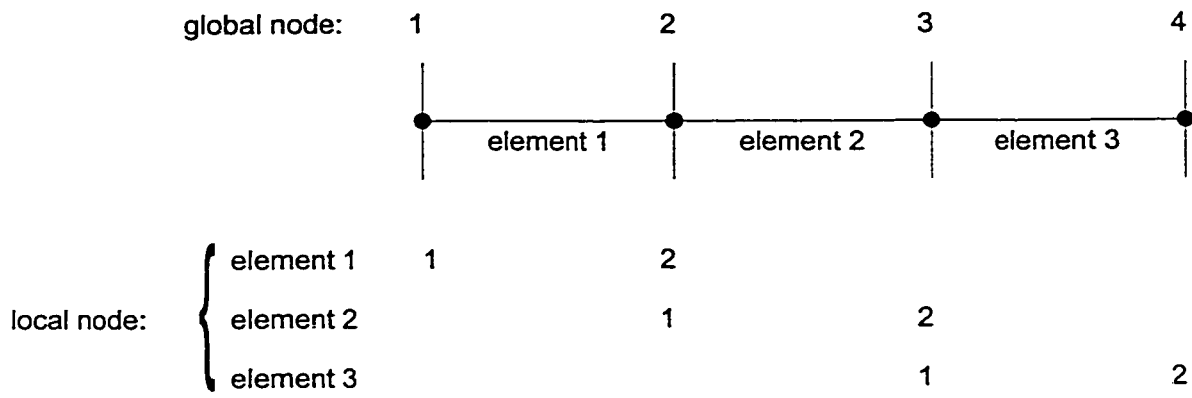
Figure A-1: Example of a 3 element system.

APPENDIX B: EQUATIONS FOR k^u_{ij}, k^w_{ij}, $k_f^w{}_{ij}$ AND p^w_i

From equation (4.4.9), the element horizontal stiffness matrix, $[k^u]$, can be evaluated for each combination of interpolation functions, i and j. The element stiffness matrix is symmetric, that is $k^u_{ij} = k^u_{ji}$; only k^u_{ij} will be shown here:

$$k^u_{1,1} = -2C\pi\left(1 + v + \frac{r_2^2 \ln(r_1)}{(r_1 - r_2)^2} - \frac{r_2^2 \ln(r_2)}{(r_1 - r_2)^2}\right) \tag{B.1}$$

$$k^u_{1,2} = \frac{2C\pi r_1 r_2(\ln(r_1) - \ln(r_2))}{(r_2 - r_1)^2} \tag{B.2}$$

$$k^u_{2,2} = 2C\pi\left(1 + v - \frac{r_1^2 \ln(r_1)}{(r_2 - r_1)^2} + \frac{r_1^2 \ln(r_2)}{(r_2 - r_1)^2}\right) \tag{B.3}$$

where all variables have been defined in chapter 4.

From equation (4.4.12), the element vertical stiffness matrix, $[k^w]$, can be evaluated for each combination of interpolation functions, i and j. This element stiffness matrix is also symmetric, that is $k^w_{ij} = k^w_{ji}$; again, only k^w_{ij} will be shown here:

$$k^w_{1,1} = \frac{18D\pi}{(r_2 - r_1)^6}(-r_1^4 + 4r_1^3 r_2 - 4r_1 r_2^3 + r_2^4 - 4r_1^2 r_2^2 \ln(r_1) + 4r_1^2 r_2^2 \ln(r_2)) \tag{B.4}$$

$$k^w_{1,2} = \frac{3D\pi}{(r_2 - r_1)^5}\left(\begin{array}{l} -3r_1^4 + 10r_1^3 r_2 + 2r_1^2 r_2^2 - 10r_1 r_2^3 + r_2^4 + 8r_1^2 r_2^2 \ln(r_1) \\ -4r_1 r_2^3 \ln(r_1) + 8r_1^2 r_2^2 \ln(r_2) + 4r_1 r_2^3 \ln(r_2) \end{array}\right) \tag{B.5}$$

$$k^w_{1,3} = \frac{18D\pi}{(r_2 - r_1)^6}(r_1^4 - 4r_1^3 r_2 + 4r_1 r_2^3 - r_2^4 + 4r_1^2 r_2^2 \ln(r_1) - 4r_1^2 r_2^2 \ln(r_2)) \tag{B.6}$$

$$k^w_{1,4} = \frac{3D\pi}{(r_2 - r_1)^5}\left(\begin{array}{l} -r_1^4 + 10r_1^3 r_2 - 2r_1^2 r_2^2 - 10r_1 r_2^3 + 3r_2^4 - 4r_1^3 r_2 \ln(r_1) \\ -8r_1^2 r_2^2 \ln(r_1) + 4r_1^3 r_2 \ln(r_2) + 8r_1^2 r_2^2 \ln(r_2) \end{array}\right) \tag{B.7}$$

$$k^w{}_{2,2} = 2D\pi \left(-\left(\frac{r_2^2(2r_1 + r_2)^2 \ln(r_1)}{(r_1 - r_2)^4} \right) + \left(\frac{\begin{array}{c}-13r_1^4 - 4vr_1^4 + 40r_1^3 r_2 + 16vr_1^3 r - 12r_1^2 r_2^2 - 24vr_1^2 r_2^2 - 8r_1 r_2^3 \\ +16vr_1 r_2^3 - 7r_2^4 - 4vr_2^4 + 16r_1^2 r_2^2 \ln(r_2) + 16r_1 r_2^3 \ln(r_2) + 4r_2^4 \ln(r_2)\end{array}}{4(r_2 - r_1)^4} \right) \right) \tag{B.8}$$

$$k^w{}_{2,3} = \frac{3D\pi}{(r_2 - r_1)^5} \left(\begin{array}{c} 3r_1^4 - 10r_1^3 r_2 - 2r_1^2 r_2^2 + 10r_1 r_2^3 - r_2^4 + 8r_1^2 r_2^2 \ln(r_1) \\ + 4r_1 r_2^3 \ln(r_1) - 8r_1^2 r_2^2 \ln(r_2) - 4r_1 r_2^3 \ln(r_2) \end{array} \right) \tag{B.9}$$

$$k^w{}_{2,4} = \frac{D\pi}{2(r_2 - r_1)^4} \left(\begin{array}{c} -3r_1^4 + 24r_1^3 r_2 - 24r_1 r_2^3 + 3r_2^4 - 8r_1^3 r_2 \ln(r_1) \\ -20r_1^2 r_2^2 \ln(r_1) - 8r_1 r_2^3 \ln(r_1) + 8r_1^3 r_2 \ln(r_2) \\ +20r_1^2 r_2^2 \ln(r_2) + 8r_1 r_2^3 \ln(r_2) \end{array} \right) \tag{B.10}$$

$$k^w{}_{3,3} = \frac{18D\pi}{(r_2 - r_1)^6}(-r_1^4 + 4r_1^3 r_2 - 4r_1 r_2^3 + r_2^4 - 4r_1^2 r_2^2 \ln(r_1) + 4r_1^2 r_2^2 \ln(r_2)) \tag{B.11}$$

$$k^w{}_{3,4} = \frac{3D\pi}{(r_2 - r_1)^5} \left(\begin{array}{c} r_1^4 - 10r_1^3 r_2 + 2r_1^2 r_2^2 + 10r_1 r_2^3 - 3r_2^4 + 4r_1^3 r_2 \ln(r_1) \\ + 8r_1^2 r_2^2 \ln(r_1) - 4r_1^3 r_2 \ln(r_2) - 8r_1^2 r_2^2 \ln(r_2) \end{array} \right) \tag{B.12}$$

$$k^w{}_{4,4} = \frac{D\pi}{2(r_2 - r_1)^4} \left(\begin{array}{c} 7r_1^4 + 4vr_1^4 + 8r_1^3 r_2 - 16vr_1^3 r_2 + 12r_1^2 r_2^2 + 24vr_1^2 r_2^2 \\ -40r_1 r_2^3 - 16vr_1 r_2^3 + 13r_2^4 + 4vr_2^4 - 4r_1^4 \ln(r_1) \\ -16r_1^3 r_2 \ln(r_1) - 16r_1^2 r_2^2 \ln(r_1) + 4r_1^4 \ln(r_2) \\ +16r_1^3 r_2 \ln(r_2) + 16r_1^2 r_2^2 \ln(r_2) \end{array} \right) \tag{B.13}$$

where all variables have been defined in chapter 4.

From equation (4.5.5), the element elastic foundation stiffness matrix, $[k_f^w]$, can be evaluated for each combination of interpolation functions, i and j. This matrix is also symmetric, with $k_f^w{}_{ij} = k_f^w{}_{ji}$; again, only $k_f^w{}_{ij}$ will be shown here:

$$k_{f\,1,1}^w = \frac{2\gamma\pi}{35}\left(-10r_1^2 + 7r_1 r_2 + 3r_2^2\right) \tag{B.14}$$

$$k_{f\,1,2}^w = \frac{\gamma\pi}{210}(r_2 - r_1)^2(15r_1 + 7r_2) \tag{B.15}$$

176

$$k^w_{f_{1,3}} = \frac{9\gamma\pi}{70}\left(r_2^2 - r_1^2\right)$$ (B.16)

$$k^w_{f_{1,4}} = -\frac{\gamma\pi}{210}\left(r_2 - r_1\right)^2\left(7r_1 + 6r_2\right)$$ (B.17)

$$k^w_{f_{2,2}} = \frac{\gamma\pi}{420}\left(r_2 - r_1\right)^3\left(5r_1 + 3r_2\right)$$ (B.18)

$$k^w_{f_{2,3}} = \frac{\gamma\pi}{210}\left(r_2 - r_1\right)^2\left(6r_1 + 7r_2\right)$$ (B.19)

$$k^w_{f_{2,4}} = \frac{\gamma\pi}{140}\left(r_1 - r_2\right)^3\left(r_1 + r_2\right)$$ (B.20)

$$k^w_{f_{3,3}} = \frac{2\gamma\pi}{35}\left(-3r_1^2 - 7r_1r_2 + 10r_2^2\right)$$ (B.21)

$$k^w_{f_{3,4}} = -\frac{\gamma\pi}{210}\left(r_2 - r_1\right)^2\left(7r_1 + 15r_2\right)$$ (B.22)

$$k^w_{f_{4,4}} = \frac{\gamma\pi}{420}\left(r_2 - r_1\right)^3\left(3r_1 + 5r_2\right)$$ (B.23)

where all variables have been defined in chapter 4.

From equation (4.6.4), the element vertical load vector, $\{p^w\}$, can be evaluated for each interpolation function, i:

$$p^w_1 = \frac{\pi q_o}{10}\left(-7r_1^2 + 4r_1r_2 + 3r_2^2\right)$$ (B.24)

$$p^w_2 = \frac{\pi q_o}{30}\left(r_2 - r_1\right)^2\left(3r_1 + 2r_2\right)$$ (B.25)

$$p^w_3 = \frac{\pi q_o}{10}\left(-3r_1^2 - 4r_1r_2 + 7r_2^2\right)$$ (B.26)

$$p^w_4 = -\frac{\pi q_o}{30}\left(r_2 - r_1\right)^2\left(2r_1 + 3r_2\right)$$ (B.27)

where all variables have been defined in chapter 4.

177

APPENDIX C: VISUAL BASIC APPLICATION

The finite element model described in chapter 4 was developed into a computer application using Visual Basic. The program, *Creep Model 1.0*, consists of a simple user-friendly interface, and requires the user to create one input file detailing the element discretization, load durations and magnitudes, and boundary conditions. The *Readme* file accompanying the program contains information pertinent to the proper use of the model.

After passing the start-up window for the model, the user is presented with the main interface window, which can be seen in Figure C-1. By clicking the *Input* button, a window appears that allows the user to choose an input file (see Figure C-2). An example of an input file can be seen in Figure C-3. An explanation of the various components of the input file can be found in the *Readme* file accompanying the program.

The user must next choose the output files for the model to create (*Output* button), and a destination folder for these output files (see Figure C-4). The default choice is to print a summary file, an elastic solution file (which also contains the elastic analytical solution), and file containing the deflection under the centre of the load at each time step. Three other files can be created if desired: the deflection bowl at each time step; the radial and tangential stresses at each time step; and the elastic, creep and total strains throughout the ice cover at each time step. These files can grow quite large, depending on the spatial and temporal discretization chosen, and selecting them as output files increases the computational time required to run the model.

The main model interface window (Figure C-1) allows the user to specify if an elastic foundation is present, and if so, give a value for the foundation modulus (γ).

Values for Young's modulus (E) and Poisson's ratio (ν) must also be chosen prior to solving the elastic problem (*Solve* button).

In the creep solution section of the main interface window, the user is given a choice of using the Euler method or the 4th Order Runge-Kutta method to estimate the creep strain increments at each time step (discussed in detail in chapter 4). Values for the creep exponent (n) and the creep coefficient (η) must be specified, along with the number of integration (Gauss) points to use in the radial and vertical directions.

Next, the time step increments (Δt) must be specified. Clicking the *Time Steps* button brings up a window in which the user can specify three different Δt values and the duration of each Δt (see Figure C-5). Each of these fields must contain a value in order for the model to run, but all Δt fields can contain the same value if only one time step increment is required.

Finally, by selecting the *Solve* button in the creep solution section (Figure C-1), the model calculates the solution and writes information to the appropriate output files at each time step. The computational time required for the model to run varies depending on the speed of the computer, the spatial and temporal discretization, and on the output files that are required; the start and finish times are shown at the bottom of the window once the model has finished all calculations.
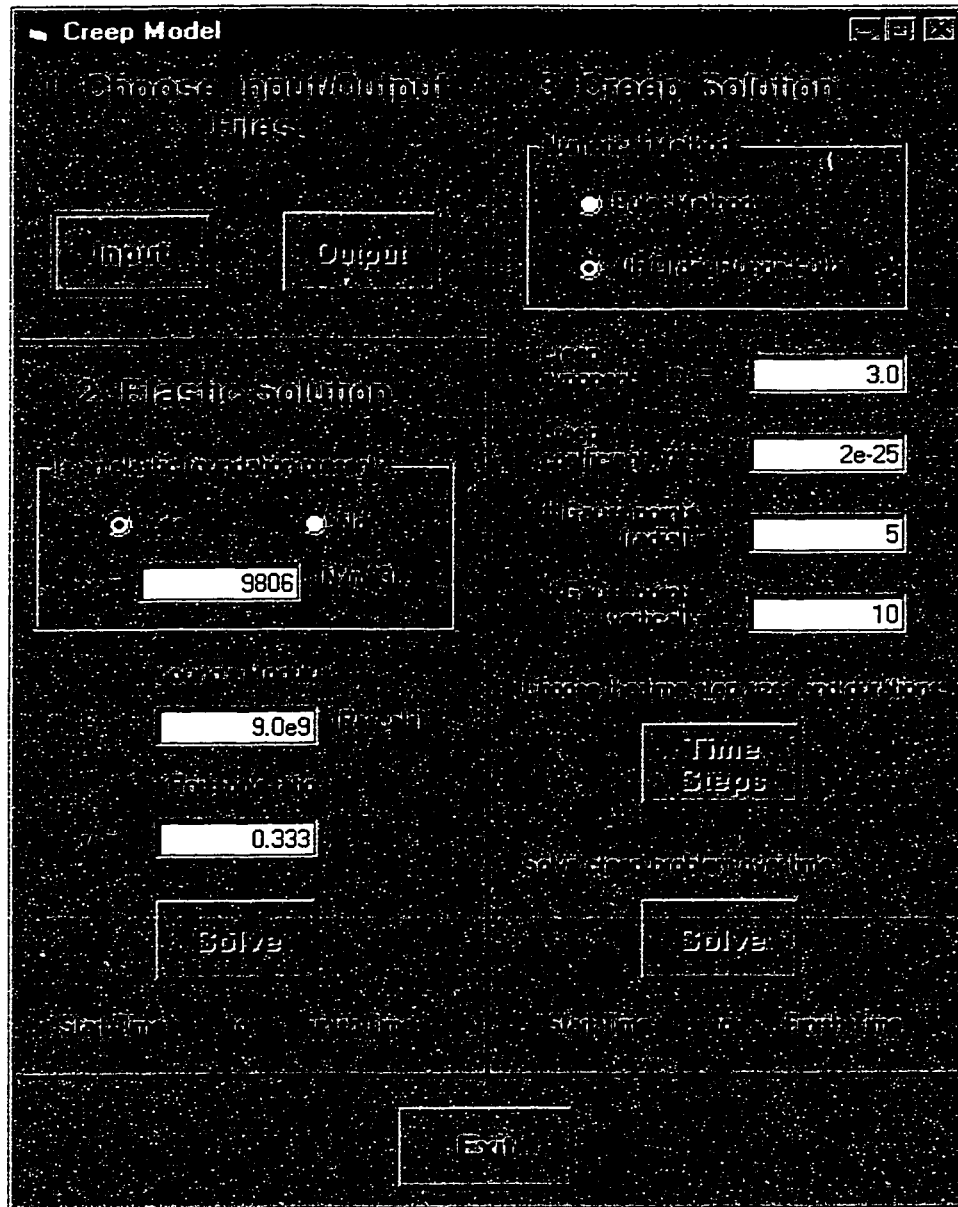
Figure C-1: Creep model main interface window.

Choose an input file:

c:

C:\
CreepModel
input

input.txt

inBessel.txt
input.txt
sample_input.txt

Text files (*.txt)
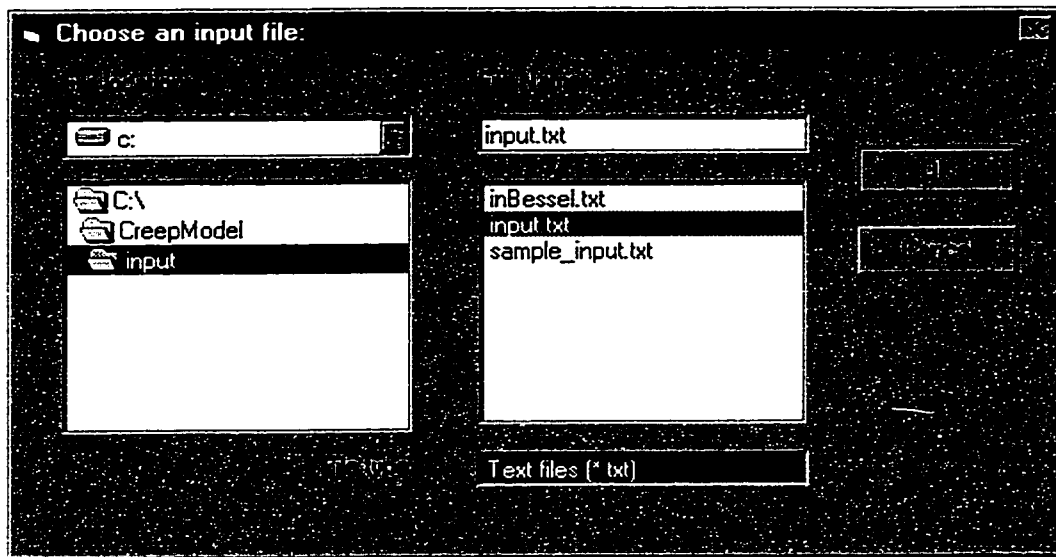
Figure C-2: Model input file selection window.

sample_input - Notepad

```
0.305
3          0          1500       5675
10
1          0          0
2          0.5        0
3          0.915      0
4          1.5        0
5          2          0
6          3          0
7          4          0
8          5          0
9          6          0
10         7          0
9
1          1          2          3134       3134       38953      39091
2          2          3          3134       3134       38953      39091
3          3          4          0          0          0          0
4          4          5          0          0          0          0
5          5          6          0          0          0          0
6          6          7          0          0          0          0
7          7          8          0          0          0          0
8          8          9          0          0          0          0
9          9          10         0          0          0          0
3
1          0
3          0
4          0
sample_input
```

Figure C-3: Sample input file for creep model.

181

Figure C-4: Model output file selection window.
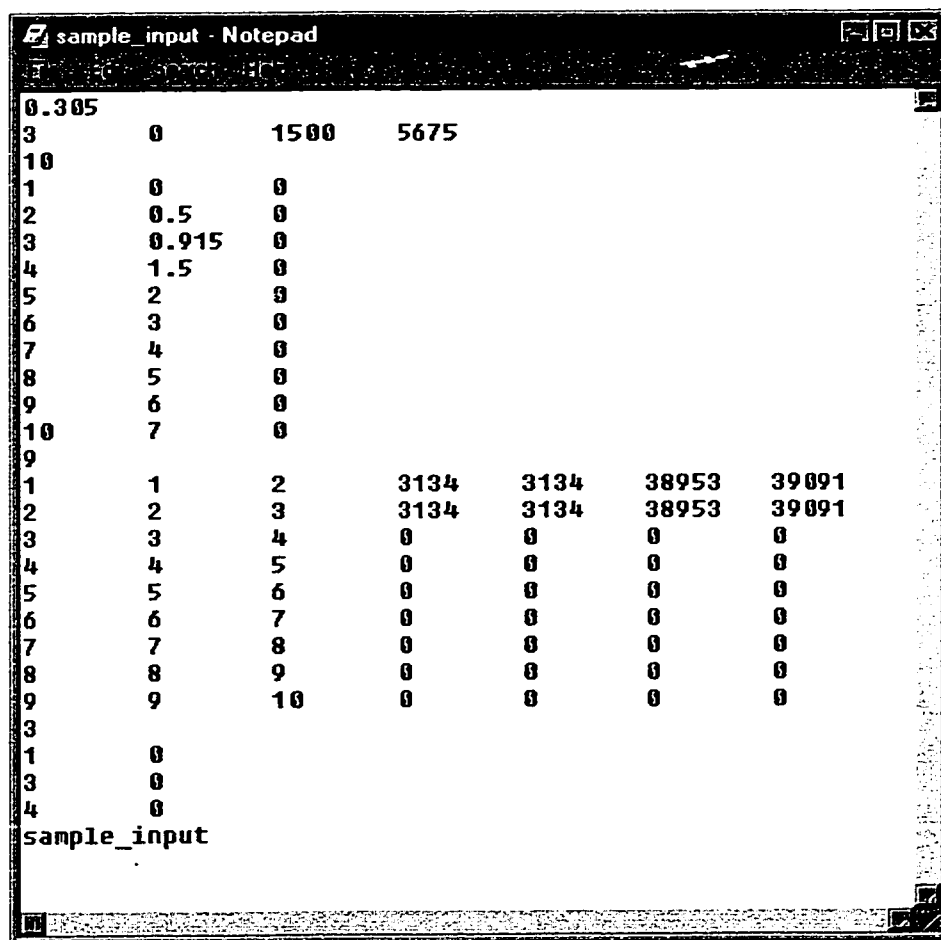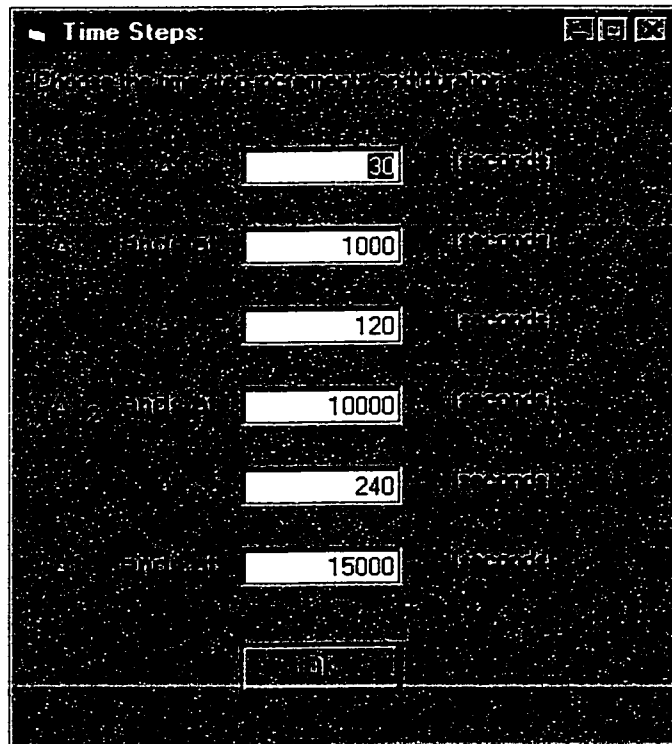

Figure C-5: Model time step increment selection window.

APPENDIX D: BESSEL FUNCTIONS

In the computation of the analytical solution for an infinite elastic plate on an elastic foundation, it is necessary to evaluate certain Bessel functions. In Wyman's (1950) analytical solution, eight Bessel functions (ber(y_0), bei(y_0), ber'(y_0), bei'(y_0), ker(y_0), kei(y_0), ker'(y_0), and kei'(y_0)) need to be evaluated for values of $y_0 \geq 0$.

For each of these Bessel functions, McLachlan (1955) gives expressions for the function for $0 \leq y_0 < 1$, and for $y_0 > 10$. For $1 \leq y_0 \leq 10$, McLachlan (1955) gives a table of values for each function, which we used to fit curves for this research for the purpose of more convenient implementation in a computer program or spreadsheet. Thus, each Bessel function is comprised of three distinct continuous functions for all values of $y_0 \geq 0$.

In the range of $0 \leq y_0 < 1$, the eight Bessel functions are evaluated with the following expressions:

$$\text{ber}(y_0) = 1 - \frac{y_0^4}{2^2 \cdot 4^2} + \frac{y_0^8}{2^2 \cdot 4^2 \cdot 6^2 \cdot 8^2} - \cdots \tag{D.1}$$

$$\text{bei}(y_0) = \frac{y_0^2}{2^2} - \frac{y_0^6}{2^2 \cdot 4^2 \cdot 6^2} + \cdots \tag{D.2}$$

$$\text{ber}'(y_0) = -\frac{4y_0^3}{2^2 \cdot 4^2} + \frac{8y_0^7}{2^2 \cdot 4^2 \cdot 6^2 \cdot 8^2} - \cdots \tag{D.3}$$

$$\text{bei}'(y_0) = \frac{2y_0}{2^2} - \frac{6y_0^5}{2^2 \cdot 4^2 \cdot 6^2} + \cdots \tag{D.4}$$

$$\text{ker}(y_0) \approx A_o + \frac{1}{4}\pi\omega^2 - \frac{1}{4}\left(A_o + \frac{3}{2}\right)\omega^4 - \frac{1}{144}\pi\omega^6 + \frac{1}{576}\left(A_o + \frac{25}{12}\right)\omega^8 \tag{D.5}$$

$$\text{kei}(y_0) \approx -\frac{1}{4}\pi + (A_o + 1)\omega^2 + \frac{1}{16}\pi\omega^4 - \frac{1}{36}\left(A_o + \frac{11}{6}\right)\omega^6 - \frac{1}{2304}\pi\omega^8 \tag{D.6}$$

$$\text{ker}'(y_0) \approx -\frac{1}{2\omega} + \frac{1}{4}\pi\omega - \frac{1}{2}\left(A_o + \frac{5}{4}\right)\omega^3 - \frac{1}{48}\pi\omega^5 + \frac{1}{144}\left(A_o + \frac{47}{24}\right)\omega^7 \qquad \text{(D.7)}$$

$$\text{kei}'(y_0) \approx \left(A_o + \frac{1}{2}\right)\omega + \frac{1}{8}\pi\omega^3 - \frac{1}{12}\left(A_o + \frac{5}{3}\right)\omega^5 - \frac{1}{576}\pi\omega^7 \qquad \text{(D.8)}$$

where $\omega = 0.5y_0$ and $A_o = 0.1159315 - \ln(y_0)$.

Between $y_0 = 1$ and $y_0 = 10$, the curves fit to the Bessel functions took one of three forms:

$$f_1(y_0) = \frac{a + c\ln y_0 + e(\ln y_0)^2 + g(\ln y_0)^3 + i(\ln y_0)^4 + k(\ln y_0)^5}{1 + b\ln y_0 + d(\ln y_0)^2 + f(\ln y_0)^3 + h(\ln y_0)^4 + j(\ln y_0)^5} \qquad \text{(D.9)}$$

or
$$f_2(y_0) = \frac{a + cy_0 + ey_0^2 + gy_0^3 + iy_0^4 + ky_0^5}{1 + by_0 + dy_0^2 + fy_0^3 + hy_0^4 + jy_0^5} \qquad \text{(D.10)}$$

or
$$f_3(y_0) = a + by_0 + cy_0^2 + dy_0^3 + ey_0^4 + fy_0^5 + gy_0^6 + hy_0^7 + iy_0^8 \qquad \text{(D.11)}$$

where the values of the coefficients a through k can be found in Table D-1.

For $y_0 > 10$, the functions took one of two forms:

$$f_1(y_0) \approx \frac{0.3989e^{(y_0/\sqrt{2})}}{\sqrt{y_0}}\left[\xi \cdot \sin(40.514y_0 + \theta)^{\rho} + \frac{\mu}{8y_0}\sin(40.514y_0 + \beta)^{\rho}\right] \qquad \text{(D.12)}$$

or
$$f_2(y_0) \approx \frac{1.2533e^{(-y_0/\sqrt{2})}}{\sqrt{y_0}}\left[\xi \cdot \sin(40.514y_0 + \theta)^{\rho} + \frac{\mu}{8y_0}\sin(40.514y_0 + \beta)^{\rho}\right] \qquad \text{(D.13)}$$

where values for θ, β, ξ, and μ can be found in Table D-2.

The eight Bessel functions can be seen graphically in Figures D-1 and D-2 for $0 \le y_0 < 11$.

184

Table D-1: Coefficients for Bessel functions for the range $1 \leq y_0 \leq 10$.

Function	Form	R^2	a	b	c	d	e
ber(y₀)	$f_1(y_0)$	0.99999802	0.9862748500	-0.9069654000	-1.0108225000	-0.3335481000	-0.1316191400
bei(y₀)	$f_2(y_0)$	0.99999987	0.0390255320	-0.0417576250	0.0601605270	-0.0471436280	0.0877288210
ber'(y₀)	$f_3(y_0)$	0.99998658	-0.0018975764	-0.0046015251	-0.0104421370	-0.0195444700	-0.0219514320
bei'(y₀)	$f_1(y_0)$	0.99999892	0.4969831600	-0.9897739700	0.0123374840	-0.0976290130	-0.4227852600
ker(y₀)	$f_1(y_0)$	0.99999992	0.2866961900	-1.2247398000	-1.0462823000	0.6951654200	1.3020882000
kei(y₀)	$f_1(y_0)$	0.99999998	-0.4949936200	-1.3293997000	1.0105644000	0.8690494400	-0.7571286100
ker'(y₀)	$f_1(y_0)$	0.99999993	-0.6946030200	-0.6739228000	1.6585027000	0.0970955700	-1.4010041000
kei'(y₀)	$f_1(y_0)$	0.99999998	0.3523850800	-0.7775237000	-0.3338997140	-0.0253802700	-0.1374127900

Function	f	g	h	i	j	k
ber(x)	0.6659075600	0.1766973400	-0.2699359600	0.0104464040	0.0358164970	0
bei(x)	0.0091099632	0.0916953510	-0.0006622287	-0.0353056970	0.0000178081	0.0025964717
ber'(x)	0.0059364390	-0.0015031097	0.0003266207	-0.0000206575	0	0
bei'(x)	0.4480626300	0.2343107400	-0.1866320400	-0.2023074000	0.0243416530	0.0756313670
ker(x)	-0.1794386700	-0.7456181400	0.0084443529	0.2027749600	0.0057724023	-0.0212977280
kei(x)	-0.2962222100	0.2479522000	0.0464570850	-0.0300541830	0.0016343391	0
ker'(x)	0.1277445300	0.5059584100	-0.0643291040	-0.0666433670	0.0171637030	0
kei'(x)	0.4106524200	0.2677729200	-0.2473458500	-0.1064822700	0.0562181480	0.0136123790

Table D-2: Coefficients for Bessel functions for the range $y_0 > 10$ (adapted from McLachlan, 1955).

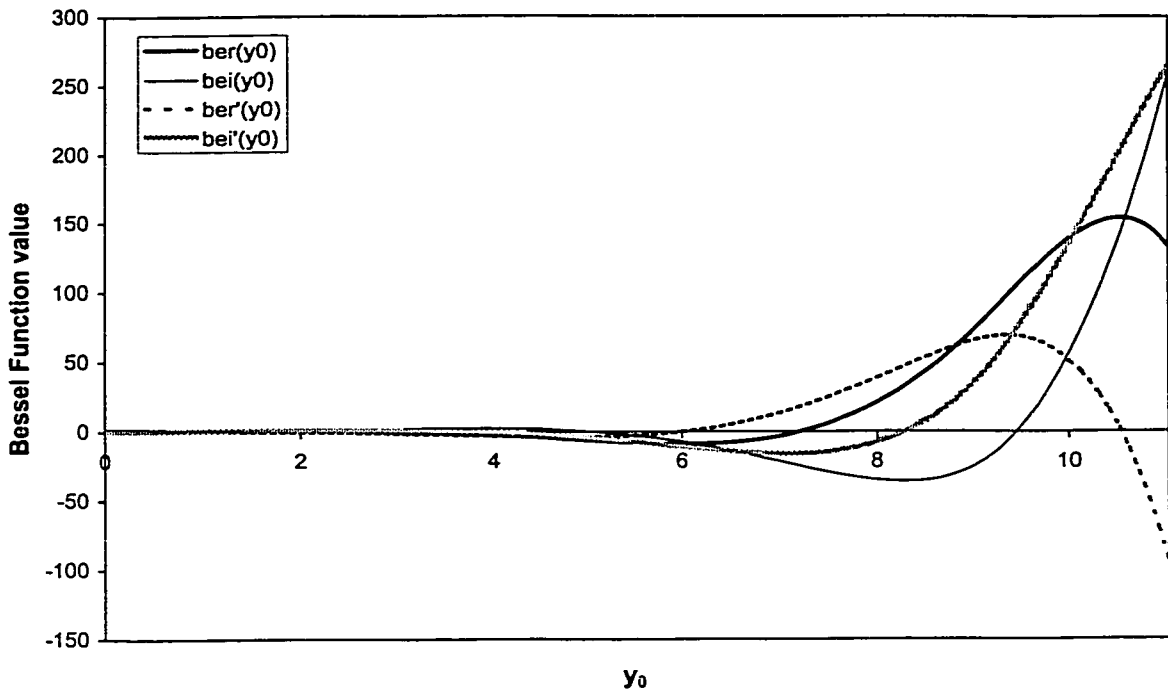| Function	Form	α	β	ξ	μ
ber(y_0)	$f_1(y_0)$	67.5	22.5	1	1
bei(y_0)	$f_1(y_0)$	-22.5	-67.5	1	1
ber'(y_0)	$f_1(y_0)$	112.5	67.5	1	-3
bei'(y_0)	$f_1(y_0)$	22.5	-22.5	1	-3
ker(y_0)	$f_2(y_0)$	112.5	-22.5	1	1
kei(y_0)	$f_2(y_0)$	22.5	67.5	-1	1
ker'(y_0)	$f_2(y_0)$	67.5	112.5	1	3
kei'(y_0)	$f_2(y_0)$	-22.5	22.5	1	3

Figure D-1: Bessel functions $ber(y_0)$, $bei(y_0)$, $ber'(y_0)$ and $bei'(y_0)$.
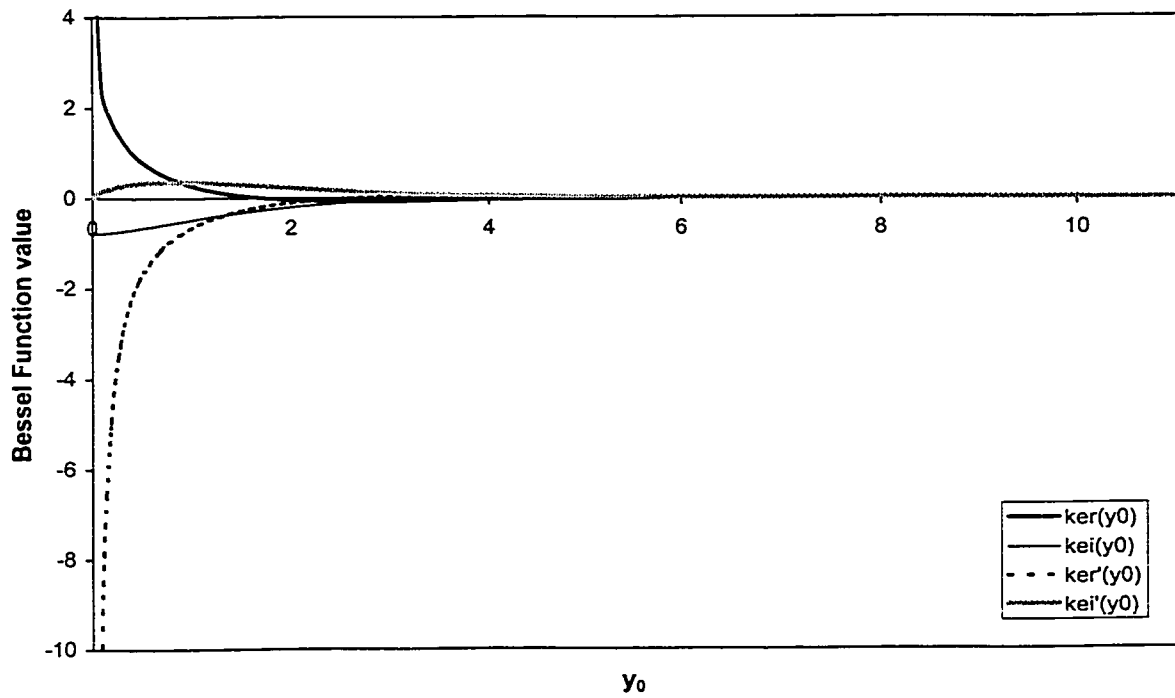

Figure D-2: Bessel functions $ker(y_0)$, $kei(y_0)$, $ker'(y_0)$ and $kei'(y_0)$.